1-1-2006

Deformation characteristics of thermoplastic elastomers.

Kishore K. Indukuri
University of Massachusetts Amherst

DEFORMATIONAL CHARACTERISTICS OF THERMOPLASTIC ELASTOMERS

A Dissertation Presented

by

KISHORE K. INDUKURI

Submitted to the Graduate School of the
University of Massachusetts Amherst in partial fulfillment
of the requirements for the degree of

DOCTOR OF PHILOSOPHY

February 2006

Polymer Science and Engineering

DEFORMATIONAL CHARACTERISTICS OF THERMOPLASTIC ELASTOMERS

A Dissertation Presented

by

KISHORE K. INDUKURI

Approved as to style and content by:

Alan J. Lesser, Chair

Richard J. Farris, Member

Henning H. Winter, Member

Shaw Ling Hsu, Department Head
Polymer Science and Engineering

DEDICATION

Amma, Naanna and Kiran

ACKNOWLEDGMENTS

I would like to thank Prof. Alan Lesser for being a great mentor. He has taught me the importance of being responsible for my own research work in the lab. I enjoyed immensely the freedom he gave me in trying out various things in the lab. This greatly enhanced my knowledge of application of the basic principles of science for solving material science problems. I am also extremely grateful to him for all the opportunities he provided me in presenting my work at various places. He taught me very patiently the importance of communicating ideas simply and effectively.

My sincere thanks to Prof. Richard J. Farris and Prof. Henning H. Winter for serving on my committee. They provided me numerous suggestions during my work that greatly improved the quality of this thesis. I consider it a great privilege for me to have such accomplished scientists on my committee. I am also thankful to Prof. Farris for letting me use deformation calorimeter for my studies.

I am extremely grateful to Prof. Edward T. Akins for his help, insight and guidance with X-ray diffraction work. I consider myself fortunate to be able to get a chance to interact closely with him in the last 1-1/2 years. I truly cherish the great discussions I had with him.

I would like to thank past members of the Lesser group Kathryn, Adam, Terry, Arun, Ramas, Manuel, Angelo and Greg for all their help in the lab. I had the pleasure of working with Kathryn not only in my first year on the modeling study, but also was able to interact with her during my thesis work on KRATON Polymers. Her suggestions and help are greatly appreciated. The present Lesser group Dr. Xianbo Hu, Donna,

Kevin, Melissa, Peter, Mohit, Joonsung and Scott are a cool bunch and we all had so much fun together both inside and outside the lab. Donna was awesome office mate for the past 5 years.

I would like to extend my thanks to Naveen Aggarwal for helping me with suggestions on the deformation calorimeter. Inspite of the distance, he gave me much needed direction (over the phone) in the initial few months to get the calorimeter up and running. Dr. Richard Lyon took an active interest in my work on deformation calorimetry and his suggestions are greatly appreciated. His thesis served as an excellent benchmark for quality Ph.D. work one should vie for in a Ph.D. I would also like to thank Dr. Amiya Tripathy for his suggestions and help.

My acknowledgements to MRSEC, CUMIRP and KRATON Polymers for all the funding support through the years. Many thanks to Lou Raboin and John Domian for all the help through the years. The graduate life became simpler with the support of the PS&E office group-Vivien, Anita, Eileen, Joan, Sophie, Ann, Andrew, Katera and others.

There are numerous friends who have made my stay at UMass very pleasant. My roommates Anwar, Santhosh, Bala, Arun, Suresh Deepak, Ramon & family for being such awesome friends through these years. Also, Radhika and Srividya for their friendship. Manuel, Margarita, Angelo and Bhavini for being such cool friends, who helped me sail through some of the rough times when things were not working in the lab. Many thanks to friends from the Art of Living group at UMass with whom I had close interaction in the last year. My heart felt thanks to Sri Sri for teaching me some of

these beautiful things through his students. Many thanks to Akshaye, Ramesh and Sheels for their kindness and warmth.

My special thanks to cousin Rajendra, his wife Lalitha and their dearest daughter Tanvi for being the closest family here in the US. Frequent trips to their house gave me the much needed break from work.

Finally, for their constant love and support, I would like to thank my father, mother and brother. My mom's constant struggle to see me as the "best of the best" instilled in me an attitude to achieve things come what may.

ABSTRACT

DEFORMATIONAL CHARACTERISTICS OF THERMOPLASTIC ELASTOMERS

FEBRUARY 2006

KISHORE K. INDUKURI, B.Sc., INDIAN INSTITUTE OF TECHNOLOGY KHARAGPUR

M.S., UNIVERSITY OF MASSACHUSETTS AMHERST

Ph.D., UNIVERSITY OF MASSACHUSETTS AMHERST

Directed by: Professor Alan J. Lesser

This thesis focuses primarily on the structure-property relationships of poly (styrene-ethylene-butylene-styrene) triblock copolymer TPEs. First evidence for strain-induced crystallization occurring in certain SEBS block copolymers has been established using unique techniques like deformation calorimetry, combined in-situ small angle X-ray and wide angle X-ray diffraction (SAXD/WAXD). Also the ramifications of such strain-induced crystallization on the mechanical properties like cyclic hysteresis, stress relaxation/creep retention of these SEBS systems have been studied. In addition, the structural changes in the morphology of these systems on deformation have been investigated using combined SAXD/WAXD setup. Small angle X-ray diffraction probed the changes at the nano-scale of polystyrene (PS) cylinders, while wide angle X-ray diffraction probed the changes at molecular length scales of the amorphous/crystalline domains of the elastomeric mid-block in these systems. New structural features at both these length scales have been observed and incorporated into the overall deformation mechanisms of the material.

Continuous processing techniques like extrusion have been used to obtain ultra long-range order and orientation in these SEBS systems. Thus well ordered crystal like hexagonal packing of cylinders, where in each element in this hexagonal lattice can be individually addressed without any grain boundaries can be realized using these robust techniques. The effect of long-range order/orientation on the mechanical properties has been studied. In addition, these well ordered systems serve as model systems for evaluating deformation mechanisms of these SEBS systems, where the relative contributions of each of the phases can be estimated.

EPDM/i-PP thermoplastic vulcanizates (TPVs) have micron size scale phase separated morphologies of EPDM rubber dispersed in a semicrystalline i-PP matrix as a result of the dynamic vulcanization process. Confocal microscopy studies, along with scanning electron microscopy (SEM) studies show that the morphology of these EPDM/i-PP systems resembles a microcellular "filled" foam in which i-PP occupies the strut regions and EPDM the inner core. Based on this, an analytical model has been developed that takes into account composition information, molecular weight, cure state and morphology into account.

TABLE OF CONTENTS

LIST OF TABLES

LIST OF FIGURES

CHAPTER 1

INTRODUCTION

1.1 Structure Property Relationships of SEBS Thermoplastic Elastomers

Styrenic block copolymer thermoplastic elastomers are one of the most widely used thermoplastic elastomers (TPEs) today. As thermoplastic elastomers (TPEs), they are elastomeric at service temperatures, but can be easily processed as thermoplastics at elevated temperatures. This ease of processing and recyclability are major advantages TPEs possess over conventional chemically cross-linked elastomers [1].

Since their introduction six decades ago, various aspects[1-22] of styrene-butadiene-styrene (SBS) and styrene-isoprene-styrene (SIS) block copolymers TPEs have been extensively studied. These studies identify several important deformation mechanisms. A four-point zigzag pattern in small angle x-ray diffraction has been observed in all of these systems at moderate strains. This has been attributed to the microbuckling of polystyrene (PS) cylinders that occurs, as they are stretched perpendicular to their orientation direction. In addition, it has been observed in some studies[10,13,15,18] that these cylindrical rods when deformed parallel to the stretching direction, break into smaller rods. Theoretical[20] and experimental[21,22] studies relating the observed structural changes in morphology to uniaxial tensile tests show that this buckling instability can be related to a sharp turnover in the stress-strain curve observed for these block copolymers.

Though the structure property relationships of un-hydrogenated SBS, SIS block copolymers have been studied by several authors [8,11,13,19,23-27], very few studies have

been devoted to commercially important SEBS block copolymers. SEBS systems are obtained by hydrogenation of butadiene segment of the SBS block copolymers and have ethylene-butylene (E/B) mid-blocks which resemble branched polyethylene chains (with ethyl branches)[1]. Increasing or decreasing the number of branches can make the E/B phase of SEBS system slightly more crystalline or completely amorphous[1,28]. It can be expected that this ability to crystallize can have significant influence on their mechanical properties.

These SEBS systems have interesting morphologies at different length scales (one at the nanometer length scale of cylinders/spheres and the other at the molecular length scales of crystallites). There are no detailed studies investigating the structural changes in morphology that occur upon deformation of SEBS systems at these two length scales. Also no detailed mechanical and mechano-calorimetric investigations have been undertaken thus far in these technologically important materials. This thesis looks at the mechanical and thermal properties of a series of model SEBS systems. The effects of the subtle changes of the mid-block architecture on the thermal, mechanical and calorimetric behavior of these SEBS systems are investigated. In-situ combined small-angle x-ray diffraction and wide-angle x-ray diffraction studies are conducted to understand the deformation behavior of these materials at two different length scales. These studies help in establishing the fundamentals of mechanisms of deformation in these technologically important materials.

1.2 Long Range Order in SEBS triblock copolymers

It has been observed for SBS and SIS triblock copolymers that orientation/long range order of the nano scale domains can be obtained by techniques such as extrusion and solution based roll casting [7,9,29,30]. In addition, external fields like electric field and high magnetic fields have been utilized for obtaining order/orientation in thin films of block copolymer systems. Often, these oriented SBS/SIS systems require further annealing steps to improve or retain order in these systems. SEBS systems on the other hand have much higher melt viscosities than SBS systems because their interaction parameters are at least two-and-one-half times greater than those of their respective SBS analogues. Their melt viscosities are extremely non Newtonian and hence there is an intact network structure which persists in the 'melt' and prevents the development of dissipative flow in shear fields even at temperatures as high as 300°C [1]. The flow for these SEBS systems is not temperature-activated at least up to 260° C, thus making SEBS systems extremely difficult to process. Hence there have not been many studies looking at the orientation/long-range order that can be obtained with conventional processing techniques like extrusion, calendering etc. on SEBS systems. This intact network structure at high temperatures could be used for preserving long-range order/orientation introduced through different processing techniques, thus avoiding successive annealing steps to improve order/orientation.

Oriented SBS/SIS samples have also been used for probing mechanical anisotropy in block copolymers since they provide well-defined initial 'single crystal' morphologies upon orientation. Keller and coworkers studied highly oriented SBS TPEs mechanically and have shown that these systems can be treated as nearly perfect

composite materials [9,23]. Thomas and coworkers [21,22] studied the deformation of cylindrical PS domains of a near single crystal styrene-isoprene-styrene (SIS) triblock copolymer by SAXS and TEM techniques and related it to the macroscopic mechanical behavior of the system. Thus, oriented systems provide well-defined morphologies for probing deformation mechanisms of these block copolymer systems. Since SEBS TPEs are one of the most widely used TPEs, probing the deformation mechanisms by preparing highly ordered SEBS systems would be highly advantageous for predicting their mechanical properties.

This thesis looks at different continuous processing techniques for obtaining long-range order in SEBS systems. Oriented systems obtained by these techniques are investigated for their mechanical behavior.

1.3 Modeling Studies of EPDM/i-PP Thermoplastic Vulcanizates

Dynamically vulcanized blends of ethylene propylene diene monomer (EPDM) rubber and isotactic polypropylene (i-PP) have emerged as a new class of thermoplastic elastomers with vastly different morphologies from those of block copolymer TPEs. These EPDM/i-PP TPEs are produced by dynamic vulcanization[31,32] and are hence commonly referred to as Thermoplastic Vulcanizates (TPVs). This process involves selective curing of the rubber component and its dispersion in semicrystalline thermoplastic resin with intensive mixing and kneading. A fine dispersion of cross-linked rubber particles (in the micron size range) in the thermoplastic matrix is produced as a result of this process. The morphologies produced by this process are influenced by composition and result in a wide range of mechanical behavior. There

has been lot of effort devoted to characterizing the various morphologies produced using this dynamic vulcanization process[33-37].

Compared to block copolymers TPEs and traditional crosslinked elastomers, little work has been done on EPDM/i-PP TPEs to relate their composition and morphology to the observed mechanical behavior. Two different modeling approaches[31,37-42] to explain the micro-mechanisms of deformation of thermoplastic vulcanizates have recently been presented. These finite element studies produce quite different results and establish completely different mechanisms of deformation for these EPDM/i-PP TPVs. Also the general effects of composition, cure state of EPDM rubber on the mechanical properties have not been clearly established. Also, finite element modeling (FEM) has to repeated each time a new formulation is devised. An analytical solution is desirable to allow formulation design with specific properties in mind compared to experimental formulations.

This thesis proposes an analytical solution, based on microcellular foam model that accounts for composition and morphology. The proposed constitutive model's viability is evaluated in terms of i-PP concentration and EPDM cure state.

1.4 Dissertation Overview

Chapter 2 deals with the mechanical behavior of three model SEBS systems. The effect of the subtle changes in the mid-block architecture of these SEBS systems on the uniaxial tensile, stress relaxation behavior, cycle hysteresis data is discussed. The low temperature melting/crystallization behavior of some of these SEBS systems has also been highlighted. The thermal and mechanical behavior of these model SEBS systems is

compared to that of crosslinked natural rubber. Internal energy changes from deformational calorimetry studies are discussed in order to gain a better understanding of the thermodynamics of deformation of these SEBS block copolymer systems. Evidence for strain-induced crystallization occurring in selected SEBS systems is provided and its effect on the mechanical and thermal properties is discussed.

Chapter 3 probes the structural changes in morphology occurring on deformation at two different length scales (one at the nano scale of the cylinders and other at the molecular scale of amorphous/crystalline regions) using combined small angle x-ray diffraction (SAXD) and wide-angle x-ray diffraction (WAXD) respectively. Strain-induced crystallization occurring in certain SEBS systems is further confirmed by the in-situ WAXD results. The development of several SAXD features including angle of X-cross pattern and layer line spacings with strain are discussed. The micromechanics of a block copolymer system is thoroughly established based on the experimental observations.

Chapter 4 presents evidence for ultra long-range order that can be obtained in SEBS block copolymers using simple continuous processing techniques like extrusion. Order/orientation obtained by other processing techniques commonly used in industry is compared to that obtained by extrusion. The effect of orientation on the mechanical properties is also discussed. In-situ SAXD studies on oriented systems are discussed to probe the contributions of the individual phases to the observed mechanical properties.

Chapter 5 examines the morphology and deformation behavior of EPDM/i-PP TPVs. Evidence for filled microcellular foam like structure for EPDM/i-PP blends is presented. Based on this filled foam morphology, an analytical model is presented

which takes into account the morphology, composition and cure state of EPDM rubber into account. Experimental data from cyclic tests is compared with the data obtained by modeling and the feasibility of the analytical model is discussed.

1.5 References

(1) Holden, G.; Legge, N. R.; Quirk, R.; Schroeder, H. E. *Thermoplastic Elastomers*, 2nd ed.; Hanser Publishers, 1996.

(2) Bates, F. S.; Fredrickson, G. H. *Physics Today* **1999**, *52*, 32.

(3) Bates, F. S.; Fredrickson, G. H. *Annual Review of Physical Chemistry* **1990**, *41*, 525-557.

(4) Lodge, T., P. *Macromol. Chem. Phys.* **2003**, *204*, 265-273.

(5) Loo, Y.-L.; Register, R. A. *Developments in Block Copolymer Science and Technology*; Wiley, 2004.

(6) Ludwik, L. *Macromolecules* **1980**, *13*, 1602-1617.

(7) Agarwal, S. L. *Polymer* **1976**, *17*, 938-956.

(8) Beecher, J. F.; Marker, L.; Bradford, R. D.; Aggarwal, S. L. *J. Polym. Sci., Part C* **1969**, *26*, 117-134.

(9) Folkes, M. J.; Keller, A.; Scalisi, F. P. *Kolloid Z.* **1973**, *251*, 1-4.

(10) Folkes, M. J., Ed. *Processing, structure, and properties of block copolymers / edited by M.J. Folkes*; Elsevier Applied Science Publishers, 1985.

(11) Folkes, M. J.; Keller, A. *Polymer* **1971**, *12*, 222-236.

(12) Dlugosz, J.; Keller, A.; Pedemonte, E. *Kolloid Z. Polym.* **1970**, *242*, 1125.

(13) Godovsky, Y. K. *Makromol. Chem. Suppl.* **1984**, *6*, 117-140.

(14) Tarasov, S. G.; Godovskii, Y. K. *Vysokomolekulyarnye Soedineniya Seriya A* **1980**, *22*, 1879-1885.

(15) Tarasov, S. G.; Tsvankin, D. Y.; Godovskii, Y. K. *Vysokomolekulyarnye Soedineniya Seriya A* **1978**, *20*, 1534-&.

(16) Falabella, R. *Ph.D. Thesis*, Polymer Science and Engineering; University of Massachusetts: Amherst, 1980; p 213.

(17) Farris, R. J. *Ph.D. Thesis*, Civil Engineering; University of Utah, 1970.

(18) Godovskii, Y. K.; Tarasov, S. G. *Vysokomolekulyarnye Soedineniya Seriya A* **1980**, *22*, 1613-1621.

(19) Pakula, T.; Saijo, K.; Kawai, H.; Hashimoto, T. *Macromolecules* **1985**, *18*, 1294-1302.

(20) Read, D. J.; Duckett, R. A.; Sweeney, J.; McLeish, T. C. B. *J. Phys. D: Appl. Phys.* **1999**, *32*, 2087-2099.

(21) Honeker, C. C.; Thomas, E. L.; Albalak, R. J.; Hajduk, D. A.; Gruner, S. M.; Capel, M. C. *Macromolecules* **2000**, *33*, 9395-9406.

(22) Honeker, C. C.; Thomas, E. L. *Macromolecules* **2000**, *33*, 9407-9417.

(23) Arridge, R. G. C.; Folkes, M. J. *J. Phys. D: Appl. Phys.* **1972**, *5*, 344-360.

(24) Campos-Lopez, E.; McIntyre, D.; Fetters, L. J. *Macromolecules* **1973**, *6*, 415-423.

(25) Diamant, J.; Williams, M., C. *Polym. Eng. Sci.* **1989**, *29*, 235-243.

(26) Pollak, V.; Romanov, A.; Marcincin, K.; Vyroubal, C. *J. Appl. Polym. Sci.* **1973**, *17*, 565-570.

(27) Zhao, Y. *Macromolecules* **1992**, *25*, 4705-4711.

(28) Sierra, C. A.; Galan, C.; Fatou, J. G.; Parellada, M. D.; Barrio, J. A. *Polymer* **1997**, *38*, 4325-4335.

(29) Bradford, E. B.; Vanzo, E. *J. Polym. Sci. : Part A-1* **1968**, *6*, 1661-1670.

(30) Morrison, F. A.; Winter, H. H. *Macromolecules* **1989**, *22*, 3533-3540.

(31) Karger-Kocsis, J. In *Polymer Blends and Alloys*; Shonaike, G. O.; Simon, G. P., Eds.; Marcel Dekker Inc.: New York, 1999; p 125.

(32) Coran, A. Y. *Rubber Chemistry and Technology* **1995**, *68*, 351.

(33) Ellul, M. D.; Patel, J.; Tinker, A. J. *Rubber Chemistry and Technology* **1995**, *68*, 573-584.

(34) Ellul, M. D. *Rubber Chemistry and Technology* **1998**, *71*, 244-276.

(35) Ellul, M. D. *Rubber Chemistry and Technology* **1998**, *71*, 1087.

(36) Choudhary, V.; Varma, H. S.; Varma, I. K. *Polymer* **1991**, *32*, 2534-2540.

(37) Karger-Kocsis, J.; Kallo, A.; Szafner, A.; Bodor, G. *Polymer* **1979**, *20*, 37-43.

(38) Kikuchi, Y.; Fukui, T.; Okada, T.; Inoue, T. *Polymer Engineering and Science* **1991**, *31*, 1029-1032.

(39) Okamoto, M.; Shiomi, K.; Inoue, T. *Polymer* **1994**, *35*, 4618-4622.

(40) Boyce, M. C.; Kear, K.; Socrate, S.; Shaw, K. *Journal of the Mechanics and Physics of Solids* **2001**, *49*, 1073-1098.

(41) Boyce, M. C.; Socrate, S.; Kear, K.; Yeh, O.; Shaw, K. *Journal of the Mechanics and Physics of Solids* **2001**, *49*, 1323-1342.

(42) Boyce, M. C.; Yeh, O.; Socrate, S.; Kear, K.; Shaw, K. *Journal of the Mechanics and Physics of Solids* **2001**, *49*, 1343-1360.

CHAPTER 2

DEFORMATIONAL CHARACTERISTICS OF SEBS TERMOPLASTIC ELASTOMERS

Three Poly (styrene-b-ethylene-co-butylene-b-styrene) (SEBS) thermoplastic elastomers (TPEs) are studied mechanically and compared to cross-linked natural rubber. It is observed that subtle alterations in the mid-block of the TPEs affect their mechanical properties significantly. The stress relaxation at room temperature is significantly altered indicating a reduced flow in systems where the ratio of ethylene to butylene segments in the mid-block is greater than one. The cyclic behavior of these systems also shows significant hysteresis. Differential Scanning Calorimetry suggests that these TPEs crystallize at low temperatures, similar to the observed behavior in cross-linked and uncrosslinked dnatural rubber. Results of internal energy changes from deformation calorimetry at room temperature provide evidence for strain-induced crystallization occurring in certain SEBS systems, similar to the internal energy changes observed for cross-linked and uncrosslinked natural rubber. Deformation calorimetry studies at higher temperatures further confirm strain-induced crystallization occurring in these SEBS systems. Strain-induced crystallization occurring in certain TPEs provides a mechanism for reduction of flow at high strains and accounts for the retention of their highly elastic behavior.

2.1 Introduction

The deformation response of several diblock and triblock copolymer TPEs [1-6] have been studied and compared by various techniques, including small angle x-ray scattering (SAXS), transmission electron microscopy (TEM), atomic force microscopy (AFM), birefringence and rheo-optical techniques. Keller and coworkers studied highly oriented TPEs mechanically and have shown that these systems can be treated as nearly perfect composite materials [7,8]. They could successfully interpret the mechanical properties in terms of microstructure for elastic deformations using simple composite theories[7]. For the inelastic region of the stress-strain curves, they predicted a breakdown of cylinders into small rods based on TEM observations and employed a shear-lag treatment for short rods (similar to a short-fiber reinforced composite) for predicting a distribution of rod lengths as a function of applied macroscopic strain. However these oriented SBS systems were deformed only to moderate strains and strains greater than 120 % were not probed.

Godovsky and coworkers [9-11] studied the energy and entropy effects resulting from deformation of styrene-butadiene-styrene (SBS) block copolymers and correlated the effects to structural changes in the morphology using SAXD and deformation calorimetry respectively. They showed that there is considerable increase of internal energy (unlike filled elastomers) during stress softening of block copolymers due to the breakdown of continuous stress-supporting rigid phase. They also postulated from their observations that upturns in stress-strain curves of SBS block copolymers are due to deformation of glassy and rigid PS domains and not due to limited chain extensibilities. Thomas and coworkers [12,13] studied the deformation of cylindrical PS domains of a near

single 'crystal' styrene-isoprene-styrene (SIS) triblock copolymer by SAXS and TEM techniques and related the structural changes in the hexagonal lattice of cylinders on uniaxial tensile deformation to observed macroscopic mechanical behavior. (The detailed structural changes on uniaxial tensile deformation of SEBS triblock copolymers will be discussed in chapter 3 of this thesis). However, most of these studies were directed at studying structural changes in morphology of unhydrogenated SBS/SIS block copolymers on uniaxial tensile deformation.

Farris and coworkers[14,15] studied the stress softening/Mullin's effect in several systems including block copolymers and modeled the behavior using permanent memory functions, where the microstructural weakening that happens on deformation is dependent on the maximums in strain history. They showed that viscoelastic constitutive equations based on the fading memory assumption are inappropriate for such materials. Figure 2.1 shows the hysteresis behavior of a filled polyurethane rocket propellant using permanent memory functions.

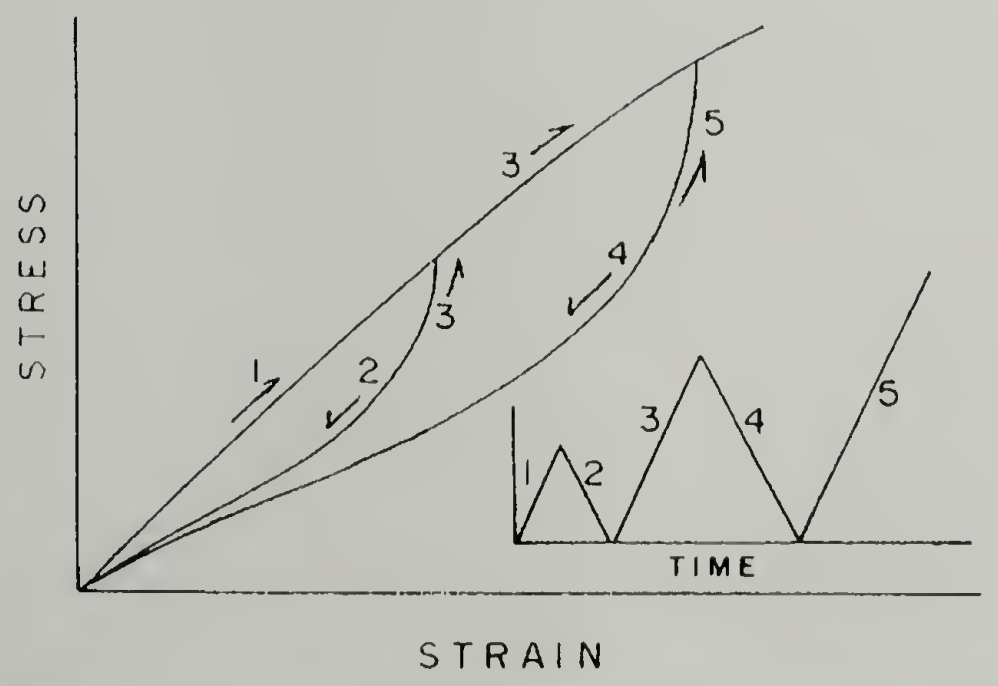

Figure 2.1 Hysteresis behavior of cross-linked highly filled polyurethane solid rocket propellant (Farris, 1970)

Diamant, Williams and coworkers[16-18] studied the non-linear uniaxial tensile, stress relaxation and cyclic test behavior of SBS block copolymers. They analyzed the strain recovery curves (in stress relaxation experiments) using a series assembly of viscoelastic Kelvin elements and obtained time constants for microstructural repair and explained the time dependence in terms of the microstructural interphase and its partial vitrification. Using these time scales for structural recovery, they modeled quantitatively the cyclic retraction curves in terms of a modified Mooney-Rivlin function and used the Mooney Moduli, G_1 and G_2 obtained to discuss the different changes occurring in the microstructure. However their fitting model does not fully explain the experimental deviations observed. Again, the systems studied were unhydrogenated SBS, SIS systems.

Most of these block copolymer systems studied so far have been styrene-butadiene-styrene (SBS) or styrene-isoprene-styrene (SIS) systems. None of these block copolymer TPE systems studied for macroscopic deformation behavior possessed crystallinity and no studies have investigated morphological/structural changes that occur at both the nanometer as well as the molecular length scale (of crystalline/amorphous) on deformation.

It has been shown that by altering the ratio of ethylene to butylene segments in the ethylene-co-butylene (EB) mid-block of the SEBS TPEs, their ability to crystallize at low temperatures can be altered [19]. Fatou and coworkers [20] have studied the thermal and mechanical properties of a series of SEBS triblock copolymers with varying % crystallinity (by changing ratio of ethylene-butylene segments) and styrene content.

Gronski and Stadler [21] have synthesized elastomeric SEBS TPEs by partially hydrogenating SBS copolymers to varying degrees and studied the effects of methylene sequence length (of the EB block) on their ability to undergo strain-induced crystallization using stress relaxation experiments. They predict that stress-induced crystallization could be used as a possible mechanism to prevent flow in TPEs at high strains. However no extensive mechanical or morphological studies have been performed on such systems.

In this chapter, results that relate the block copolymer structure to its resulting thermal and mechanical response are presented. In particular, the effects of the subtle changes in the mid-block architecture on the origins of elasticity and recovery are discussed. It has been shown that one critical reason for high elastic strength and recovery is associated with strain-induced crystallization similar to that observed in vulcanized natural rubber [22-28]. Internal energy measurements obtained from deformation calorimetry highlight the differences that the mid-block structure imposes on the overall mechanical properties and provide evidence for strain-induced crystallization.

2.2 Materials and sample preparation

Three poly (styrene-b-ethylene-co-butylene-b-styrene) (SEBS) research formulations referred to as GRP6924, GRP6926 and RP6936 and provided by KRATON Polymers, U.S. LLC. were used in this study. All these three systems have the same amount of Polystyrene (PS) 20 % in their end blocks. GRP6924 has a ratio of ethylene to butylene segments less than 1 while GRP6926 and RP6936 have this ratio

greater than 1. RP6936 has additional styrene incorporated into the mid-block in a controlled way with more styrene present near the center than at the ends[29]. The structure of a typical SEBS triblock copolymer a) and RP6936 b) is shown in Figure 2.2. In figure 2.2b) the vertical lines in the mid-block indicate the additional PS introduced into the system.

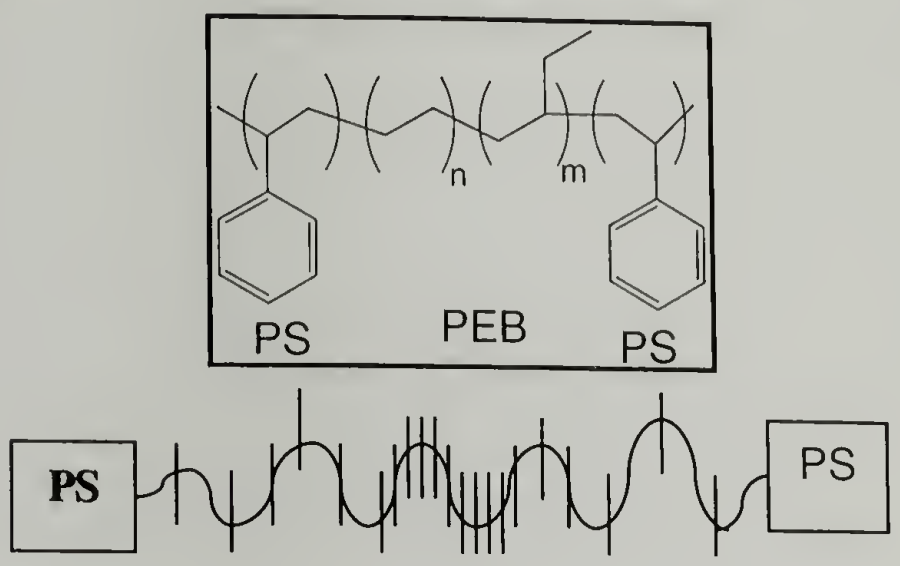

Figure 2.2 Structure of a typical SEBS system and structure of RP 6936 (S40E)

For the sake of convenience, a simplified four letter naming convention has been adopted for these systems. The first three letters denote the total percentage of PS in the system, while the last letter denotes whether the mid-block has more number of ethylene or butylene segments. For example, system GRP 6924 with 20 % PS and more butylene segments than ethylene segments is referred to as S20B. The compositions of these three systems along with the naming convention are listed in the Table 2.1. The three systems GRP6924, GRP6926 and RP6936 will henceforth be referred to as S20B, S20E and S40E respectively.

Kraton weight%	GRP6924	GRP6926	RP6936
Simplified naming convention	S20B	S20E	S40E
Overall Polystyrene %	20%	20%	40.1%
Polystyrene content in end block	20%	20%	20%

Table 2.1 Compositional details of the SEBS systems

Triblock copolymer samples were dissolved in toluene to obtain 3.5 weight % solutions. Solvent evaporation was controlled to occur over two weeks. The films were then dried at 40° C under vacuum for 6 hours and then annealed at 115°C for 24 hours. A natural rubber (NR) system was also used in this study and served as a reference for a chemically cross-linked elastomeric system.

2.3 Experimental

2.3.1 Morphological Characterization

Sections 40-100 nm in thickness were obtained by cyro-microtoming bulk films with a Leica EM-FCS® microtome at –90°C. These sections were collected and then stained with ruthenium tetroxide for about 12 minutes. Transmission Electron Microscopy (TEM) studies were performed using a JEOL 2000 FX TEM operating at 200 KV. Small angle X-ray diffraction (SAXD) measurements were performed on a Molecular Metrology® SAXS machine. Wide angle X ray diffraction (WAXD) measurements were performed using a Rigaku RU-H3R rotating anode X-ray

diffractometer and a home built evacuated Statton-type scattering camera. Scattering patterns were acquired with a 10 cm × 15 cm Fuji ST-VA image plates in conjunction with a Fuji BAS-2500 image plate scanner.

2.3.2 Mechanical Testing and Thermal Analysis

Tensile, cyclic and stress relaxation tests at different temperatures were performed on an Instron® 5800 tensile testing machine, equipped with heating/cooling stage. ASTM D1708 test geometry was employed for all the samples used for mechanical testing. Differential scanning Calorimetry (DSC) and Modulated Differential Scanning Calorimetry (MDSC) were performed on a TA® Instruments Q100 DSC.

2.3.3 Deformation Calorimetry

2.3.3.1 Description

Deformation calorimetry is a technique that measures energy changes (internal energy changes, heat absorbed) on deformation and has the potential to unravel the true thermodynamic nature of the system on deformation. It has been used successfully by Farris and coworkers to study the heat, internal energy changes in strain-crystallizing natural rubber [30,31], polyurethane-urea elastomers [9,32-34], thermoplastics [35] and blends [36]. The incremental work done, $d\mathbf{W}$, heat absorbed, $d\mathbf{Q}$ and hence the internal energy changes, $d\mathbf{U}$ during deformation are measured using a deformation calorimeter, which has been described previously by Farris and coworkers[37,38]. Figure 2.3 shows a schematic of the deformation calorimeter used in this study. The small heat changes that

occur as a result of the stretching the sample change the differential pressure in the sample chamber (with respect to the reference chamber) as shown in figure 2.3. This differential pressure (monitored by the differential pressure transducer) can be related back to the heat absorbed/dissipated using simple linear hereditary integrals. Equations relating heat flow, dynamic heat flow to the differential pressure changes have been derived and described previously [31,37,38].

$$\Delta P(t) = \int_0^t K(t-\xi)\frac{\partial Q(\xi)}{\partial \xi}d\xi$$

$$K(t) = \frac{1}{C\tau}e^{-t/\tau} \qquad \text{.....(1)}$$

$$Q(t) = C\int_0^t \Delta P(\xi)d\xi + C\tau\Delta P(t)$$

$$\dot{Q}(t) = C\Delta P(t) + C\tau\frac{d\Delta P(t)}{dt} \qquad \text{.....(2)}$$

ΔP(t) denotes the differential pressure change, Q the heat absorbed/dissipated, $\dot{Q}(t)$ the heat flux, C the thermal capacitance of the calorimetric system and τ, the time constant of the calorimeter at a particular temperature.

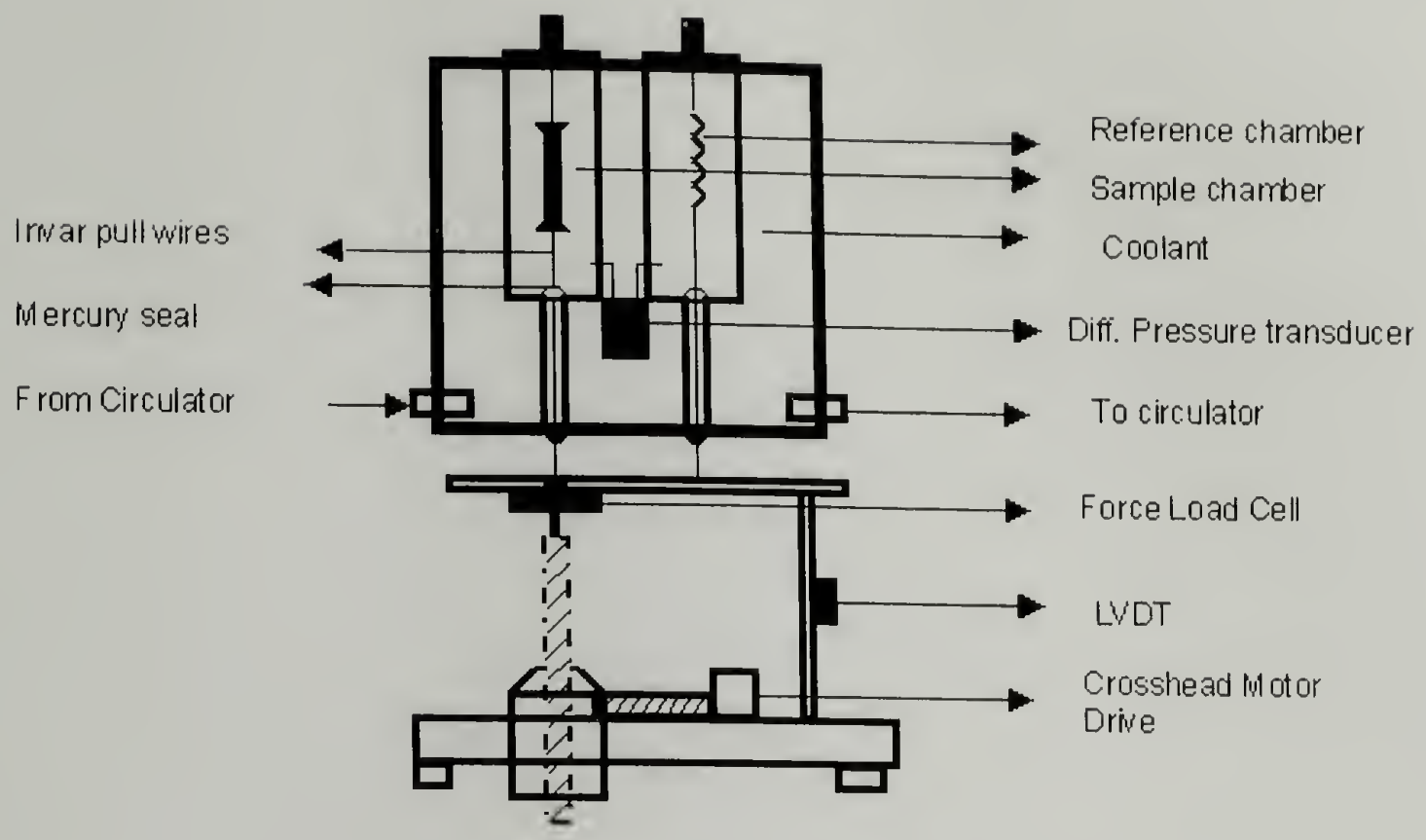

Figure 2.3 Schematic of a Deformation Calorimeter

The calorimeter cell consisting of the sample chamber and reference chamber sits submerged in a temperature-controlled bath. The sample chamber and the reference chamber are connected across a very sensitive differential pressure transducer (0.02 psid for a full scale deflection of 5V). These chambers are isolated from the outside pressure changes by valves at the top and by frictionless mercury seals at the bottom. The sample is deformed using Invar pull wires that exit the bottom of the sample chamber through the frictionless mercury seal. An identical Invar pull wire present in the reference chamber compensates for the volume-induced pressure changes in the sample cell. The exiting Invar pull wires are then connected to a load cell and LVDT, which measure the force and displacement respectively. A motorized screw drive pulls the invar wires and

thus deforms the samples. All tests in this study were performed on an ASTM D1708 test geometry samples at a strain rate of 0.91 mm/mm/min and at 25°C.

2.3.3.2 Calibrations for the deformation calorimeter at 298.7 K

Electrical calibrations are performed using Nichrome heating wires to relate the differential pressure to the heat flow and also calculate the system time constants, the thermal capacitance and time constant of this calorimetric equation. Small heat pulses are input into the sample chamber using a Nichrome heating wire connected to a RC timing circuit which inputs constant pulses of current for a definite amount of time. One such heat pulse and its effect on the differential pressure at 298.7 K (25.7°C) has been plotted in figure 2.4. Table 2.2 below enlists the different heat-pulses that are inputted through timing circuits and the resultant steady state pressure and area under the pressure-time curves.

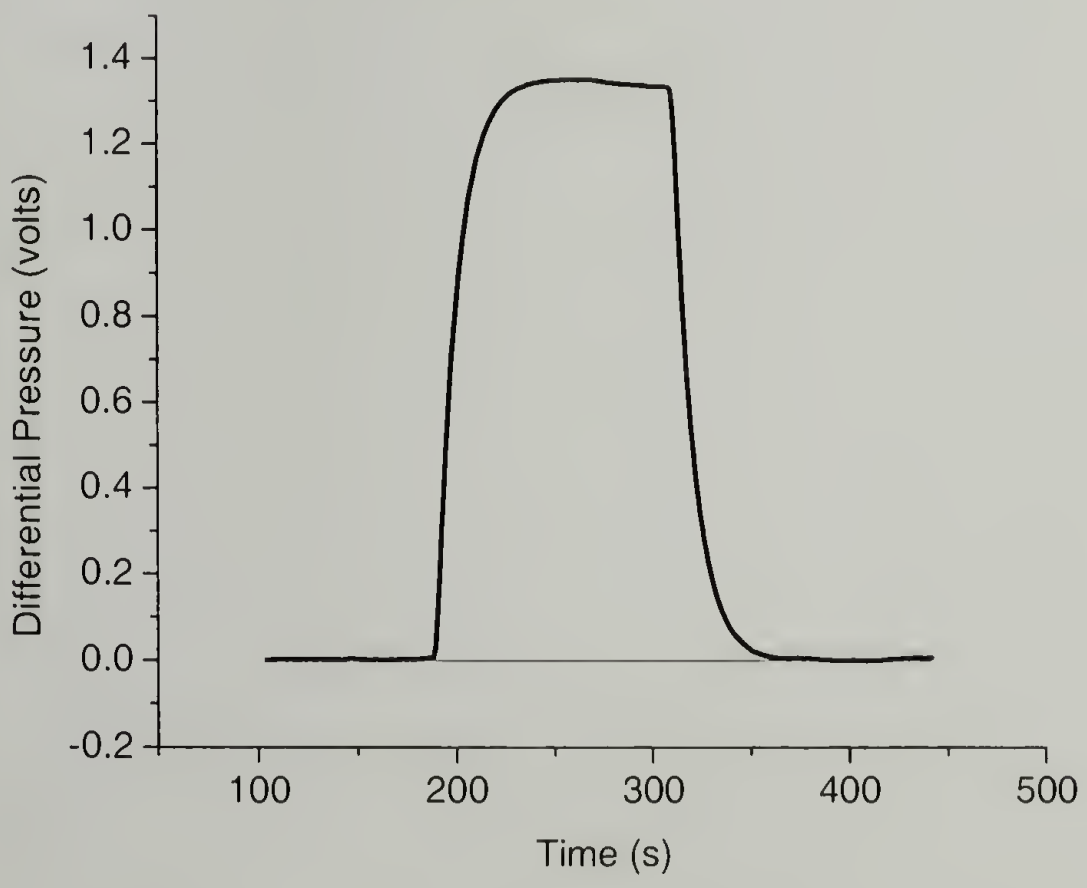

Figure 2.4 Differential pressure response to a heat pulse

Voltage (V)	Current (mA)	Time (s)	Input heat (mJ)	Input Power (mW)	Steady state Pressure (V)	Area under P-t curve (Vs)
0.353	42	60	889.5	14.8	0.99	61.1
0.351	42	120	1769.0	14.7	1.00	121.2
0.351	42	180	2653.5	14.7	1.00	180.2
0.351	42	241	3538.1	14.7	1.01	244.0
0.351	42	300	4422.6	14.7	1.01	302.8
0.408	49	120	2399.0	19.9	1.36	163.2
0.518	63	120	3916.1	32.6	2.13	256.4
0.567	69	120	4694.7	39.1	2.53	305.1
0.721	88	120	7613.7	63.4	4.00	482.2

Table 2.2: Measured steady state pressure and area under Pressure (P)-time (t) curve for different heat pulses at 298.7 K (25.7° C)

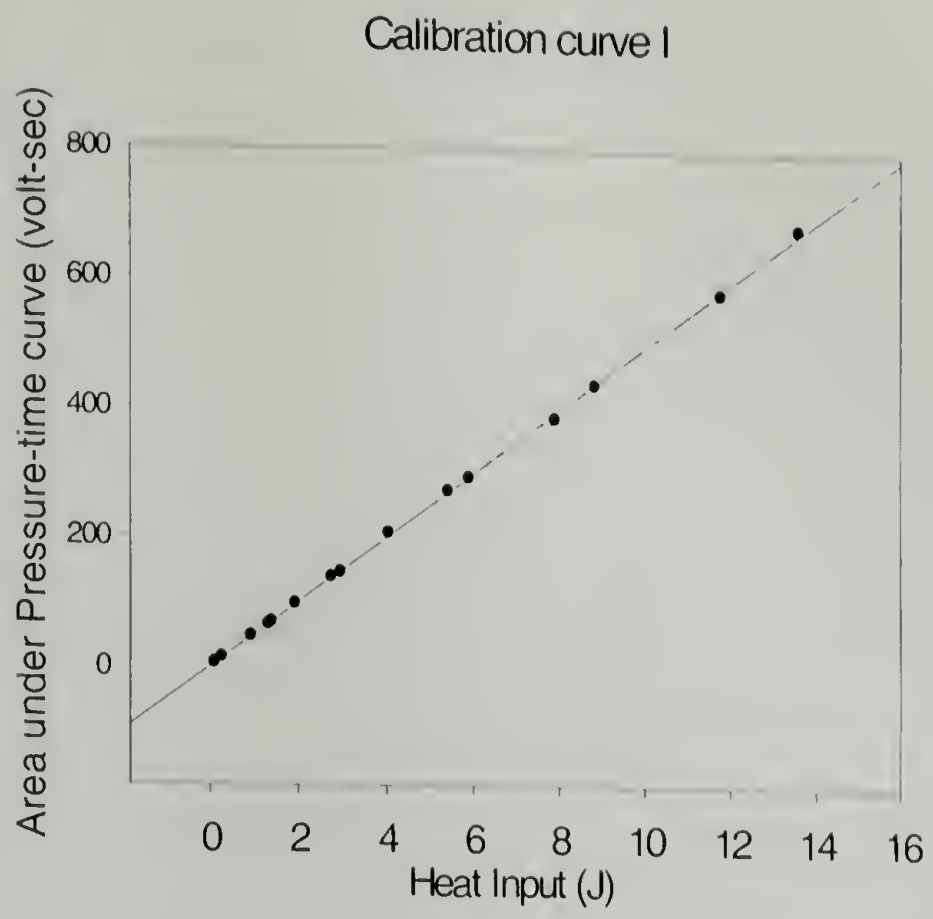

Figure 2.5 Area under P-t curve versus heat input for the calorimeter at 298.7 K

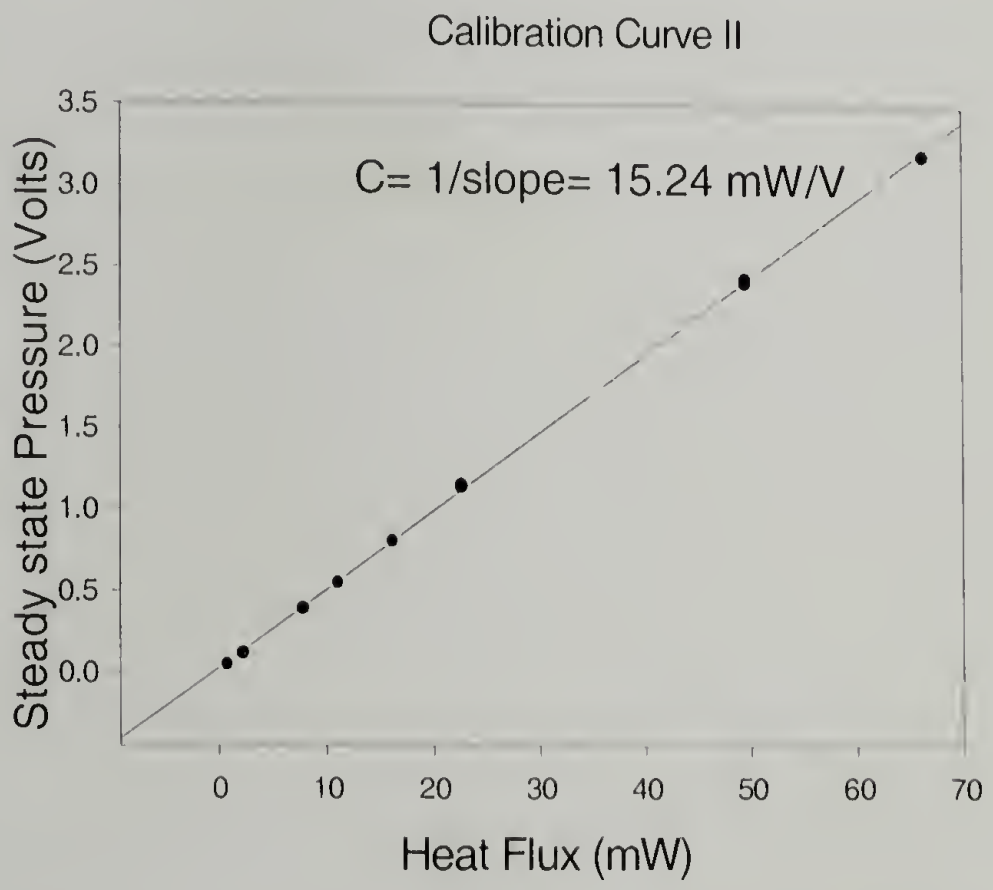

Figure 2.6 Steady state pressure versus heat flux for the calorimeter at 298.7 K

Slope of these calibration curves shown in figures 2.5 and 2.6 along with fitting the exponential rise or fall of the pressure signal with heat pulses yield the system constants for the calorimeter. From the above measurements, the average time constant (for the differential pressure signal to decay or rise) and the thermal capacitance have been calculated to be 11.7 seconds and 15.24 milliWatts/Volt respectively at 298.7 K (25.7°C).

2.3.3.3 Calibrations at 318.1 K

Similarly calibrations (figures 2.7 and 2.8) were done on the calorimeter at 318.1 K (45.1°C). As expected a value similar to that obtained at 298 K for thermal capacitance was obtained for 318.1 K. The average time constant at 318.1 K was a few 1/10ths of a second lower than that obtained at 298.7 K (25.7°C).

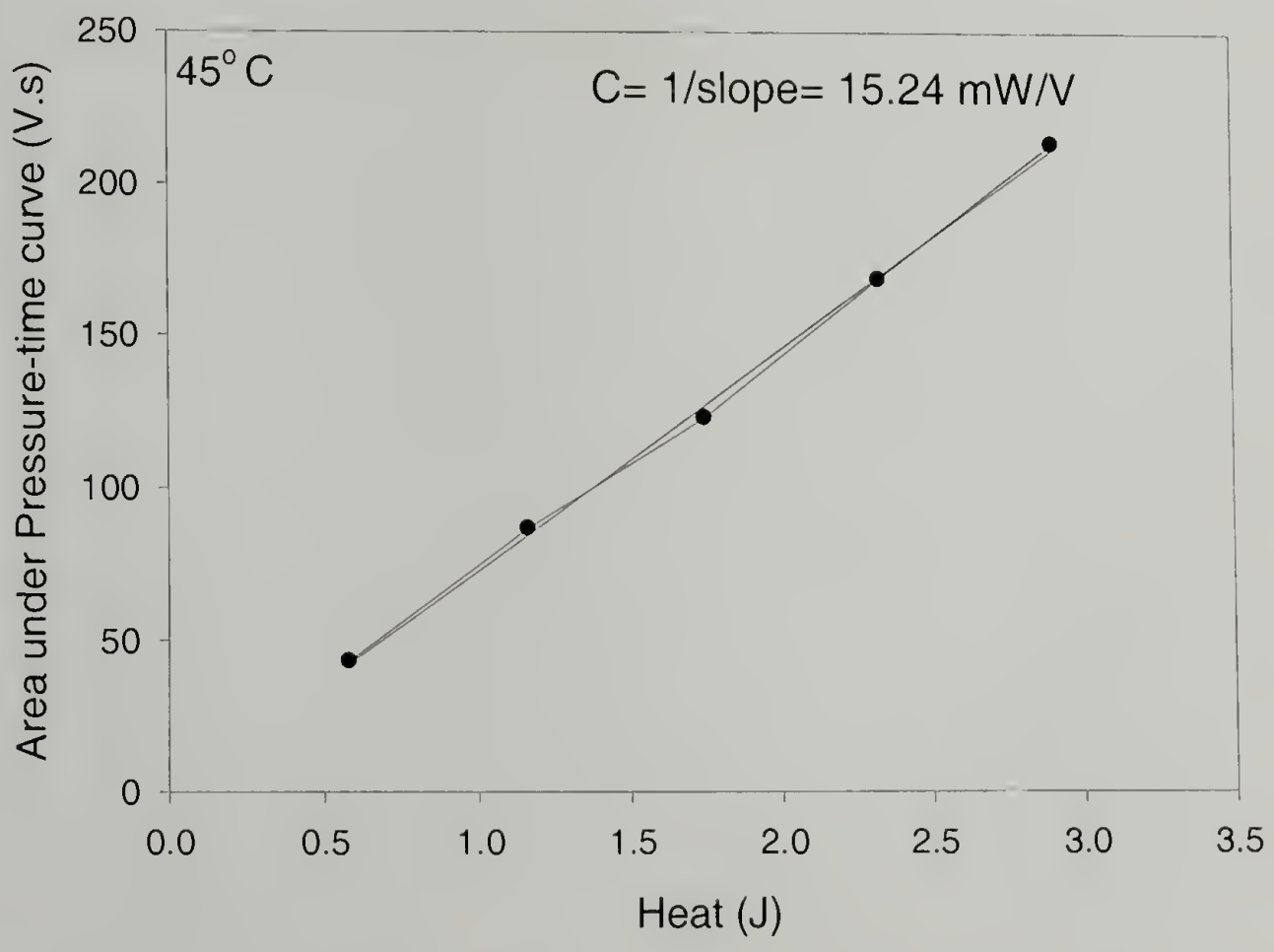

Figure 2.7 Area under P-t curve versus heat input for the calorimeter at 318.1 K

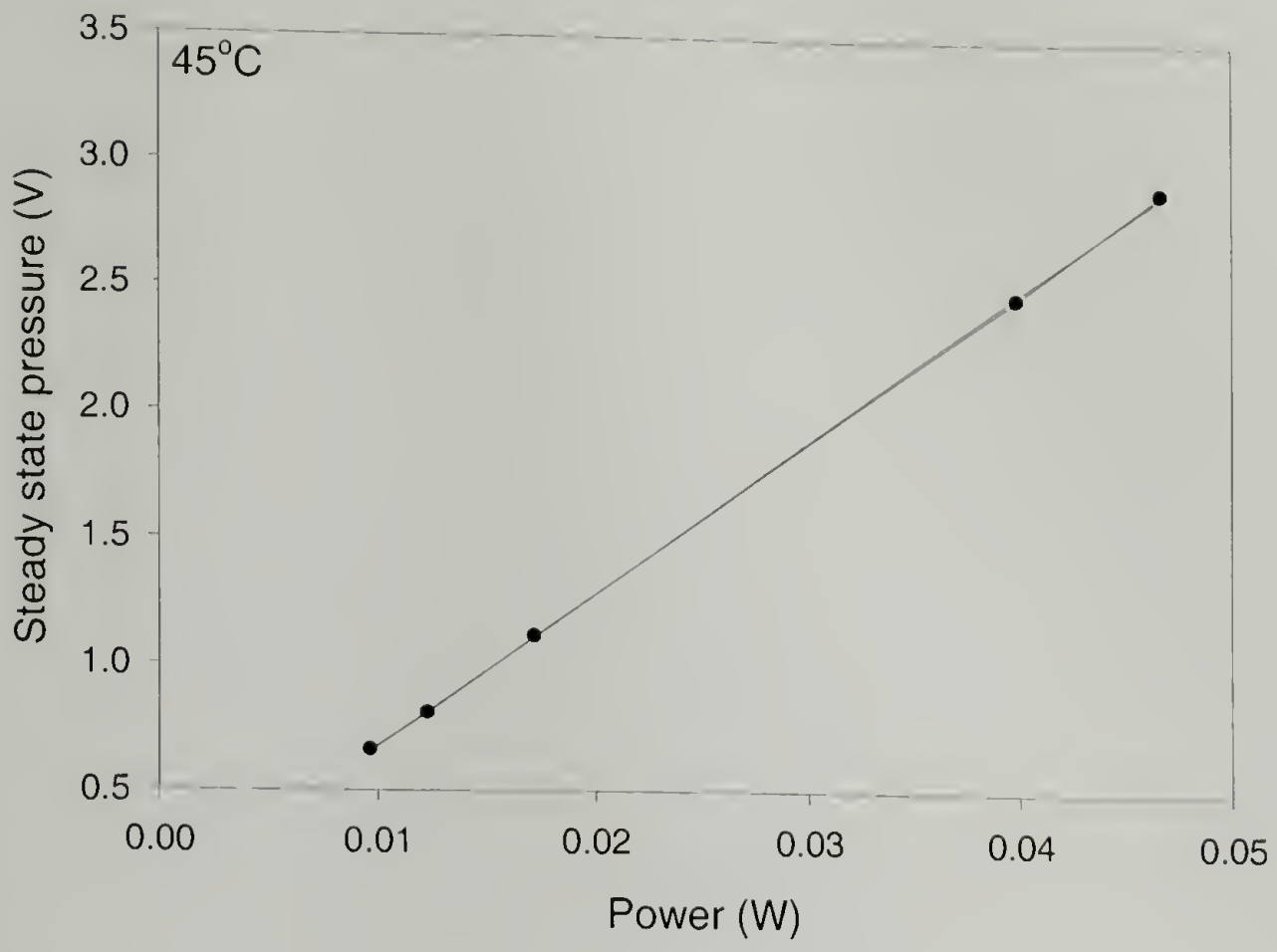

Figure 2.8 Steady state pressure versus heat flux for the calorimeter at 318.1 K

2.4 Results and Discussion

Investigation of S20B, S20E and S40E by TEM, (Figure 2.9) shows the same overall morphology. The PS domains coalesce into cylindrical rods that are packed in a two-dimensional hexagonal lattice embedded within the poly (ethylene-co-butylene) (PEB) matrix. This is expected as all these three systems have same amount of PS (20%) in their end-blocks. This is also in accordance with what is expected from the triblock copolymer phase diagram for a 15-35% volume fraction PS system. Small angle x-ray scattering (SAXS) on these systems confirms hexagonal packing of PS cylinders in a PEB matrix. The inter-cylinder d-spacings for S20B, S20E and S40E have been calculated to be 25.8 nm, 26.1 nm and 29 nm respectively.

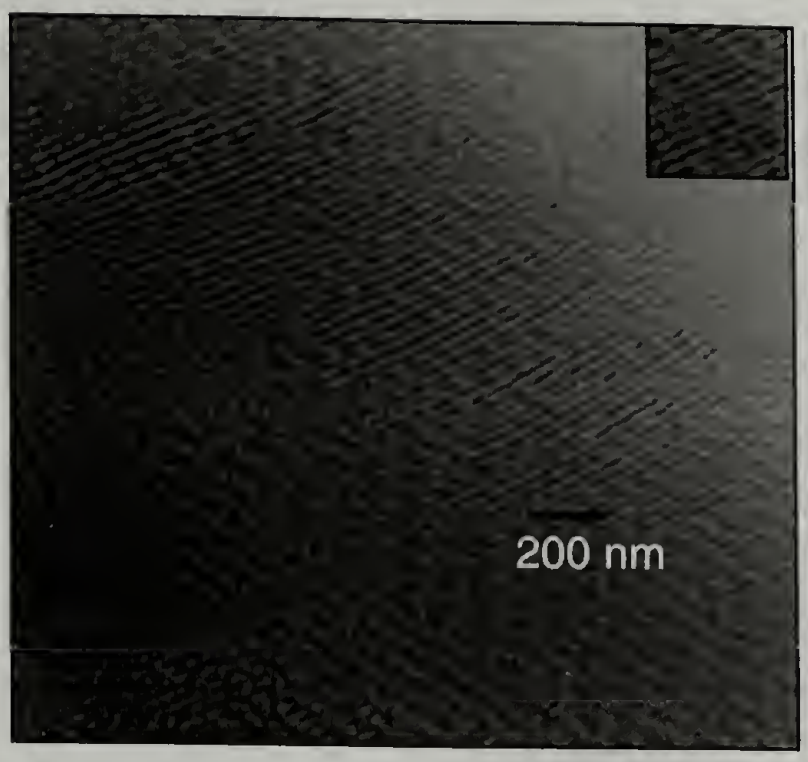

S20B

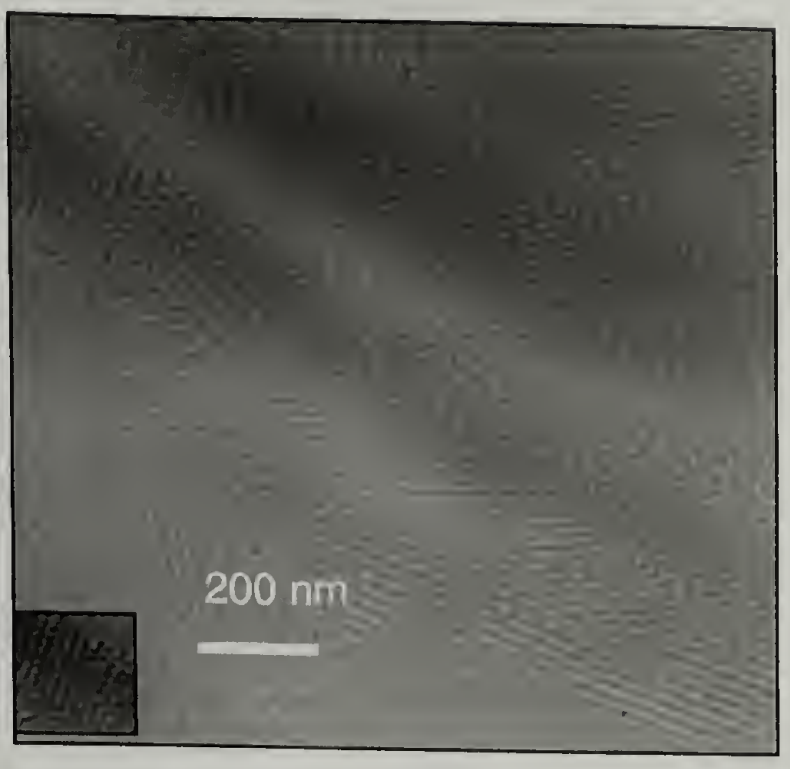

S20E

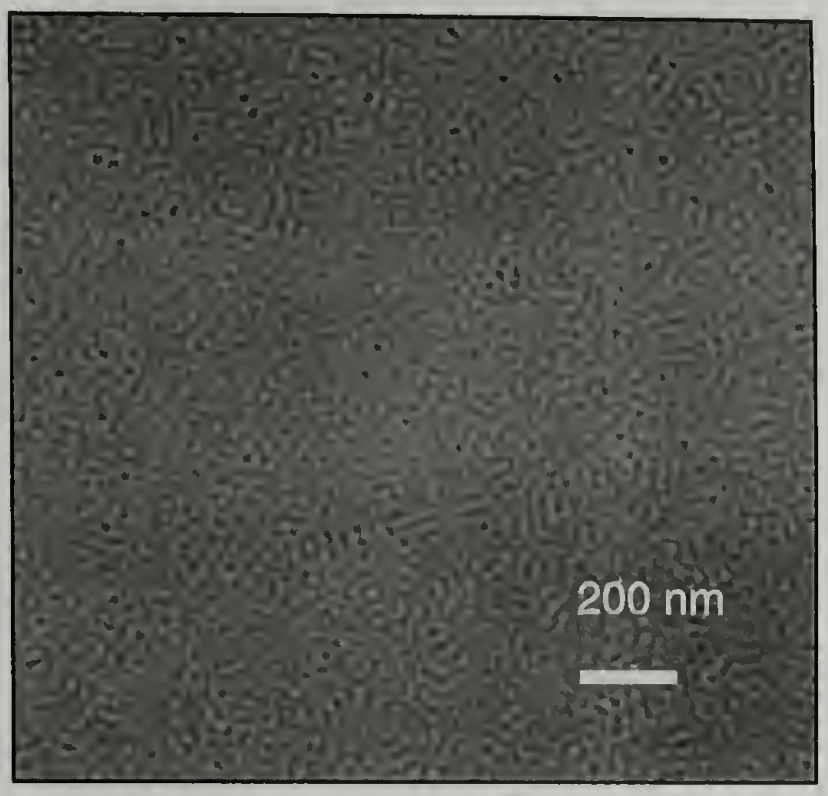

S40E

Figure 2.9 TEM pictures of three SEBS systems studied

Stress-extension ratio curves for the three systems (Figure 2.10) demonstrate that subtle changes in the mid-block architecture have a significant effect on the uniaxial tensile response. Both the initial strain response (low strain regime) as well as the strain

hardening behavior (large strain response) are significantly different. Note that the modulus of S20E is significantly higher than that of S20B. Thus there appears to be a direct correlation between the increase in the ratio of ethylene to the butylene segments in the EB mid-block and the modulus of the SEBS systems. Conversely, the extensibility of S20E becomes lower compared to that of S20B, indicating a reverse relationship. The higher modulus and lower extensibility of S40E compared to the other systems could be due to the additional glassy PS incorporated into the middle block for this system.

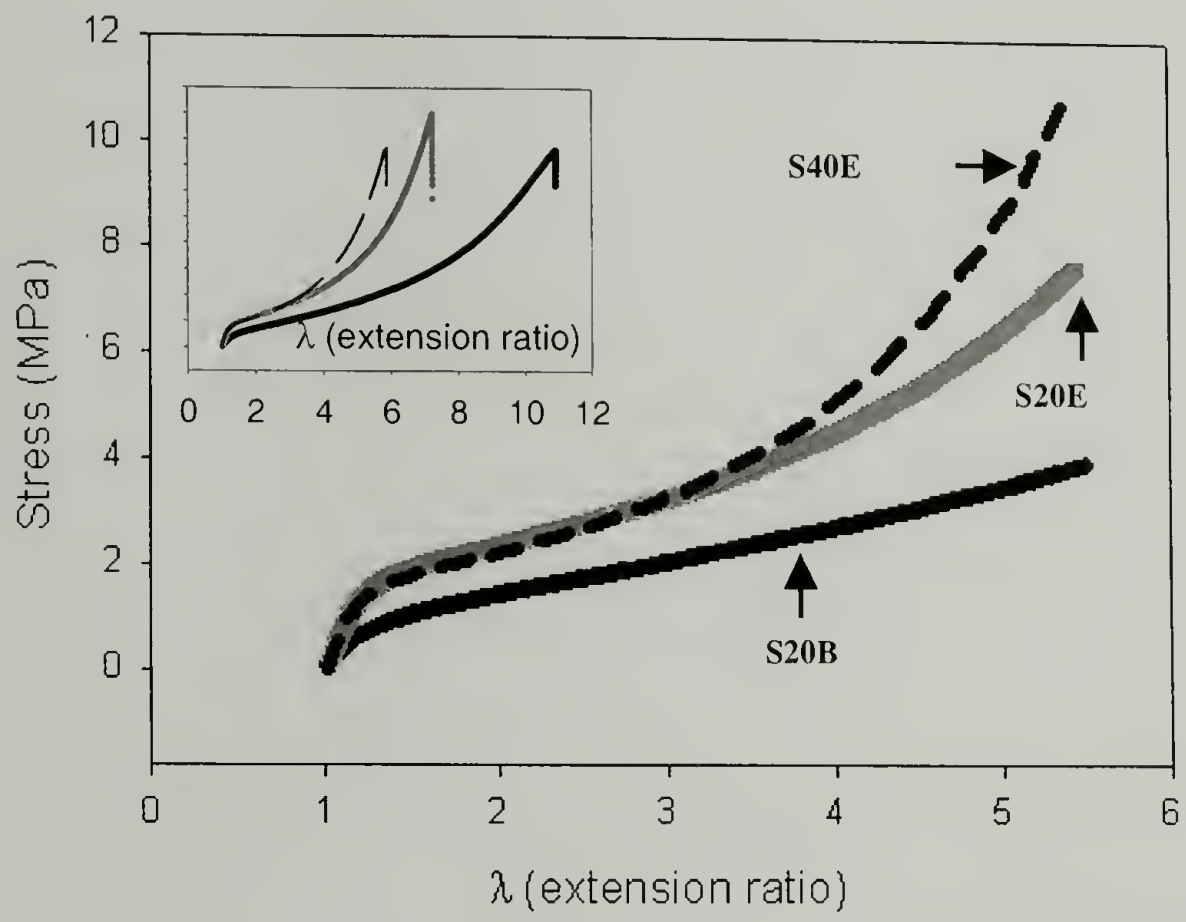

Figure 2.10 Stress–extension curves for three systems

Cyclic tests were also performed on these samples, with each sample cycled five times after an initial stretch. The initial stretch (which conditions the system for

Mullin's effect) has been indicated (in the corresponding figures 2.11, 2.12, 2.13 and 2.14) with a dotted line to differentiate from the consecutive loading and unloading cycles. For natural rubber (NR), it can be seen from figure 2.11 that the hysteresis is almost negligible up to an extension ratio of 4. However on further straining NR to extension ratios of 4 and beyond produces pronounced hysteresis. This hysteresis vanishes when the sample is unloaded back to an extension ratio of 2.5. This behavior has been widely attributed to strain induced crystallization that occurs in natural rubber [39]. Similar hysteresis was obtained (at large extension ratios) when birefringence was plotted as a function of the extension ratio at room temperature because of strain-induced crystallization in NR.

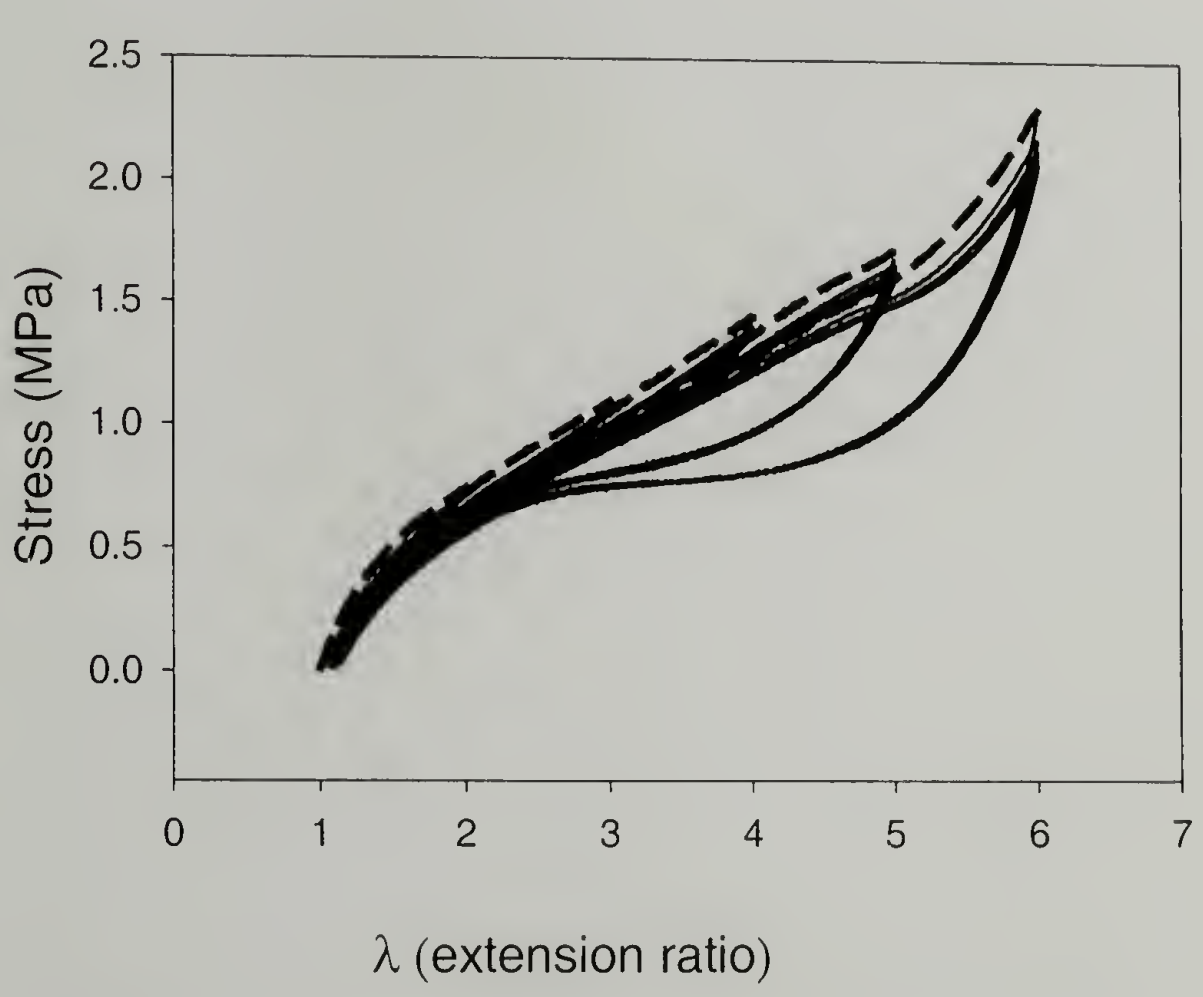

Figure 2.11 Cyclic loading-unloading behavior of strain-crystallizing natural rubber

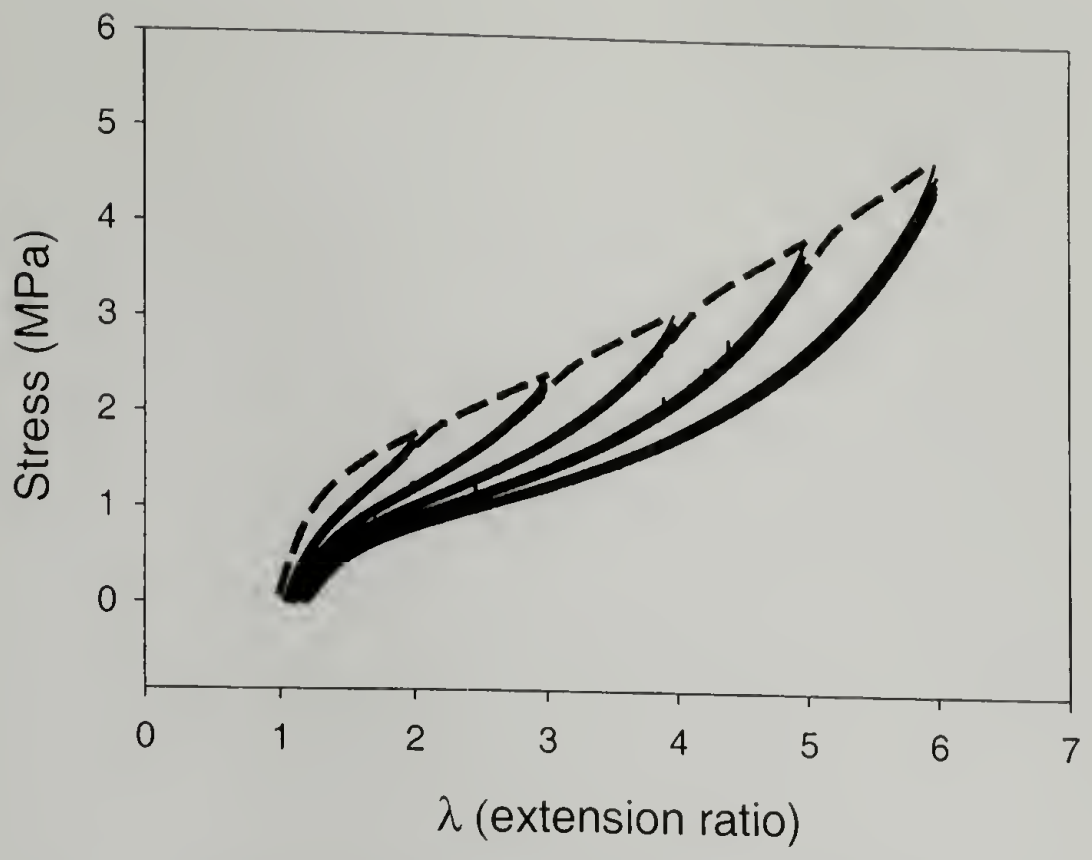

Figure 2.12 Cyclic behavior of SEBS system S20B

Figure 2.12 shows the cyclic behavior of S20B. The initial stretch cycle resembles a thermoplastic like response. (This initial stretch cycle has been shown in dotted line for clarity). However, after its initial stretch, the system behaves like a typical elastomer with a relatively low amount of hysteresis. Figure 2.13 also shows that S20E loads initially like a thermoplastic (indicated by dotted line) and then on subsequent cycling follows an elastomeric behavior. However, S20E shows significant hysteresis. Figure 2.14 shows that S40E behaves similar to that observed for S20E, but with a much lower hysteresis.

Although hysteresis in elastomers can be produced by a number of different phenomena, one such phenomenon is strain-induced crystallization. If strain-induced crystallization is the cause for the observed hysteresis in TPEs, then the results would

suggest that S20B contains no strain-induced crystals, while S20E does and S40E, a lower amount than S20E.

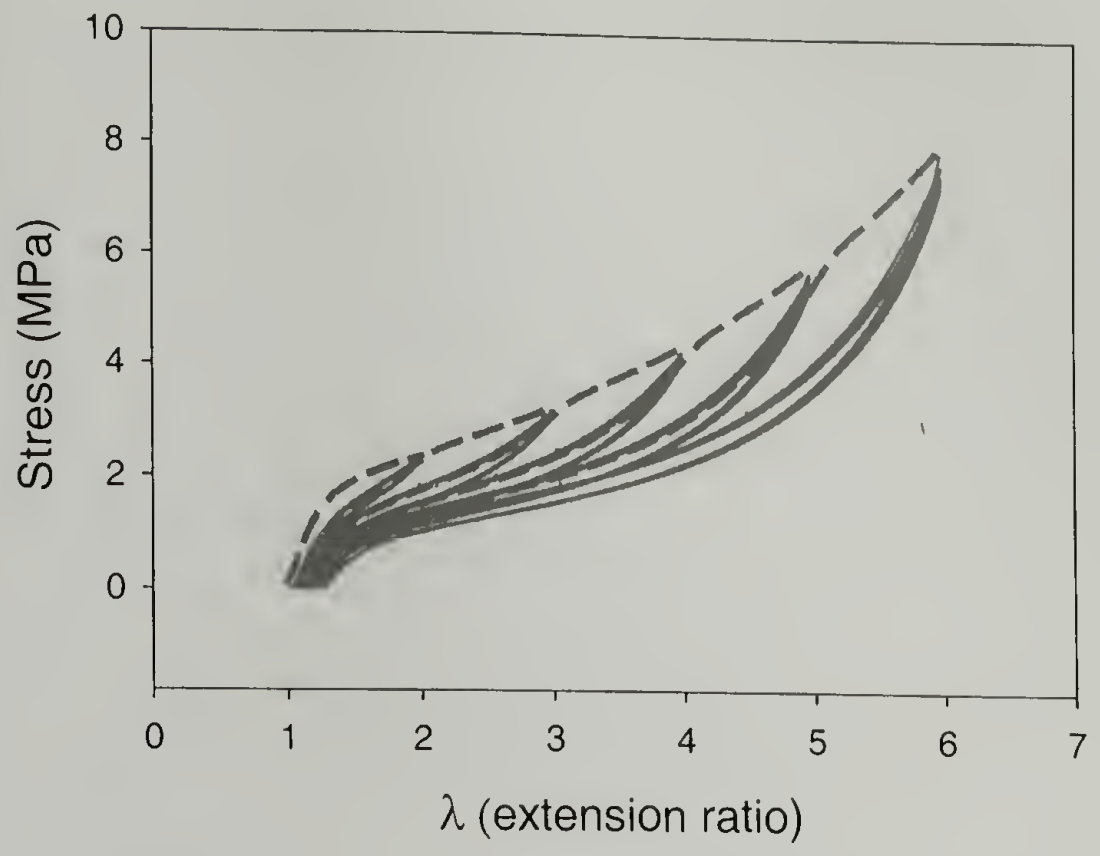

Figure 2.13 Cyclic behavior of SEBS system S20E

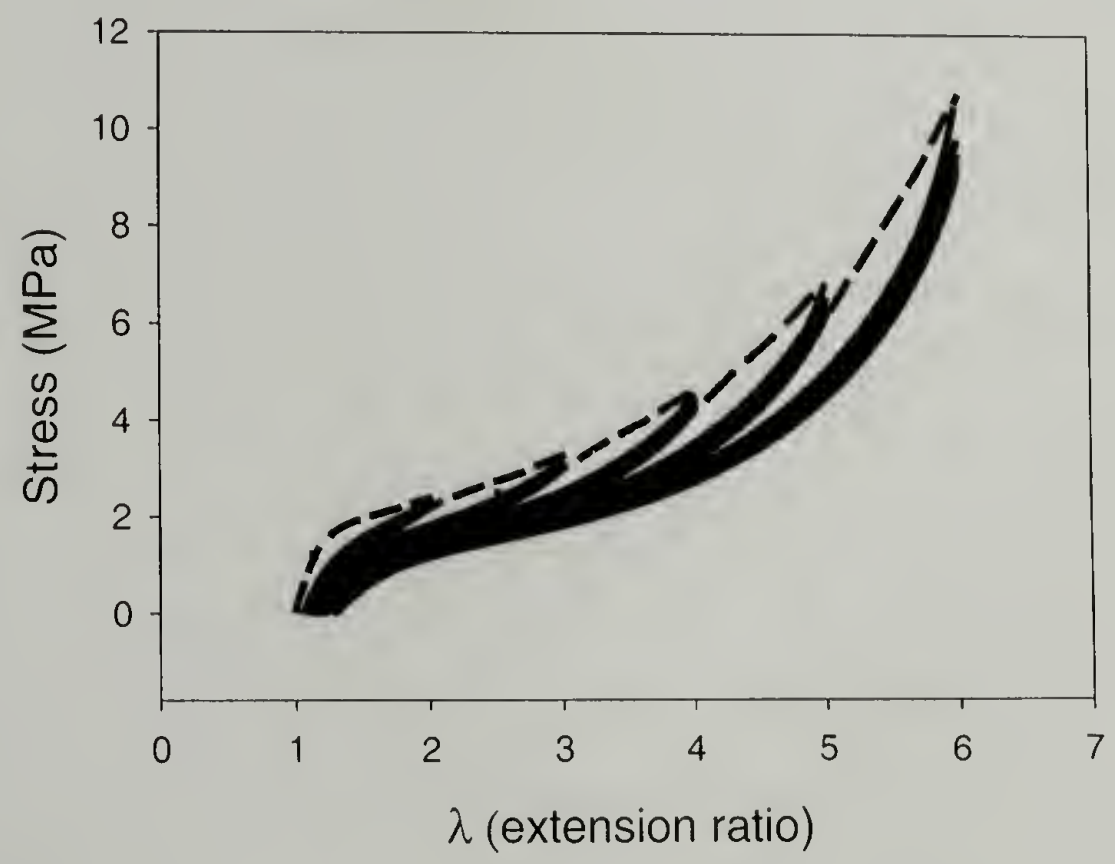

Figure 2.14 Cyclic behavior of SEBS system S40E

Figure 2.15 shows the permanent set of each system after being cycled to higher extensions. S20B and S20E show the same level of permanent set to extension ratios of 4, after which the set for S20E increases slightly. It can also be seen that S40E has a higher permanent set than the other two compositions. This can be expected because S40E has higher % of glassy PS than S20B and S20E. Natural rubber in comparison shows very little permanent set and does not change much on cycling to higher extensions.

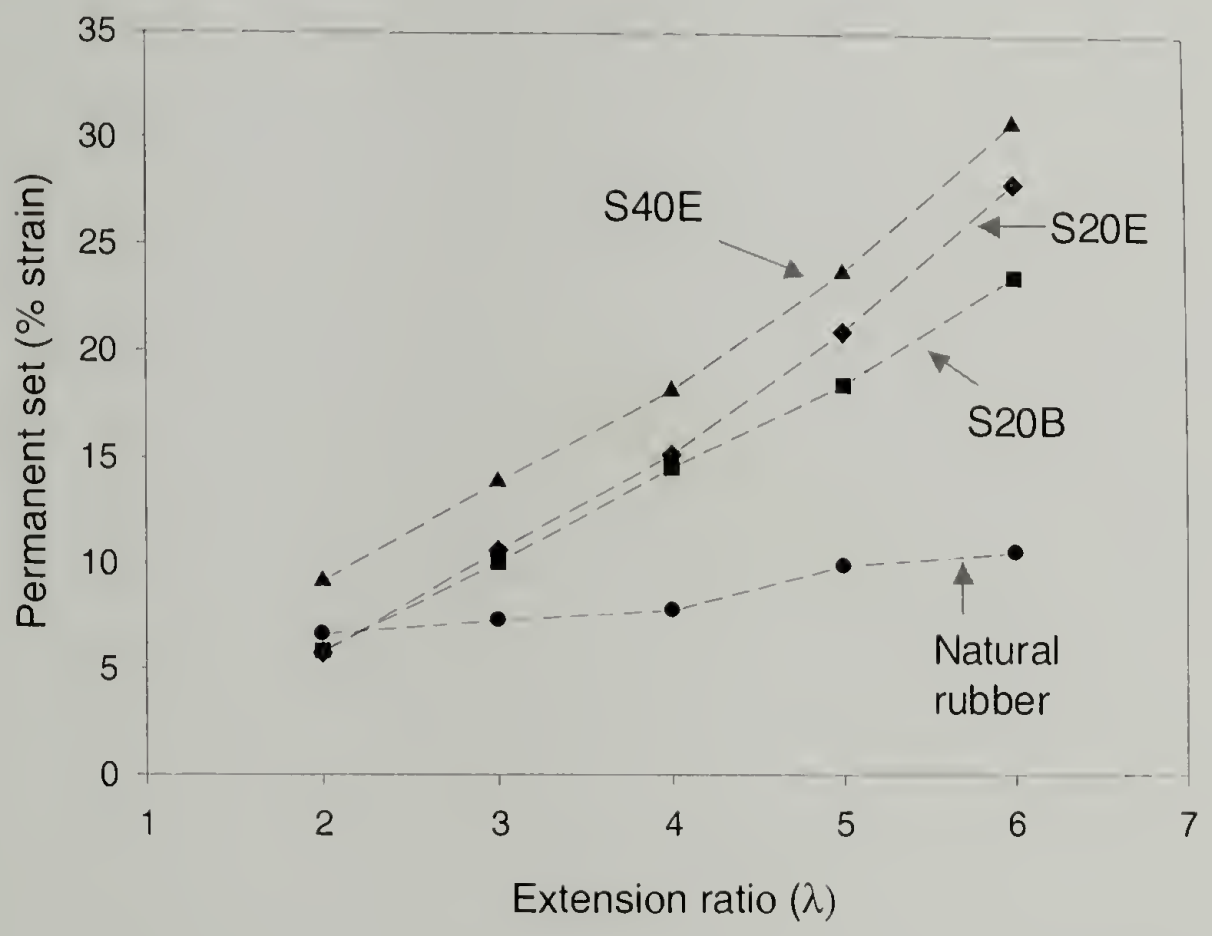

Figure 2.15 Permanent set at end of each unloading in a cyclic test

Again, taking a cue from work done on natural rubber [39], cyclic tests at different temperatures were performed on system S20E to further investigate the heterogeneity causing hysteresis. Figure 2.16 shows the cyclic stress strain behavior of S20E at 50° C.

Performing cyclic tests at elevated temperatures for S20E, it is observed that as the temperature increases from 25° C to 50° C, the observed hysteresis disappears (for loading-unloading cycles after its initial stretch to condition for Mullin's effect). It can be suggested that the stress-induced crystals formed at room temperatures melt on heating to 50° C and hence the heterogeneity disappears resulting in no hysteresis. This behavior is similar to that reported for natural rubber where the hysteresis loops observed at room temperatures show a progressive diminution with rising temperature [39,40]. The complete melting of natural rubber strain-induced crystals occurs at 57° C and hence there is small hysteresis in birefringence data still present at 50° C (figure 2.17). However this hysteresis completely disappears on raising the temperature to 75° C.

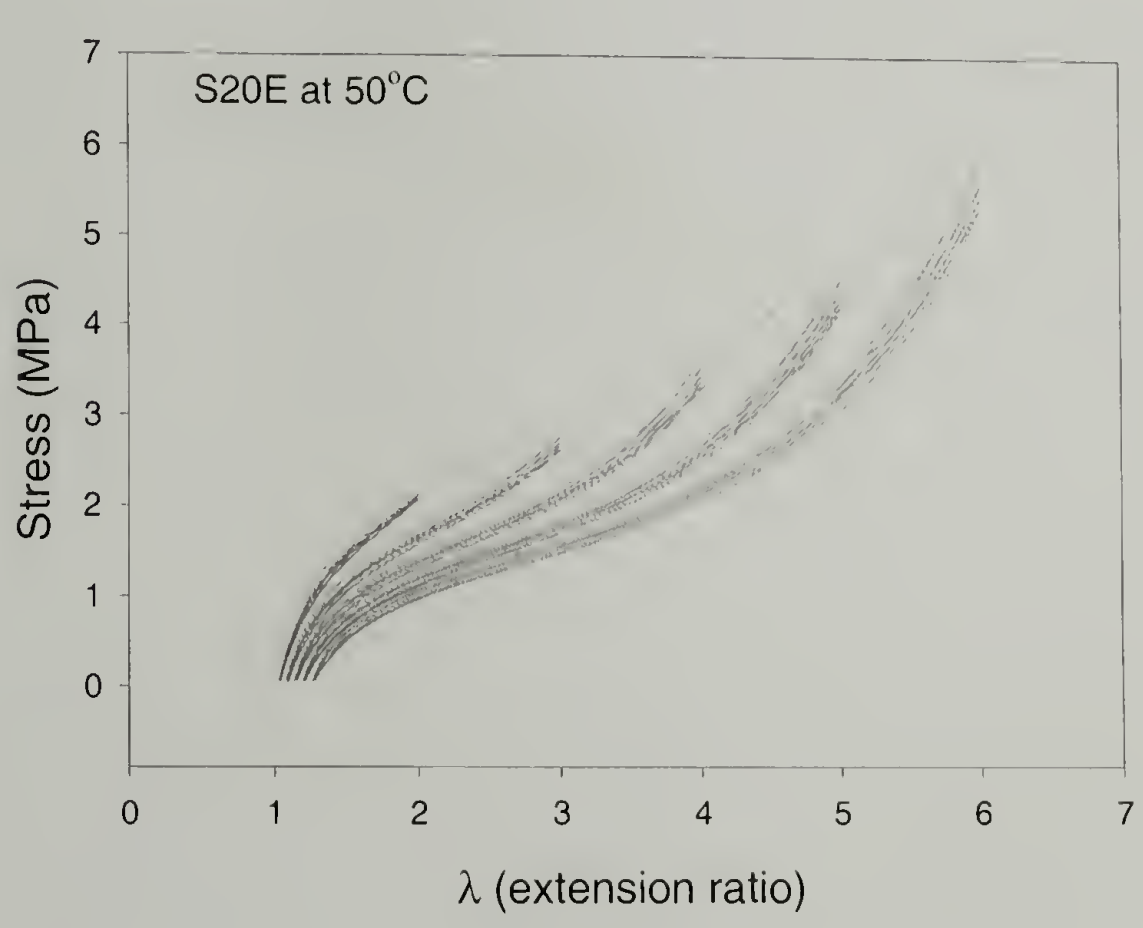

Figure 2.16 Cyclic stress-strain curves for S20E at 50° C

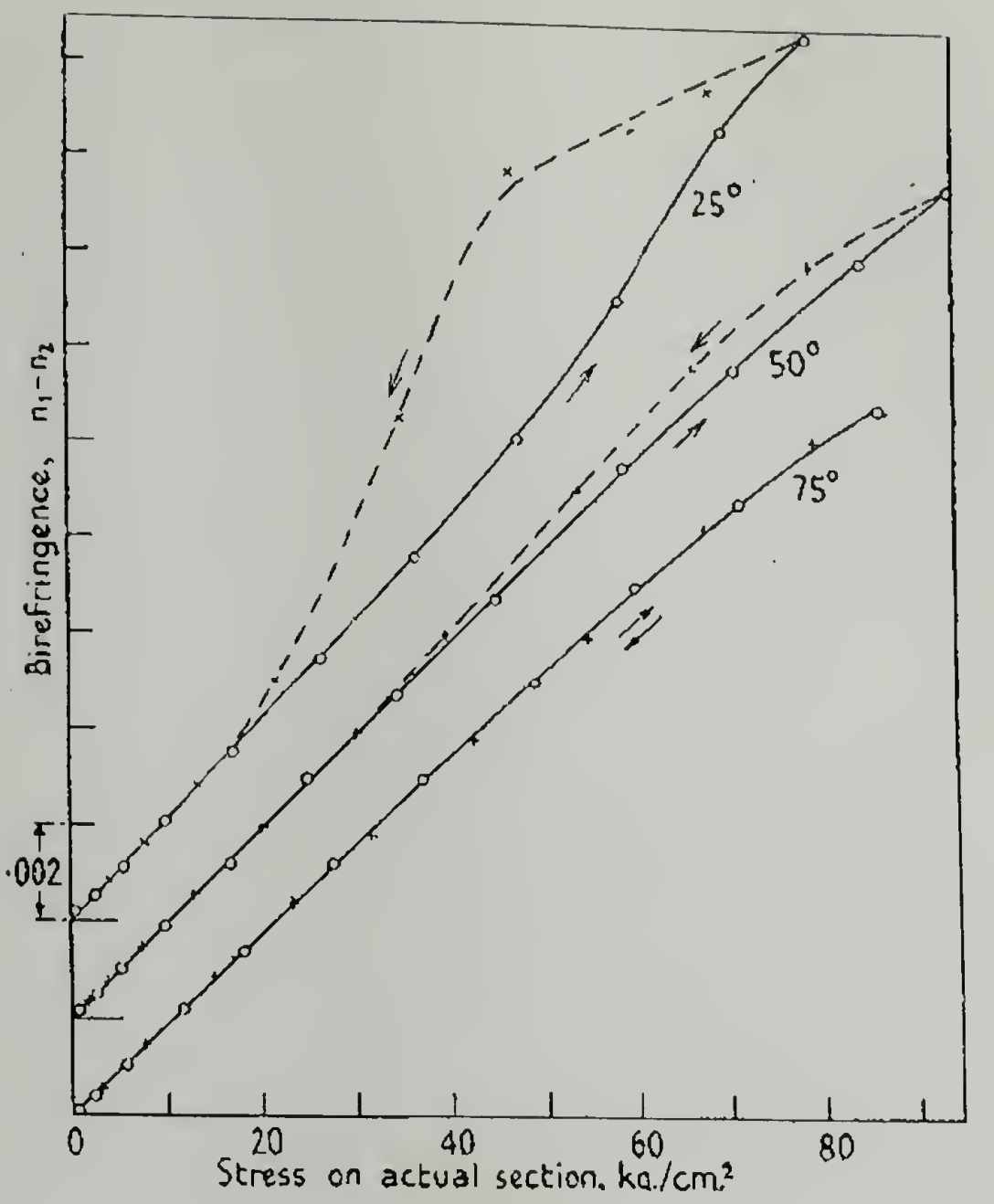

Figure 2.17 Birefringence versus stress curves at different temperatures[39] (Treolar 1946, 1947)

Stress relaxation tests at different temperatures provide important information about the nature of physical and chemical relaxation processes occurring in a material. Also stress relaxation tests have been effectively used in studying strain-induced crystallization in cross-linked natural rubber [22,23,41]. In order to probe these characteristics in SEBS materials, stress relaxations at different temperatures were performed. Figures 2.18, 2.19 and 2.20 show the relaxation modulus of S20B, S20E and S40E with time at different temperatures. The temperatures chosen lie between the glass

transition of the elastomer phase and the glass transition of the glassy PS phase. At temperatures below room temperature, all three systems show similar stress relaxation behavior. At temperatures above room temperature (25°C) and approaching the glass transition temperatures of PS (100°C), significant relaxation in stress is observed and is attributed to the enhanced mobility of the PS phase.

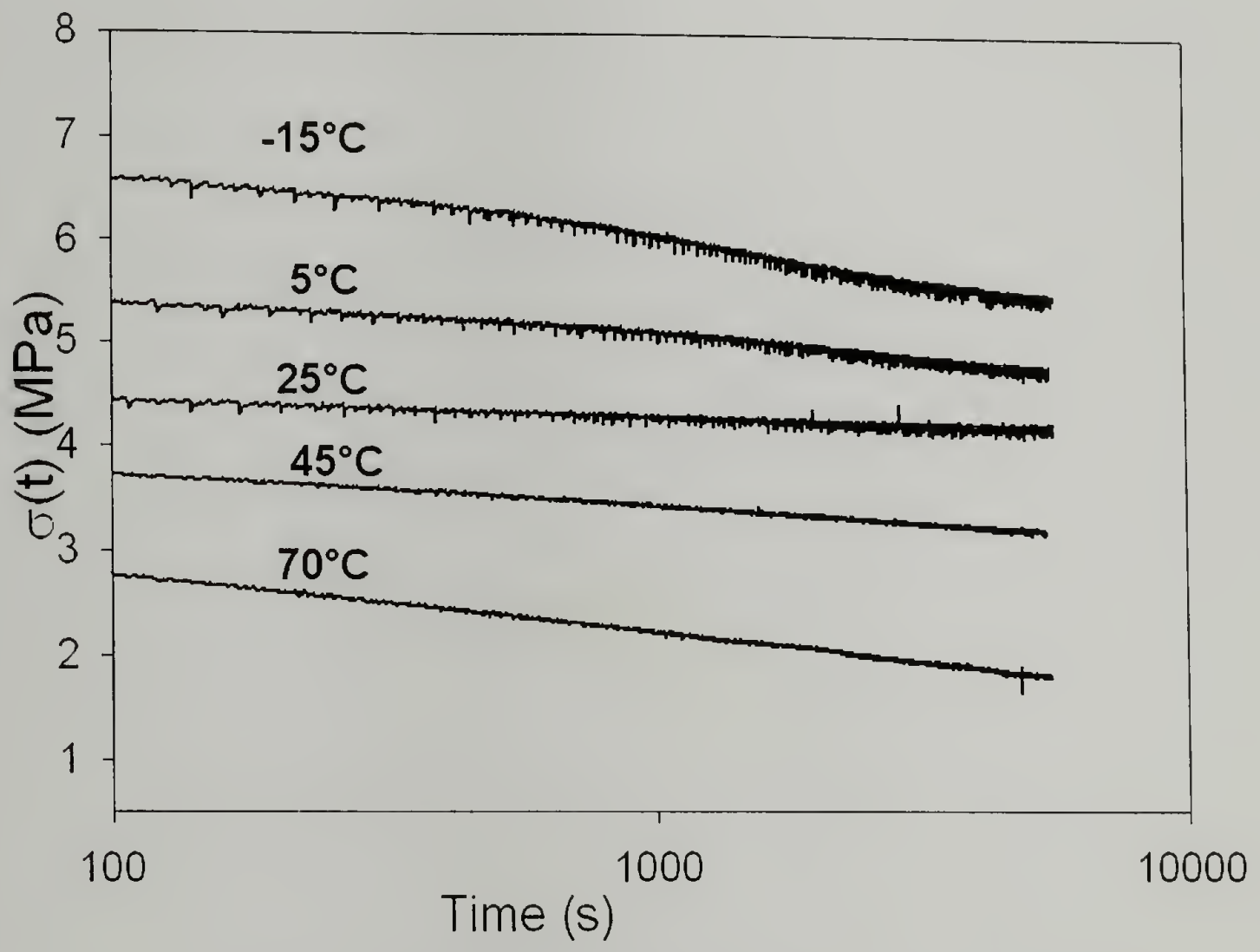

Figure 2.18 Stress Relaxation behavior of system S20B

The most interesting behavior can be seen for S20E at room temperature in figure 2.19, where there is little or no stress relaxation. It should be pointed out that all stress relaxation experiments here were done by first equilibrating the samples at specified temperatures and desired strain was subsequently applied. In such an experiment, if any strain-induced crystallization occurs in the system, it would occur

concurrently with stretching. Thus, stress relaxation behavior observed could be due to a combination of two effects, one due to the tendency to further crystallize leading to reduction in stress and other due to an increase in the number of effective junction points leading to an increase in stress [39]. These results in combination with the cyclic test data suggest that there may be the formation of strain-induced crystals in the system S20E.

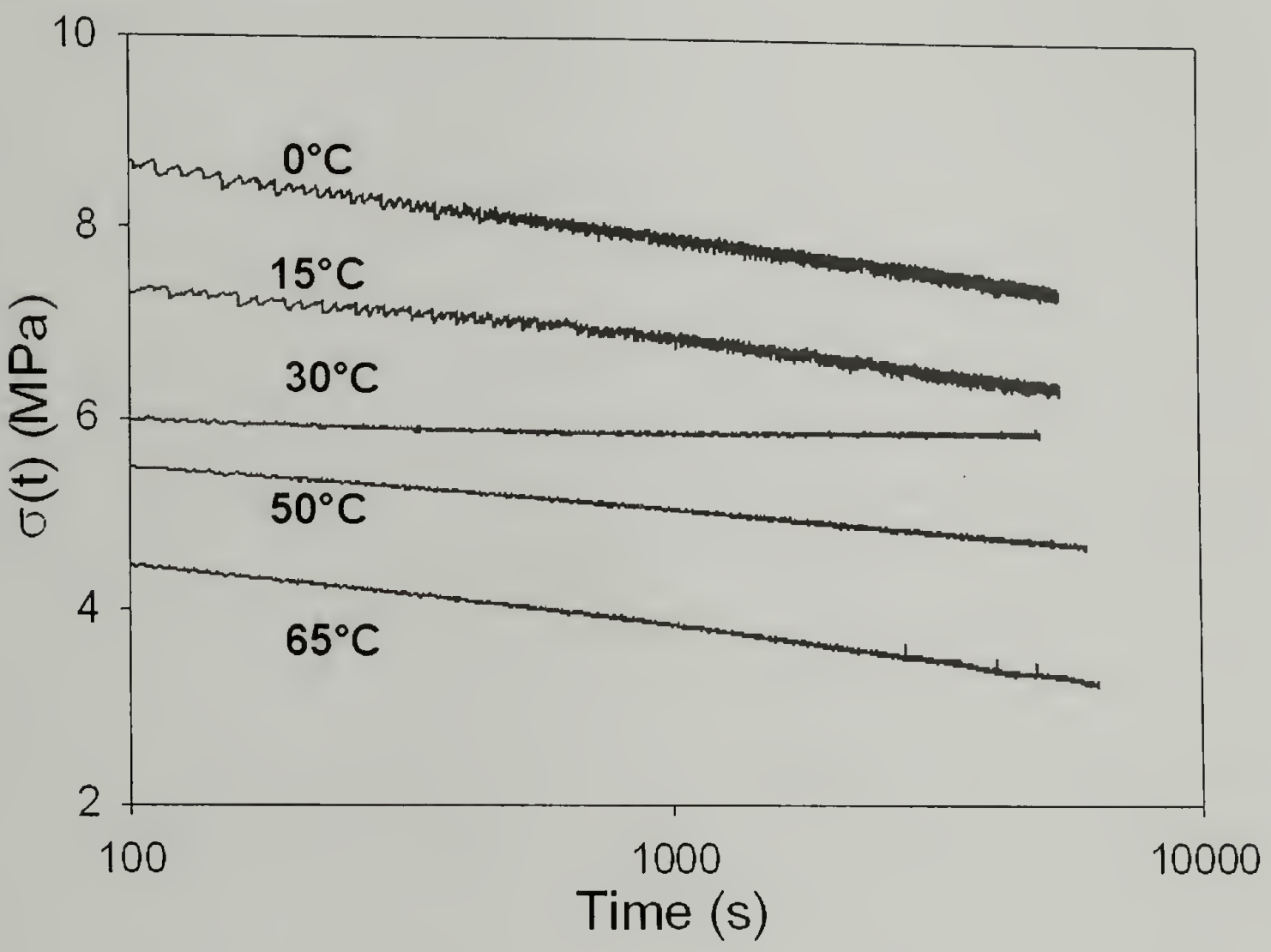

Figure 2.19 Stress Relaxation behavior of system S20E

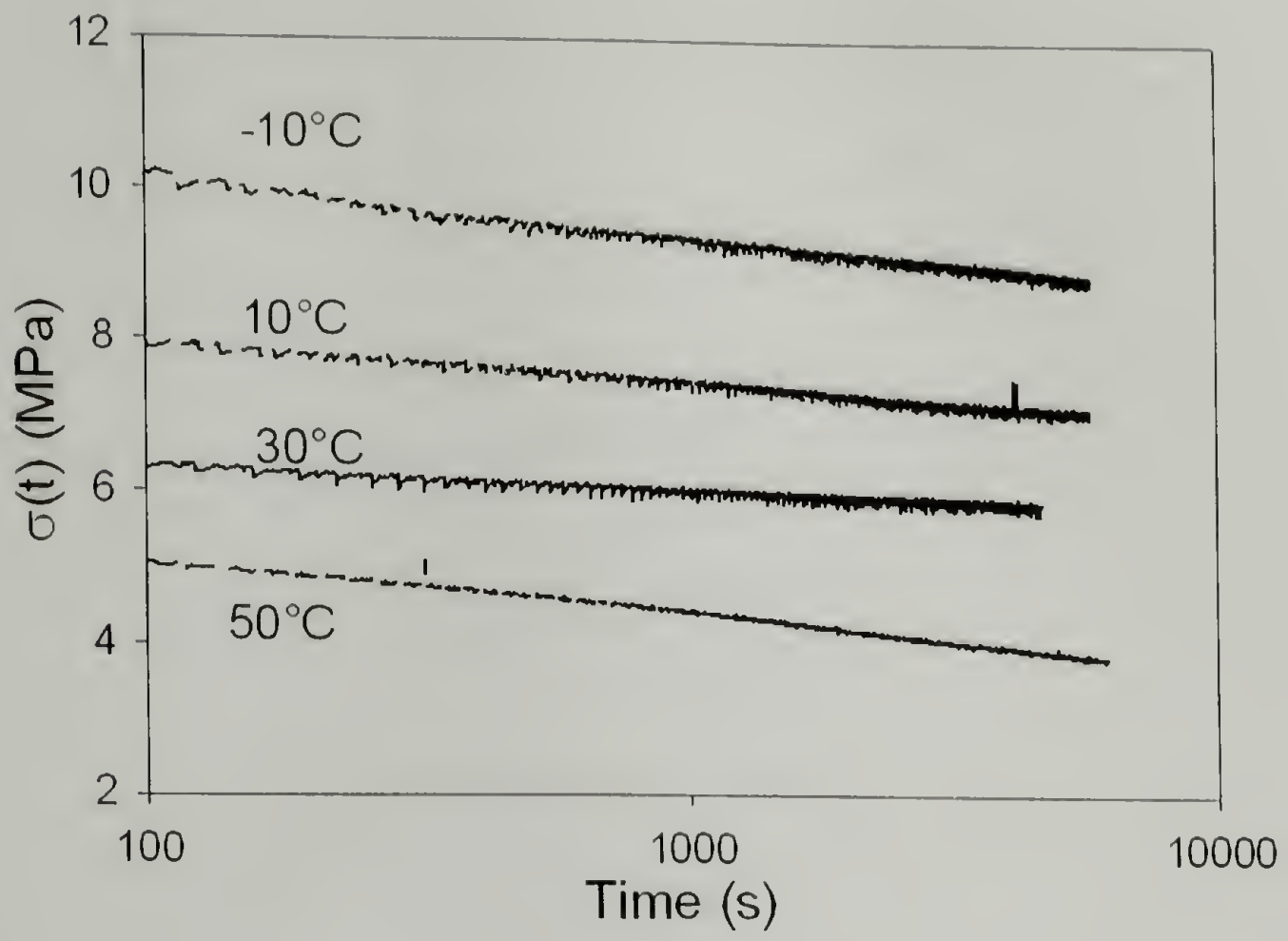

Figure 2.20 Stress Relaxation behavior of system S40E

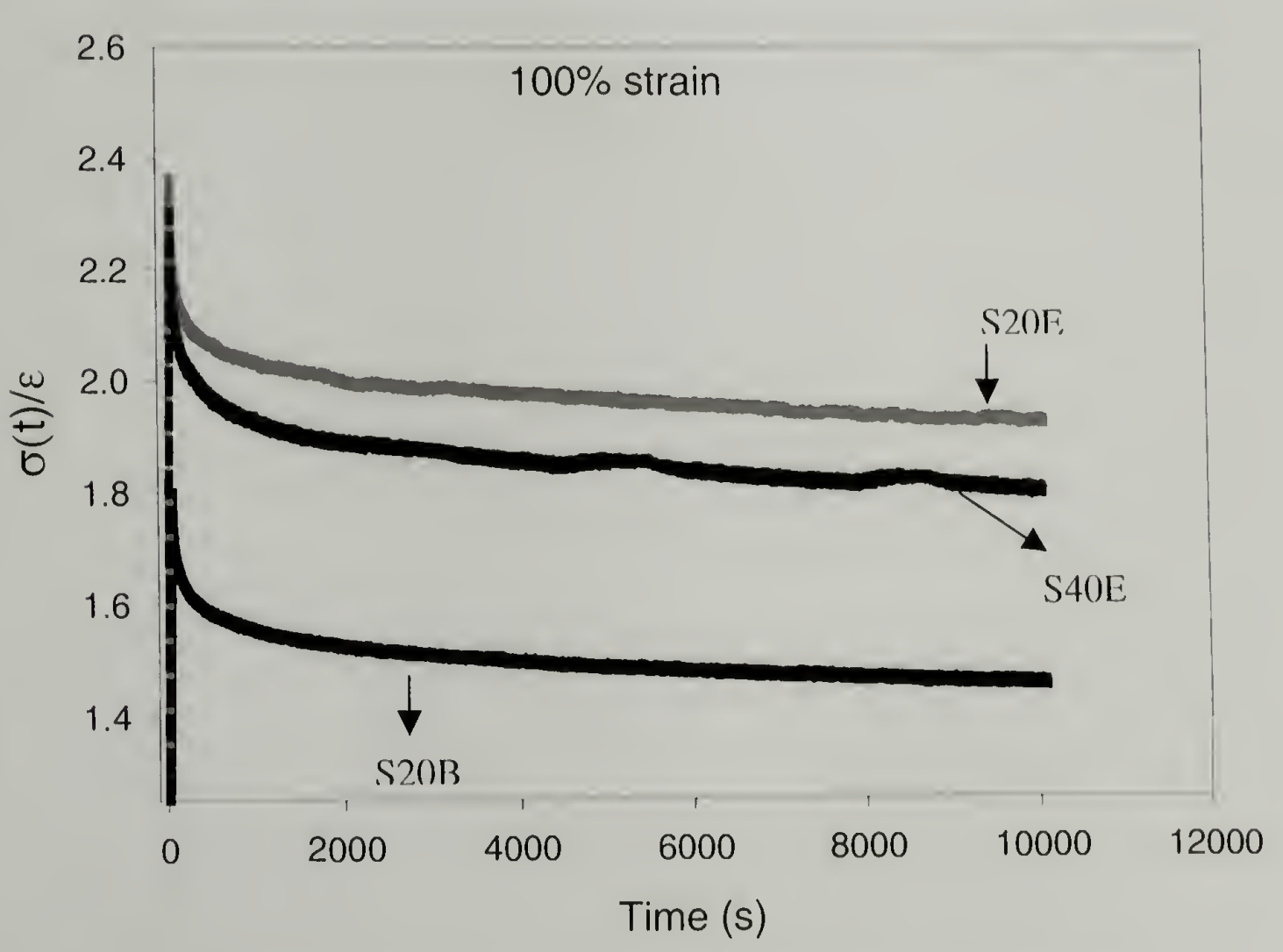

Figure 2.21 Stress relaxation behavior at 100 % strain at 25° C

In order to further study the relaxation behavior of the SEBS systems, stress relaxation experiments were carried out at 100% strain at room temperatures (figure 2.21). Again similar interesting results observed at 25% strain are observed at 100 % strain in these materials, with S20E showing the lowest relaxation of stress with time. This again suggests that there might be some strain-crystallizing occurring in S20E.

In order to probe the ability of these systems to crystallize thermally, Differential scanning calorimetry (DSC) studies were done. Figure 2.22 and 2.23 show the DSC heating and cooling scans of SEBS systems. The measured glass transition temperatures (Tg) are –55°C for both S20B and S20E and –34°C for S40E. This increase in Tg can be expected for S40E as it contains additional PS in the mid-block that raises the Tg of the elastomeric phase. S20E also shows a broad endotherm ranging from -40°C to 30°C, in addition to a Tg at –55°C. This could be due to the melting of small crystals of varying size or thickness present in S20E. On following the cooling scan for S20E, the crystallization exotherm ranging from -40°C to +10°C can be observed. Such broad endotherms have been reported in the literature for other EB based block copolymer systems [20,42] . However the endotherms observed here do not change with the sample preparation procedure as has been observed for some Poly (EBEE) block copolymer systems [42].

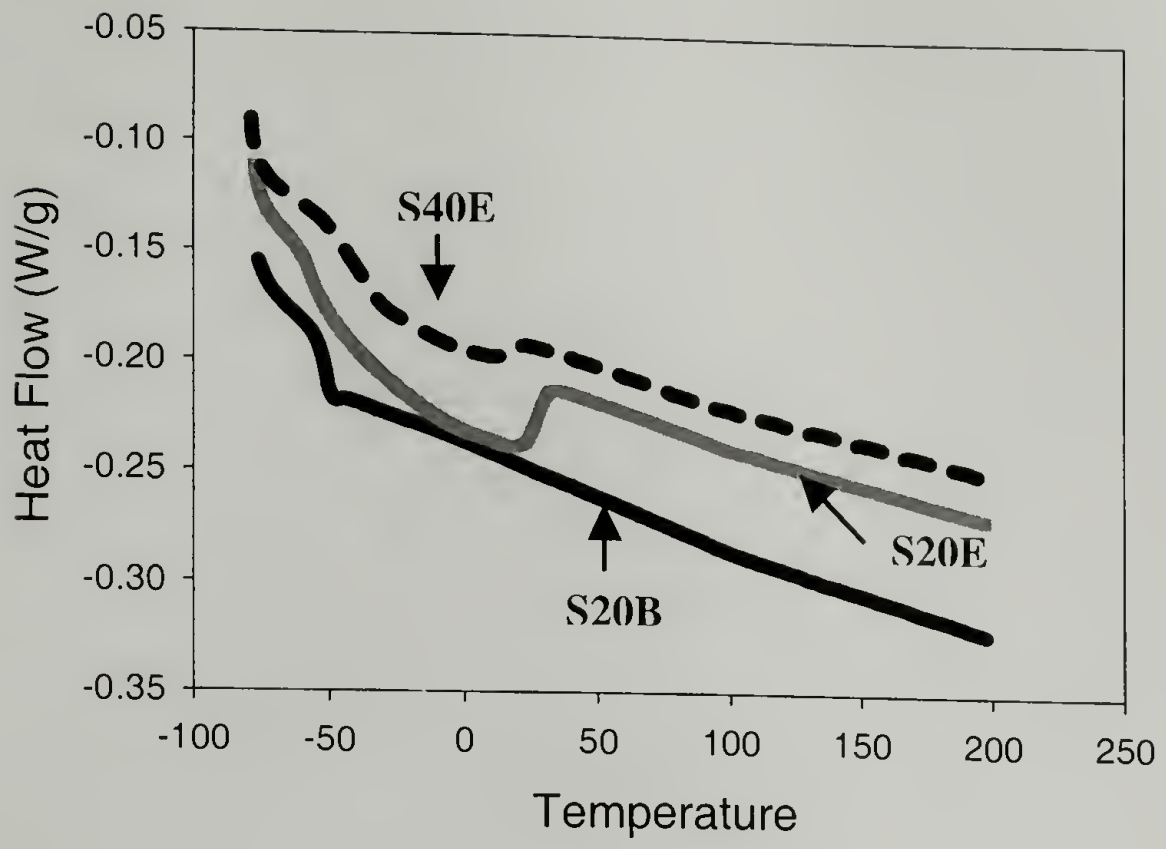

Figure 2.22 Heating DSC scans of three SEBS systems

The system S20E with higher number of ethylene than butylene segments shows this broad endotherm, suggesting that as the number of ethylene like sequences increases, its ability to crystallize increases. S20B on the other hand does not show any melting or crystallization endotherms in the heating and cooling scans respectively. The greater number of butylene segments in this system introduce large number of branches/defects and hinders the system from ordering/crystallizing. S40E shows melting/crystallization behavior similar to S20E, but the behavior is much less pronounced than S20E. This can be explained on the basis that even though there are more ethylene segments than butylene segments, the achievable crystallinity is further frustrated by the incorporation of additional styrene in EB mid-block of S40E. It can

also be observed that the broad melting endotherms in S20E and S40E overlap with glass transition endotherms.

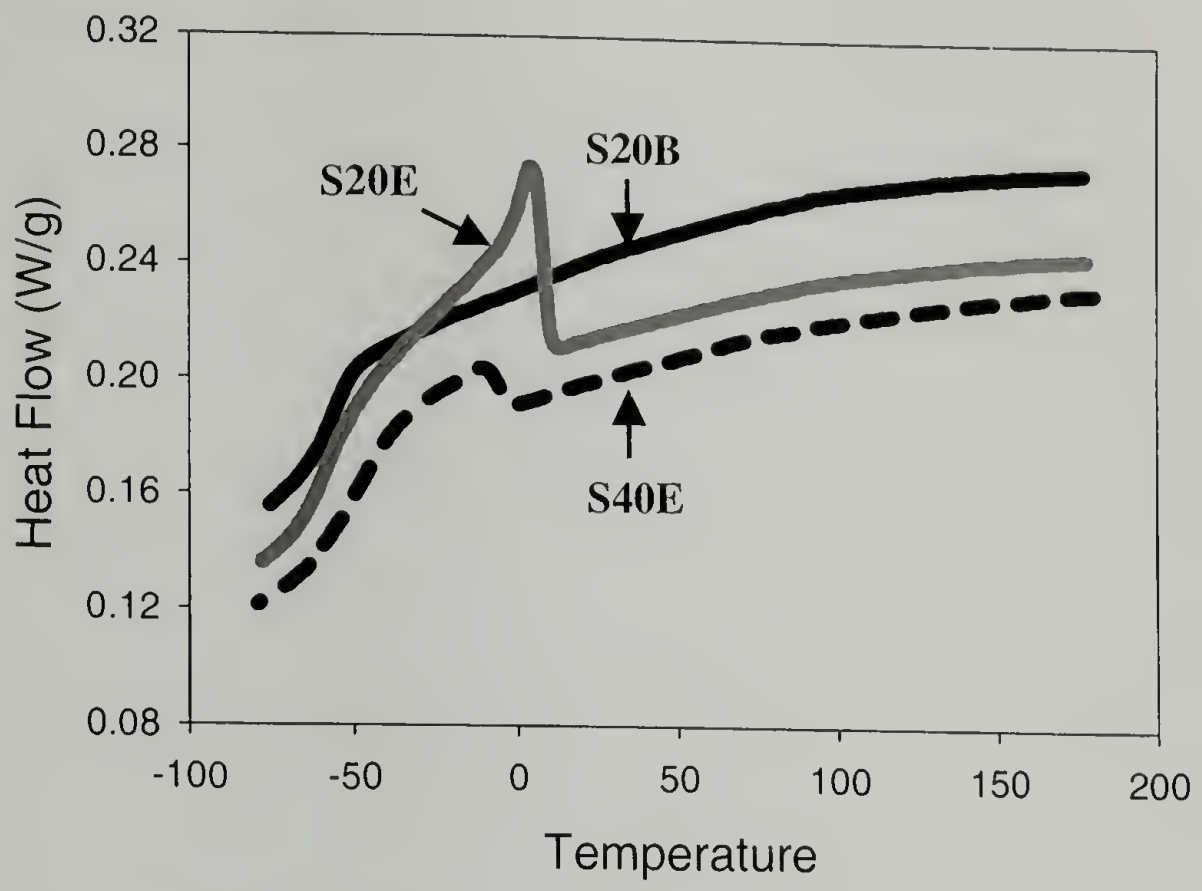

Figure 2.23 Cooling DSC scans of three SEBS systems

In order to deconvolute the glass transition behavior from the melting endotherm, Modulated DSC was employed. Using this technique, the heat flow can be deconvoluted to give the thermodynamic and kinetic components of the heat flow. This is obtained by superimposing a modulated heating rate +/-0.45°C for every 60 seconds on top of a constant ramp rate. Figures 2.24 and 2.25 shows the modulated DSC cooling and heating scan of S20E. From the reversing heat flow component, Tg information can be accurately determined. Tables 2.3 and 2.4 list the % crystallinity and the crystallization temperatures for three systems calculated from MDSC cooling and heating scans respectively. The DSC measurements clearly show low-temperature

melting/crystallization behavior for systems S20E and S40E. There is evidence for the presence of small crystallites, but all these crystallites melt below room temperature. Again, this low temperature melting and crystallization behavior is similar to that observed in natural rubber [39].

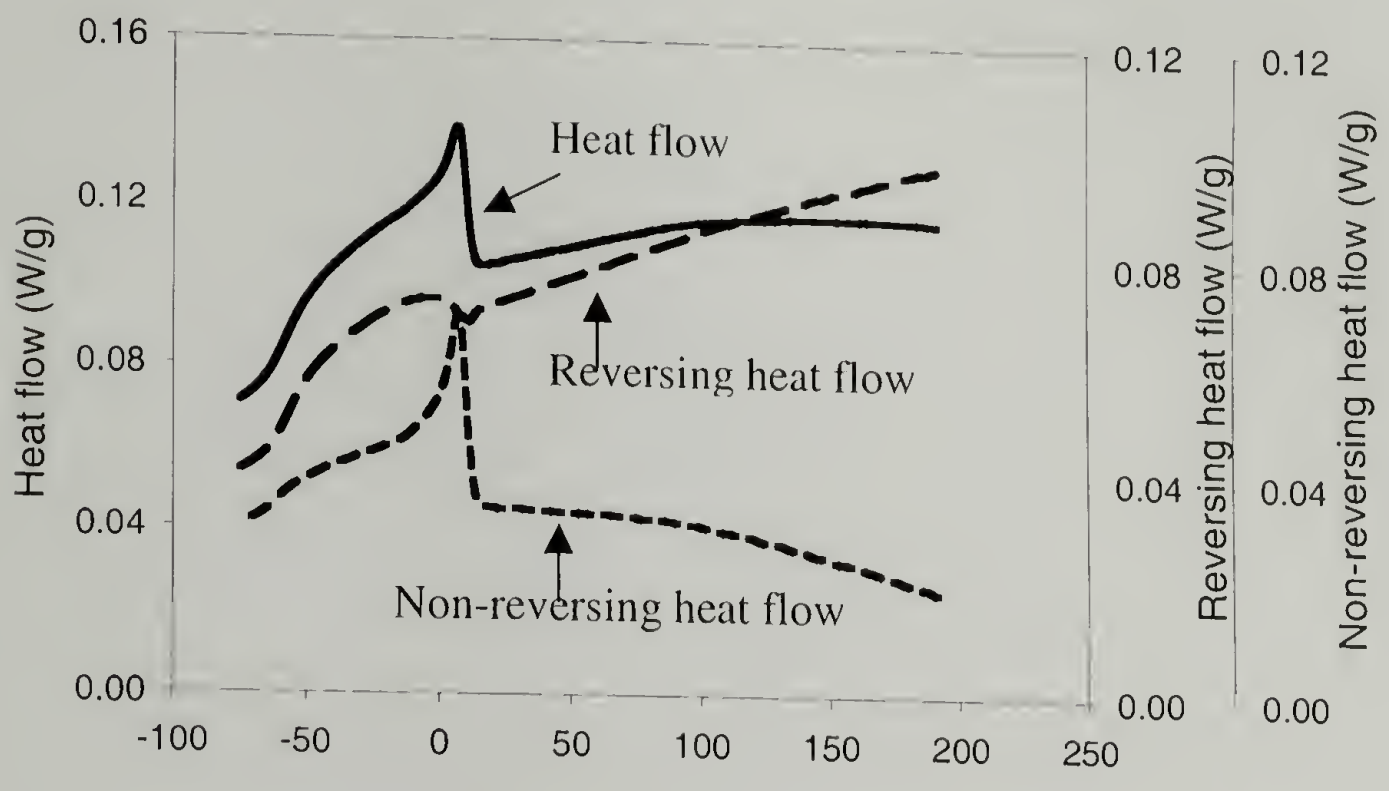

Figure 2.24 Modulated DSC cooling scan of system S20E

Kraton	Glass Transition of the rubbery phase	Approximate Crystallization temperature	% Crystallinity (corrected for PS end blocks)
S20B	-50°C	-----	-----
S20E	-55°C	7°C	14%
S40E	-34°C	-3°C	5%

Table 2.3 % crystallinity (cooling cycle)

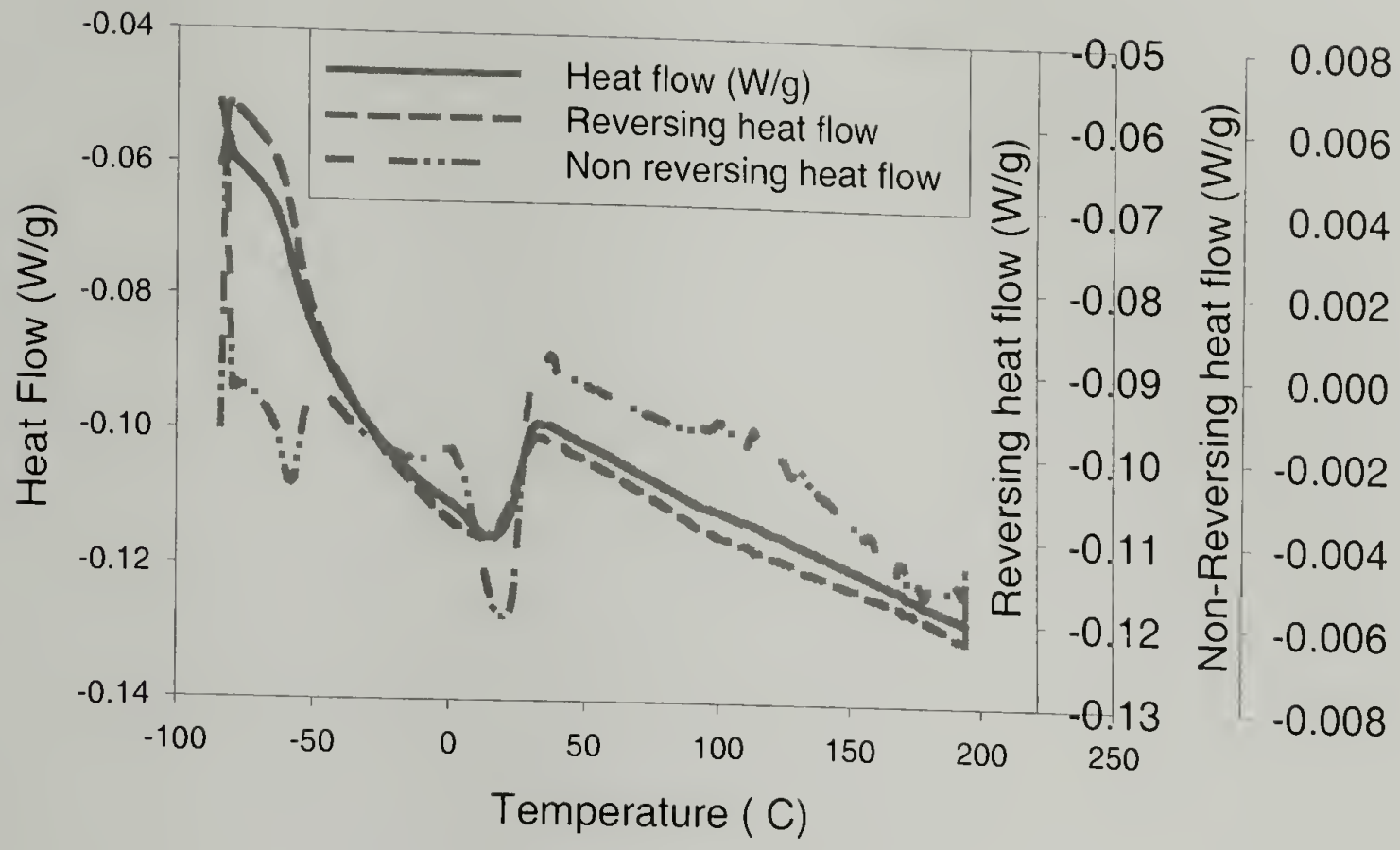

Figure 2.25 Modulated DSC heating scan of system S20E

Kraton	Glass Transition, T_g	Approx. Melting Temperature	% Crystallinity (corrected for PS end blocks)
S20B	-50°C	-----	-----
S20E	-55°C	23°C	15%
S40E	-34°C	10°C	6%

Table 2.4: % crystallinity (heating cycle)

WAXD measurements were performed on these three systems at room temperature to verify the DSC experiments. Figure 2.26 and Table 2.5 shows the WAXD intensities and full width at half maximum (FWHM) of the reflections for these

three SEBS systems at room temperature. These measurements show sharp amorphous halos without any crystal reflections for all the three systems.

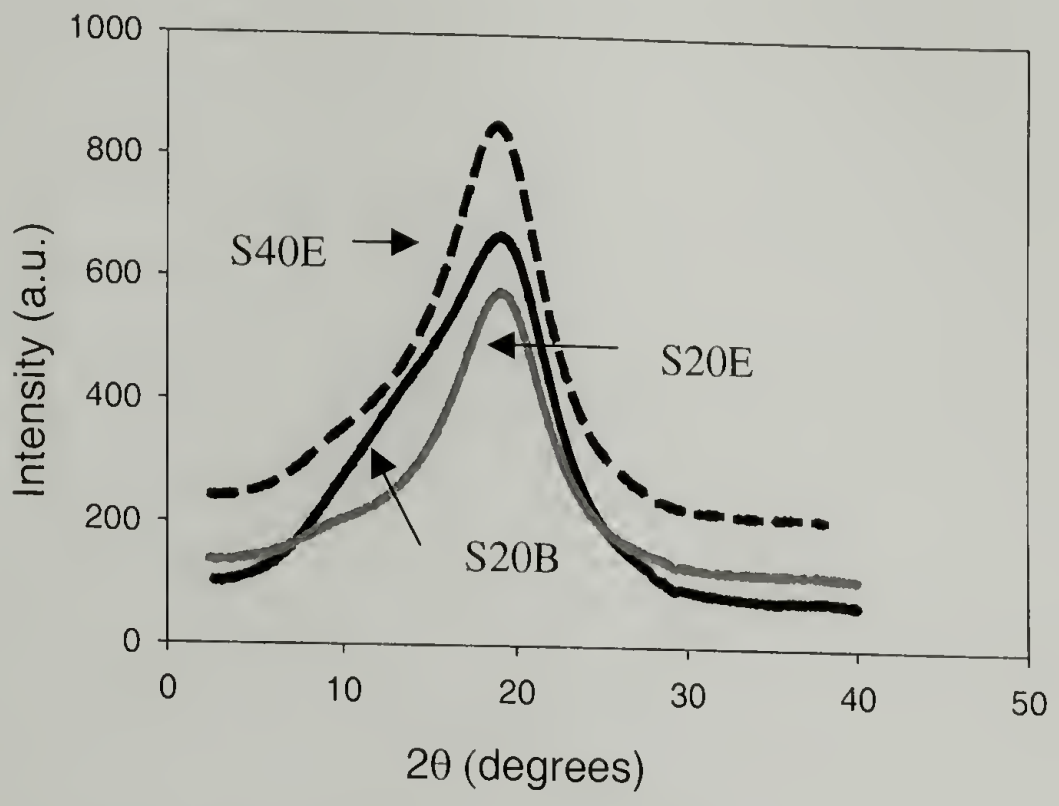

Figure 2.26 WAXD intensities for three SEBS systems at room temperature

But it can be observed that the FWHM for the amorphous halos of systems S20E and S40E are smaller compared to that of S20B and suggest their ability to order and crystallize. But this does not explain the elastic hysteresis and stress relaxation behavior of S20E. Both stress relaxation and elastic hysteresis occur when the sample is stretched or strained. Natural rubber provides an excellent example of an elastomeric system, which exhibits low temperature melting/crystallization behavior, shows no crystallinity at room temperature but crystallizes on stretching it to 400% strain.

Polymer	Peak-mean position (2θ)	Full width at half maximum (FWHM) 2θ degrees
S20B	19.1	11.4
S20E	19.0	7.5
S40E	19.1	8.3

Table 2.5: FWHM of the diffraction peaks of the three systems

In order to study the ability of these systems to undergo strain-induced crystallization, deformation calorimetry studies were performed on these SEBS systems. Figure 2.27 displays the heat Q, work, W and internal energy change, ΔU for an ideal linear rubbery solid for small strains. The internal energy of a linear rubbery solid increases linearly with extension ratio as it is being stretched (tension). (An ideal rubber has no overall ΔU on distortion). However, any non-linear effects like strain-induced crystallization, strain induced phase mixing in two-phase TPEs, hydrogen bonding etc. affect this ideal linear internal energy increase in elastomers.

Figure 2.27 Heat, Q, Work, W and Internal energy change, ΔU for a linear rubbery solid for small strains

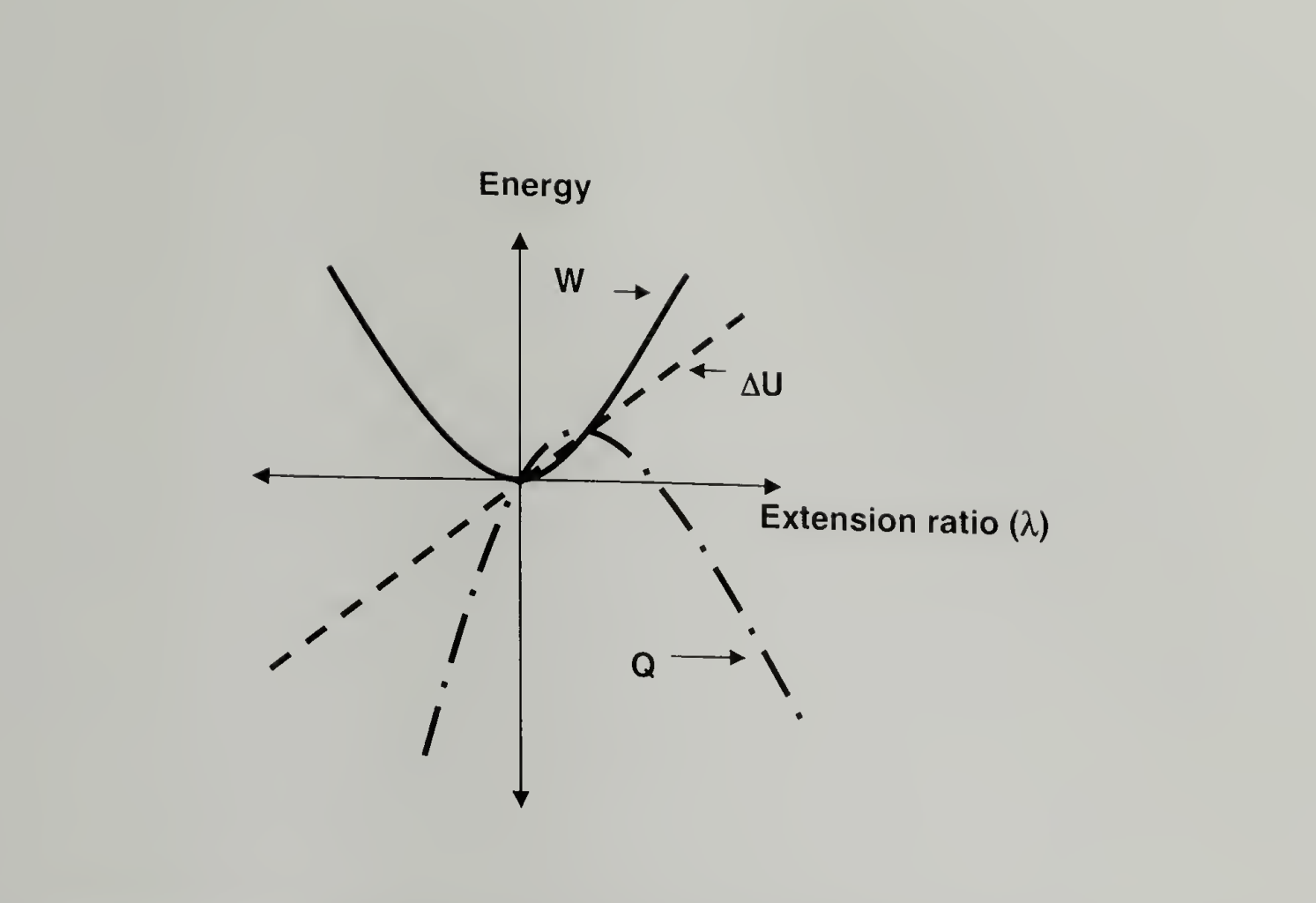

Figure 2.28 Energetics of deformation of Natural Rubber

Figure 2.28 displays the calculated heat, work and internal energy profiles in natural rubber, normalized by the weight of the sample, as a function of the extension ratio. Stress versus extension ratio plot has been overlaid on the background for reference. As can be seen in figure 2.28 and reported elsewhere for natural rubber [31], at lower extension ratios (up to 4), the changes in internal energy are positive and rise gradually as expected for an elastomeric solid. However on further deformation of sample above $\lambda = 4$, there is a sharp drop in internal energy, with the change in internal energy now becoming negative and dropping to about –8 Joule/gm on reaching an extension ratio of 5.6. This drop in internal energy has been attributed [31] widely to the strain-induced crystallization occurring in natural rubber at these extension ratios. The unloading curve shows a slightly different response. There is a protracted endotherm at higher extension ratios suggesting some possible melting and recrystallization of strain-induced crystals upon unloading. The combination of these two processes during unloading delays the complete melting of strain-induced crystals to much lower extension ratios than that required to initiate crystallization during loading. It can also be observed that large internal changes observed at higher extension ratios are completely recoverable on unloading, suggesting that crystallization and melting occur to yield no net change in the internal energy. Since the change in internal energy over the complete load-unload cycle is zero, the hysteresis in work matches exactly that in the heat absorbed/dissipated. All these observations are in accordance with previous studies on crosslinked natural rubber [31,36,43].

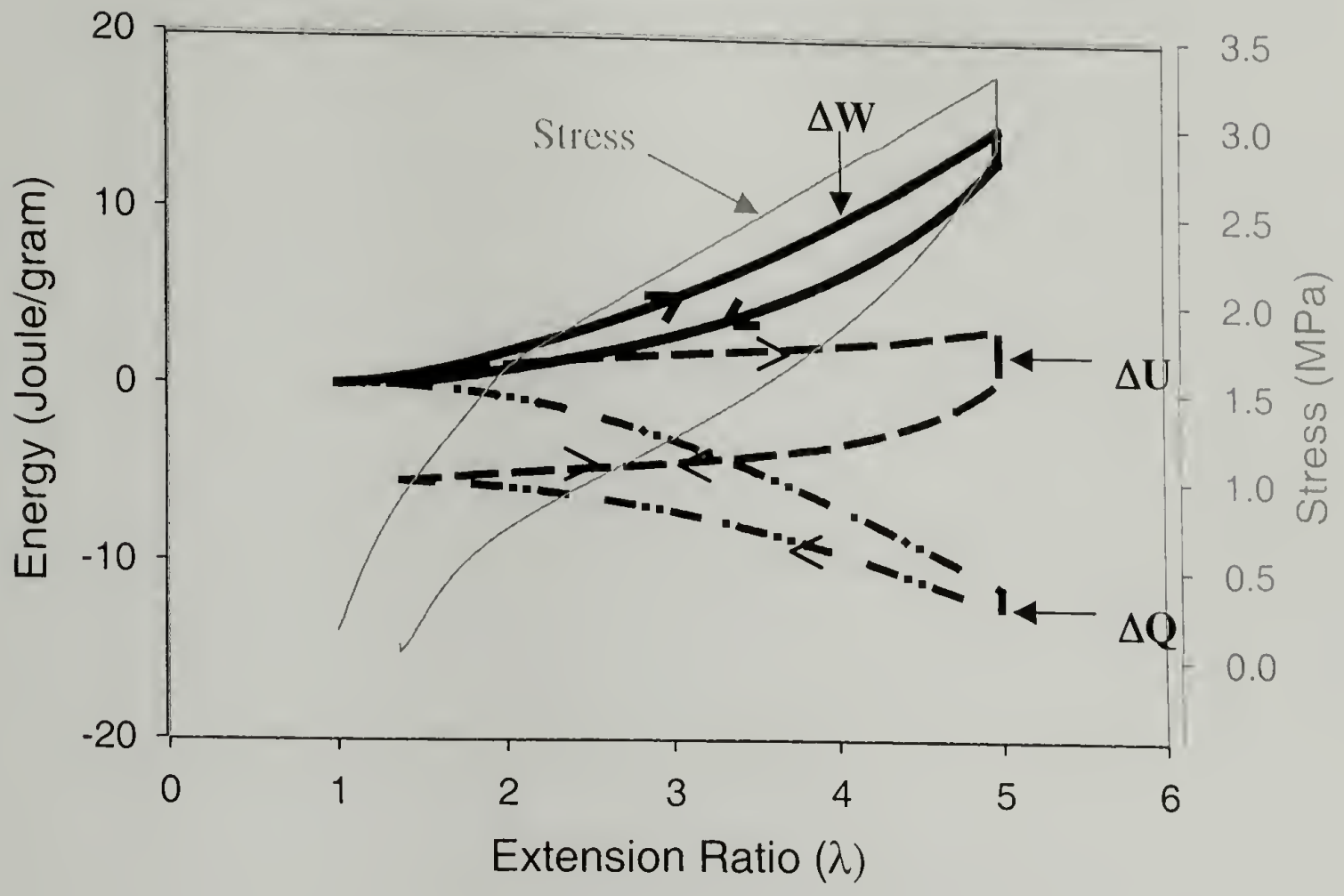

Figure 2.29 Energetics of deformation of S20B

From figure 2.29, it can be seen that as work done (ΔW) on the S20B system increases with increasing extension ratio, its internal energy also rises proportionately with increasing stretch and hence behaves very close to a linear rubbery solid depicted in figure 2.27. This behavior can be anticipated for S20B system from our earlier results on mechanical testing, DSC and WAXD where this system does not crystallize either thermally at low temperatures or under strain. The change in the internal energy rises upon loading the sample and drops similarly upon unloading the sample. It can be observed that the changes in internal energy and the changes in heat absorbed are not fully reversible. There is a lot of irrecoverable internal energy in the material corresponding to about 5 J/g upon unloading the sample. A residual strain of

approximately 25% remains in the material upon unloading. These changes can be expected because of the deformation of glassy PS domains as the system is loaded to high extension ratios.

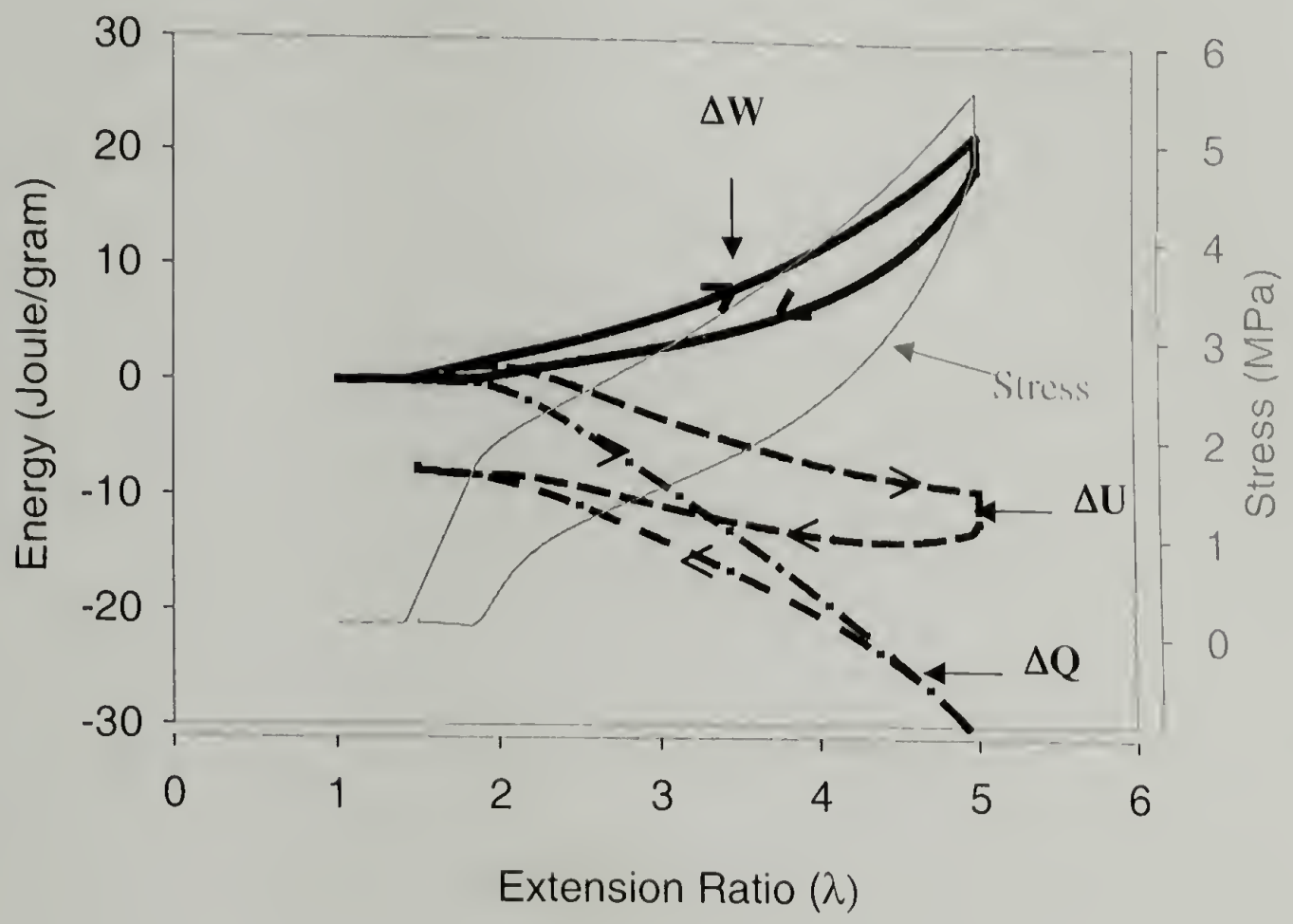

Figure 2.30 Energetics of deformation of S20E

Figure 2.30 shows the energetics of deformation of S20E. It can be immediately observed from the change in internal energy, ΔU, that this system behaves entirely different from S20B. The change in internal energy resembles that of natural rubber in that there is considerable drop in internal energy upon extension. This negative change in internal energy provides strong evidence for strain-induced crystallization in S20E similar to that observed in natural rubber. Also important differences can be observed for S20E in comparison with natural rubber. First the internal energy drop for the system

S20E starts occurring at low extensions and continues to decrease on further extension. Secondly, there is a residual strain of about 35% left in the material on unloading the system. This is in agreement with independent permanent set data obtained from cyclic test data. Also, there is significant irrecoverable internal energy in the material as the sample is unloaded, different from completely recoverable internal energy observed for natural rubber. These changes can be expected and are due to permanent deformation of cylindrical PS domains at higher extensions. The negative internal energy changes for S20E at low extension ratios suggest that strain-induced crystallization occurs in S20E at extensions much lower compared to those at which strain-induced crystallization occurs in natural rubber. This result is in complete agreement with the results obtained from stress relaxation behavior of S20E at 25% strain. Even at such low strains, the relaxation behavior is significantly altered for S20E. Also, the cyclic test data suggests that the formation of strain-induced crystals (leading to hysteresis) occurs at lower strains and persists as the sample is strained to an extension ratio of 6. The deformation calorimetric data thus supports strain-induced crystallization at low strains for S20E. An internal energy change of -12 J/g for an extension ratio of 5, obtained by strain-induced crystallization corresponds to 5 % crystallinity (after correcting for end block PS content). This value has been estimated using the heat of fusion of an equilibrium crystal of PE (290 J/g). However, it can be expected that this value is a lower bound for % crystallinity. Similar results for strain-induced crystallization at lower extensions has been reported previously [31] for polyurethane-urea elastomers (with polyether soft segments) using deformation calorimetry studies.

Figure 2.31 shows the energetics of deformation of S40E. As the work done on the system (ΔW) increases with stretch ratio, change in internal energy (ΔU) also rises proportionately. This behavior is similar to that observed for S20B. Until an extension ratio of 3 is reached, the internal energy rises like that of an linear elastomeric solid, but then on further extension beyond λ=3, there is a slight drop in internal energy though the overall internal energy change still remains positive. This slight drop in internal energy suggests some strain-induced crystallization occurring in S40E, although to a much lower extent than S20E. It can be observed that this system also shows the highest residual strain of all three SEBS systems studied. This can be explained on the basis of the increased amount of PS present in the elastomeric matrix for the S40E system.

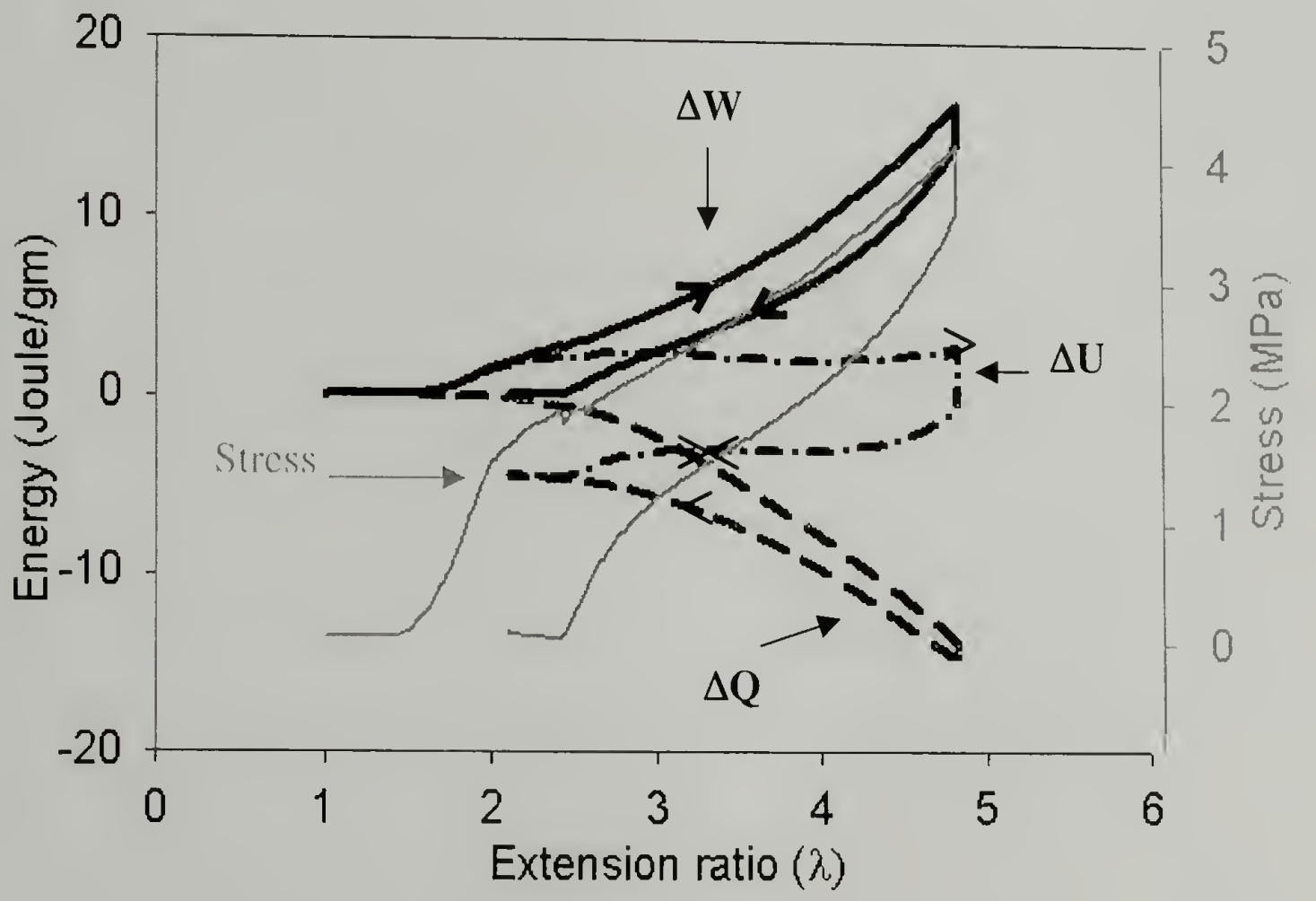

Figure 2.31 Energetics of deformation of S40E

In order to observe the deformation characteristics of these SEBS materials at higher temperatures, deformation calorimetry experiments were performed at 45° C. Figure 2.32 shows the energetics of deformation of S20B at 45° C. It can be observed from this curve (in comparison with the one at 25° C) that the internal energy again increases linearly as work is being done on the sample. Thus this system behaves like a linear elastomer at 45.1 °C.

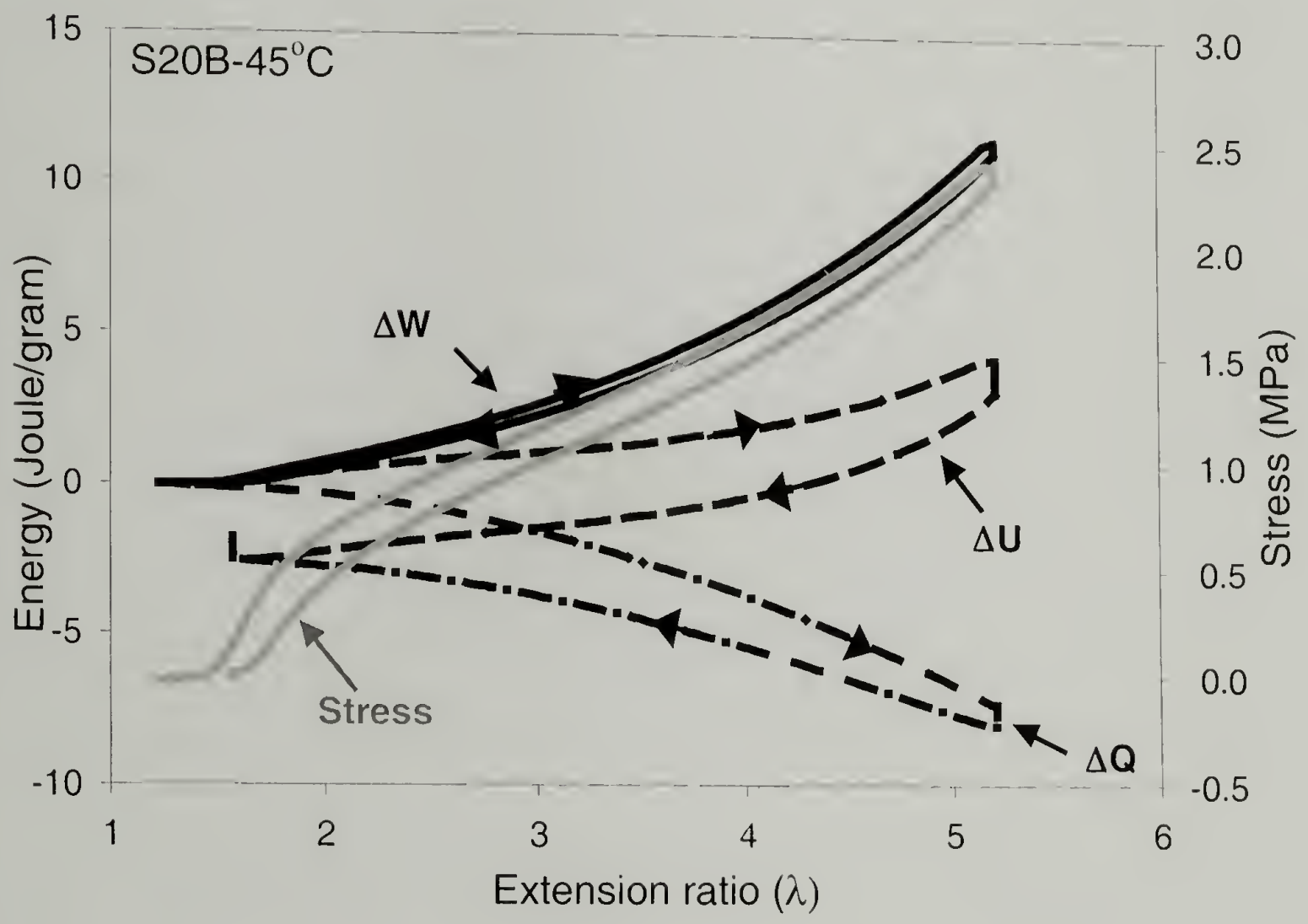

Figure 2.32 Energetics of deformation of S20B at 45.1 °C

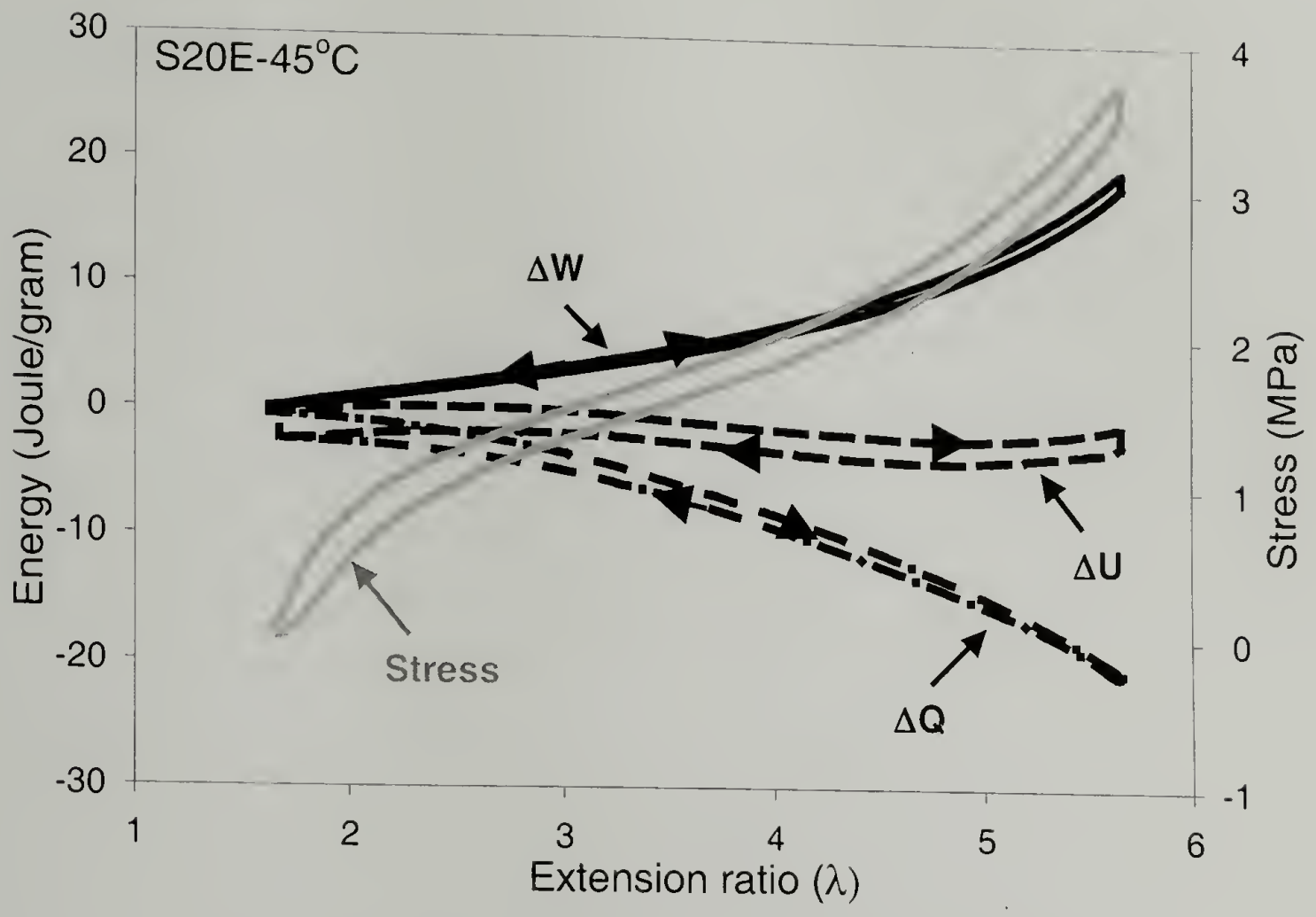

Figure 2.33 Energetics of deformation of S20E at 45.1 °C

Figure 2.33 shows the energetics of deformation of S20E at 45.1 °C. It can be immediately seen that the large negative internal change attributed to strain-induced crystallization of S20E at room temperature (25.7 °C) is significantly reduced when the temperature of the system is raised to 45.1 °C.

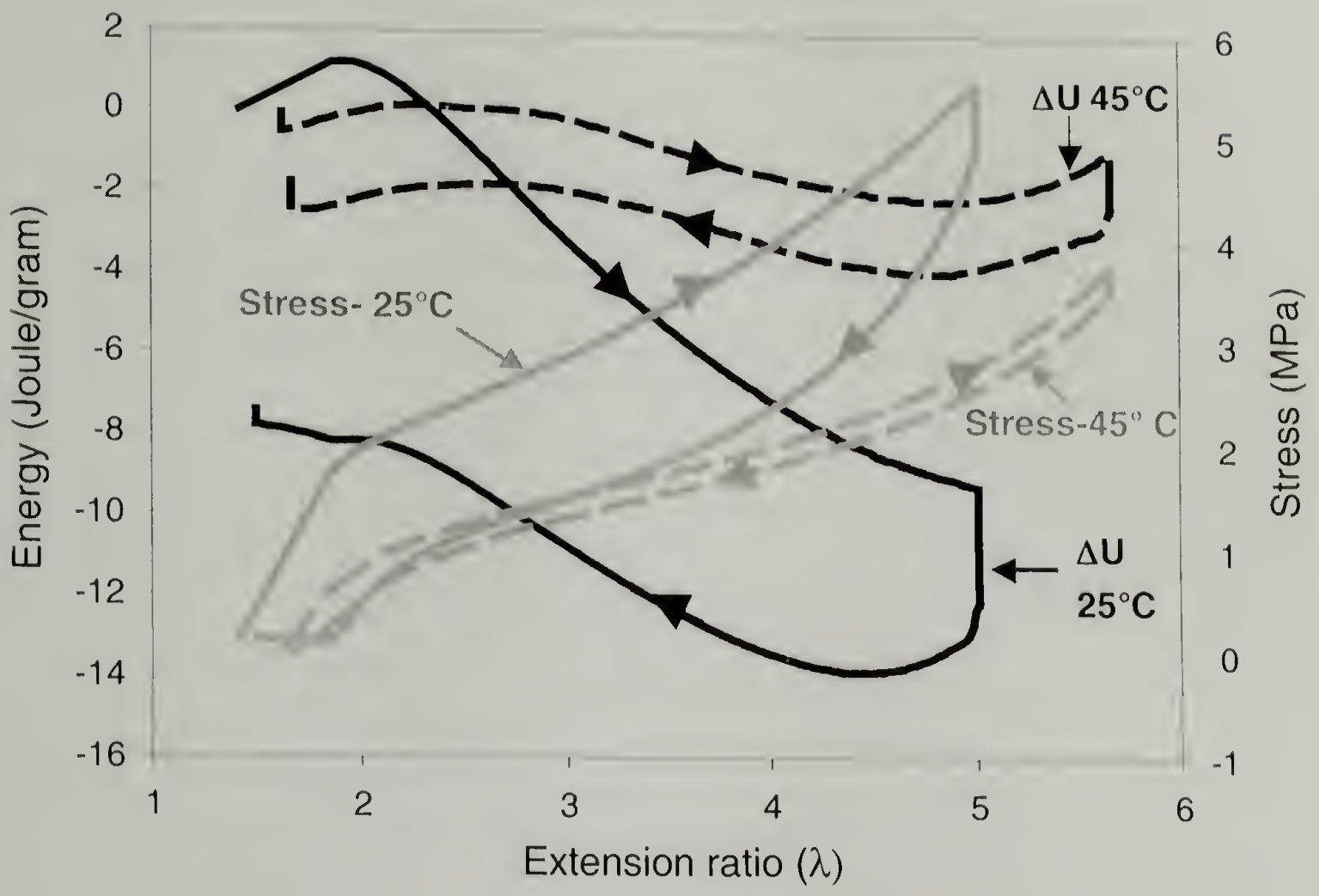

Figure 2.34 Internal energy changes at 25.7 °C and 45.1 °C

Figure 2.34 clearly points out the difference in internal change at these two temperatures. At 25.7 °C, a negative internal energy change of –12 Joule/gram (corresponding to a crystallinity of 5 %) is obtained for an extension ratio of 5, however at 45.1°C, the negative internal energy observed is –2.2 Joule/gram for an extension ratio of 5.6. This behavior is similar to the hysteresis in birefringence data for natural rubber. Natural rubber shows significant hysteresis when cycled at 25 °C, but at high temperatures, the hysteresis disappears gradually. This is because of the melting of strain-induced crystals in NR as the temperature increases to 57°C (melting temperature of strain crystals in NR). Similar response is observed from internal energy

measurements for the system S20E at 45.1 °C. It can be expected that if temperature is raised further, the negative internal energy change would disappear and system S20E would reveal a response closer to that of S20B.

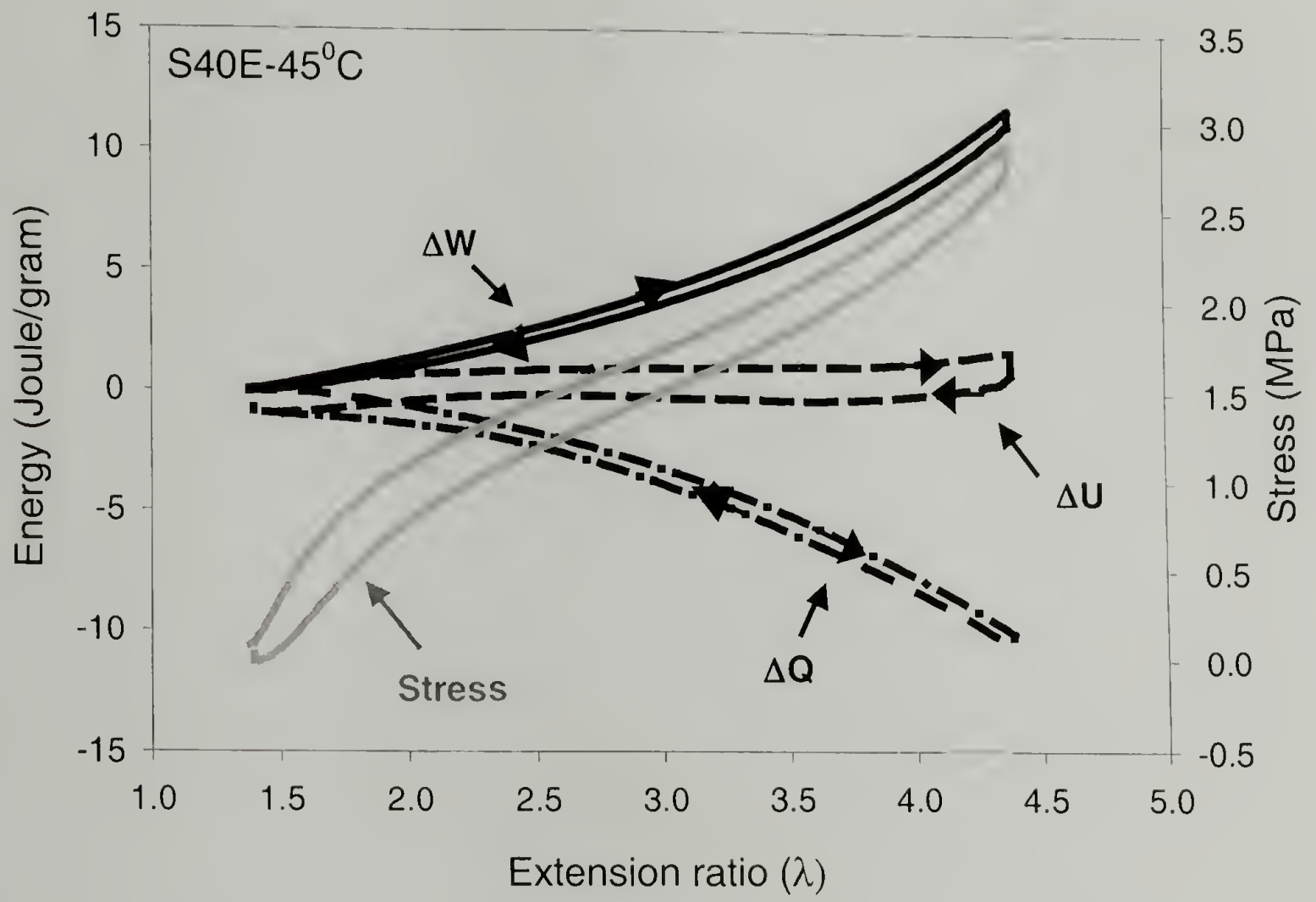

Figure 2.35 Energetics of deformation of S40E at 45.1 °C

The energetics of deformation of the system S40E (with additional styrene incorporation) at 45.1 °C can be seen in Figure 2.35. The internal energy changes show no evidence of strain-crystallization in this system. It can also be seen that there is very little hysteresis in the work done and heat absorbed curves at 45.1°C compared to those curves at 25.7°C (as seen in figure 2.31). These deformation calorimetry studies at higher temperatures provide further evidence for strain-induced crystallization occurring

in S20E. This behavior is similar to the observed response of cross-linked natural rubber.

2.5 Conclusions

Evidence for strain-induced crystallization in certain SEBS triblock copolymer TPE systems is presented and related to the interesting mechanical behavior, including reduction in flow as observed from stress relaxation tests, elastic hysteresis observed in cyclic tests. Similarities between mechanical and thermal behavior of cross-linked natural rubber and these SEBS systems have been highlighted. The low temperature melting behavior of such systems, having increased number of ethylene-like sequences, (ethylene to butylene ratio greater than one) has also been highlighted. Also, increased modulus and decreased extensibility have been accounted for on the basis of PS content, mid-block architecture and the ethylene to butylene ratio of the mid-block. Deformation Calorimetry establishes the differences in internal energy behavior of these three systems and provides evidence for strain-induced crystallization occurring in systems with increased number of ethylene-like sequences.

2.6 References

(1) Beecher, J. F.; Marker, L.; Bradford, R. D.; Aggarwal, S. L. *J. Polym. Sci., Part C* **1969**, *26*, 117-134.

(2) Inoue, T.; Masahiko, M.; Hashimoto, T.; Kawai, H. *Macromolecules* **1971**, *4*, 500-507.

(3) Pakula, T.; Saijo, K.; Kawai, H.; Hashimoto, T. *Macromolecules* **1985**, *18*, 1294-1302.

(4) Agarwal, S. L. *Polymer* **1976**, *17*, 938-956.

(5) Huy, T. A.; Adhikari, R.; Michler, G. H. *Polymer* **2003**, *44*, 1247-1257.

(6) Seguela, R.; J., P. h. *Macromolecules* **1988**, *21*, 635-643.

(7) Arridge, R. G. C.; Folkes, M. J. *J. Phys. D: Appl. Phys.* **1972**, *5*, 344-360.

(8) Folkes, M. J.; Keller, A.; Scalisi, F. P. *Kolloid Z.* **1973**, *251*, 1-4.

(9) Godovsky, Y. K. *Makromol. Chem. Suppl.* **1984**, *6*, 117-140.

(10) Tarasov, S. G.; Godovskii, Y. K. *Vysokomolekulyarnye Soedineniya Seriya A* **1980**, *22*, 1879-1885.

(11) Tarasov, S. G.; Tsvankin, D. Y.; Godovskii, Y. K. *Vysokomolekulyarnye Soedineniya Seriya A* **1978**, *20*, 1534-&.

(12) Honeker, C. C.; Thomas, E. L.; Albalak, R. J.; Hajduk, D. A.; Gruner, S. M.; Capel, M. C. *Macromolecules* **2000**, *33*, 9395-9406.

(13) Honeker, C. C.; Thomas, E. L. *Macromolecules* **2000**, *33*, 9407-9417.

(14) Falabella, R. *Ph.D. Thesis*, Polymer Science and Engineering; University of Massachusetts: Amherst, 1980; p 213.

(15) Farris, R. J. *Ph.D. Thesis*, Civil Engineering; University of Utah, 1970.

(16) Diamant, J.; Williams, M., C. *Polym. Eng. Sci.* **1989**, *29*, 235-243.

(17) Diamant, J.; Williams, M., C. *Polym. Eng. Sci.* **1989**, *29*, 227-234.

(18) Diamant, J.; Williams, M., C. *Polym. Eng. Sci.* **1989**, *28*, 207-220.

(19) Holden, G.; Legge, N. R.; Quirk, R.; Schroeder, H. E. *Thermoplastic Elastomers*, 2nd ed.; Hanser Publishers, 1996.

(20) Sierra, C. A.; Galan, C.; Fatou, J. G.; Parellada, M. D.; Barrio, J. A. *Polymer* **1997**, *38*, 4325-4335.

(21) Stadler, R.; Gronski, W. *Colloid & Polymer Science* **1986**, *264*, 323-331.

(22) Gent, A. N. *Trans. Faraday. Soc.* **1954**, *50*, 521-533.

(23) Gent, A. N. *Rubb. Chem. Tech.* **1955**, *28*, 36-50.

(24) Luch, D.; Yeh, G. S. Y. *J. Macromol. Sci. , Phys.* **1973**, *7*, 121-155.

(25) Roberts, D. E.; Mandelkern, L. *J. Am. Chem. Soc.* **1955**, *77*, 781-786.

(26) Toki, S.; Fujimaki, T.; Okuyama, M. *Polymer* **2000**, *41*, 5423-5429.

(27) Trabelsi, S.; Albouy, P.-A.; Rault, J. *Macromolecules* **2003**, *36*, 7624-7639.

(28) Mark, J. E. *Polym. Eng. Sci.* **1979**, *19*, 409-413.

(29) Bening, R. C.; Handlin JR., D. L.; Sterna, L. L.; Willis, C., L.; US Patent Application Publication: USA, 2003.

(30) Lyon, R. E.; Farris, R. J. *Polym. Eng. Sci.* **1984**, *24*, 908-914.

(31) Lyon, R. E. *Ph.D. Thesis*, Polymer Science and Engineering; University of Massachusetts: Amherst, 1985; p 214.

(32) Lyon, R. E.; Wang, D. X.; Farris, R. J.; MacKnight, W. J. *J. Appl. Polym. Sci.* **1984**, *29*, 2857-2872.

(33) Godovsky, Y. K.; Bessonova, N. P. *Colloid. Polym. Sci.* **1983**, *261*, 645-651.

(34) Godovsky, Y. K.; Bessonova, N. P. *Thermochimica Acta* **1994**, *247*, 19-33.

(35) Adams, G. W.; Farris, R. J. *J. Polym. Sci., Part B: Polym. Phys.* **1988**, *26*, 433-445.

(36) Agarwal, N. *Ph.D. Thesis*, Polymer Science and Engineering; University of Massachusetts: Amherst, 1998; p 249.

(37) Lyon, R. E.; Raboin, P. J. *J. Therm. Anal.* **1995**, *44*, 777-793.

(38) Lyon, R. E.; Farris, R. J. *Rev. Sci. Instrum.* **1986**, *57*, 1640-1646.

(39) Treolar, L. R. G. The Physics of Rubber Elasticity; Oxford University Press, 1975.

(40) Erman, B.; Mark, J. E. Structures and Properties of RubberLike Networks; Oxford University Press, 1997.

(41) Gent, A. N.; Zhang, L.-Q. J. Polym. Sci. : Part B: Polym. Phys. 2001, 39, 811-817.

(42) Douzinas, K., C.; Cohen, R. E. *Ph.D. Thesis*, Chemical Engineering; Massachusetts Institute of Technology: Cambridge, 1991; p 382.

(43) Adams, G. W. *Ph.D. Thesis*, Polymer Science and Engineering; University of Massachusetts: Amherst, 1987; p 255.

CHAPTER 3

COUPLED STRUCTURAL CHANGES DURING MECHANICAL DEFORMATION OF SEBS TRIBLOCK COPOLYMERS

A SEBS Kraton® Triblock copolymer, consisting of two glassy-like, atactic polystyrene (PS) end blocks coupled with a poly (ethylene/butylene) (PE/B) flexible mid-block, has been studied using simultaneous small- and wide-angle X-ray diffraction (SAXD/WAXD) during uniaxial tensile deformation. In-situ WAXD data along with deformation calorimetry results prove strain-induced crystallization of the flexible ethylene/butylene matrix in these SEBS materials. These results suggest a pseudo-hexagonal phase of branched polyethylene-like strain-induced crystals occurring at strains as low as 60% in these materials. SAXD data shows that as the strain increases, a four-point X-cross pattern develops and emerges from the circular 2-D hexagonal lattice diffraction ring of the unstrained sample. Occurrence of this four-point X-pattern has been related to the co-operative microbuckling of PS cylinders, which in turn is responsible for the apparent 'yield-like' response observed in a typical uniaxial tensile test. The estimated buckling wavelength provides information about the relative contributions of each of the phases to the observed mechanical properties. It has also been established that initial 2-D hexagonal lattice of cylinders transforms with strain into lamellar-like sheets of micro-buckled PS cylinders. In addition, evidence for discrete layer lines appearing orthogonal to the strain direction is provided. These changes in layer line spacing with increasing strain along with increasing X-cross angle provide additional insight into the mechanisms of deformation occurring in the

elastomer with shearing of buckled PS cylinder layers relative to each other. These simultaneous SAXD/WAXD results, along with supporting mechanical and deformation calorimetric evidence provide valuable information on both the overall nature of the deformation and the coupling of specific deformation-induced structural changes at different length scales.

3.1 Introduction

Styrenic triblock copolymers with cylindrical morphologies are one of the most widely used TPE systems commercially, and hence extensively studied [1-14] for their morphology and mechanical properties.

Keller and coworkers prepared highly oriented SBS TPEs and studied the deformation behavior at low to moderate strains (<120 % strain) using Small angle X-ray diffraction (SAXD), Transmission electron microscopy (TEM) and Birefringence [9-11,15,16]. These studies revealed several important structural features on deformation at moderate deformations. However deformation behavior at large strains was not investigated. The structural changes in morphology at large strains and the energy absorption characteristics upon deformation of oriented 'single crystals' and macroscopically isotropic SBS block copolymers have been studied by Godovsky and coworkers [7,8,12] using SAXD and deformation calorimetry respectively. They observed that for highly oriented 'single-crystal' specimens, the deformation orthogonal to the axes of the cylinders is accompanied by a transformation into a 'zig-zag' structure in real space (four-point X-cross in SAXD patterns), while longitudinal deformation results in the breakdown of the cylindrical entities into smaller (e.g. spherical like)

particles. These studies also suggest that the macroscopically isotropic SBS samples on deformation show structural characteristics similar to those obtained from deformation of highly oriented 'single-crystal' specimens.

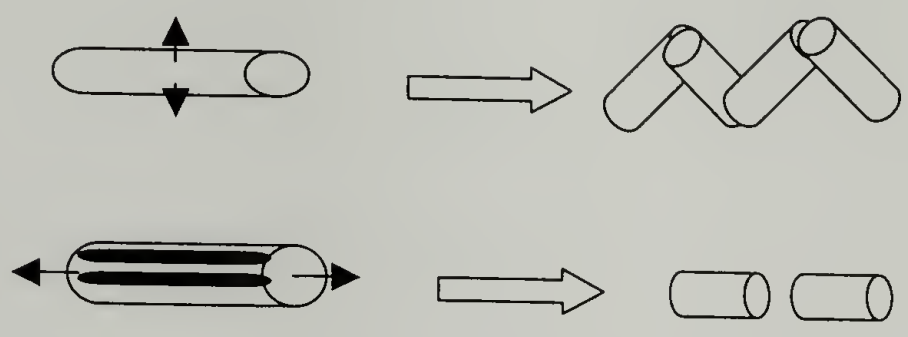

Figure 3.1 Proposed mechanisms of deformation of SBS systems by Godovsky et al.[12,17].

However no implication of what these observed structural changes in morphology means to the micromechanics of these block copolymer systems have been proposed. The deformation behavior of SBS triblock copolymers with cylindrical morphologies has also been studied by Hashimoto, Pakula and co-workers[3] using SAXD technique on both unoriented as well as oriented samples. They observed that in oriented samples, irrespective of the deformation direction (0°, 45° and 90°), they observed a universal high deformation state (four-point patterns) at large strains and postulated that this was controlled by the molecular orientation. However, these studies again only provide a 2-D model and do not elucidate the 3-D deformation of these PS cylinders in real space.

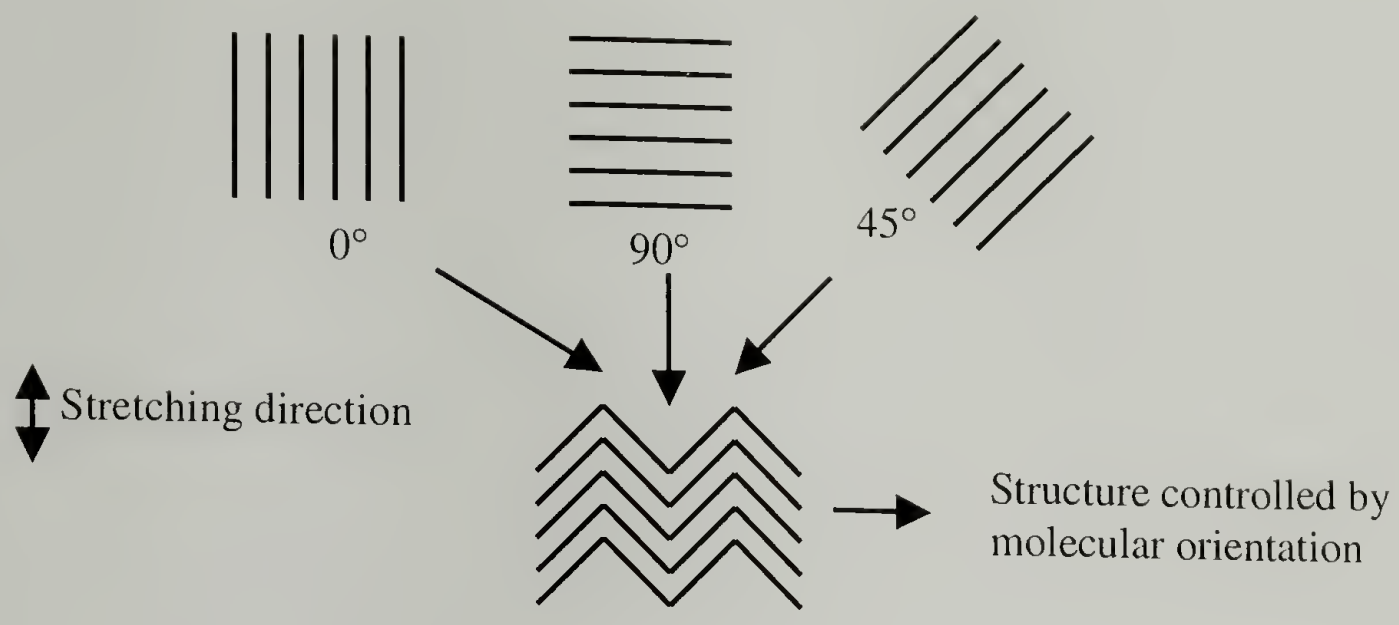

Figure 3.2 Universal high deformation state of cylinders by Hashimoto et al.[3]

The 'zig-zag' structure or chevron instability in SBS block copolymer TPEs and other multi-layered structures has been modeled theoretically by Read et. al. [14] using analytical as well as finite element techniques. It was shown from these studies that the orthogonal deformation of multi-layered structures causes an initial sinusoidal buckling, that at higher strains develops into a chevron texture. In addition, the buckling instability was predicted to correspond to the sharp turn over observed in the stress-strain curves for SBS block copolymers. Thomas and coworkers [18,19] studied in detail the deformation of cylindrical PS domains of a near 'single crystal' styrene-isoprene-styrene (SIS) triblock copolymer processed by roll-casting using synchrotron SAXD and transmission electron microscopy (TEM) techniques in uniaxial tensile tests. They observed that the deformation proceeded in two stages, (1) a small strain regime extending to 100-130% strain, where the deformation is nearly affine and (2) a large strain regime where the angle between the arms of four-point X-cross pattern (formed in

transition regime and seen from the bend in the stress-strain curve at 100-130% strain) increases asymptotically without any change in the inter-cylinder spacing. The morphological observations are interpreted in terms of a kinking instability in which the plain strain rate imposed by the oriented cylinders is relieved by their kinking into a chevron pattern, similar to that predicted by modeling by Read et. al. [14]. However these studies only looked at the deformation behavior of the PS cylinders and do not probe the changes happening at the other length scale of the matrix.

Most of the styrenic block copolymer TPEs studied for the impact of deformation on morphology so far have been styrene-butadiene-styrene (SBS), styrene-isoprene-styrene (SIS) systems, both of which have non hydrogenated elastomeric mid-blocks. Seguela and Prud'homme[13] studied the deformation behavior of SEBS systems with cylindrical morphologies and observed that for extension ratios up to 2.3, a strain ellipsoid model could be used to relate the Bragg spacing strains of elliptical lattice reflections to macroscopic strains applied. One recent study[20] by Fairclough et al, involving the application of oscillatory strain to SEBS materials revealed that deformation was non-affine even at low strains. However these studies neither give a full account of the deformation of the PS cylinders nor looks at the deformation of the E/B mid-block. SEBS systems are obtained by hydrogenation of butadiene segment of the SBS block copolymers and have ethylene-butylene mid-blocks which resemble branched polyethylene chains (with ethyl branches)[21]. Increasing or decreasing the number of branches can make E/B of SEBS system a little more crystalline or completely amorphous[21,22]. These SEBS systems thus have interesting morphologies at different length scales i.e. one at the nanometer length scale of cylinders/spheres and

other at the molecular length scales of crystallites. There are no detailed studies investigating the structural changes in morphology of SEBS systems on deformation at these two length scales. Also no detailed mechanical and mechano-calorimetric investigations have been undertaken thus far in these technologically important materials.

This chapter investigates the structural changes occurring in the morphology with deformation of a SEBS triblock copolymer using simultaneous SAXD and WAXD. These structural changes in morphology are also related to the changes observed in the uniaxial tensile and deformation calorimetric behavior of this system that were discussed in chapter 2.

3.2 Experimental

3.2.1 Materials and sample preparation

The system investigated here is the SEBS triblock copolymer S20E that was discussed in chapter 2. The structure of which is shown again here in figure 3.3.

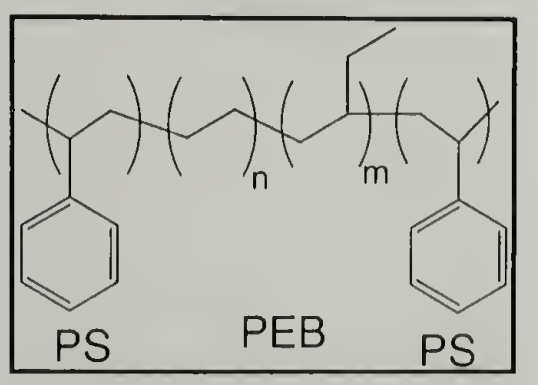

Figure 3.3 Structure of system S20E

As described in chapter 2, S20E has 20% a-PS as the end block and in the mid-block has more number of ethylene than butylene segments. It has a total molecular weight of 122 K gm/mole as determined by GPC with a PDI of 1.09. Thus the block molecular weights are (12.2-97.6-12.2) K gm/mole. The ethylene-butylene mid-block has about 37% butylene segments. Samples are prepared using solution casting as described in chapter 2.

3.2.2 Simultaneous SAXD/WAXD

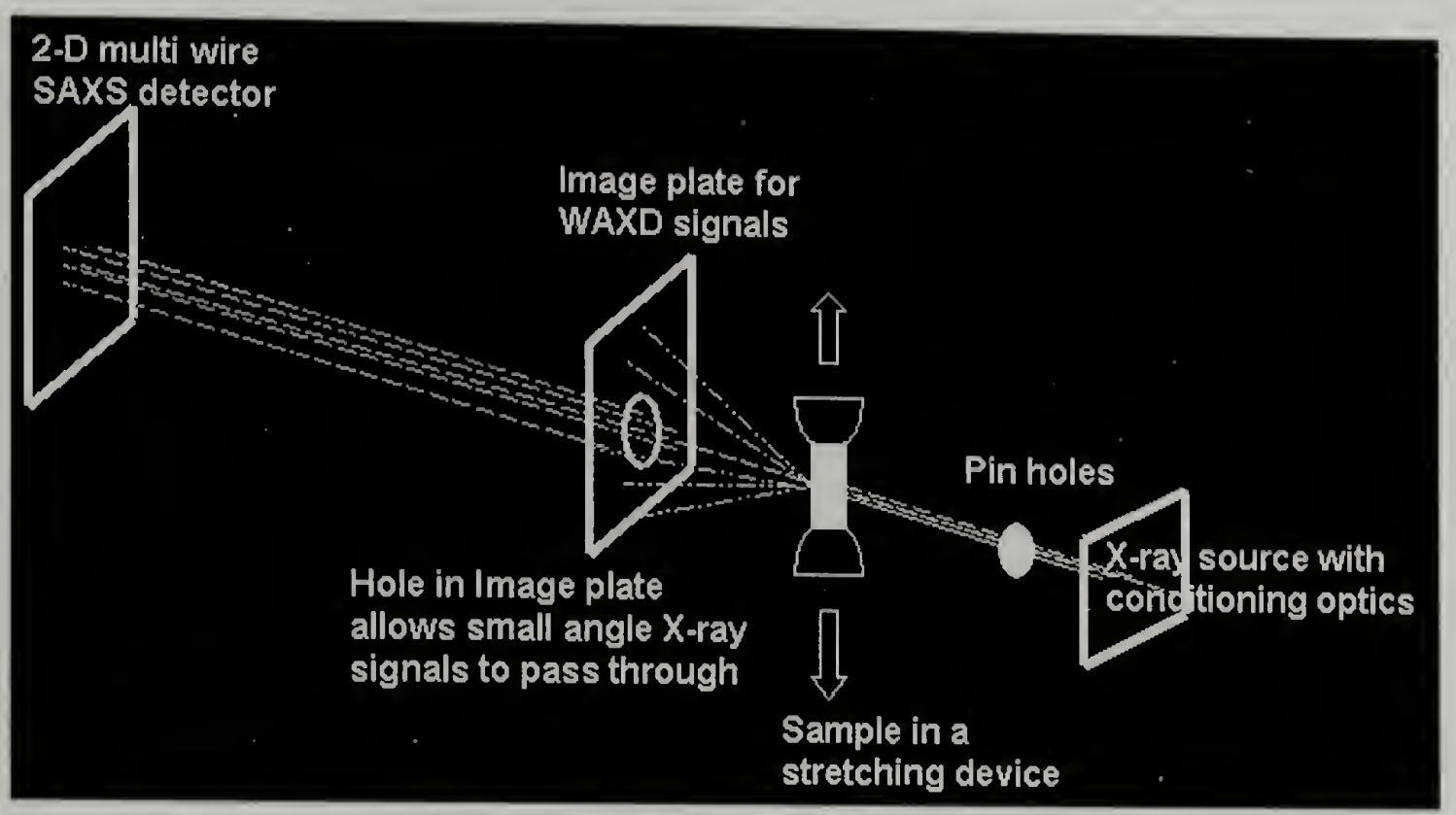

Figure 3.4 Combined SAXD/WAXD setup

SAXD and WAXD data was collected as a function of mechanical strain in a Molecular Metrology® SAXS machine using a setup described in figure 3.4. An image plate with a hole introduced in the middle captures the WAXD patterns. The sample to detector distances for SAXD and WAXD were approximately 1500 mm and 155 mm respectively. The SAXD images were calibrated using a turkey tendon collagen

standard. WAXD images were collected on a Fuji ST-VA image plate (IP) with a central aperture allowing the SAXD pattern to be recorded on a 2-D wire detector. Tricosan and calcium carbonate crystals were used to calibrate the WAXD patterns.

3.3 Results and Discussion

3.3.1 Small-angle (130 nm – 6 nm) and Wide angle (region 10nm-0.1 nm)

Figure 3.5 shows a SAXD pattern on the left (a) and its schematic in the middle (b) as obtained from a SEBS triblock copolymer S20E under no strain. At zero strain the SAXD pattern in Fig. 3.5 (a & b), shows a series of four diffraction rings, decreasing rapidly in relative intensity with increasing reciprocal radius, at spacings: 26.00 nm, 15.01 nm; 13.00 nm and 9.83 nm, respectively. These values are in the ratio 1: √3: 2: √7 and represent the first four consecutive orders: d_{10}, d_{11}, d_{20} and d_{21}, respectively, from a two-dimensional hexagonal superlattice of side, a = 30.02 nm.

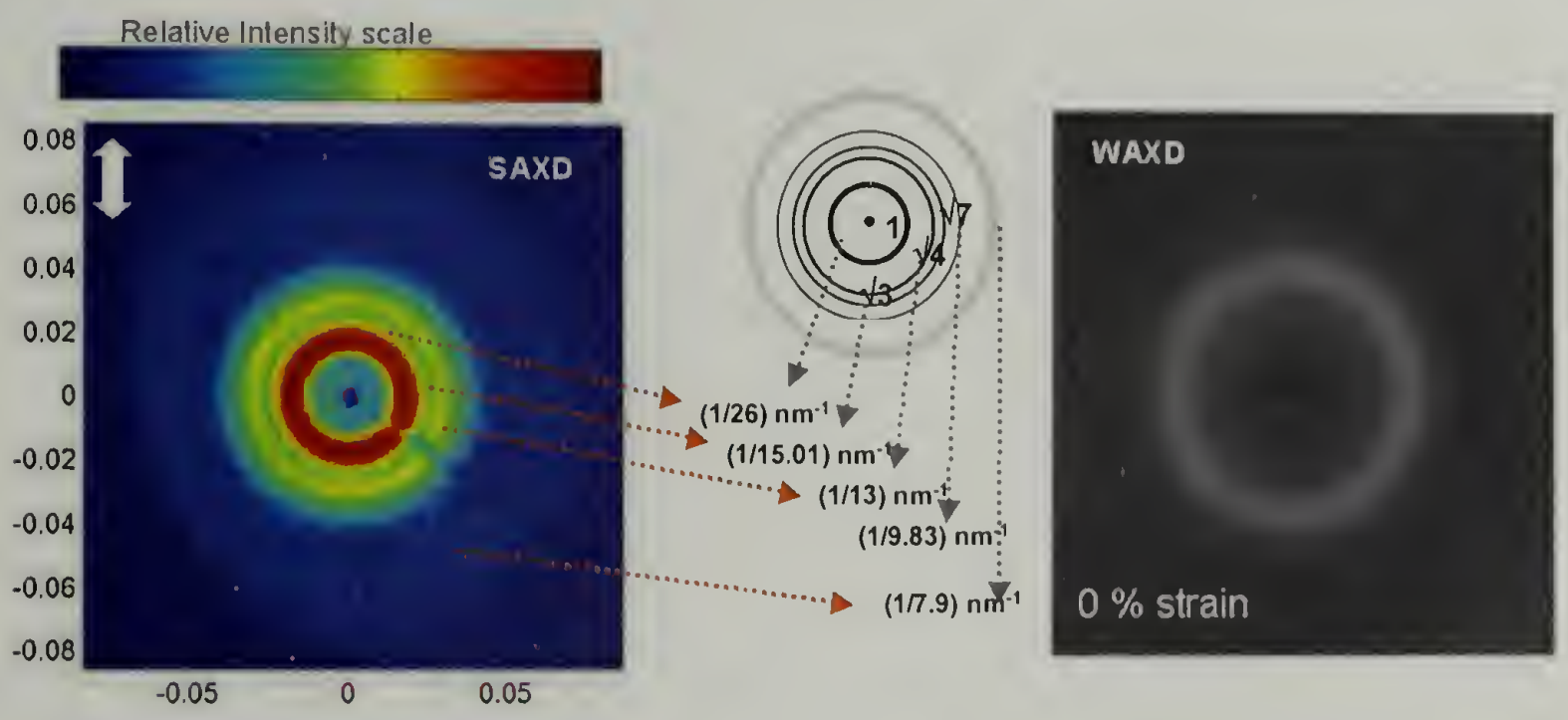

a) b) c)

Figure 3.5 (a) SAXD pattern at 0 % strain (b) schematic of SAXD pattern with d-spacings in reciprocal space (c) WAXD pattern

This diffraction data supports a model of parallel cylinders, each composed of a-PS units, packing in a planar hexagonal lattice arranged orthogonal to the cylinder axes in a localized region and distributed randomly with overall spherical symmetry within the macroscopic sample. In addition, a noticeably broader diffraction ring centered at a spacing of 7.90 nm is observed. The intensity profile character and its ***d***-spacing does not match any of the predicted successive reciprocal hexagonal superlattice sampling points, which would occur at ***d***-spacings: 8.67 nm (d_{30}), 7.51 nm (d_{22}) and 7.21 nm (d_{31}), respectively. Indeed, it can be deduced that the correlation length (size) of the localized hexagonal superlattice is such that reciprocal lattice point sampling is wholly suppressed after the 4th order; i.e. ***d***-spacings smaller than 9.83 nm. This 7.90 nm broad diffraction signal will be discussed later as strain is applied to the system, when the behavior of this 7.9 nm signal is monitored as the sample is successively strained.

Figure 3.6 (left) TEM image of S20E (right) schematic representation of different grains

A TEM image of this SEBS system under no strain confirms the observations made from SAXD pattern at 0% strain. Figure 3.6 (left) shows the TEM image and 3.6 (right) shows its schematic outline. Hexagonally packed polystyrene cylinders embedded in the elastomeric matrix can be clearly observed. This image also indicates that there is no preferred global long-range order present in this solution cast system. Grains of cylinders with different orientations can be clearly noticed.

Simultaneous WAXD patterns were obtained from the sample during the stretching experiments. Figure 3.5 c shows the diffraction pattern obtained at 0% strain. Since the atactic polystyrene component is anticipated to remain amorphous throughout, the salient features in the wide-angle X-ray diffraction patterns are expected to emanate from the partially decorated (with CH_2CH_3 side groups from the butylene units) flexible PE chains that are covalently connected to the aPS domains. Figure 3.5 c reveals a sharp amorphous halo, a single diffraction ring with full width at half maximum (FWHM) of 7.5 and centered at a ***d***-spacing of 0.46 nm. This suggests that the mid-block has the ability to crystallize, but at room temperatures (in an unstretched state) there is no crystallinity. This has been confirmed using differential scanning calorimetry (DSC) experiments[23] (as shown in chapter 2). Those studies prove that this system S20E shows only low-temperature crystallinity and at room temperatures all the crystals have melted.

At 15% strain, it can be seen from SAXD diffraction pattern in figure 3.7 (a & b) that noticeable anisotropy occurs, with the prominent $\boldsymbol{d}_{10}$ diffraction ring (formally the $\{10\bar{1}0\}$ family of diffracting planes) appearing to change into a pair of arcs centered on the equator.

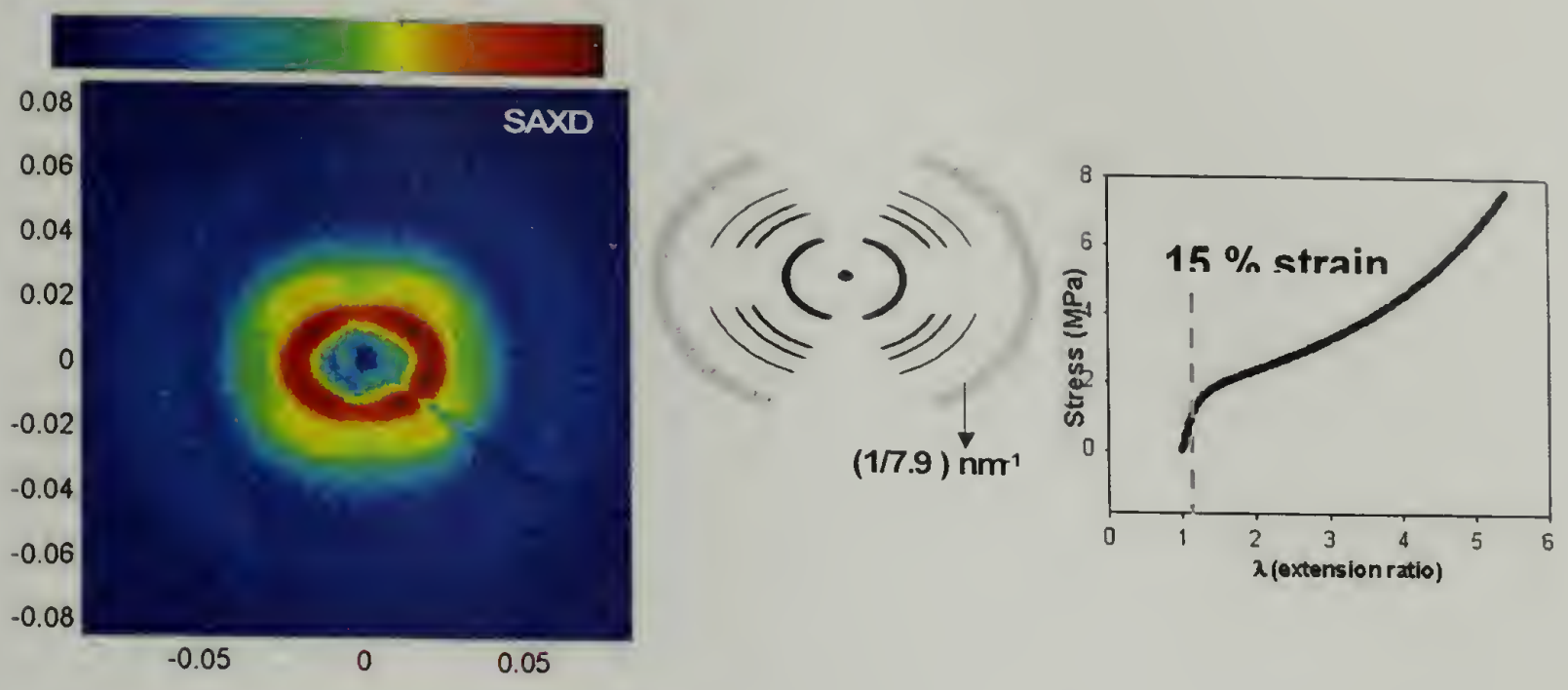

a) b) c)

Figure 3.7 (a) SAXD pattern at 15 % strain (b) schematic of SAXD pattern with d-spacings in reciprocal space (c) corresponding stress-extension ratio curve

In addition figure 3.7 (a) reveals evidence for new diffraction features that start to emerge at 15 % strain. Some of these features have been sketched in the schematic 3.7 (b) for clarity. It can be expected that if this is indeed a true response then those features should emerge stronger as the strain is increased. The corresponding stress-extension ratio curve has been plotted on the right (figure 3.7 c) for reference. It can also be observed that 15 % strain falls in the initial elastic region of the stress-extension ratio plot. At 30% strain (figure 3.8) little change in the SAXD diffraction pattern (from 15% strain) can be noticed.

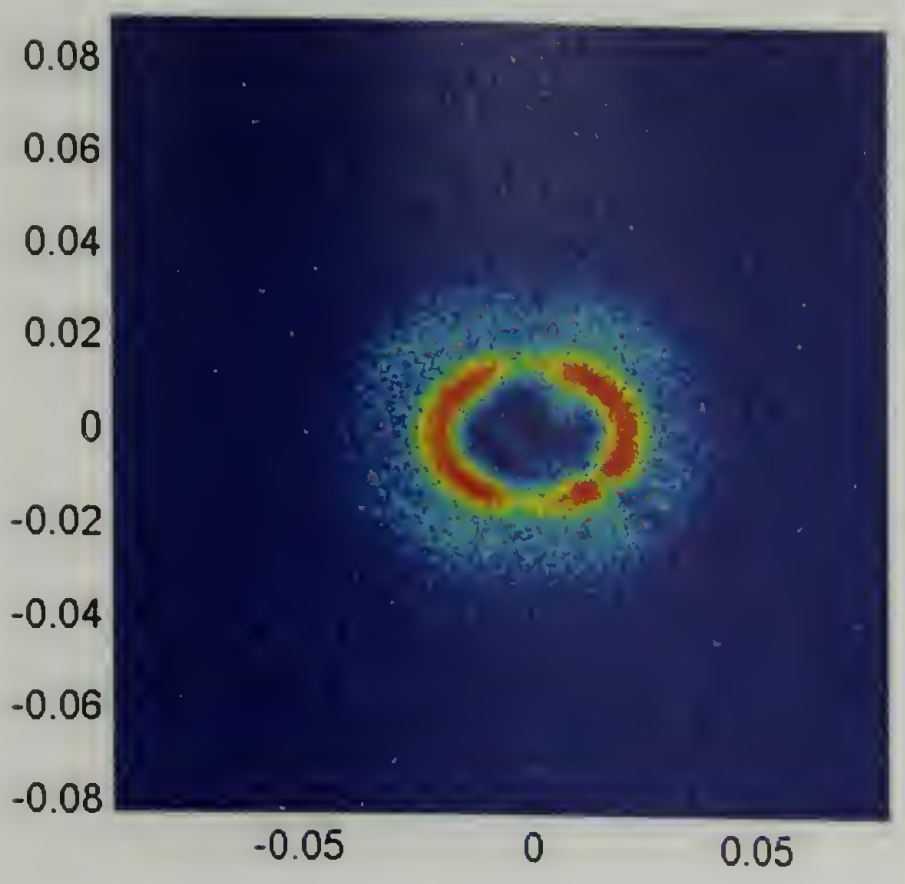

Figure 3.8 SAXD pattern of S20E at 30% strain.

At 63% strain as shown in figure 3.9 (a & b) new diffraction features are noticeably evident in the SAXD. It can be observed that the equatorial d_{10} arcs present at low strains disappear and instead a cross-X four-point pattern, with each diffraction spot in the shape of a comma and with the tails running to the equatorial line can be distinctly noticed. The angle of the cross-X relative to the vertical bisector is ≈ 50°. Therefore, in the previous figure 3.8 at 15% strain (and also at 30% strain) one has the false impression of a pair of equatorially centered arcs. These are in reality nascent four point X-cross patterns that are starting to emerge with strain. These four-point X-cross patterns observed in SAXD reciprocal space corresponds to a chevron pattern or a herringbone type pattern of bent cylinders in real space. This is because of a micro-buckling instability which causes produces bent PS cylinders in a PEB matrix and confirms other theoretical[14] and experimental findings[18]. Also the d-spacing of this X-

cross signal increases by about 6.5 % to 31.97 nm from the original d-spacing of the hexagonal lattice of cylinders. It can also be seen that this X-pattern observed near 63% strain corresponds with the region near the 'apparent' yield like pattern in the stress-strain curve (figure 3.9 c). This observation for the present isotropic/unoriented SEBS system is similar to intermediate strain regime proposed by Thomas and coworkers[18] for the onset of four-point X-pattern in oriented SIS systems. Such a broad strain regime corresponding to a broad 'apparent' yield point is expected because of differences in cylinder orientation with respect to the stretching direction in an isotropic/unoriented sample. This apparent yield pattern corresponding to the co-operative microbuckling instability marks the transformation from initially rigid-like to an elastomer-like material. In fact, the sharpness and location of this 'apparent' yield point provides indirect evidence for the amount of long-range order/orientation present in the sample. For samples macroscopically aligned in one direction using different processing techniques, we could establish that the apparent yield point becomes sharper and goes to lower strain-levels as the stretching direction becomes parallel to the direction of PS cylinder orientation. This effect of processing conditions[24] on the apparent-yield point will be one of the subjects in chapter 4.

In addition, comparing unsaturated SBS, SIS systems with the present hydrogenated SEBS systems, it can be seen that the apparent yield point in SEBS systems occurs at much lower levels of strain than in the SBS systems. The present system shows a broad apparent yield point from 30-60% strain. However, this occurs only at values above 100% strain in SBS/SIS materials.

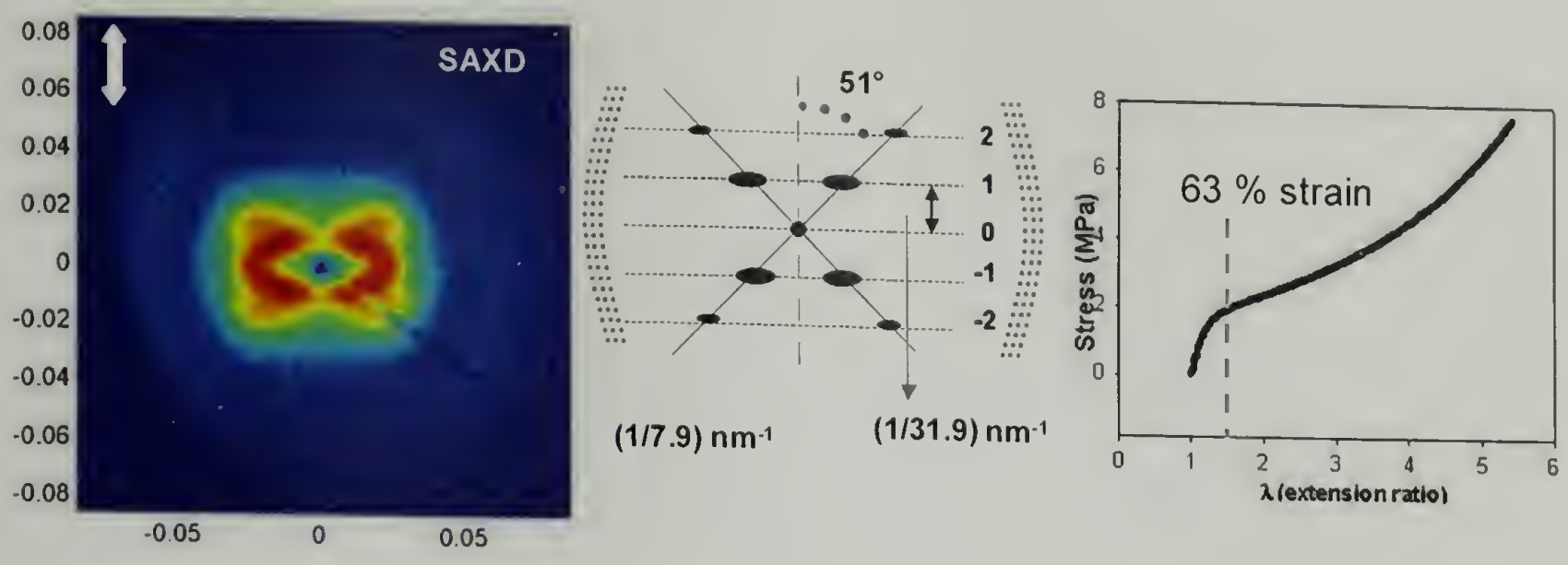

a) b) c)

Figure 3.9 (a) SAXD pattern at 63% strain-four point X-pattern (b) schematic of the SAXD pattern depicting the layer line spacings (c) stress-strain curve showing the apparent yield region-where buckling instability is predicted

This micro-buckling phenomenon has been studied extensively in systems like fiber-reinforced composites etc. [25-27] where there is a high modulus material embedded in a soft material. It was also observed that microbuckling occurs as a sinusoidal deformation in such fibers. The critical wavelength of such a sinusoidal pattern has been predicted & simplified by the analyses of Darby, Kanellopoulos[28] and Sadowsky et al.[29] Baer and coworkers studied microbuckling in model fiber reinforced composite systems with single fiber/matrix and multiple fiber/matrix samples[26,27]. They studied interactive effects of multiple fibers embedded in a matrix to simulate a fiber reinforced composite and predicted co-operative microbuckling modes in these systems under certain conditions. Since the SEBS system behaves similarly to a fiber-reinforced composite, where high modulus polystyrene cylinders are present in a soft rubbery matrix, some of

the analyses described above describe the features of microbuckling observed in SAXD patterns. Since the PS cylinders are chemically linked to each other through the rubbery (E/B) matrix, a co-operative microbuckling mode can be expected as opposed to an extensional mode of buckling. Using the simplified analysis of Darby and Kanellopoulos[28], the buckling wavelength λ_B is related to moduli of the two phases and to the diameter of the buckling phase with this simple relationship:

$$\lambda = \pi d \left[\frac{3E_s^{\,2}}{8E_m^2} \right]^{1/8} \tag{3.1}$$

Here d is the diameter of PS cylinders, E_s is the modulus of PS cylinders and E_m the modulus of the PEB matrix. It can be seen from this relationship that the buckling wavelength strongly depends on the diameter of the PS cylinders and only weakly depends on the ratio of moduli of the two phases. Using the approximate value of moduli of the two phases ($E_{Styrene}$ = 2 GPa and E_{matrix} = 5 MPa) and the diameter of PS cylinders (16 nm) observed experimentally from TEM image in figure 3.6, the predicted buckling wavelength has been calculated to be approximately 200 nm from the above equation (3.1). This value also compares well with the buckling wavelength observed in TEM images of stretched SBS (unhydrogenated) block copolymers by Thomas et al. [19] using electron beam irradiation to preserve morphology in the strained state.

Going back to figure 3.9 (a & b), in addition to a first-order X-cross four point pattern, a second order (weaker) diffraction signal is observed along each arm of the

cross. The ratio of d-spacings of the first order to second order four-point X-cross patterns is now 1: 2 rather than the previous 1: $\sqrt{3}$ relationship (that existed for an unstrained 2-D hexagonal lattice of cylinders). This has been judged to be a clear signal that the structure is behaving in a stacked lamellar-like mode where in planes of micro-buckled PS cylinders deform in layer-like sheets together. The thickness of these lamellar-like sheets is on the same scale as the original inter-cylinder distance of 30.02 nm. This feature is reinforced and embroidered upon by the fact that the prominent intercylinder or interlamellar diffraction signals are transforming into streaks along the layer lines (reciprocal planes orthogonal to the (vertical) stretch direction) with a calculated layer line spacing of 38.10 nm. This aspect will be treated later, suffice to stay at this stage the feature is reminiscent of shear parallel to the stretch direction[30].

Also at 63% strain from figures (3.9 a & b), there is the first hint that the broad 7.90 nm diffraction signal is behaving differently from the superlattice diffraction signals, since it seems to be genuinely centering on the equator.

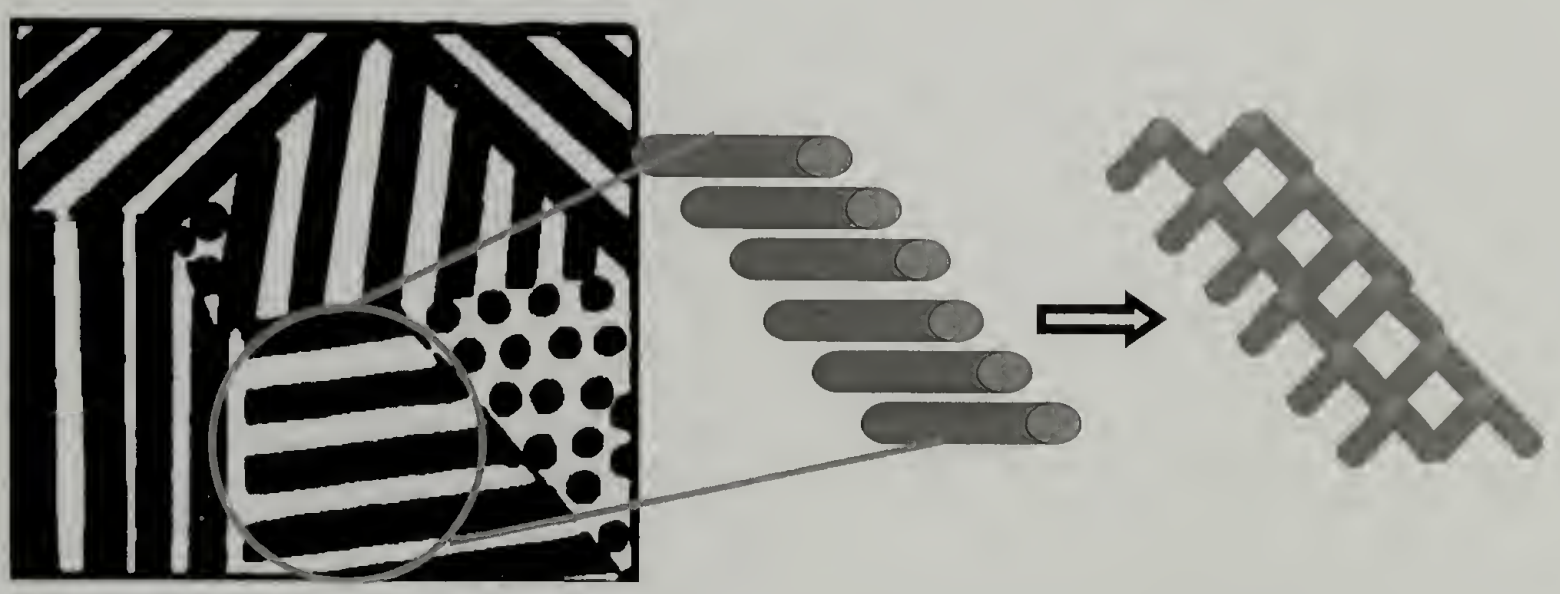

Figure 3.10 Schematic of deformation of cylinders from a grain with one orientation (in an overall 2-D hexagonal lattice) deforming into lamellar like sheets of microbuckled cylinders

At a strain of 130% from figures 3.11 (a & b), further developments are noticeable in SAXD. The angle of the cross-X has changed to 65° but with no change in the inter-lamellar spacing of 31.97 nm; consequently the calculated layerline spacing has increased to 68.56 nm. The increase in the angle of X-pattern suggests the rotation of cylinders into the stretching direction and hence consequent shear of the PE/PB matrix. It can now be seen that the broad 7.90 nm diffraction signal is truly centered on the equator and its apparent arc length is reducing.

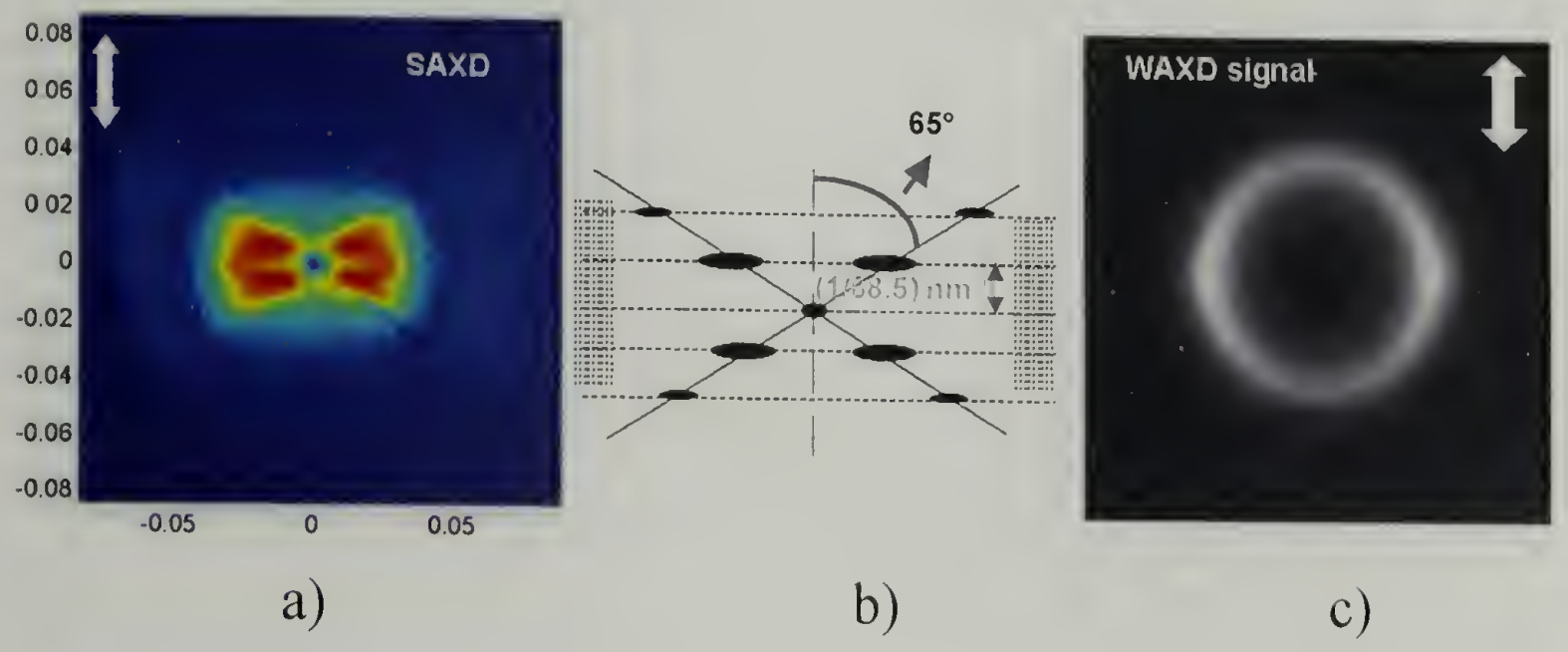

Figure 3.11 (a) SAXD pattern at 130 % strain (b) schematic of SAXD pattern with d-spacings in reciprocal space (c) corresponding WAXD signal.

The shear deformation imposed elongates the chains in the PE/PB matrix leading to orientation of the PE/PB chains. Observing the WAXD pattern at 130 % strain (looking at PE/PB chains), it can be seen that with this shear deformation, some degree of orientation begins to emerge as seen (Figure 3.11c) by the enhancement in the relative intensity on the equator (orthogonal to stretch direction) at 130% strain.

At the higher strain of 200% from figure 3.12a, the changes in the small X-ray diffraction pattern develop along the similar lines as at 130 % strain: the inter-lamellar spacing remains the same at 31.97 nm and the cross-X angle increases to 71°; thus, the calculated layer line spacing increases to 92.85 nm. This further increase in the angle of X-pattern at 200 % strain suggests increased rotation of cylinders into the stretching direction and hence significant shear deformation imposed on the PE/PB matrix.

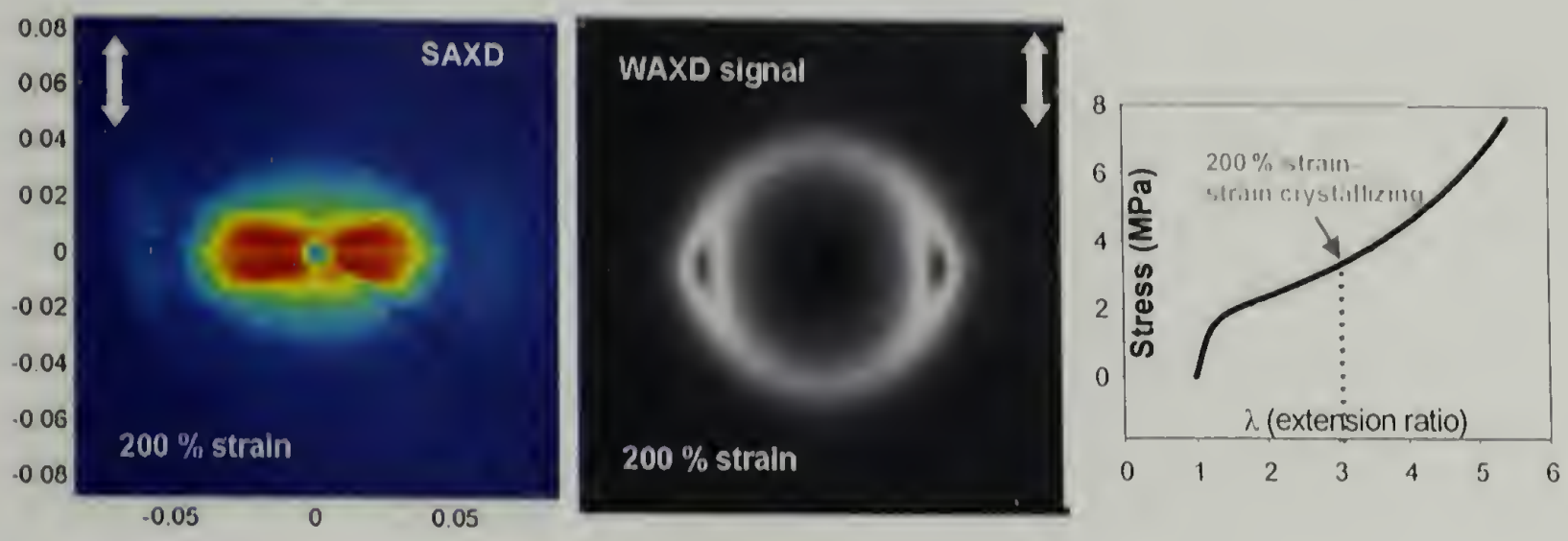

a) b) c)

Figure 3.12 (a) SAXD pattern at 200% pattern (b) WAXD pattern with a crystalline peak on top of the amorphous halo (c) corresponding stress-extension curve

In addition, at this strain, a new feature emerges: the broad 7.90 nm diffraction signal is converting into a vertical streak as opposed to an arc. The possible origin of the 7.90 nm diffraction signal will be discussed later. Observing the effects of further shear deformation of the PE/PB matrix by examining WAXD patterns at 200 % and 275 % strain (figures 3.12b & 3.13b), it can be seen that the pair of equatorially positioned diffraction signals grow in relative intensity at the expense of the original diffraction

ring with successive increase in strain to 200% and 275%. This feature remains to the final strain of 350% (maximum strain imposed in the experiment), however owing to sample thinning the exposure times became inconveniently long. These results show that the backbone PE chains are orienting and crystallizing with increasing strain in excess of ≈ 130% strain. Further, the PE/PB chains are adopting a structure similar to the hexagonal structural phase of PE. This spacing is 7% larger than the reported[31] d_{10} value (0.43 nm) for the characteristic inter-chain distance in the hexagonal structure of crystalline PE. It would therefore appear that the ethyl branches in PE/PB chains have resulted in a 7% increase in the inter-chain spacing.

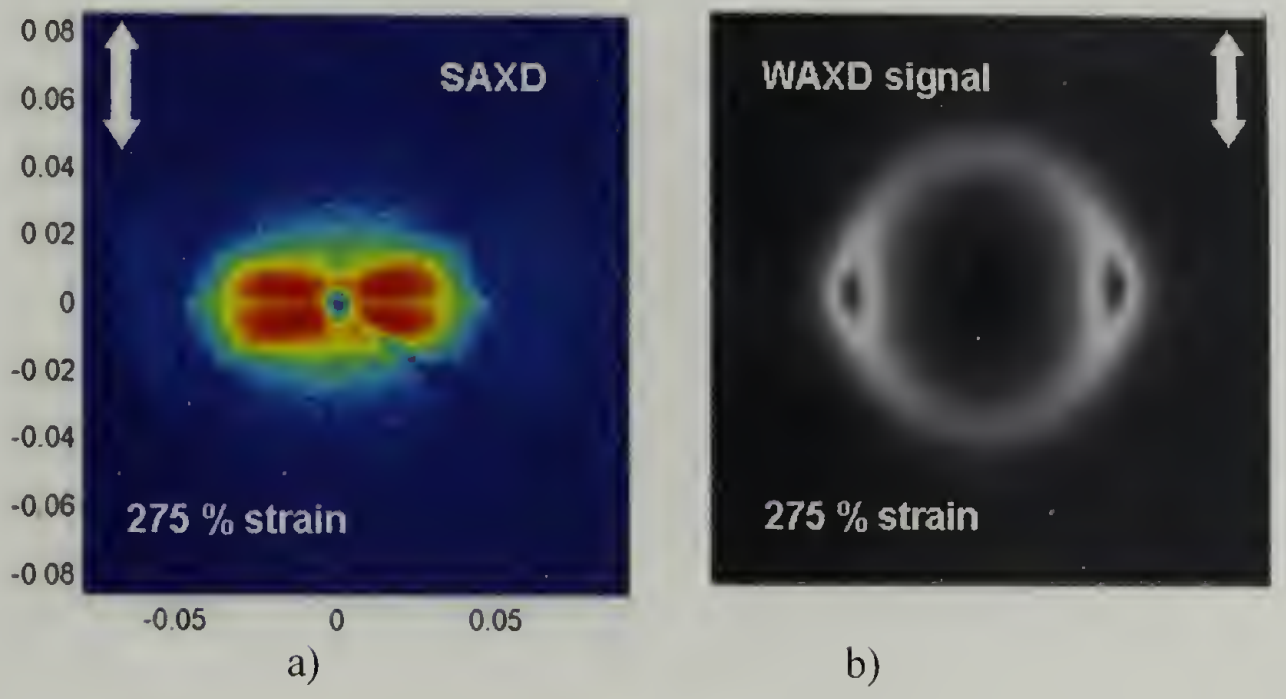

Figure 3.13 (a & b) SAXD and WAXD patterns of S20E at 275% strain

It can be seen from the WAXD diffraction patterns at 200 % and 275 % strains that there are no second order signals from the crystalline lattice. However internal energy changes measured from deformation calorimetry, as discussed in chapter 2, also

prove strain-induced crystallization occurring in these systems. Internal energy measurements (ΔU) as plotted in figure 2.30 (chapter 2) show that as work done (ΔW) on the system increases, ΔU starts to increase. However, at very low strains (60% strain) corresponding to the apparent yield pattern in the stress-strain curve (shown in the background for reference), the internal energy starts to drop and decreases steadily with further stretching. For about 400% strain, $\Delta U \cong -12$ J/g is observed. This feature is reminiscent of the behavior of strain crystallizing natural rubber[32] and confirms strain induced crystallization in the system S20E. An internal energy change of -12 J/g for an extension ratio of 5, obtained by strain-induced crystallization corresponds to 5 % crystallinity (after correcting for end block PS content). This data thus fully supports the above reported WAXD data. The influence of such strain induced crystallization in system S20E on the mechanical properties have been fully elaborated in a publication[23] and discussed in chapter 2.

These internal energy measurements also provide information about the onset of strain-induced crystallization in these systems. Even though WAXD patterns only show amorphous halo intensification at low strains, internal energy measurements confirm that strain-induced crystals start to form at these low strains (60% strain) in these SEBS materials.

Stretching to 275% (figure 3.13) and beyond exhibit little change in the small angle x-ray diffraction data, and since the sample is thinning significantly, the exposure times are inconveniently long; thus the patterns obtained at 350% strain appears rather weak.

the incident beam directed at different azimuthal angles to the specimen but still orthogonal to the stretch direction. Figures 3.14a-3.14c show how the diffraction pattern changes as the incident beam is directed normal to the wide face of the ribbon-like sample. The cross-X 4-point pattern is seen similar to the series of X-ray patterns shown in figure 3.14a. However, on changing the azimuthal angle by 90° one arm of the cross-X disappears as seen in Figure 3.14c. At an intermediate azimuthal angle (Figure 3.14b) this change is captured partway through the transformation, i.e. one arm of the cross-X is weakened. These results show that the transformations during the stretching of the samples have planar rather than cylindrical symmetry.

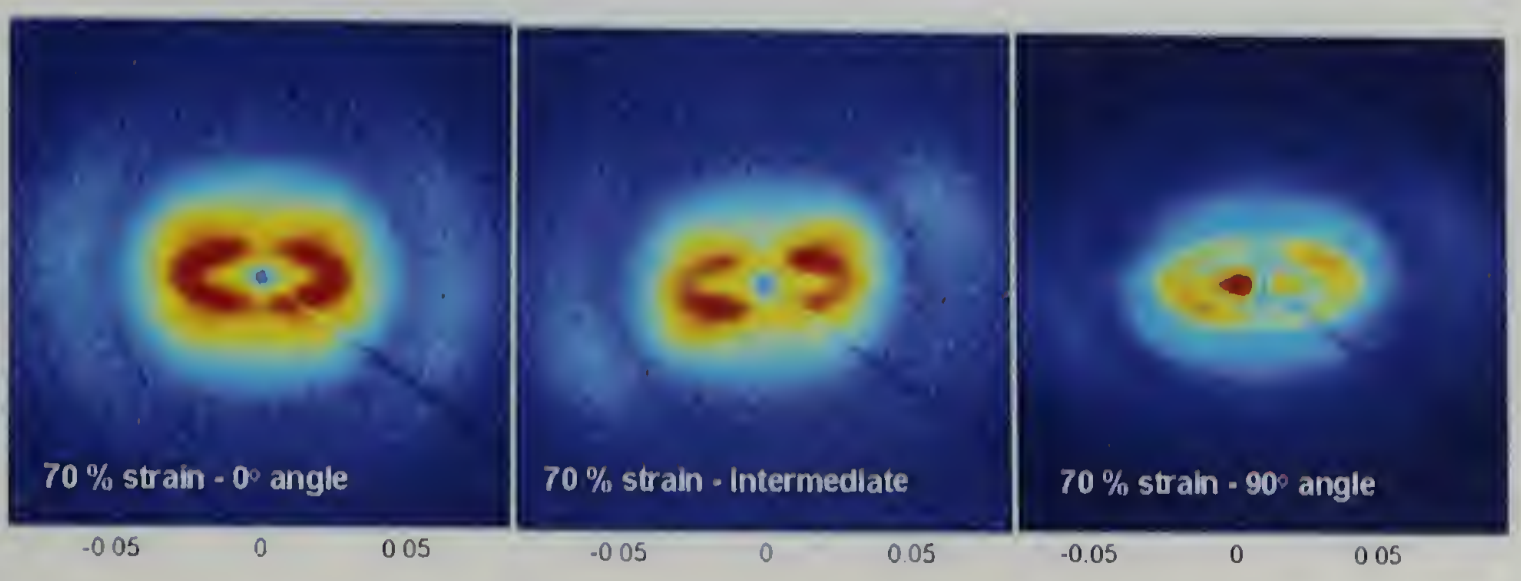

a) b) c)

Figure 3.14 SAXD images at different azimuthal angles to confirm planar symmetry

3.3.2 7.90 nm diffraction signal

The possible origin of the broad 7.90 nm diffraction signal that transformed from a circle at 0% strain into a streak, parallel to the stretch direction, at strains in excess of 130% will be discussed now. This single diffraction signal cannot be part of the original hexagonal superlattice emanating from the packing a-PS cylinders; the

excess of 130% will be discussed now. This single diffraction signal cannot be part of the original hexagonal superlattice emanating from the packing a-PS cylinders; the diffraction data proves that reciprocal lattice sampling has stopped well before (1/0.79) nm^{-1}. This is further supported by the fact that as the hexagonal organization transformed at higher strains ($\geq$ 63%) into a lamellar or sheet-like organization the 0.79 nm diffraction signal remained intact. The typical interchain and intrachain PE /PB spacings are less than 5 nm. Thus, a complete explanation for the 0.79 nm diffraction signal cannot be offered from the SAXD experiments that have been undertaken.

3.4 Conclusions

SAXD at no strain reveals not only a hexagonal packing of PS cylinders embedded in a PE/PB matrix, but also the presence of a broad diffraction ring at 0.79 nm of a completely different character. SAXD patterns at 60 % strain reveal the emergence of a four-point cross X pattern which has been related to a chevron pattern of micro-buckled PS cylinders that in turn leads to an apparent yield like pattern in these block copolymers. The wavelength of this cooperative micro-buckling instability has been estimated and provides invaluable information regarding the relative mechanical properties of the hard versus soft phases and would serve as an invaluable design tool for tailoring the properties of block copolymer TPEs. Also it has been established that the initial 2-D hexagonal lattice of cylinders transform with strain into lamellar-like sheets of bent cylinders. The angles of X-pattern, layer-line spacings increase with further strain suggesting the increased rotation of cylinders into the stretching direction and hence consequent shearing of the PE/PB matrix. This shear deformation elongates

the chains in the PE/PB matrix leading to strain-induced crystallization observed from WAXD patterns at higher strains. Internal energy measurements from deformation calorimetry support the WAXD evidence for strain-induced crystallization. This strain-induced crystallization helps reduce flow in TPEs under strain and could be introduced into block copolymer TPEs effectively while designing new block copolymer formulations.

3.5 References

(1) Beecher, J. F.; Marker, L.; Bradford, R. D.; Aggarwal, S. L. *J. Polym. Sci., Part C* **1969**, *26*, 117-134.

(2) Inoue, T.; Masahiko, M.; Hashimoto, T.; Kawai, H. *Macromolecules* **1971**, *4*, 500-507.

(3) Pakula, T.; Saijo, K.; Kawai, H.; Hashimoto, T. *Macromolecules* **1985**, *18*, 1294-1302.

(4) Agarwal, S. L. *Polymer* **1976**, *17*, 938-956.

(5) Huy, T. A.; Adhikari, R.; Michler, G. H. *Polymer* **2003**, *44*, 1247-1257.

(6) Seguela, R.; J., P. h. *Macromolecules* **1988**, *21*, 635-643.

(7) Tarasov, S. G.; Godovskii, Y. K. *Vysokomolekulyarnye Soedineniya Seriya A* **1980**, *22*, 1879-1885.

(8) Tarasov, S. G.; Tsvankin, D. Y.; Godovskii, Y. K. *Vysokomolekulyarnye Soedineniya Seriya A* **1978**, *20*, 1534-&.

(9) Arridge, R. G. C.; Folkes, M. J. *J. Phys. D: Appl. Phys.* **1972**, *5*, 344-360.

(10) Folkes, M. J.; Keller, A.; Scalisi, F. P. *Kolloid Z.* **1973**, *251*, 1-4.

(11) Folkes, M. J.; Keller, A. *Polymer* **1971**, *12*, 222-236.

(12) Godovsky, Y. K. *Makromol. Chem. Suppl.* **1984**, *6*, 117-140.

(13) Seguela, R.; Prudhomme, J. *Macromolecules* **1988**, *21*, 635-643.

(14) Read, D. J.; Duckett, R. A.; Sweeney, J.; McLeish, T. C. B. *J. Phys. D: Appl. Phys.* **1999**, *32*, 2087-2099.

(15) Folkes, M. J., Ed. *Processing, structure, and properties of block copolymers / edited by M.J. Folkes*; Elsevier Applied Science Publishers, 1985.

(16) Odell, J. A.; Keller, A. *Polym Eng & Sci* **1977**, *17*, 544.

(17) Godovskii, Y. K.; Tarasov, S. G. *Vysokomolekulyarnye Soedineniya Seriya A* **1980**, *22*, 1613-1621.

(18) Honeker, C. C.; Thomas, E. L.; Albalak, R. J.; Hajduk, D. A.; Gruner, S. M.; Capel, M. C. *Macromolecules* **2000**, *33*, 9395-9406.

(19) Honeker, C. C.; Thomas, E. L. *Macromolecules* **2000**, *33*, 9407-9417.

(20) Fairclough, J. P. A.; Salou, C. L. O.; Ryan, A. J.; Hamley, I. W.; Daniel, C.; Helsby, W. I.; Hall, C.; Lewis, R. A.; Gleeson, A. J.; Diakun, G. P.; Mant, G. R. *Polymer* **2000**, *41*, 2577-2582.

(21) Holden, G.; Legge, N. R.; Quirk, R.; Schroeder, H. E. *Thermoplastic Elastomers*, 2nd ed.; Hanser Publishers, 1996.

(22) Sierra, C. A.; Galan, C.; Fatou, J. G.; Parellada, M. D.; Barrio, J. A. *Polymer* **1997**, *38*, 4325-4335.

(23) Indukuri, K. K.; Lesser, A. J. *Polymer* **2005**, *46*, 7218-7229.

(24) Indukuri, K. K.; Atkins, E. T.; Lesser, A. J. *Journal of Applied Polymer Science* **2005**, *Submitted.*

(25) Rosen, B. W.; ASM, Metals Park, Ohio, 1965; p 37.

(26) Mueller, C.; Gorius, A.; Nazarenko, S.; Hiltner, A.; Baer, E. *Journal of Materials Science* **1995**, *31*, 2747-2755.

(27) Dale, W. C.; Baer, E. *Journal of Materials Science* **1974**, *9*, 369-382.

(28) Darby, M. I.; Kanellopoulos, V. N. *J. Phys. D: Appl. Phys.* **1987**, *20*, 298.

(29) Sadowsky, M. A.; Pu, S. L.; Hussian, M. A. *J. Appl. Mech.* **1967**, *34*, 1967.

(30) James, R. W. *The Optical Principles of the Diffraction of X-rays*; G. Bell and Sons: London, 1967; Vol. II.

(31) Ungar, G.; Keller, A. *Polymer* **1980**, *21*, 1273-1277.

(32) Lyon, R. E. *Ph.D. Thesis*, Polymer Science and Engineering; University of Massachusetts: Amherst, 1985; p 214.

CHAPTER 4

CONTINUOUS PROCESSING LONG-RANGE ORDER IN SEBS TRIBLOCKS

Ultra long range order has been obtained in poly (styrene-b-ethylene-co-butylcne-b-styrene) (SEBS) triblock copolymers with simple continuous extrusion processes. The effects of extrusion processing conditions such as temperature and shear rate on the long-range order have been investigated using small angle x-ray scattering and rheometric techniqucs. Comparison has been made to long-range order obtained by different processes, including compression molding and calender roll pressing. Mechanical properties of these systems have been characterized and compared to isotropic unoricnted systems.

4.1 Introduction

Block copolymer bulk samples preparcd by solution casting and other processes have been shown to form ordered structures locally. Keller and coworkers[1-4] reported the preparation of highly orientcd TPEs with significant long range ordcr for ccrtain styrenc-butadiene-styrene (SBS) block copolymers using a mechanical extrusion process. It was also shown that these 'single-crystal' systems with PS cylinders parallel to the extrusion dircction can be trcated as nearly perfect composite materials [1,5]. Since then, the ability of shear fields to orient or reoricnt block copolymcr layers has been recognized and utilized. Godovsky, Tarasov and coworkers[6-8] have prepared orientcd samples of SBS block copolymers by hot pressing samplcs at 140 °C under high pressurcs. A similar approach to oricnt solution cast films was uscd by Hashimoto and coworkers[9]. Hadziioannou ct al. have used a reciprocating shear devicc to orient micro-

phase separated styrene-isoprene-styrene (SIS) block copolymers [10]. Winter and coworkers[11] have done systematic experiments by subjecting systems to various amounts of shear strain at a constant shear stress in a cone and plate geometry at higher temperatures (melt state). They found that at sufficiently high strains, flow disrupts the micro-domain structure and the partially disrupted and reformed micro-domains align in the flow field. For SBS system, in a constant stress experiment, approximately 30-40 shear units are necessary for global orientation after which it has been observed that the morphology becomes saturated. They also postulated that flow mechanism is a combination of domain dissolution and flow of grains. Other studies by Winter and coworkers[12] on oriented samples using special techniques showed that shear flow introduces irreversible textural changes that are progressive with the amount of applied shear. Again, it has been postulated that the structuring process requires the cylindrical domains to break temporarily and heal again.

Thomas and coworkers [13] have used a roll casting process with block copolymer solutions to obtain long range order in bulk samples of SIS block copolymers. They also studied the impact of morphological orientation on the mechanical properties of triblock copolymer systems [14]. However all the systems studied for long-range order and orientation have been either SBS or SIS triblock copolymers. There are not many studies [15] on the oriented hydrogenated mid-block counterparts of SBS/SIS block copolymers. Hydrogenation of SBS/SIS block copolymers leads to block copolymers with increased segmental incompatibility, thereby significantly increasing the melt viscosities of the systems [16,17]. Their melt viscosities are extremely non-newtonian and hence have a intact network structure which persists in the 'melt' and prevents the

development of dissipative flow in shear fields even at temperatures as high as 300°C [16]. The flow for these SEBS systems is not temperature activated at least up to 260° C, thus making SEBS systems extremely difficult to process. This intact network structure at high temperatures could be used for preserving long-range order/orientation introduced through different techniques, thus avoiding successive annealing steps to improve order/orientation.

There are no systematic studies devoted to studying long-range order obtained in different SEBS block copolymer systems, with subtle alterations in their mid-block. Also, long-range order obtained through different techniques like extrusion, calendering and melt pressing have not been compared. In this chapter, results that compare long-range order obtained in different styrene-b-ethylene-co-butylene-b-styrene block copolymers are presented. The effect of different processing conditions on the long-range order obtained is discussed and structure obtained through different processes are compared. In Chapter 3, evolution of structure at two different length scales during uniaxial deformation has been studied using combined SAXD/WAXD. Oriented block copolymers serve as ideal systems for studying the individual contributions of each phase to the observed mechanical properties. The effect of orientation on the mechanical properties will also be a subject of discussion in this chapter. It is shown that the tensile deformation of an isotropic SEBS sample shows the development of a structure closely resembling that of a 'single-crystal' structure obtained by using different processing techniques.

4.2 Materials and Sample Preparation

4.2.1 Materials

The systems used are SEBS materials S20B, S20E and S40E described previously in Chapter 2. All these three systems have same amount of polystyrene (20% PS) in their end blocks. The first three letters of the naming convention denote the total and overall amount of polystyrene present in the system. The last letter indicates whether it is an ethylene-rich system (E) or a butylene-rich system (B). In S40E, additional styrene is incorporated into the mid-block in a controlled distribution with more styrene present in the middle of mid-block than at the ends. The detailed synthesis of such a system has been described [18]. The structure of a typical SEBS triblock copolymer a) and S40E b) is shown in chapter 2 in figure 2.3 (a) & (b).

4.2.2 Extrusion

The extruded samples were prepared by feeding a sample through a DACA® Twin screw extruder at various temperatures and shear rates of mixing. Samples were extruded over a wide range of processing temperatures starting from 240 °C to 300 °C. The parameters of a typical processing run on the DACA Twin screw extruder for S20B were 250 RPM at 240 ° C.

4.2.3 Roll pressing

Bulk SEBS block copolymer samples 3 mm in thickness were roll pressed in a STANAT® 2-roll calender at 180 °C to obtain a final thickness of 1 mm. The initial

materials required for roll pressing were obtained either by solution casting or melt pressing.

4.2.4 Compression Molding

Samples were compression molded into 3 mm thick plaques at 200°C at a pressure of 3.5 MPa for approximately 20 minutes followed by water cooling.

4.3 Characterization and Testing

4.3.1 Electron Microscopy

Transmission electron Microscopy (TEM) studies were performed using a JEOL 2000 FX TEM operating at 200 KV on ruthenium tetroxide stained samples obtained by cyro-microtoming thin sections of SEBS bulk samples.

4.3.2 Small angle X-ray scattering

Small angle x-ray diffraction (SAXD) measurements were performed on a Molecular Metrology® SAXS machine. SAXD images were calibrated using a naturally oriented turkey tendon standard.

4.3.3 Mechanical testing

Tensile tests on extrudates were performed on an Instron 5800 tensile testing machine. Rheological Measurements were obtained using a Viscotech® Rheological Mechanical Spectrometer operated in constant stress (200 Pa) mode, with a frequency

sweep from 10^{-2} Hz to 10^{+2} Hz. Parallel plate geometry was employed, with the thickness and diameter of the sample discs being 1.5 mm and 25 mm respectively.

4.4 Results and Discussion

Morphological investigation of solution cast S20B, S20E and S40E by TEM, (as shown in figure 2.9), reveals the existence of grains of oriented cylinders present in each system. This result is in accordance with several previous findings[19,20].

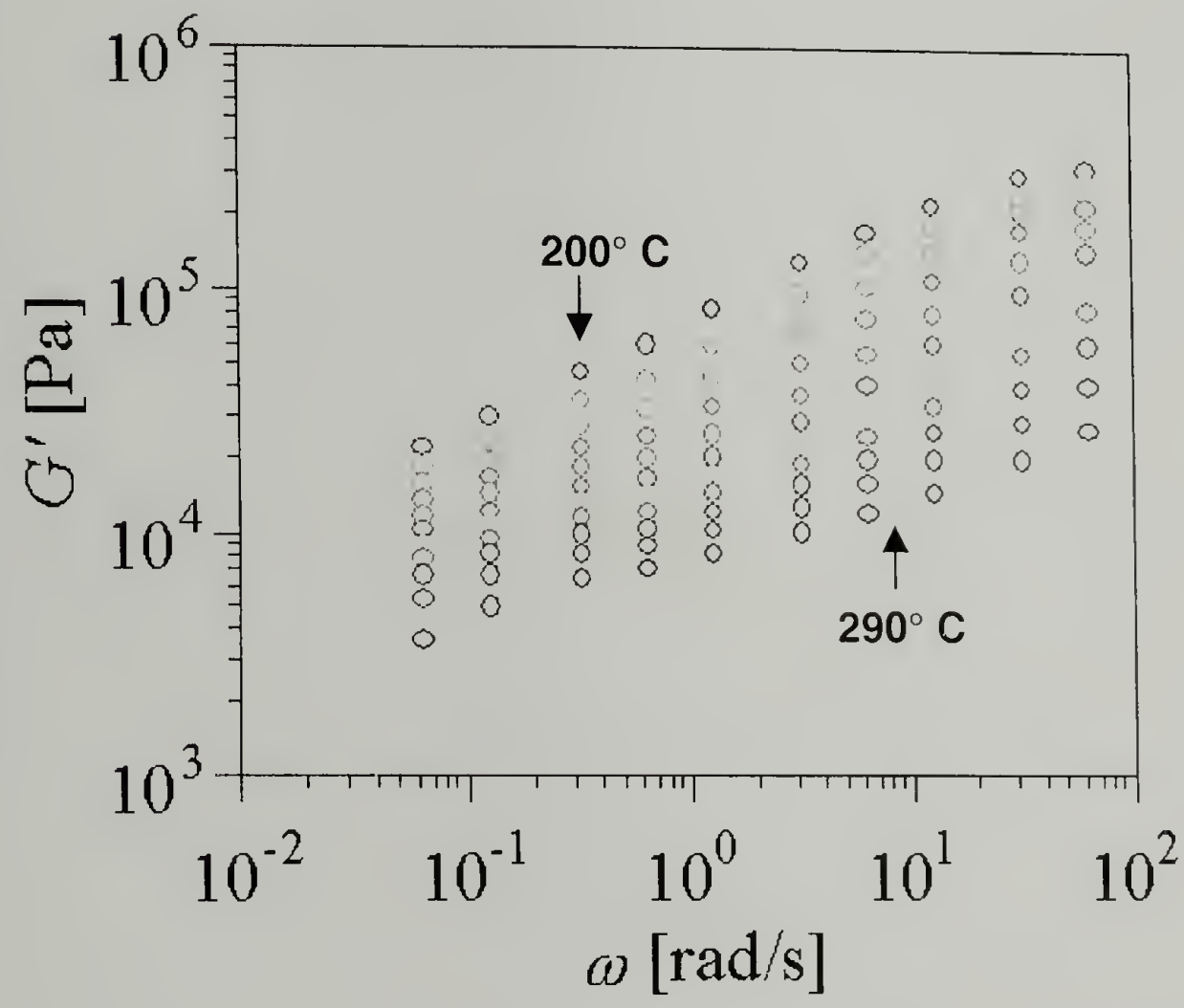

Figure 4.1 Dynamic Storage Modulus versus frequency for system S20B

Rheological experiments were performed in parallel plate geometry with 25 mm diameter circular discs. Strain amplitude of 0.02 was used in these experiments on 1.5 – 2 mm thick samples. Figure 4.1 shows the dynamic storage modulus as a function of

frequency for system S20B. It can be seen that this system shows very high moduli at all the test frequencies. This behavior persists even to temperatures as high as 290 °C. This shows that this system S20B does not show any order to disorder transition below 300 °C. Thus order to disorder transition (ODT) of this system is very high and does not occur until its decomposition temperature (380 °C). The loss modulus of the system shown in figure 4.2 also exhibits similar response.

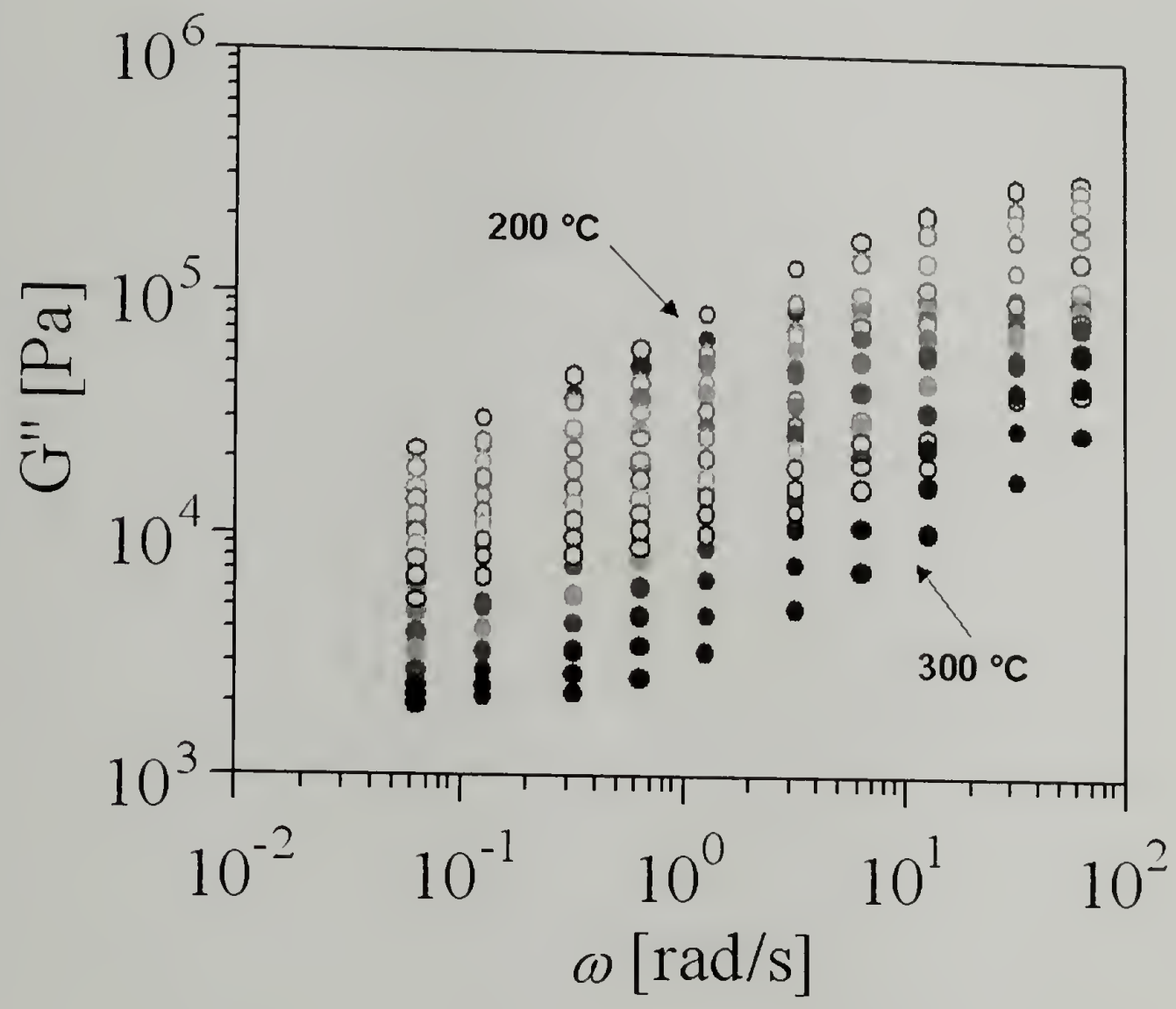

Figure 4.2 Dynamic Loss Modulus versus frequency for system S20B

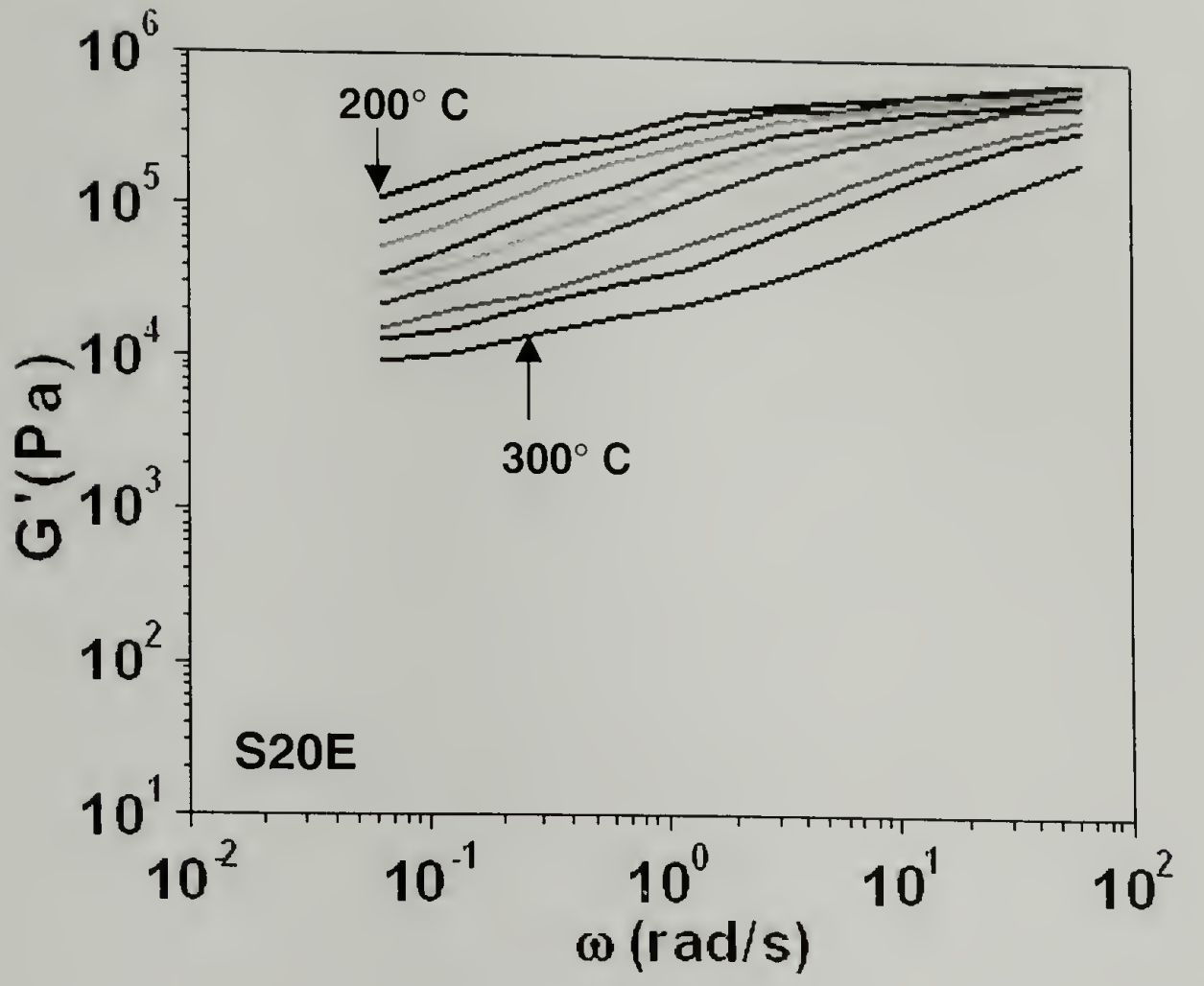

Figure 4.3 Dynamic Storage Modulus versus frequency for system S20E

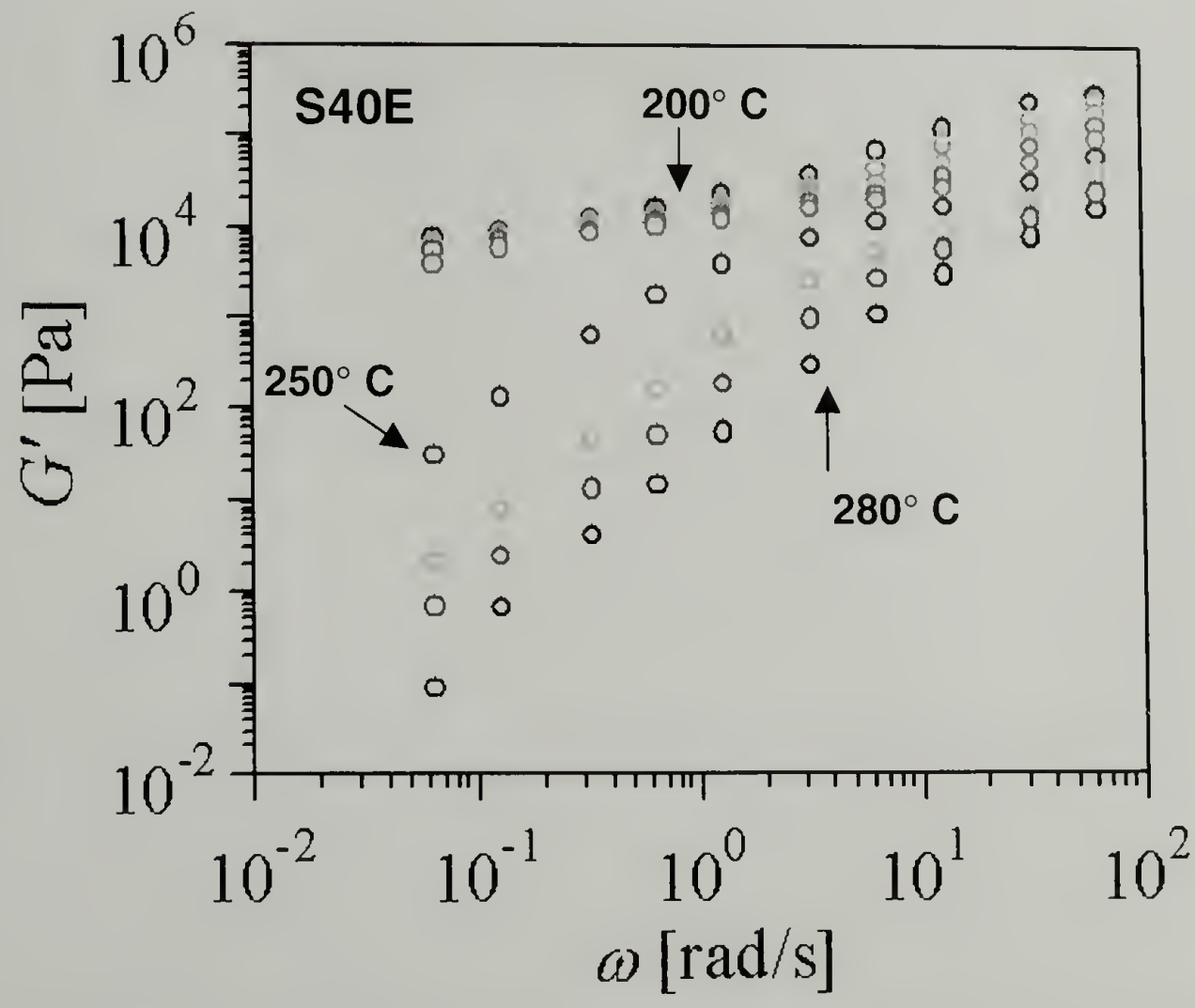

Figure 4.4 Dynamic Storage Modulus versus frequency for system S40E

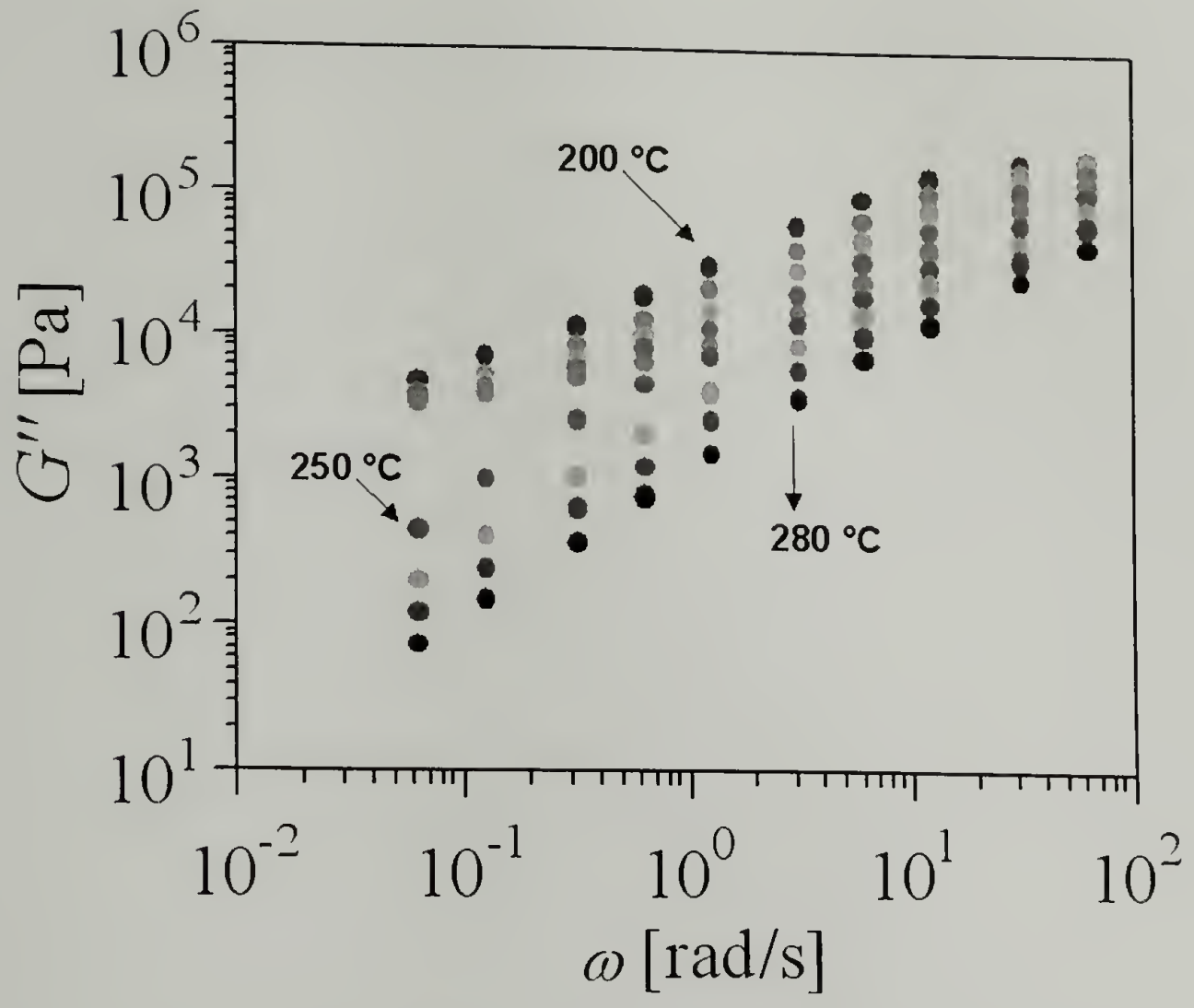

Figure 4.5 Dynamic Loss Modulus versus frequency for system S40E

Figure 4.3 shows the dynamic modulus versus frequency at different temperatures for system S20E. It can be seen that this system shows much higher G' values than those for system S20B at all frequencies for all temperatures from 200 °C to 300 °C. The values of moduli are atleast an order of magnitude higher at all frequencies for all temperatures for system S20B. This implies that this system is more strongly phase separated and the dissipative field cannot disrupt this network structure even at temperatures as high as 300 °C. Hence S20E also does not show any ODT below 300 °C.

Figure 4.4 shows the dynamic modulus versus frequency at different temperatures for system S40E. It can be seen that at lower temperatures from 200 °C to

240 °C, the system S40E shows moduli similar to those of S20B in the frequency range investigated. However, it can be clearly noticed that once the temperature increases to 250 °C, two orders of magnitude drop in dynamic storage modulus can be observed. Beyond this 250 °C temperature, the storage modulus drops significantly and the system S40E flows easily as the temperature is increased further. S40E thus exhibits an ODT at 250 °C. Similar response is observed from the loss modulus curve at different temperatures depicted in figure 4.5. This drop in ODT of the system S40E to 250 °C can be expected by observing the subtle changes done to the SEBS block copolymer. S40E has additional 20% styrene incorporated into the mid-block in a random but controlled fashion. This reduces the interaction parameter between PS end blocks and styrene-incorporated PEB mid-blocks. Thus, phase segregation behavior is dramatically affected as can be observed by the drop in ODT. This drop in ODT is expected to have tremendous impact on its processing behavior as it is much easier to process block copolymer systems above their ODT. Additionally, their ordering and orientation behavior can be expected to change depending on whether the system is processed above or below its ODT.

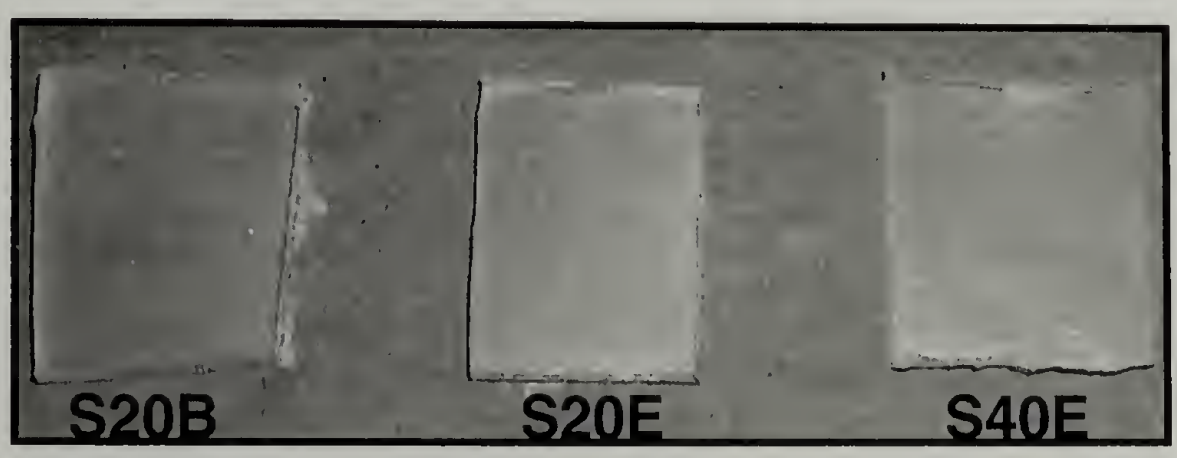

Figure 4.6 Compression molded samples at 200 °C and 3.5 MPa

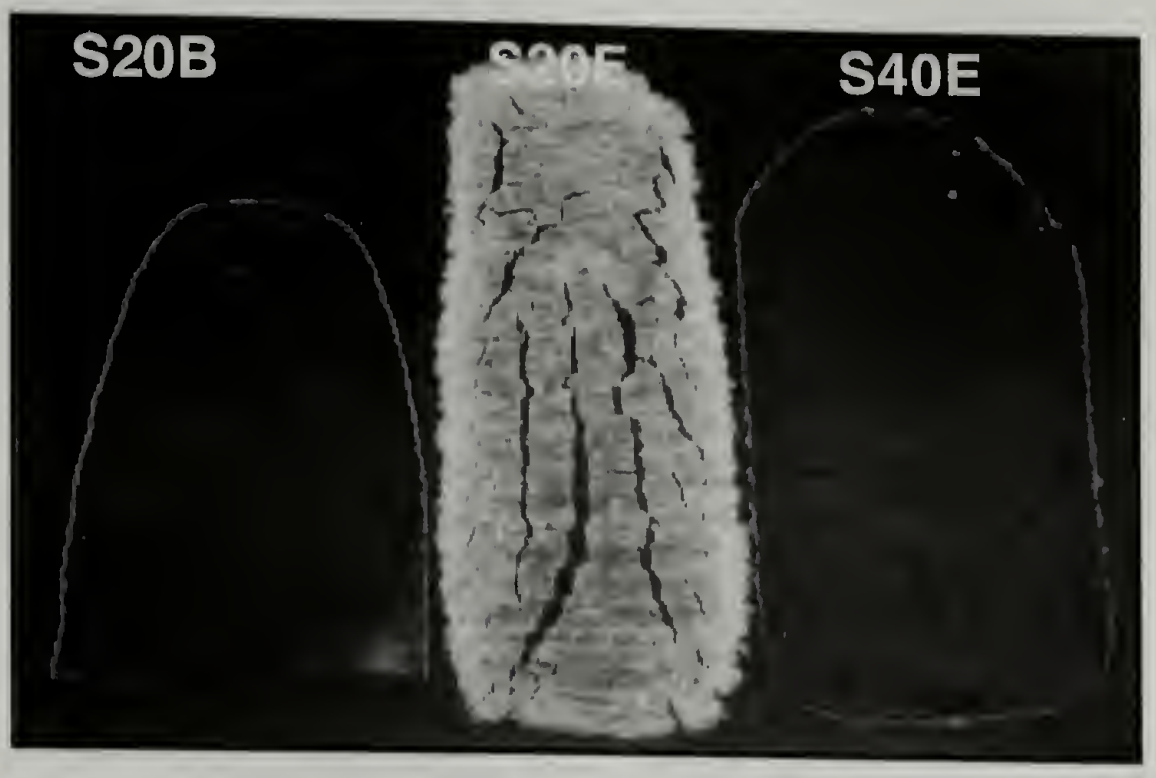

Figure 4.7 Roll pressing at 180 °C Calendering

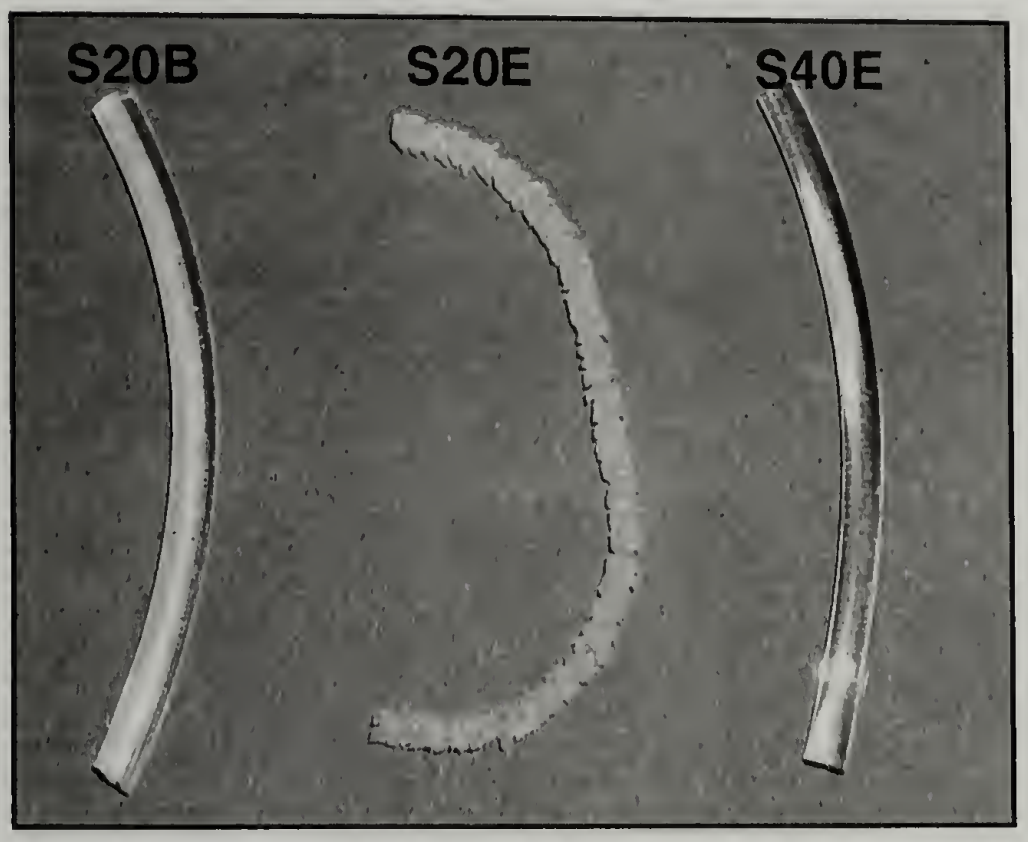

Figure 4.8 Extrusion processing at 240 °C-DACA Twin Screw Extruder

Figure 4.6 shows the photograph of compression molded (melt pressed) samples at 200 °C and 3.5 MPa. It can be seen from this visual inspection that all the three systems S20B, S20E and S40E processed under these conditions are transparent. Figure 4.7 shows the photograph of roll pressed (calendered) samples at 180 °C and compression ratio of 3:1. It can be immediately seen that the system S20E shows extensive melt fracture under these process conditions. The rheological data for S20E shown in figure 4.3 lends evidence to this result. It can be recalled that S20E has the highest moduli of all the three systems and hence would be the most difficult to process. The same behavior is apparent in figure 4.8 for S20E. At 240 °C, the system S20E melt-fractures extensively in the twin screw extruder and breaks apart into smaller extrudates. This suggests that temperatures much higher than 240 °C are needed to melt process S20E. In addition, shear rates employed for extrusion processing qualitatively reveals that S40E is the easiest to process, followed by S20B. S20E is the most difficult system to process. Decreasing the temperature of processing while maintaining the other mechanical properties intact is an added benefit as it drives down the energy costs. The mechanical behavior of the systems S20B and S40E under different processing conditions will now be discussed in detail. It can be expected that S20E processed at higher temperatures (relative to S20B) will exhibit behavior similar to that of S20B.

Figure 4.9 shows the SAXD pattern obtained on S40E extrudate processed at 270 °C and 100 RPM. The direction of X-ray incidence here is perpendicular to the long axis of the extrudate.

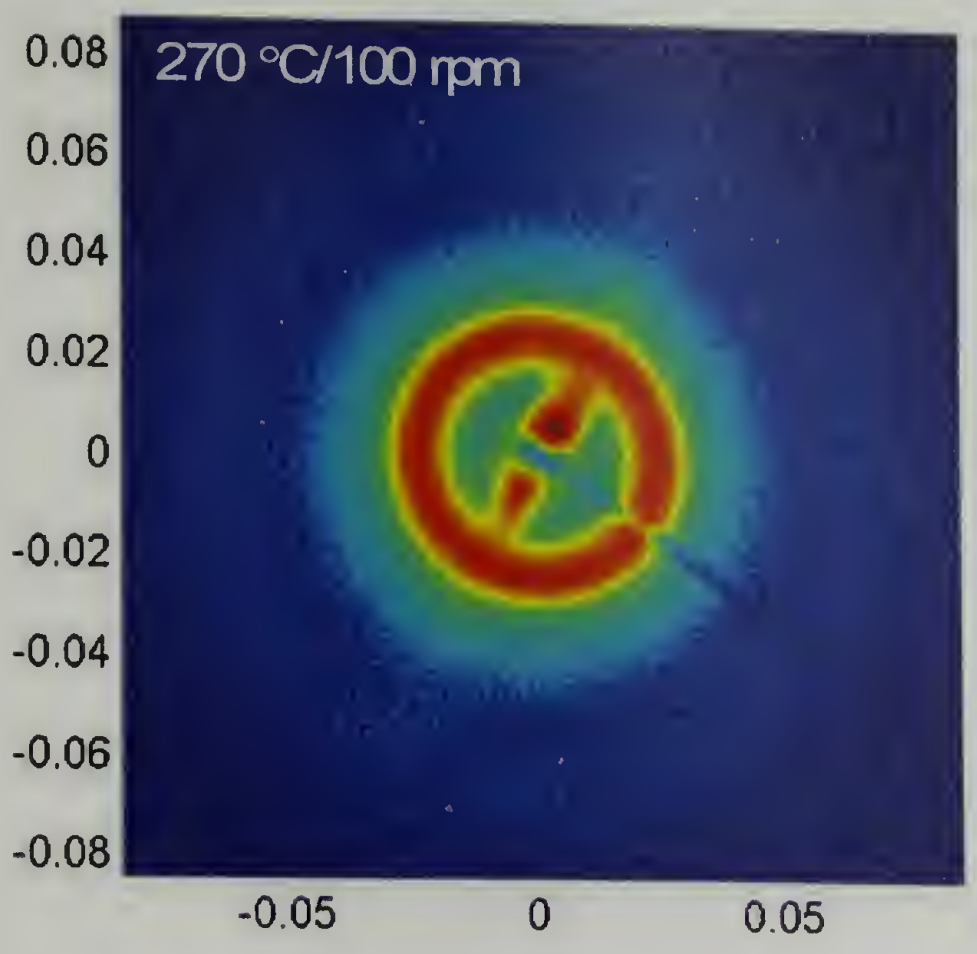

Figure 4.9 S40E processed above its ODT-270 °C/100 RPM

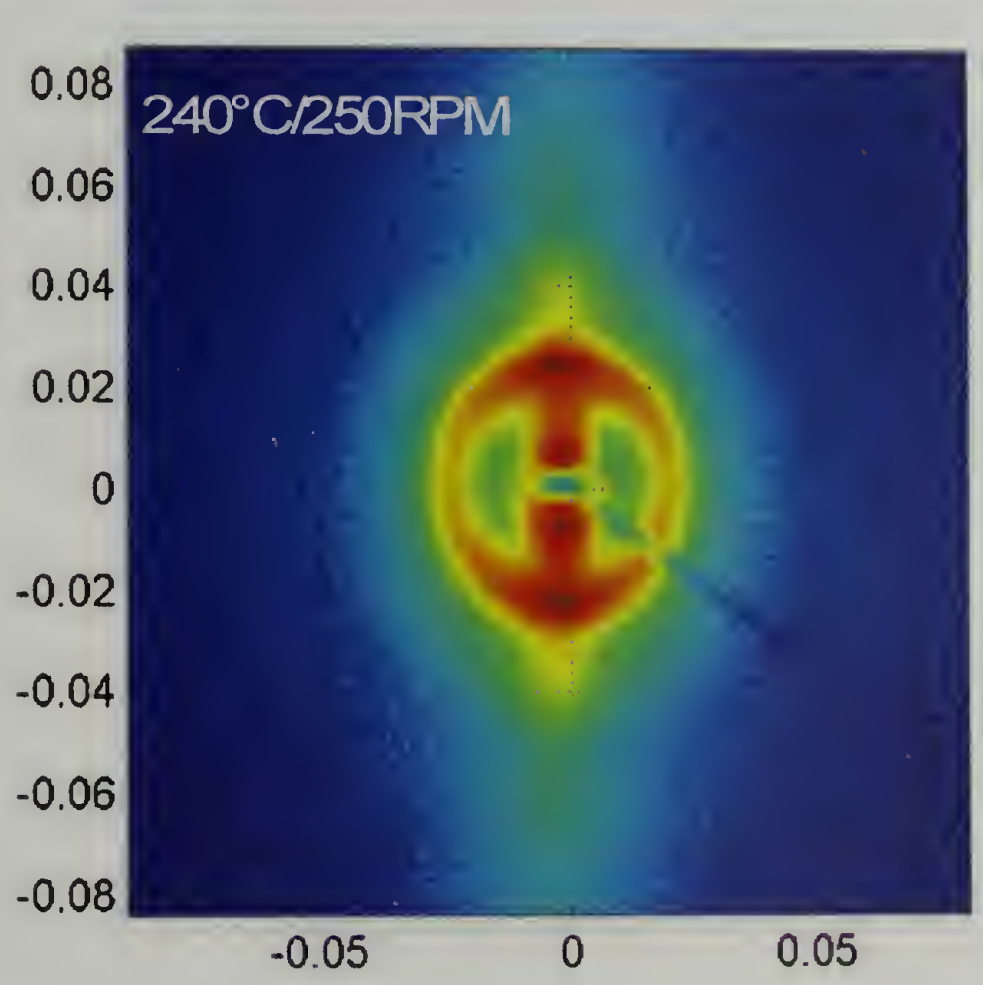

Figure 4.10 S40E processed below its ODT-240 °C/250 RPM

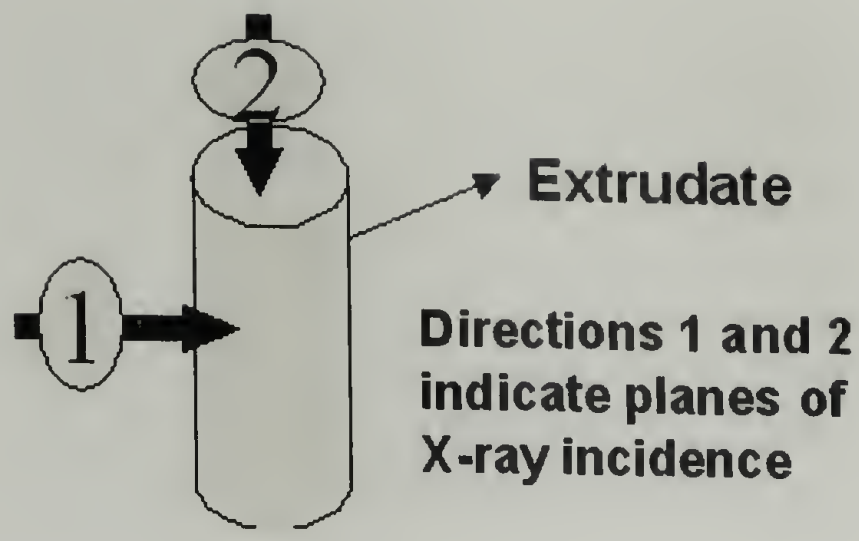

Figure 4.11 Directions of small angle x-ray incidence for extrudates

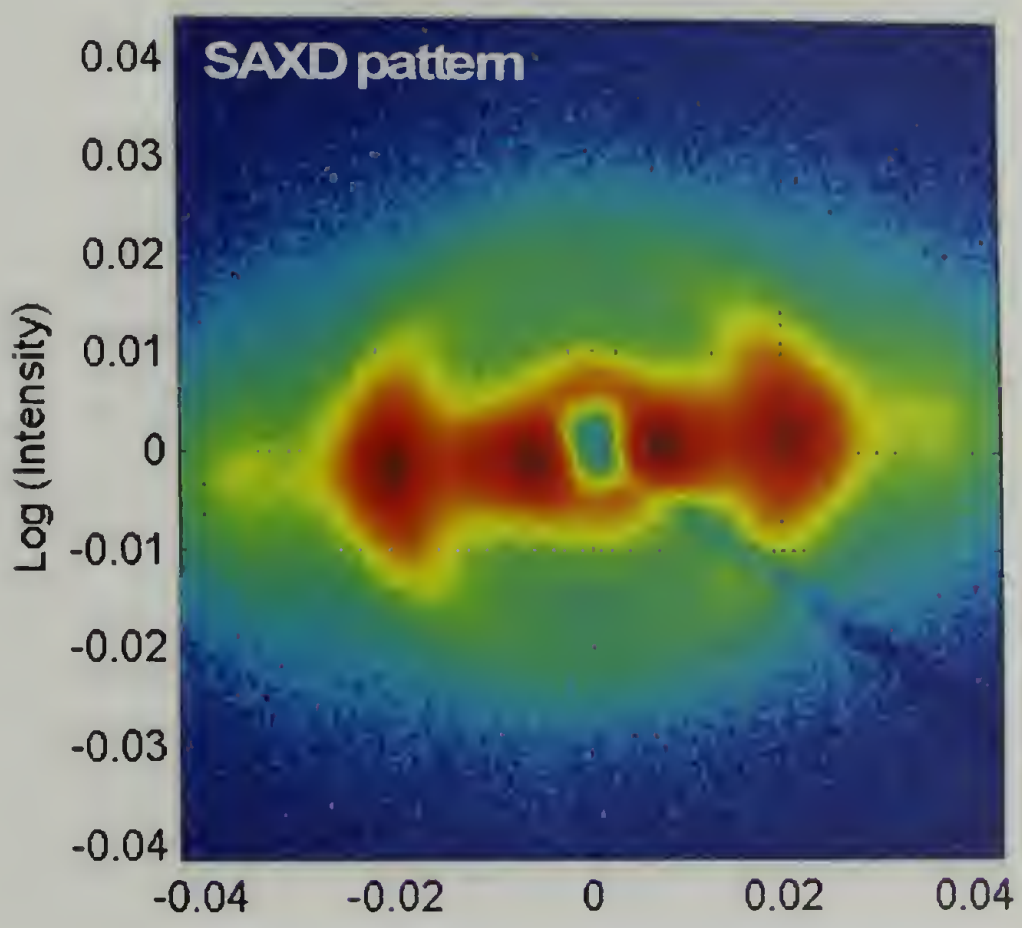

Figure 4.12 Orientation of S20B-2 point patterns-direction of incidence 1

Figure 4.13 Schematic of long-range orientation (2-point pattern in figure 4.11)

The SAXD pattern in figure 4.9 shows a random arrangement of cylinders without any preferential global alignment. This can be expected because the processing temperature here is greater than the order to disorder transition temperature of S40E. This also shows that the system has to below its ODT in order to get long-range order/orientation of polystyrene (PS) cylinders. Figure 4.10 shows a SAXD pattern of S40E processed below its ODT at 240 °C and at 250 RPM. The SAXD pattern shows a characteristic 2-point pattern suggesting globally oriented cylinders. The 2-point pattern observed is very sharp without much broadening qualitatively suggesting long-range orientation.

Extrusion of the system S40E above its ODT is very simple and very low shear rates are necessary for disrupting the order in the block copolymer. However processing below its ODT, S40E shows long-range orientation. This can be expected to significantly affect the mechanical properties of the S40E extrudate. This would be discussed in detail shortly. Extrusion processing is usually used in the TPE industry to mix mineral fillers and other additives to enhance the various properties of the TPE product. Thus orientation or the absence of orientation can have tremendous impact on the properties of the extruded product.

From rheological studies, S20B does not show ODT below 300 °C. It can be expected that extrusion-processing S20B at any temperature below its ODT produces some level of orientation in the system. Figure 4.12 shows the SAXD pattern of S20B extrudate. The direction of x-ray incidence is 1, which has been described in figure 4.11. It was observed that S20B shows long-range orientation under wide range of processing

speeds and temperatures from 240 °C/200 RPM to 300 °C/30 RPM. Direction 1 of observation reveals the two orders in the two-point pattern. The ratio of the peaks in the two-point pattern is 1:√3 suggesting hexagonally packed cylinders with long-range orientation in the S20B extrudate. Figure 4.13 shows a schematic of such global orientation obtained in S20B extrudate. In order to confirm this TEM, a real space technique has been used. Figure 4.14 shows the long range orientation obtained in system S20B using system S20B.

In order to make structures with long range order and orientation, it is important to pattern/prepare each surface such that each point on the lattice be defined and be precisely addressed. In order to investigate such long-range order, SAXD patterns were obtained edge-on onto the extrudate (direction 2) as shown in figure 4.13. It can be seen (from figure 4.13) that the system shows a clear six-point pattern to atleast two orders. The ratio of the two orders of peaks in this six-point pattern is 1:√3 confirming hexagonally packed polystyrene cylinders. This six-point pattern suggests that there is long-range order present in the system. This SAXD pattern has been obtained on 2 mm long extrudates proving that this long-range order and orientation extends to macroscopic dimensions. The indexing of reflections from this hexagonal lattice has been done as shown in figure 4.16 which shows a schematic of the six-point pattern observed in figure 4.15. The dotted circular rings refer to intensity distribution from a randomly oriented sample. The larger points with indexed reflections refer to diffracted peak positions from a perfect lattice, an oriented 'single crystal' like sample.

Thus, a truly global order and orientation of nano-scale cylinders is obtained using simple extrusion processing for system S20B. The extrusion technique is hence a

robust and inexpensive method for obtaining long-range order/orientation. An additional benefit is that no annealing steps were required to produce such an order.

Figure 4.14 TEM real space image of long-range orientation in S20B

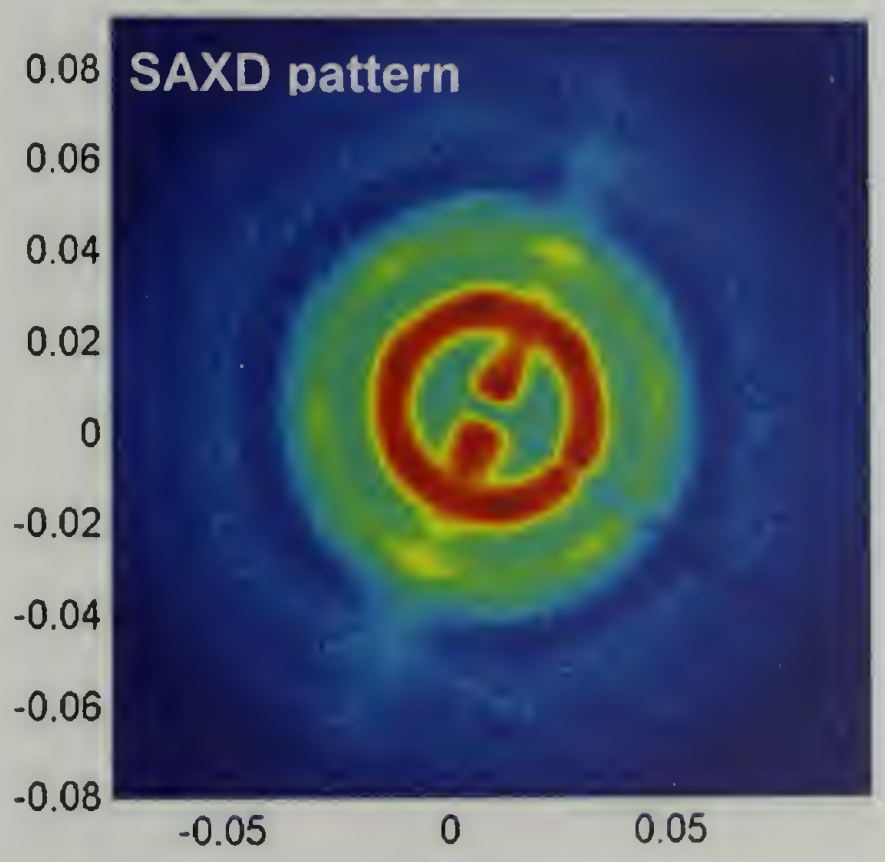

Figure 4.15 SAXD pattern in direction 2 for S20B

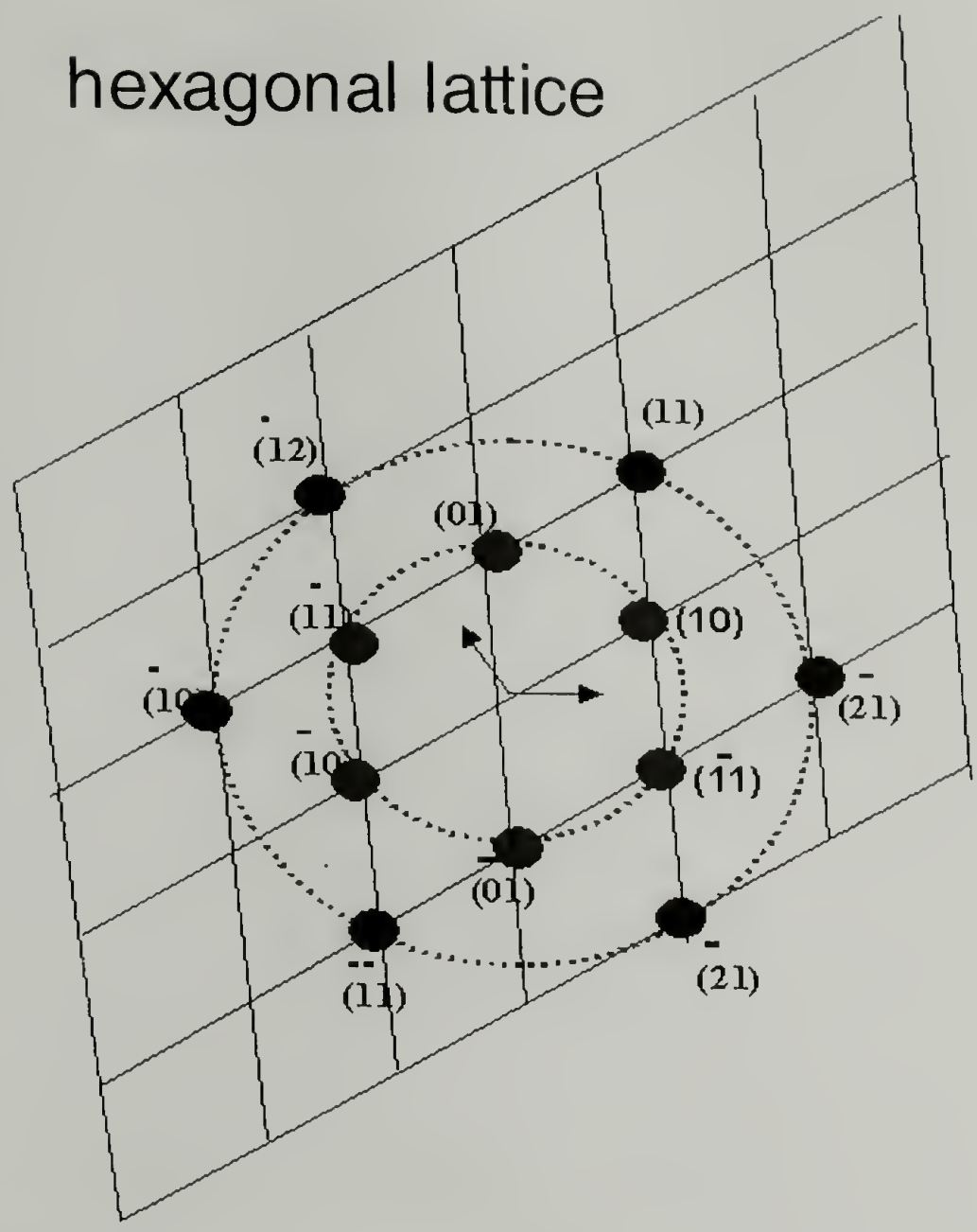

Figure 4.16 Schematic representation of the order in S20B

In addition, extrusion technique was used to mix block copolymers with nano clays. Cloisote 15 A, a modified clay (with a d-spacing of 30.6 A^{o}) was used for mixing with S20B. Figures 4.17 show the SAXD pattern of S20B+ 4% Cloisote 15 A clay and the long-range orientation obtained as a result of the extrusion process. WAXD pattern shown in figure 4.18 shows that clay platelets also get aligned as a result of this extrusion process. An intercalated system has been obtained with the d-spacing of clay increasing by about 12% to 35.6 A^{o}.

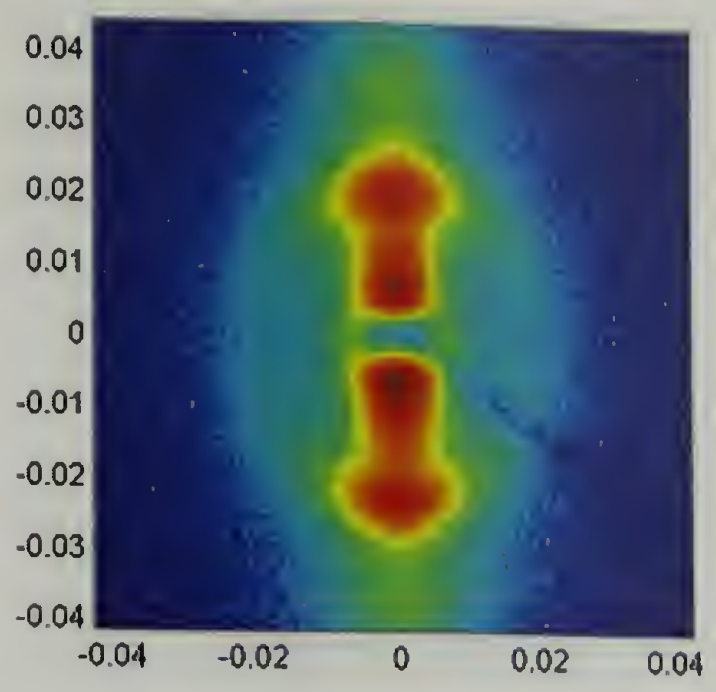

Figure 4.17 SAXD pattern of an extrudate of S20B+4% Cloisote 15A clay

Figure 4.18 WAXD pattern of 15A clay orientation in an extrudate of S20B+4% Cloisote 15A clay

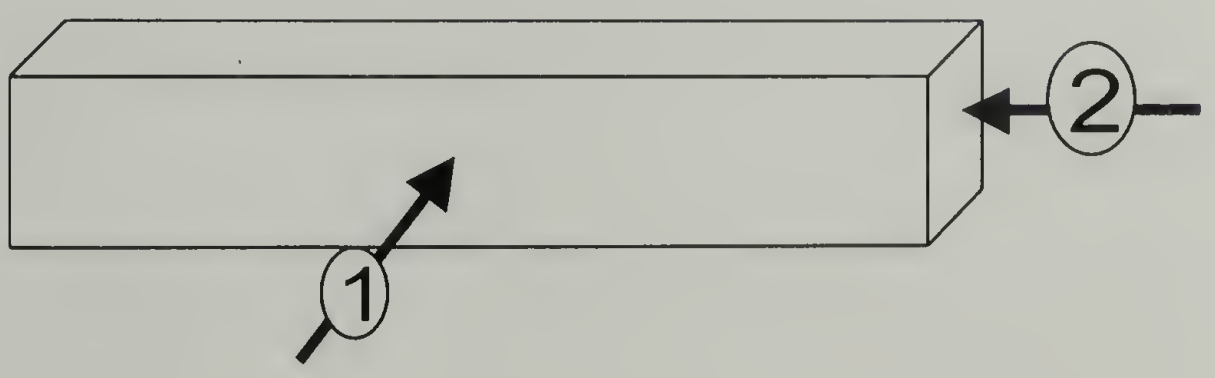

Figure 4.19 Directions of X-ray incidence on melt presses and roll pressed samples

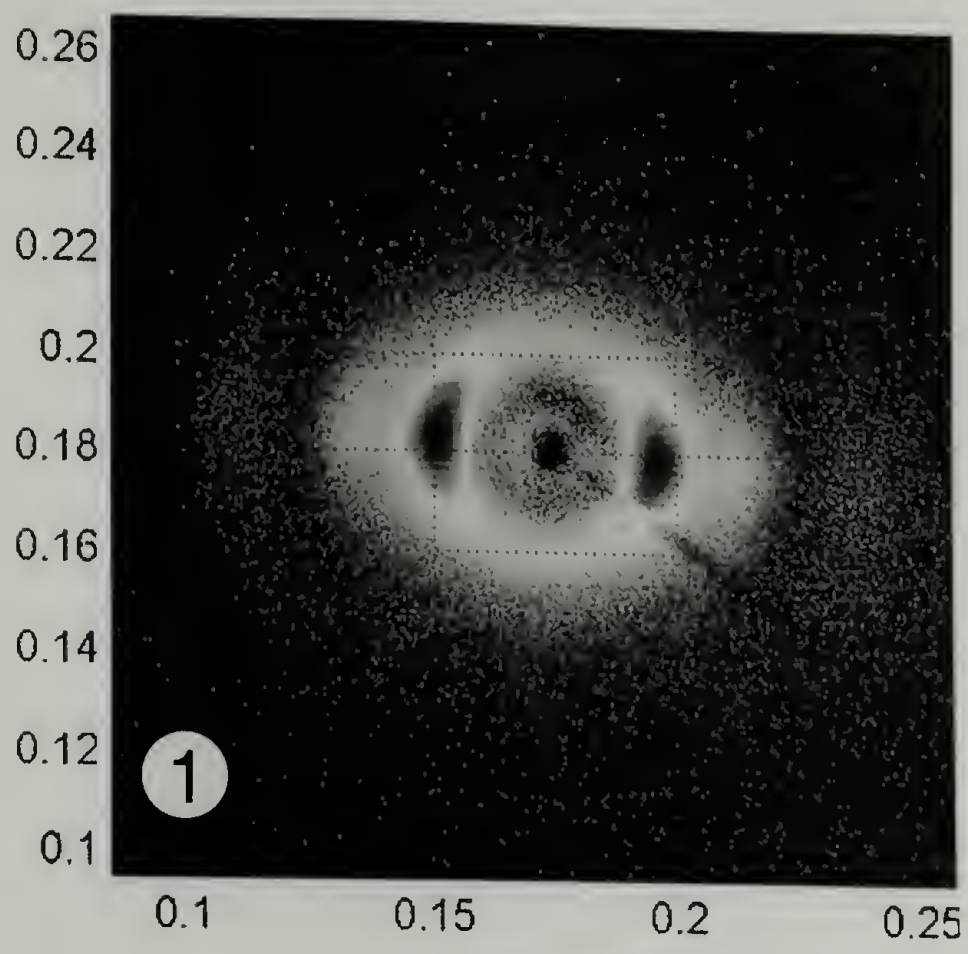

Figure 4.20 SAXD of roll pressed S20B film in direction 1

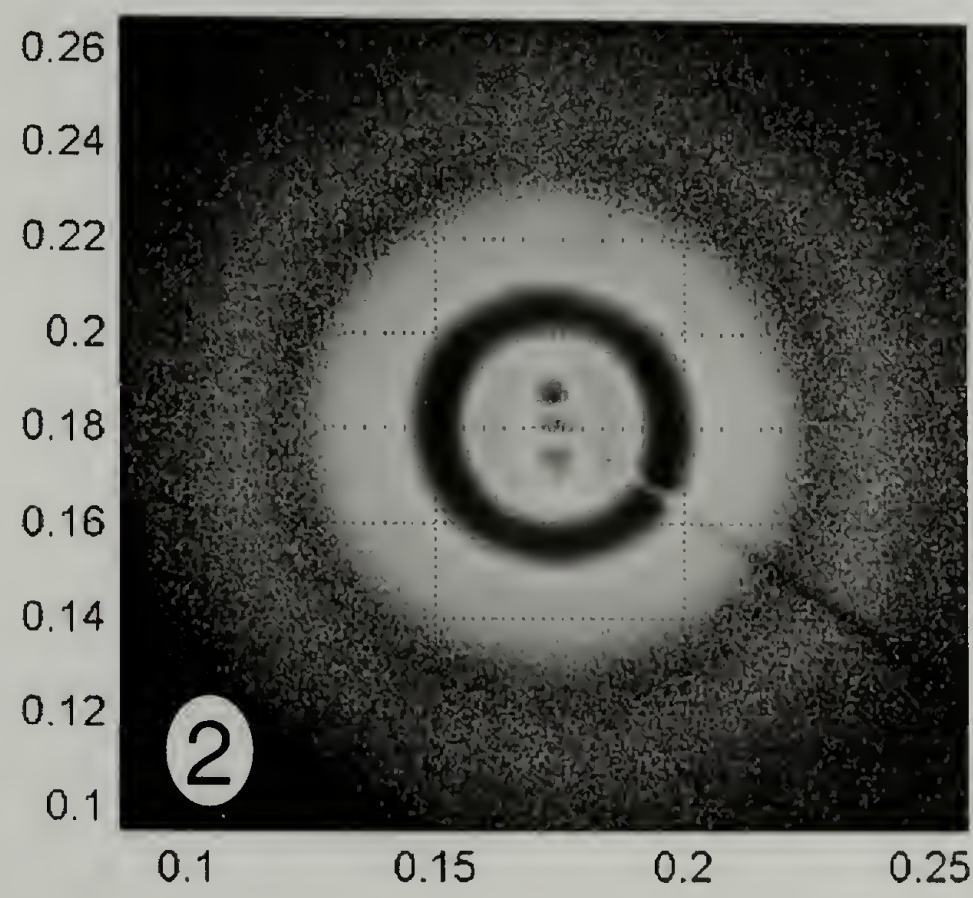

Figure 4.21 SAXD of roll pressed S20B film in direction 2; X-ray incidence edge-on to the sample

Compression molding (melt pressing) and calendering (roll pressing) are commonly used processing techniques for block copolymer TPEs in industry. The effects of these processing techniques on the orientation and order obtained in block copolymer TPEs are also examined in this study. Figure 4.19 shows the different directions of x-ray incidence onto the two distinct cross-sectional areas of the processed samples. Figures 4.20 and 4.21 show the SAXD patterns of S20B roll pressed (compression ratio 3:1 and temperature of 180 °C) samples in the directions 1 and 2, perpendicular to the long direction of the film and edge-on onto the sample respectively. Figure 4.20 clearly shows sharp two point patterns suggesting long-range orientation obtained in the sample. However observing figure 4.21 for SAXD pattern in the other direction shows a more or less circular diffraction ring. This suggests that there is no long-range order present in the sample, even though sample shows long-range orientation.

Compression molded also shows results similar to those of roll pressed samples. Figures 4.22 and 4.23 show the SAXD patterns of S20B samples compression molded (at 200 °C and 3.5 MPa) in the directions 1 and 2, perpendicular to the long direction of the film and edge-on onto the sample respectively. Figure 4.22 clearly shows sharp two point patterns suggesting long-range orientation obtained in the sample. Also two orders of peaks in the ratio $1:\sqrt{3}$ can be clearly seen in this two-point pattern. However observing figure 4.23 for SAXD pattern in the other direction shows a more or less circular diffraction ring, suggesting a random arrangement. This suggests that there is no long-range order present in the sample, even though sample shows long-range

orientation. Thus compression molded as well as calendered samples show less long-range order and orientation than that obtained from that of an extrudate.

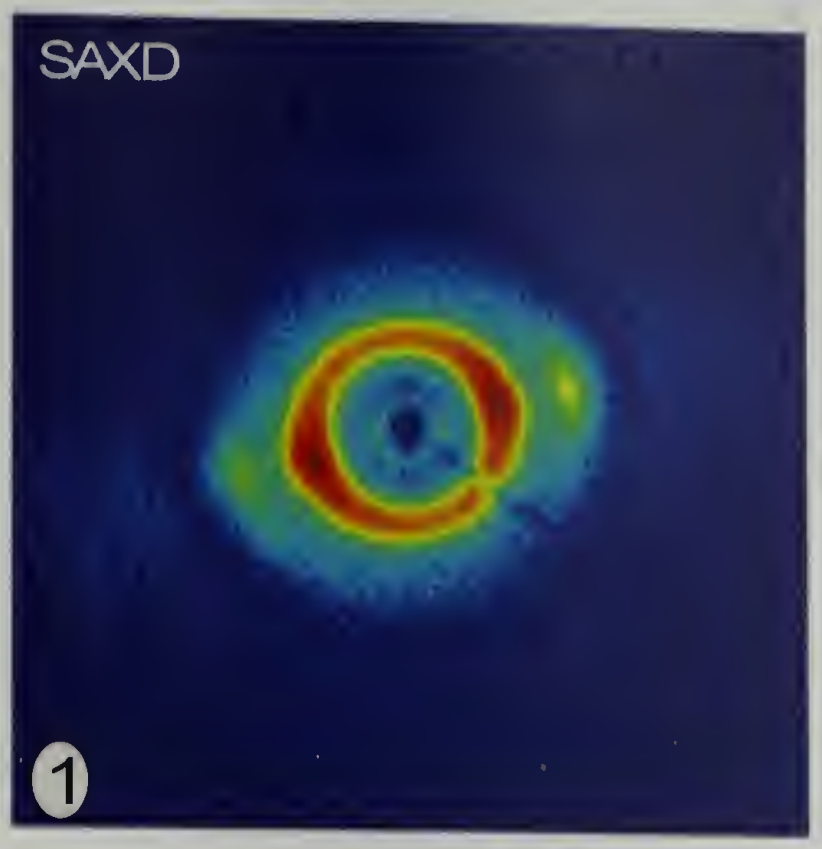

Figure 4.22 Orientation of S20B obtained by melt pressing; X-ray incidence is direction 1 perpendicular to the cross-sectional area of the melt pressed sample

Figure 4.23 SAXD pattern of melt pressed S20B; X-ray incidence edge-on to the sample

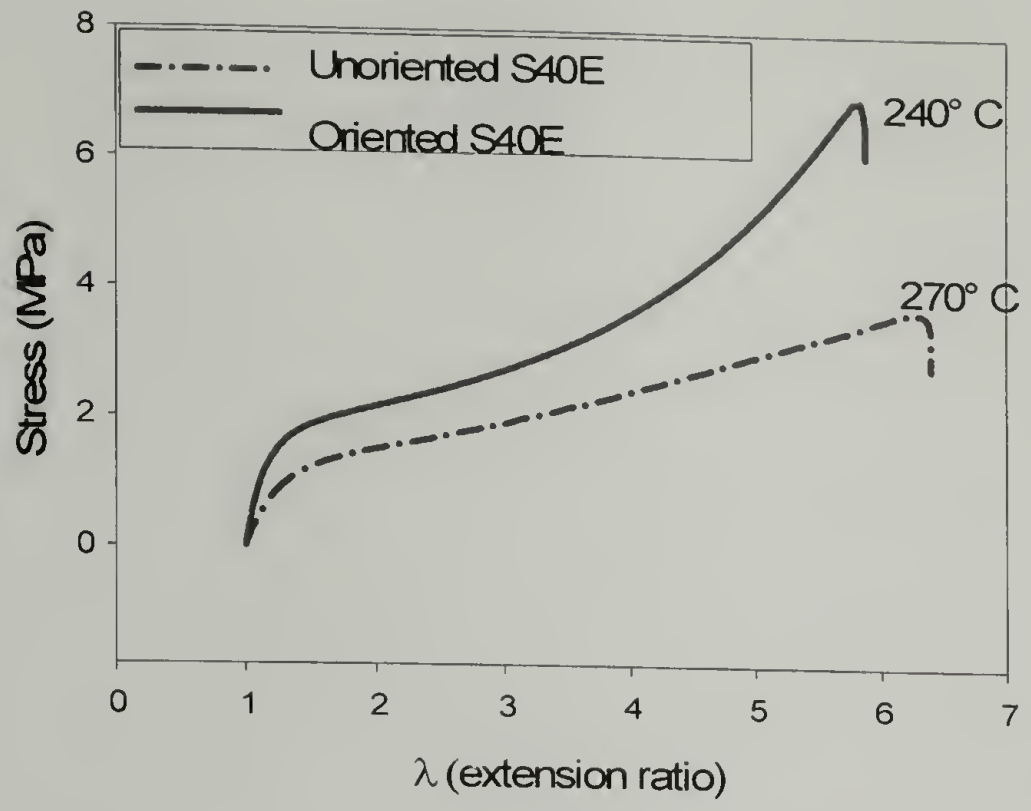

Figure 4.24 Uniaxial tensile tests on S40E extrudates processed above and below their ODTs

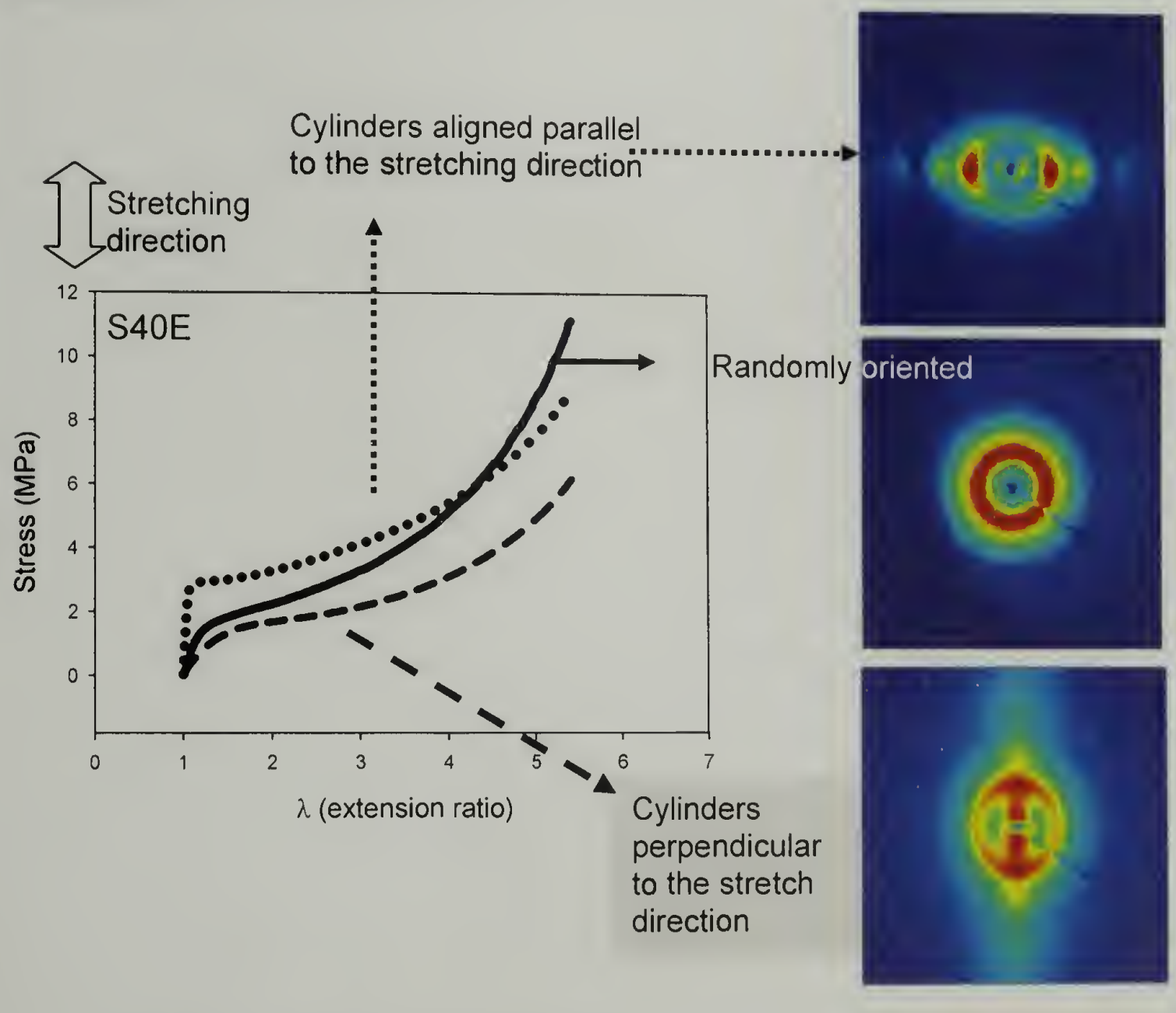

Figure 4.25 Uniaxial tensile testing of roll pressed samples of S40E

To examine the influence of orientation on the mechanical properties, uniaxial tensile tests were performed on oriented and unoriented extrudates of S40E. These oriented and unoriented extrudates were obtained by processing below or above their ODTs. Figure 4.24 clearly reveals the difference in the mechanical behavior between oriented and unoriented extrudates. The modulus and tensile strength of the oriented extrudate is noticeably larger than that of the unoriented extrudate.

Figure 4.25 compares the mechanical properties of oriented samples of S40E obtained by roll pressing in different directions in comparison with those of randomly oriented solution cast samples. SAXD patterns on the right in figure 4.25 show the different orientations of the samples. It can be clearly observed that when the cylinders are aligned parallel to the stretching direction, the initial modulus increases several-fold. This behavior is similar to the behavior of fiber reinforced composites. Also it can be noticed that the initial yield point associated with micro-buckling instability (discussed in chapter 3) moves to lower strain levels from those of randomly oriented samples. In addition, it can be noticed that this onset region of microbuckling instability is much sharper than that for randomly oriented sample. In addition, it can be observed that both the onset as well as the sharpness of the apparent yield point decreases in the order of samples with cylinders aligned parallel to the stretching direction, randomly oriented and aligned perpendicular to the stretch direction respectively.

Figure 4.27 shows the mechanical properties of oriented samples of S20B obtained by compression molding and then cut at different angles to the overall global orientation direction in comparison with those of randomly oriented solution cast samples. SAXD patterns on the right in figure 4.26 show the different orientations of the

samples. The observations here are similar to those obtained from the previous experiments on S40E roll pressed samples. It is interesting to observe that the samples cut at 45° to the orientation direction closely follows the randomly oriented solution cast sample until break.

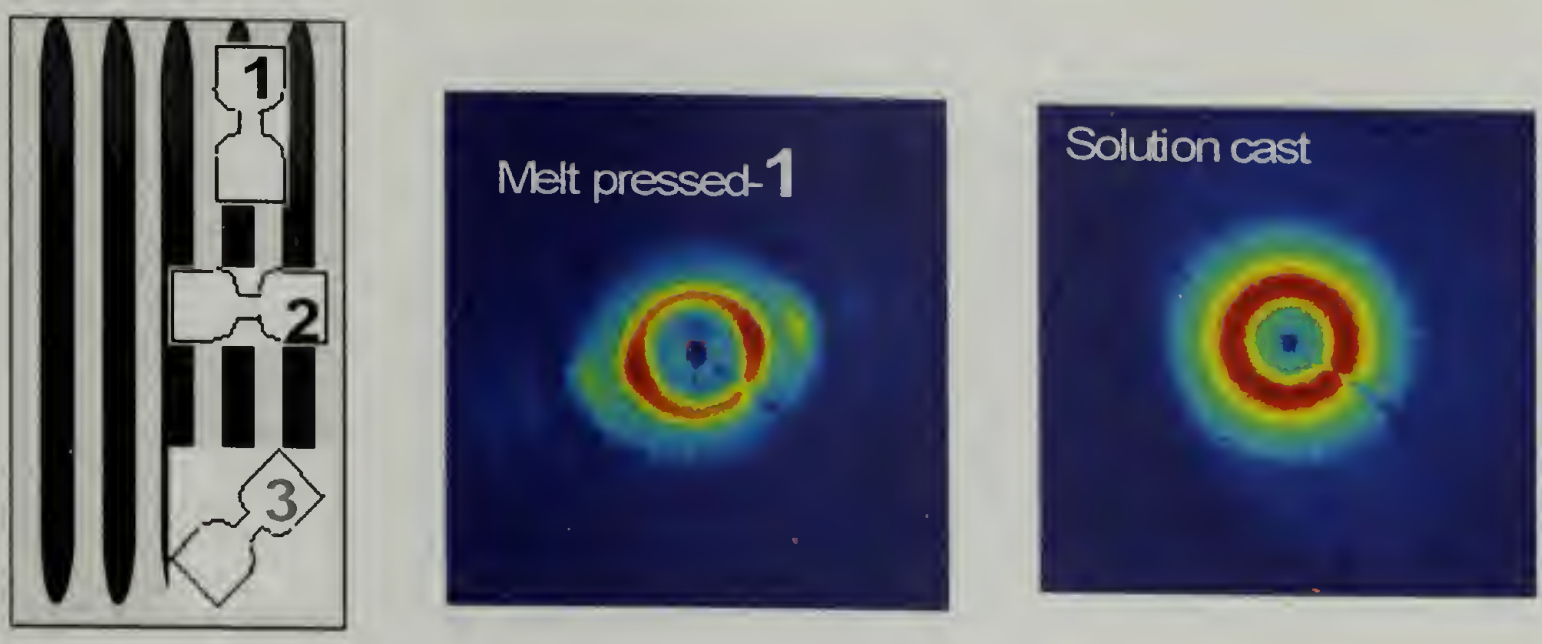

Figure 4.26 Directions of samples cut from melt pressed films with different angles to the alignment direction

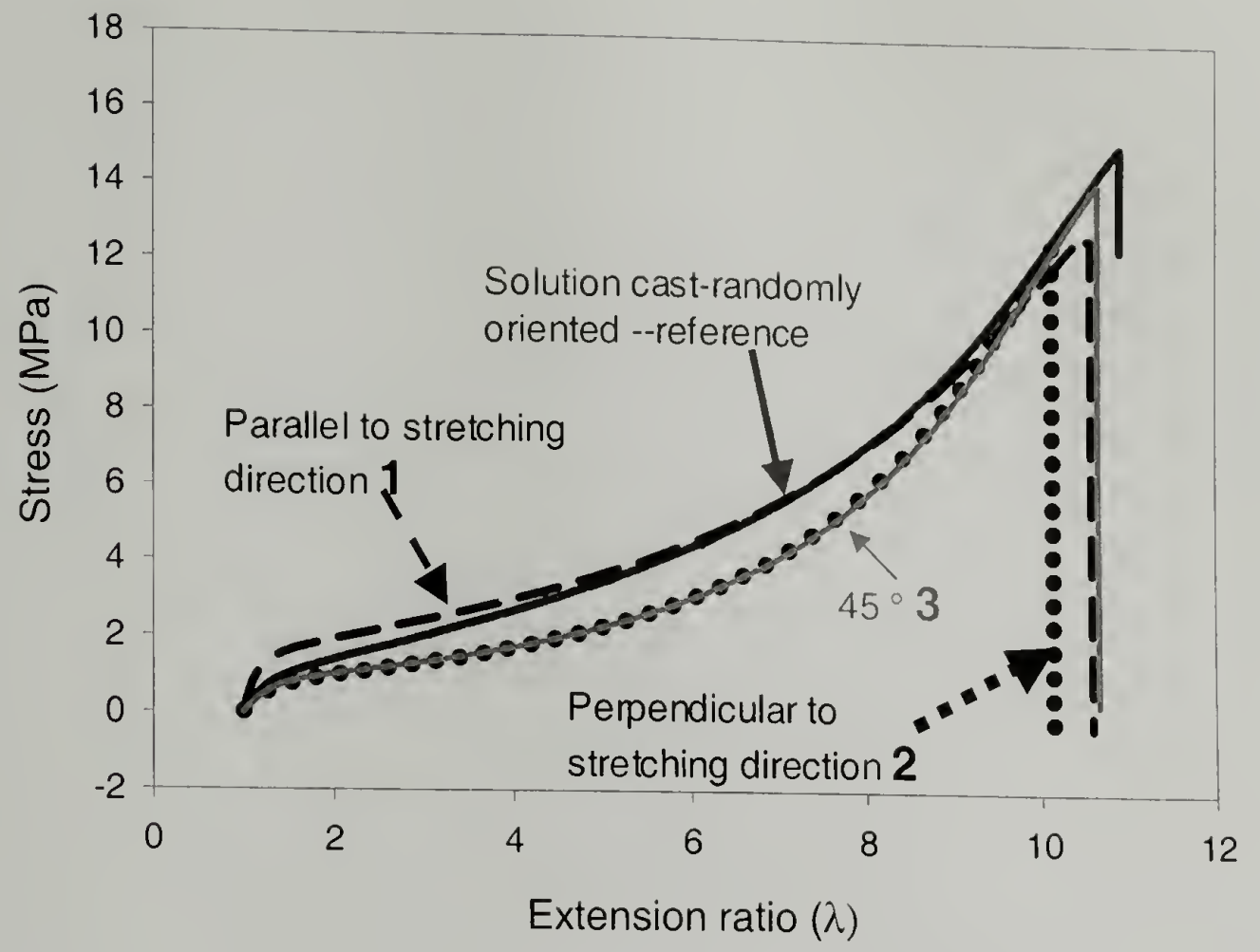

Figure 4.27 Uniaxial tensile tests on S20B samples globally aligned by melt pressing and cut at different angles to the orientation direction (shown in figure 4.26)

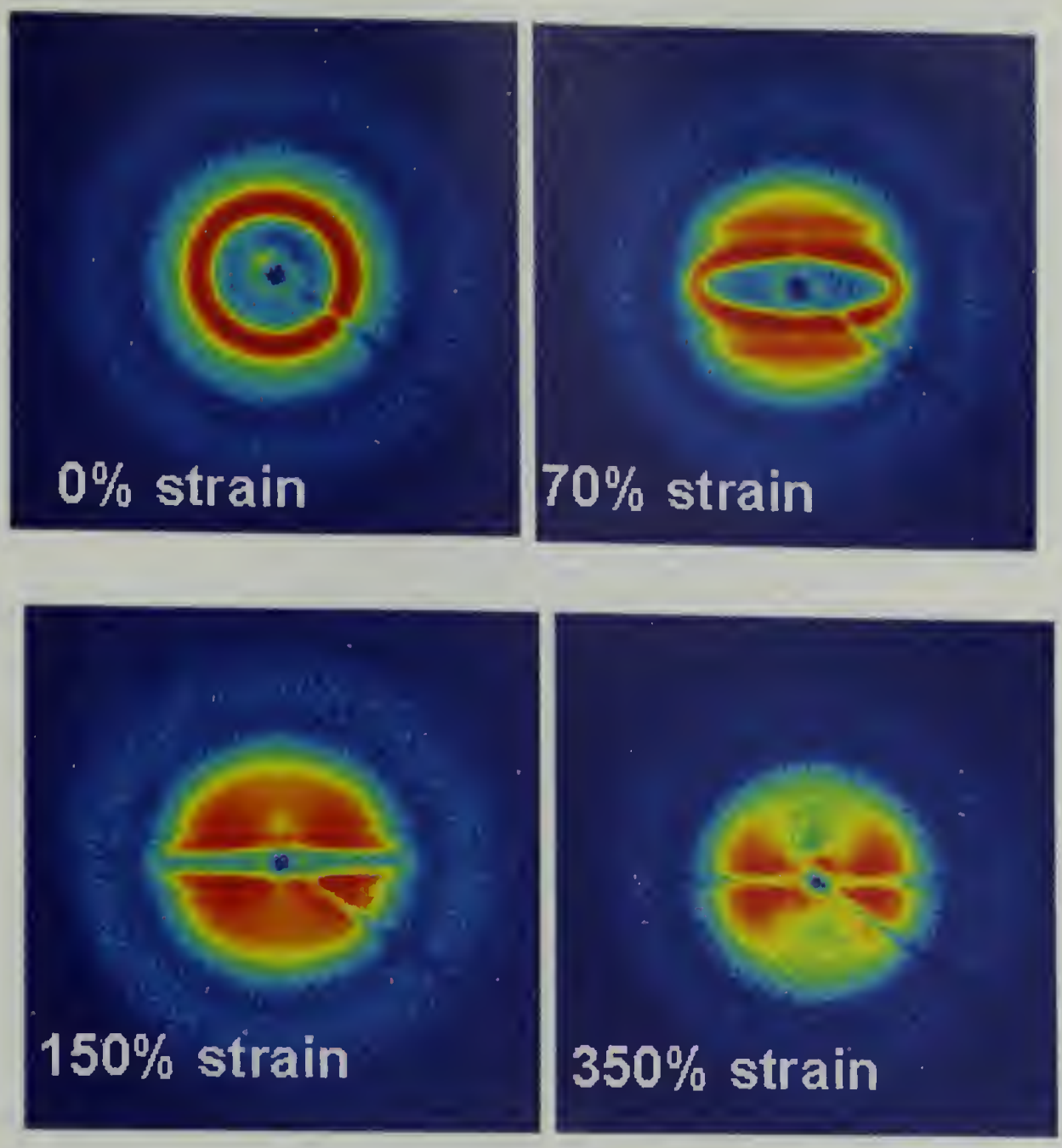

Figure 4.28 SAXD patterns at different strains on unoriented solution cast samples of S20B

In order to study the development of a structure with strain, SAXD experiments were performed onto oriented as well as unoriented samples of S20B. Oriented samples were obtained by extrusion and unoriented samples were obtained by solution casting. Figure 4.28 shows the SAXD patterns of S20B sample being stretched to different strains in a uniaxial test. As the strain increases, the initial isotropic hexagonal lattice changes into an ellipsoid and then changes into a four-point X-pattern at 70% strain.

Similar structural features were observed in the deformation behavior of isotropic S20E samples discussed in chapter 3 and are also in accordance with the observed deformation behavior of SBS/SIS systems [21,22]. However this system S20B does not strain crystallize and remains amorphous at all strains. In addition layer line spacings can be clearly noticed at 150% strain in SAXD patterns. Also the angle of X-cross pattern increases with strain. This suggests increased shear and rotation of micro-buckled PS cylinders into the stretching direction similar to that observed in S20E (chapter 3).

The deformation behavior of oriented extrudates can be observed by following the SAXD patterns in figure 4.29. Completely new features can be noticed in the reciprocal space SAXD patterns. There is no clear development of four point patterns as has been reported by other studies. The two-point pattern observed at 0% strain persists till very large strains with some broadening starting to occur in the two-point patterns. These results warrant further studies to understand the structural changes in morphology on deformation of oriented extrudates.

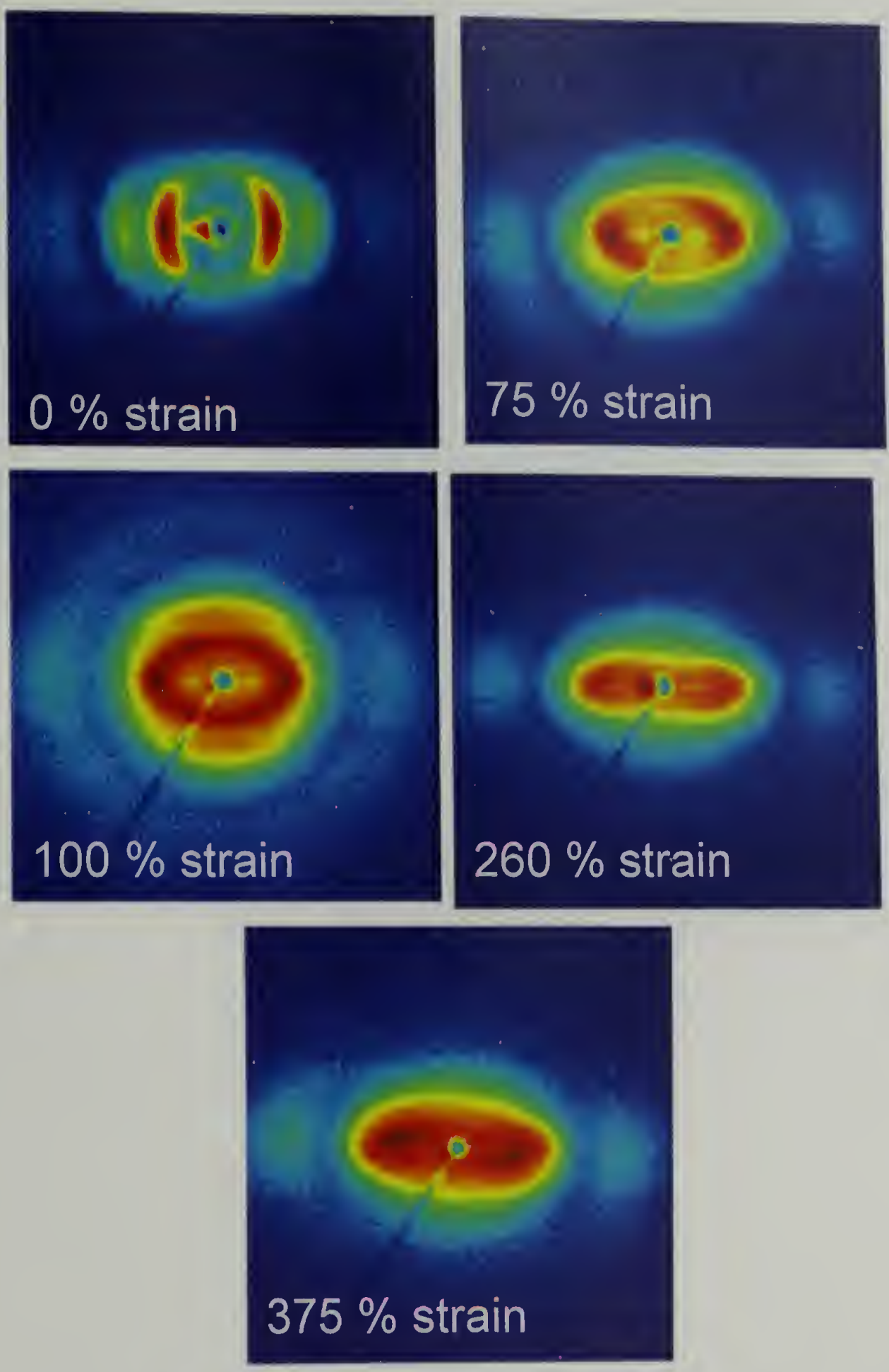

Figure 4.29 SAXD patterns at different strains on oriented extrudates of S20B

4.5 Conclusions

Extrusion process has been utilized to obtain ultra-long range order in certain SEBS block copolymer systems. The effect of ODT on the processing behavior of SEBS block copolymers has been elucidated. Calendering and compression molding techniques also introduce long-range orientation and order into block copolymer systems, albeit to a lower extent than extrusion process. The mechanical properties of such oriented systems have been compared to those of randomly oriented systems. Structural changes in morphology on the deformation of an isotropic, unoriented block copolymer have been compared to those obtained from deformation of oriented 'single crystal' like extrudates of SEBS block copolymers.

4.6 References

(1) Folkes, M. J.; Keller, A.; Scalisi, F. P. *Kolloid Z.* **1973**, *251*, 1-4.

(2) Folkes, M. J.;Keller, A. *Polymer* **1971**, *12*, 222-236.

(3) Folkes, M. J., Ed. *Processing, structure, and properties of block copolymers / edited by M.J. Folkes*; Elsevier Applied Science Publishers, 1985.

(4) Odell, J. A.; Keller, A. *Polym Eng & Sci* **1977**, *17*, 544.

(5) Arridge, R. G. C.; Folkes, M. J. *J. Phys. D: Appl. Phys.* **1972**, *5*, 344-360.

(6) Tarasov, S. G.; Godovskii, Y. K. *Vysokomolekulyarnye Soedineniya Seriya A* **1980**, *22*, 1879-1885.

(7) Tarasov, S. G.; Tsvankin, D. Y.; Godovskii, Y. K. *Vysokomolekulyarnye Soedineniya Seriya A* **1978**, *20*, 1534-&.

(8) Godovsky, Y. K. *Makromol. Chem. Suppl.* **1984**, *6*, 117-140.

(9) Pakula, T.; Saijo, K.; Kawai, H.; Hashimoto, T. *Macromolecules* **1985**, *18*, 1294-1302.

(10) Hadziioannou, G.; Mathis, A.; Skoulis, A. *Colloid. Polym. Sci.* **1979**, *257*.

(11) Morrison, F. A.; Winter, H. H. *Macromolecules* **1989**, *22*, 3533-3540.

(12) Scott, D. B.; Waddon, A. J.; Lin, Y.; Karasz, F. E.; Winter, H. H. *Macromolecules* **1992**, *25*, 4175-4181.

(13) Albalak, R. J.; Thomas, E. L. *J. Polym. Sci., Part B: Polym. Phys.* **1993**, *31*, 37-46.

(14) Honeker, C. C.; Thomas, E. L. *Chem. Mater.* **1996**, 1702-1714.

(15) Fairclough, J. P. A.; Salou, C. L. O.; Ryan, A. J.; Hamley, I. W.; Daniel, C.; Helsby, W. I.; Hall, C.; Lewis, R. A.; Gleeson, A. J.; Diakun, G. P.; Mant, G. R. *Polymer* **2000**, *41*, 2577-2582.

(16) Holden, G.; Legge, N. R.; Quirk, R.; Schroeder, H. E. *Thermoplastic Elastomers*, 2nd ed.; Hanser Publishers, 1996.

(17) Legge, N. R. *Rubb. Chem. Tech.* **1987**, *60*.

(18) Bening, R. C.; Handlin JR., D. L.; Sterna, L. L.; Willis, C., L.; US Patent Application Publication: USA, 2003.

(19) Agarwal, S. L. *Polymer* **1976**, *17*, 938-956.

(20) Bradford, E. B.; Vanzo, E. *J. Polym. Sci. : Part A-1* **1968**, *6*, 1661-1670.

(21) Huy, T. A.; Adhikari, R.; Michler, G. H. *Polymer* **2003**, *44*, 1247-1257.

(22) Honeker, C. C.; Thomas, E. L.; Albalak, R. J.; Hajduk, D. A.; Gruner, S. M.; Capel, M. C. *Macromolecules* **2000**, *33*, 9395-9406.

CHAPTER 5

MORPHOLOGICAL STUDIES AND MICROCELLULAR MODEL EVALUATION FOR DEFORMATION OF THERMOPLASTIC VULCANIZATE EPDM/I-PP BLENDS

The origins of elasticity in thermoplastic vulcanizates (TPVs) have been debated for the past decade. Previous modeling attempts using finite element analysis (FEA) provide numerical solutions that make assessment of constituent concentration and interactions unclear. Detailed morphological studies using scanning electron microscopy (SEM) and confocal microscopy provide evidence for TPV structure resembling microcellular foam. Based on these morphological observations, a microcellular modeling approach that takes into account composition and cure state information is proposed and evaluated herein to describe the steady-state behavior of dynamically vulcanized blends of ethylene-propylene-diene monomer (EPDM) and isotactic polypropylene (i-PP). Three types of deformation are accounted for: elastic and plastic deformation of i-PP, elastic deformation of EPDM, and localized elastic and plastic rotation about i-PP junction points. The proposed constitutive model's viability is evaluated in terms of i-PP concentration and EPDM cure state.

5.1 Introduction

Thermoplastic Vulcanizates (TPVs) are a special class of thermoplastic elastomers (TPEs) generated from synergistic interaction of an elastomer-thermoplastic blend. EPDM/i-PP Thermoplastic vulcanizates (TPVs) have a unique morphology due to the process of dynamic vulcanization[1-4]. This morphology has been investigated by

many authors [5-11] and consists of a chemically crosslinked EPDM rubber phase embedded within a continuous i-PP semicrystalline thermoplastic matrix. Even though the rubber phase is not continuous, dynamic vulcanizates behave elastically. The investigation of morphology using confocal microscopy is also a subject of study in this chapter. Over the past several decades, the origins of this elasticity have been debated and several finite element studies and constitutive models have been proposed. A primary limitation of these studies is that none clearly identify how composition and morphology influence deformational characteristics. Another problem with these studies is that each time a new formulation is devised, the FEM analysis needs to be performed again in order to predict its properties. This study presents and evaluates a new modeling approach to describe the steady-state deformation behavior of dynamically vulcanized EPDM/i-PP blends. An analytical expression is developed by combining concepts from microcellular solids with plastic hinge formation and strut yielding to approximate the deformational response of these elastomers. Contributions from i-PP concentration and EPDM cure state are included.

Two different modeling approaches to explain the micro-mechanisms of deformation of thermoplastic vulcanizates have recently been presented. In the first approach Kikuchi[12] and Okamoto[13] focus on the origins of elasticity of EPDM/i-PP thermoplastic vulcanizates under uniaxial tension with two-dimensional finite element modeling. Their results indicate that yielding in the thermoplastic matrix begins around the EPDM particles in an equatorial direction perpendicular to the applied load. The yielding then propagates around the embedded rubber particles shifting toward the loading direction. Upon considerable strain only i-PP polar ligaments remain unyielded.

These unyielded ligaments serve to connect the rubber domains and allow for recovery. Once significant strain has been imposed on the system that causes yielding of the polar ligaments, no elastic recovery takes place. While this model qualitatively describes elasticity for one loading condition, it does not take composition, cure state, molecular weight, domain size, domain shape, or domain polydispersity into account. This approach also requires a significant amount of i-PP inelastic deformation to produce large strains. This is a direct consequence of the imposed representative volume geometry and loading configuration.

In the second modeling approach, Boyce and coworkers[14-17] use finite element modeling to describe the micromechanisms of deformation and recovery in thermoplastic vulcanizates. Their simulations indicate that upon yielding a pseudo-continuous rubber phase develops due to the drawing of i-PP ligaments and shear of rubber particles. The initial matrix ligament thickness appears to control the initial stiffness and flow stress. They also observe that the majority of the matrix material does not deform during large deformations but undergoes rigid body motion as the pseudo-continuous rubber phase shears and contorts around the unyielded rigid matrix regions. Finite element simulations are also used to describe stress-softening of thermoplastic vulcanizates in plane strain compression[16]. The simulations indicate that additional compliance in the early stages of reloading is attributed to changes in the matrix/particle configuration induced during the initial loading cycle. The thinnest matrix ligaments are left in a configuration favorable for elastic bending and rotation upon reloading instead of additional plastic straining. These deformation modes occur at lower stress levels and would thus be responsible for increased compliance. After sufficient strain

occurs upon reloading, the tangent modulus increases indicating that a strain has been reached where the particle/matrix interaction now requires additional plastic straining of the i-PP ligaments.

The qualitative results of current modeling efforts are in marked contrast with one another. In one case, the majority of the i-PP matrix yields around the embedded rubber particles with the exception of unyielded ligaments at the particle poles due to lower stress concentrations. These unyielded polar ligaments connect the rubber domains and allow for elastic recovery[1,12,13]. In another case the majority of the i-PP matrix does not yield at all. Only the thin ligaments between particles yield while the rubber domains shear around the undeformed i-PP regions creating a pseudo-continuous EPDM phase[14-16]. Similar to finite element analysis, the proposed microcellular model also assumes an initial geometry and mode of failure. However, the microcellular model described below provides an analytical solution that includes terms for composition and morphology. An analytical solution is desirable to allow formulation design with specific properties in mind compared to experimental formulations.

5.2 Experimental Section

5.2.1 Materials used

EPDM/i-PP blends of various composition, cure state, and iPP molecular weight provided by Advanced Elastomer Systems were used in this study. Table 5.1 lists the six compounds examined where all compositions are given in weight percent. A hydrocarbon paraffin oil incorporated as a processing aid is also listed in the table. High

and low molecular weight i-PP are used in the formulations and is differentiated by melt flow rate (MFR) in accordance with ASTM D1238. Low, medium, and high EPDM cure states are also examined.

To accommodate all these variables and for ease of comparison, a simplified naming convention is adopted. The sample name consists of four letters in which the first letter refers to the majority volume fraction: P for iPP rich or E for EPDM rich. The second letter refers to the molecular weight of the iPP: H for high molecular weight or L for low molecular weight. The third and fourth letters refer to the extent of crosslinking of the EPDM rubber: XL for a low crosslinking density, XM for a medium crosslinking density, or XH for a high crosslink density. For example, PHXM is i-PP rich with high molecular weight i-PP and has a medium crosslink density of the EPDM rubber.

TPV	EPDM	i-PP	Oil	i-PP MFR	Cure state
PHXM	25%	50%	25%	0.7	Medium
PLXM	25%	50%	25%	20	Medium
EHXL	40%	20%	40%	0.7	Low
EHXM	40%	20%	40%	0.7	Medium
EHXH	40%	20%	40%	0.7	High
ELXH	40%	20%	40%	20	High

Table 5.1 EPDM/i-PP TPV compositions studied

Samples are compression molded into 3 mm thick plaques at 210 °C at a pressure of 3.5 MPa for approximately 20 minutes and then water-cooled.

5.2.2 Morphological characterization

A Leica® confocal microscope in reflection mode has been used to study the morphology of these TPVs. A stretching device for confocal microscopy has been built in order to study the in-situ deformation of the observed morphology.

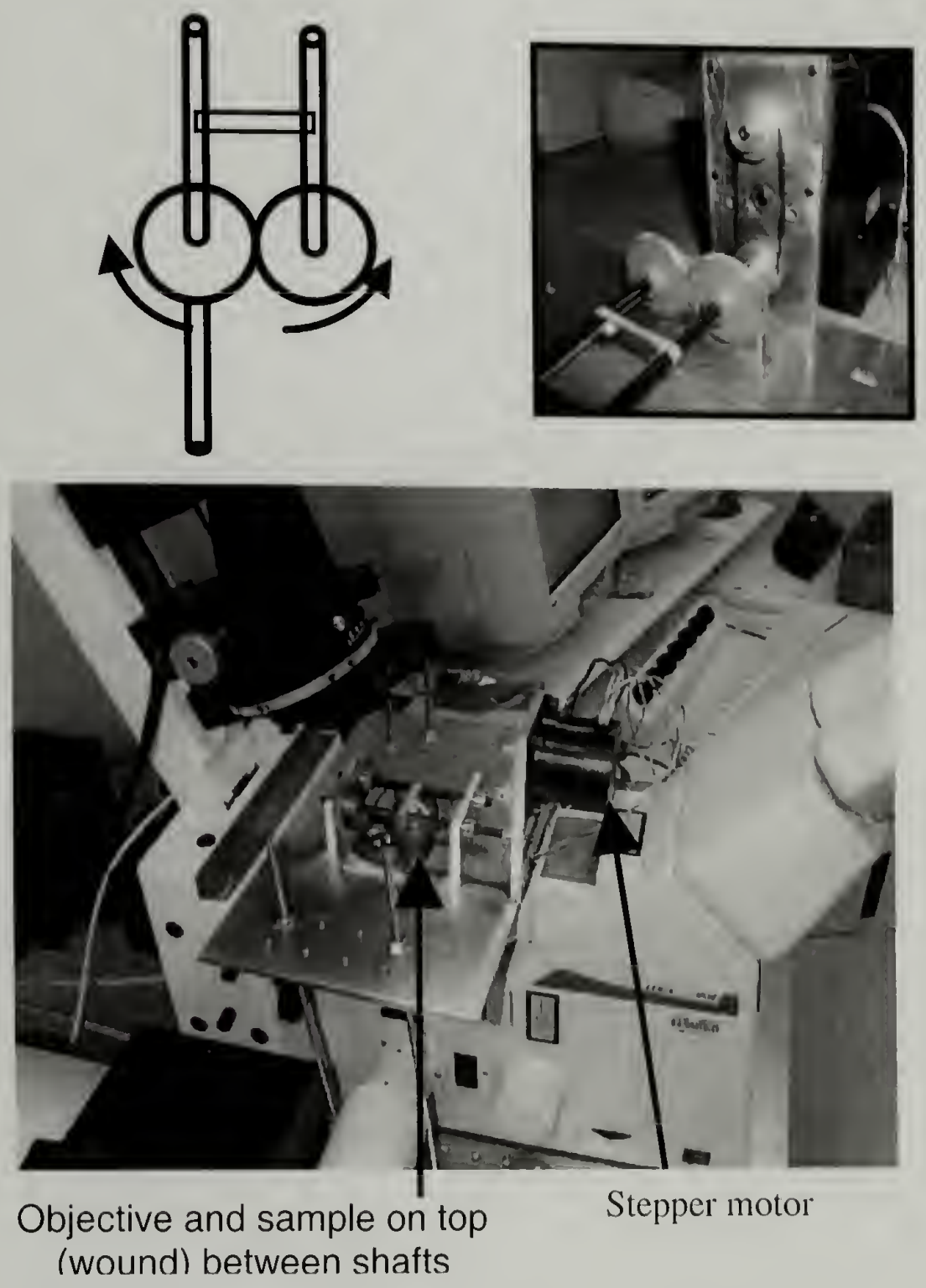

Figure 5.1 In-situ stretching device used for confocal microscopy

Figure 5.1 shows the schematic of the meshing-gear system used and photographs of the in-situ stretching device mounted in the confocal microscope. A meshing gear system driven by a stepper motor ensures that same point is focused on during stretch. Also large deformations can be attained in a small confined region.

5.2.3 Cyclic and uniaxial tensile testing

In order to evaluate the proposed model in terms of steady-state deformation the compositions are examined under cyclic loading. Tensile specimens are cut to an ASTM D638 type V geometry and tested on a servohydraulic Instron 8511. Specimens are gripped so that only the 7.62 mm gauge length is between the grips. This gripping geometry is used to measure strain more accurately than the traditional tab gripping. All samples experience the same loading condition. A ramp function, followed by 30 oscillatory sine waves and 30 triangular waves is imposed on the samples under displacement control. Various static offsets and amplitudes are examined with the condition that the material unloads to approximately zero stress during the fourth quarter of each sine and triangle wave. Since the current goal is to describe the steady-state behavior after removal of stress softening, only the 30^{th} sine and triangle wave are analyzed.

Pure i-PP resin of 0.7 and 20 MFR, virgin EPDM samples of various cure states were studied for their stress-strain behavior of using an Instron 1123. Tensile specimens are cut according to ASTM D638 on a Tensile Kut router in a type IV geometry.

5.2.4 Rheological testing

The shear behavior of crosslinked virgin EPDM samples is examined using an ARES Rheometric Scientific rheometer in a parallel plate geometry. A frequency sweep is performed and shear storage modulus is measured.

5.3 Morphological results

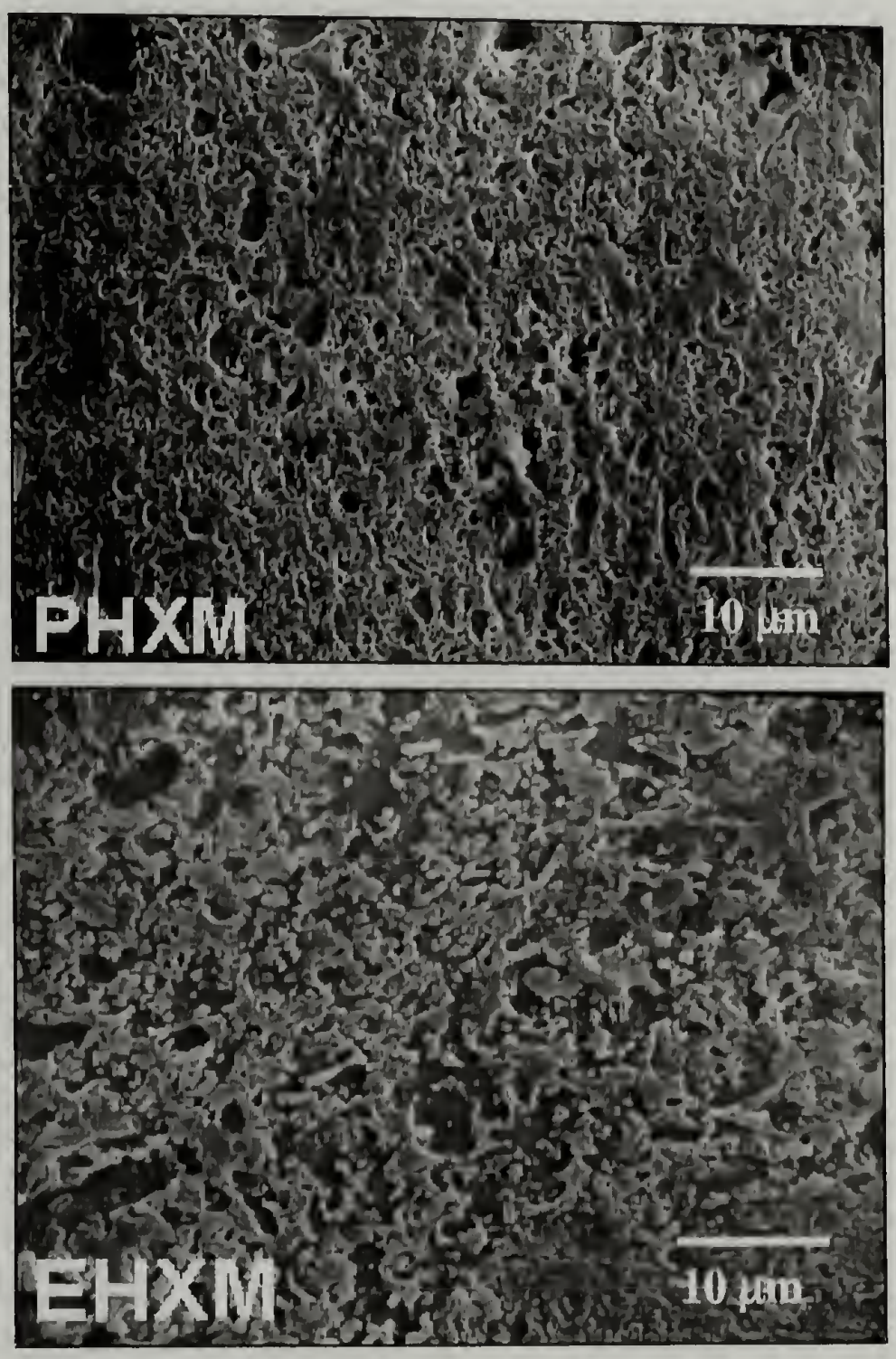

Figure 5.2 SEM images of PHXM and EHXM

The morphologies of dynamically vulcanized EPDM/i-PP blends have been studied previously[11] using scanning electron microscopy. The contrast for scanning electron micrographs is obtained by chemical etching using parmanganic acid. The parmanganic acid etches away EPDM rubber leaving raised regions of semicrystalline i-PP. The SEM images in figures 5.2 reveal a continuous i-PP structure irrespective of the composition. However, this etching process is not very selective. There is a possibility of amorphous regions of i-PP also getting etched by parmanganic acid. Since characterizing the initial morphology accurately is an important step in formulating an analytical model, confocal microscopy has been used to study the morphology of these systems extensively. Also in-situ deformation devices can be easily built for optical microscopy techniques than for electron microscopy techniques. The domain sizes of EPDM/i-PP TPVs fall in the optical range and hence are ideal candidates for confocal (optical) microscopy.

There is not sufficient contrast between these two phases in confocal microscopy due to close refractive indices of i-PP and EPDM phases and hence contrast enhancement techniques are necessary. Contrast in optical Microscopy can be usually enhanced by staining the sample i.e. altering the light absorbing qualities of components of the sample or by phase contrast i.e. using the refractive index changes in the sample. Since there is no refractive index difference between the two phases, phase contrast is not a viable option. Staining is the only possible approach for obtaining contrast for this TPV. Ruthenium tetroxide (RuO_4) is a common staining agent used in electron microscopy to enhance the electron density of stained regions. Changing the electron

density also changes the optical absorption characteristics of the sample. Hence RuO_4 staining has been used for generating optical contrast.

RuO_4 stains the amorphous EPDM domains very easily. In addition, studies[18] indicate that absorption of RuO_4 into crystalline regions of i-PP starts only after 10 hours of staining. Also studies[19] show that RuO_4 staining depends on the molecular mobility in the amorphous region and staining should be carried out above the Tg of the polymer. Thus staining at different temperatures has also been done to investigate the morphology. This technique also avoids etching away of domains as was done for SEM images.

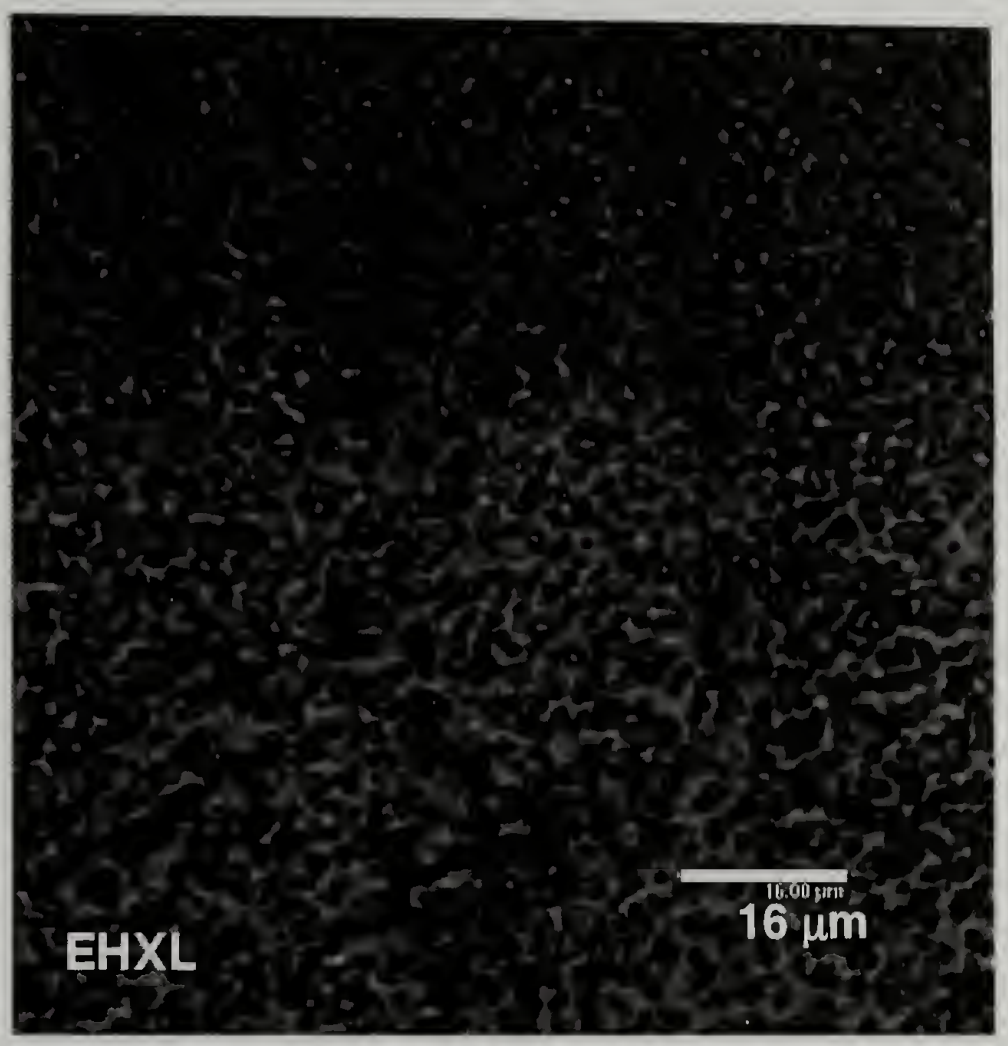

Figure 5.3 Confocal image of EHXL obtained by staining for 60 minutes

Figure 5.3 below shows the confocal microscopy image of EHXL in reflection mode obtained by staining in RuO_4 for 60 minutes. The darker domains represent EPDM rubber phases and the lighter regions indicate i-PP not affected by staining. This structure resembled the structure seen in SEM images shown in figure 5.2. The structure clearly shows that i-PP is the continuous phase and EPDM is the dispersed phase. In order to ascertain the extent to which amorphous regions of i-PP also get stained along with the EPDM domains, the staining has been done at temperatures between –10 ° C and 0° C. It has been shown that efficiency of RuO_4 staining depends on the molecular mobility in the amorphous region and staining should be carried out above the glass transition temperature of the polymer. EPDM has a T_g around –50° C, while polypropylene shows a T_g around 0° C. The images obtained for EHXM show that staining near 0° C reduces the overall mobility of RuO_4 staining and hence do not produce images as clear as those obtained at room temperature. Increasing the stain time to 3-4 hours did not produce any significant improvement in the images. Thus room temperature staining is ideal for producing the best contrast.

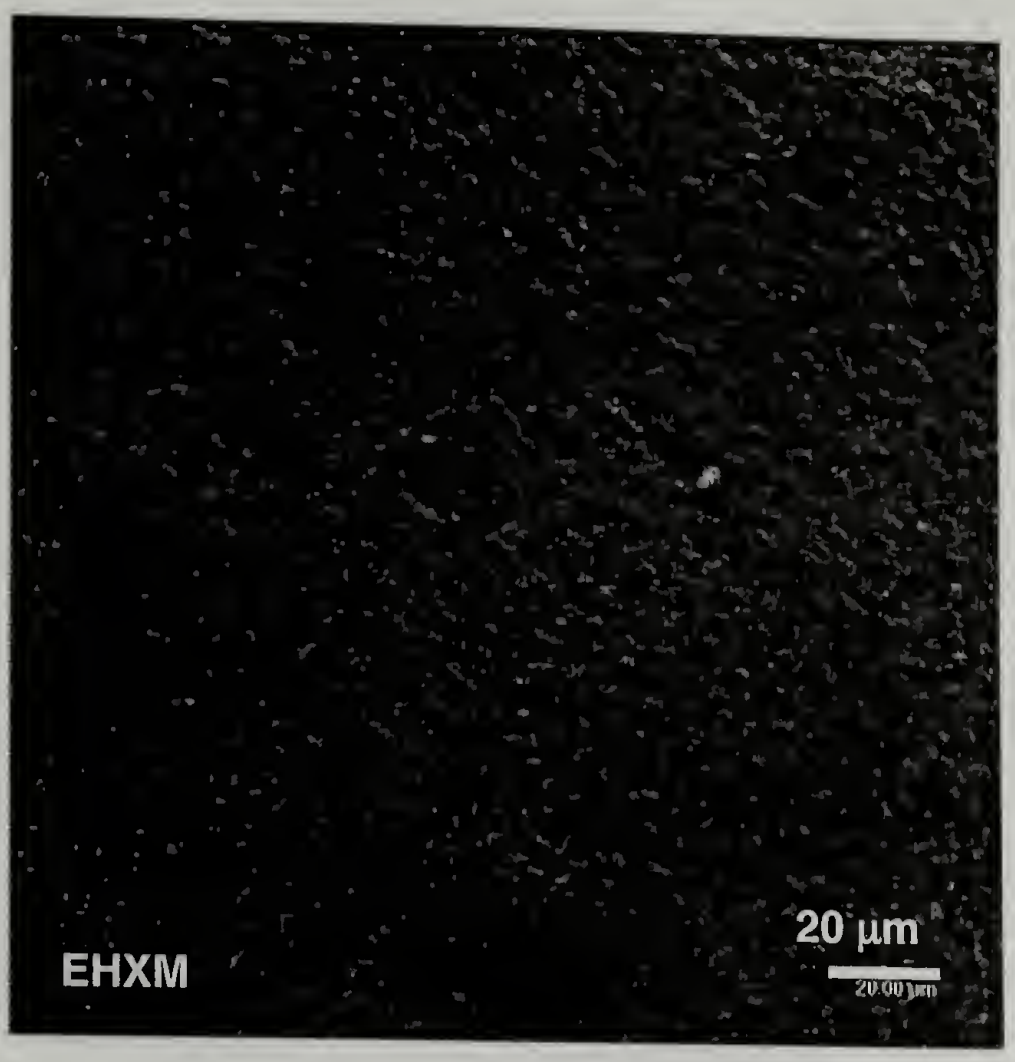

Figure 5.4 EHXM confocal image obtained by staining at -0° C

Figure 5.5 below shows the confocal microscopy image of ELXH in reflection mode obtained by staining in RuO_4 for 60 minutes. ELXH structure not only shows a continuous phase of i-PP, but also reveals a structure closely resembling that of a microcellular foam[20]. A microcellular foam made out of rigid polystyrene like material can extend to large deformations just because of its geometry[20,21]. This provides a clue as to whether the EPDM/I-PP TPVs extend to large deformations due to their structure resembling a microcellular foam. Instead of having air inside typical foam, EPDM/I-PP TPVs have filled EPDM domains inside the struts of isotactic polypropylene. The proposed model is based on this morphology of filled microcellular foam.

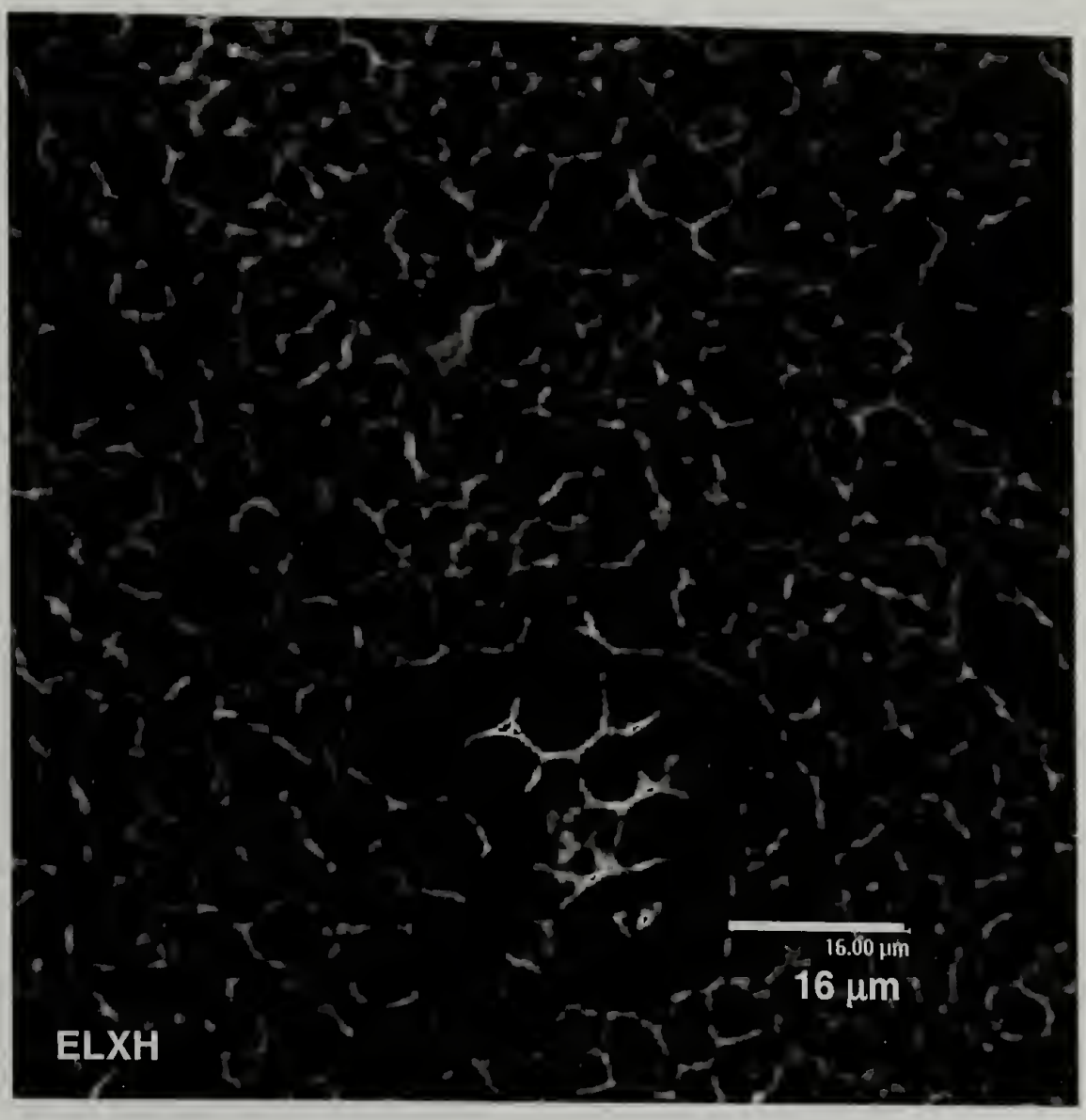

Figure 5.5 Confocal microscopy image of ELXH TPV

Deformation studies on these TPV systems using the in-situ stretching device for confocal microscopy indicate that the deformation is affine till very large deformations, similar to that expected from a filled microcellular foam.

5.4 Proposed Model

The first objective of the proposed model is to describe the steady-state loading and unloading of EPDM/iPP blends including contributions from composition and morphology. The second objective is to determine if the proposed model can be used to predict the steady-state behavior over a broad range of compositions.

Idealized strut models are typically used as a morphological tool to describe mechanical and physical responses of non-ideal microcellular geometries[20,21].The composite foam response is assessed in terms of strut geometry and intrinsic polymer properties. The collapse or failure mechanisms of microcellular foams generally occur in one of two forms, either through strut buckling or through the formation of localized plastic hinges at the strut junction points[20]. Both failure mechanisms were explored in developing the proposed microcellular model. Microcellular collapse through plastic hinge formation requires the least amount of energy and as such is incorporated in the deformation response. One would expect a viscoelastic material to dissipate energy to different degrees when exposed to various loading rates. Figure 5.6 illustrates the irreversible work exhibited under two loading conditions for EHXM. Triangular loading deforms the materials at a constant strain rate while sinusoidal loading applies a constantly changing strain rate. It is evident that the hysteresis exhibited by EPDM/iPP vulcanizates is similar under these two loading conditions. Therefore, it can be assumed that some mechanisms other than viscoelasticity are responsible for dissipation in these systems. In the proposed model, the work required to rotate the plastic hinges provides a possible mechanism for dissipation. The origins of elasticity from a microcellular analysis arise from a competition between the restoring force of the elastically deformed rubber and iPP struts and the strain energy necessary to rotate the plastic hinges. The proposed model may also capture geometrical strain hardening to some degree due to alignment of the struts as the hinges rotate and the struts align into a parallel configuration.

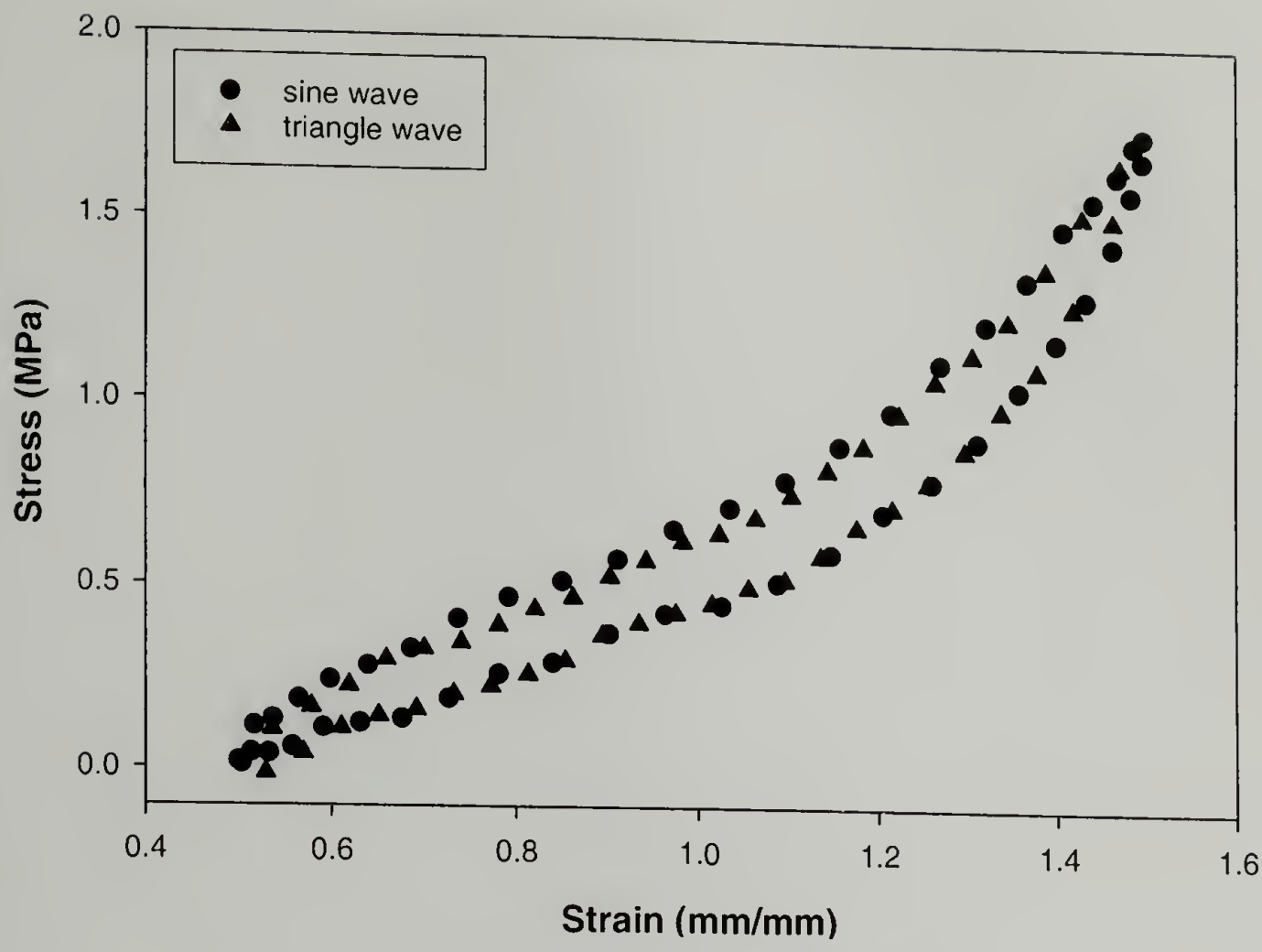

Figure 5.6 Cyclic loading for EHXM: Sine and triangular waves

By imposing a microcellular representative volume element (RVE) and ensuing deformation, the proposed model will have some of the same limitations as finite element analysis: the geometry and kinematically admissible displacement field are both prescribed and the displacement may not be a lower bound solution. However, an analytical solution will result allowing the microcellular model to be used as a formulation tool.

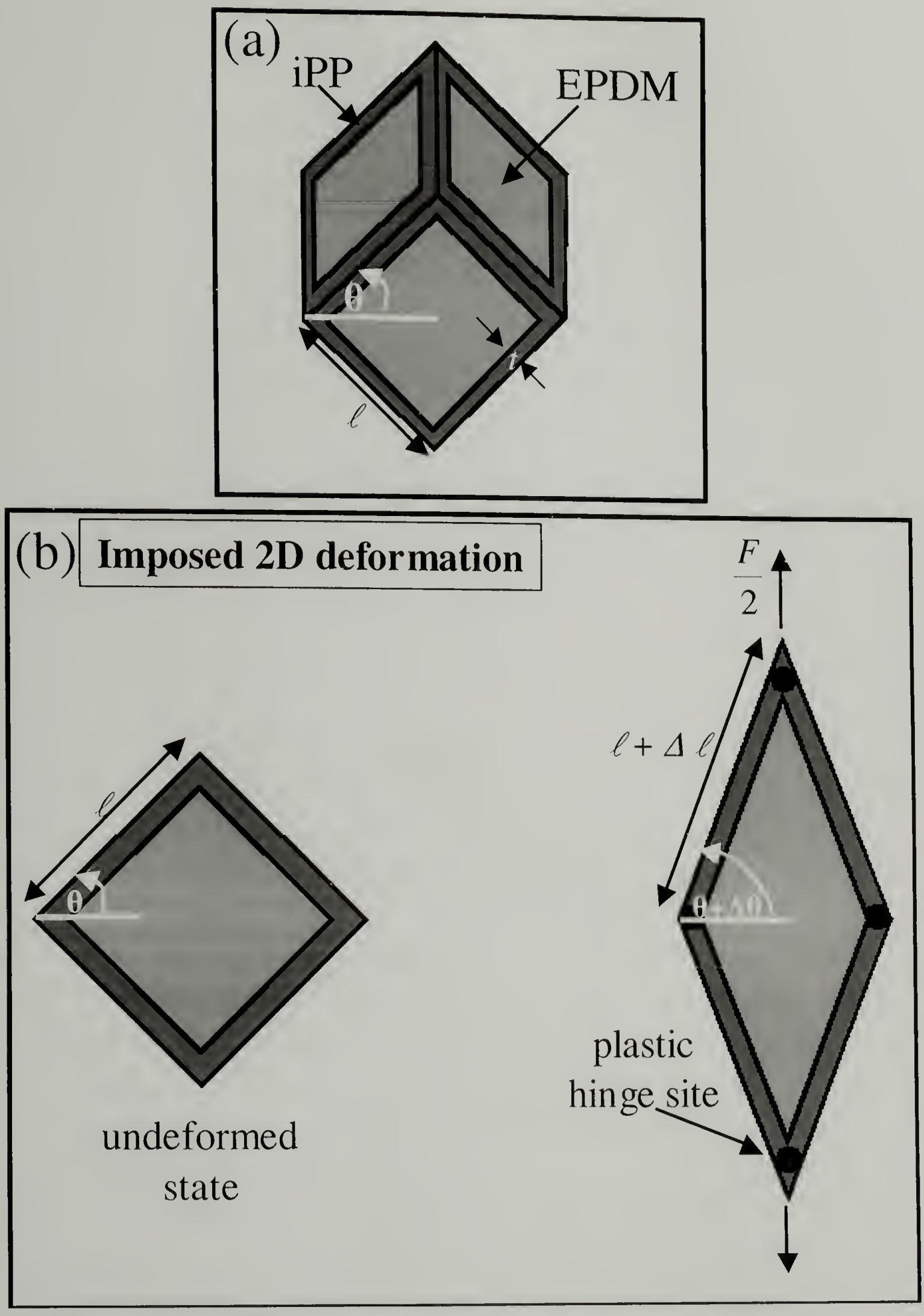

Figure 5.7 RVE of a filled foam and its uniaxial deformation

The RVE is shown in figure 5.7 a where the morphology is considered as a *filled* foam; the foam struts are regions of i-PP and the foam interstices are filled with EPDM rubber. In this geometry, t is the strut thickness, ℓ is the strut length, and 2θ is the angle at the junction of two i-PP struts. For a microcellular geometry, the volume fraction of strut material (C) is directly proportional to the strut density (S) as well as the square of the thickness to length ratio given by equation 1[20].

$$\frac{V_{pp}}{V_{Tot}} = S\left(\frac{t}{l}\right)^2 = C \qquad (1)$$

A two-dimensional uniaxial deformation is imposed on the RVE as shown in figure 5.7 b. Three types of deformation are included in the proposed microcellular model: elastic deformation of the EPDM, elastic and plastic deformation of the i-PP struts, and localized elastic and plastic rotation at the strut junction points through the formation of plastic hinges.

A complete derivation of the microcellular model is given in the appendix. However, the final expressions for extension and far-field stress are discussed below. An expression for the axial strain in an i-PP strut is expressed by equation 2 where i-PP modulus (E), EPDM shear modulus (G), and far-field stress (σ_∞) are variables.

$$\varepsilon = \frac{S}{EC}\left\{\left[\frac{\sqrt{2}}{4}\sigma_\infty - \frac{(1-C)^{2/3}}{2}G\tan(\theta - \pi/4)\right]\left[\frac{1}{\sin\theta}\right] \mp 2m\left(\frac{C}{S}\right)^{3/2}\cot\theta\right\} \qquad (2)$$

The first term in equation 2 is due to deformation of i-PP struts. The second term is due to shear deformation of the EPDM. The third term of equation 2 is due to localized hinge rotation at the strut junction points. The minus sign is used for loading

and the plus sign for unloading. The normalized rotational moment (m) will have two values: one corresponding to initial deformation that is within and elastic regime (m_e) and one corresponding to high levels of deformation within the plastic regime (m_p). In the plastic regime, rotation occurs through the formation of plastic hinges. These values of m are given by equation 3 where the first term corresponds to m_e and the second corresponds to m_p.

$$m = \begin{Bmatrix} \alpha\sqrt{\frac{C}{S}}E(\theta - \pi/4) \\ 1/4\,\sigma_y \end{Bmatrix} \qquad (3)$$

In equation 3, α is a factor that defines the degree of constraint on the struts and its value determines when plastic hinges form. σ_y is the yield stress of the i-PP ligaments, and all other terms are as defined previously.

An expression for the far-field stress can be written as in equation 4; where now the plus portion refers to the loading curve while the minus portion refers to the unloading curve.

$$\sigma_\infty = \sqrt{2}\left\{\frac{2EC\sin\theta}{S}\left(\frac{1}{\sqrt{\sin 2\theta}} - 1\right) + (1-C)^{2/3} G\tan(\theta - \pi/4) \pm 4m\left(\frac{C}{S}\right)^{3/2}\cos\theta\right\} \qquad (4)$$

The corresponding uniaxial extension ratio is expressed by equation 5.

$$\lambda = \sqrt{2}(1+\varepsilon)\sin\theta \qquad (5)$$

At large deformations the i-PP struts undergo plastic yielding. As such, the deformation response of the blend will have a history dependence on the elastic strain. As such it is necessary to calculate the imposed strain in relation to the maximum

previous strain. This can be accomplished using equation 6 where ε' is the new strain after a maximum previous extension of ε_f.

$$\varepsilon' = \frac{\frac{\sigma_y}{E} + \varepsilon - \varepsilon_f}{1 + \varepsilon_f - \frac{\sigma_y}{E}}$$

The microcellular model described above results in an analytical solution that includes terms for i-PP concentration (C) and EPDM cure state (G). Morphological terms such as domain size are mathematically eliminated from the equations for far-field stress and total extension. However, if the processing conditions remain constant, domain size is directly related to composition by equation 1. Morphological studies indicate that TPV structure is directly related to cure state as well as i-PP concentration. In addition, it can be observed that the morphology is also independent of i-PP molecular weight.

5.5 Model Evaluation

In order to evaluate the proposed microcellular model in terms of the steady-state deformational characteristics, it is first necessary to understand how the various compositional parameters influence this behavior. Figure 5.8a, 5.8b, and 5.8c show steady-state hysteresis loops as a function of i-PP volume fraction, EPDM cure state, and i-PP molecular weight, respectively. It is evident from Figure 5.8a that i-PP volume fraction is the compositional parameter that influences hysteresis and strain hardening to the greatest degree. Figure 5.8b shows that as cure state increases, the amount of irreversible work increases slightly as does the strain hardening response. Of the available compositions listed in Table 1, EHXL is the only composition with a low

cure state. However, EHXL has poor fatigue life and as such a steady-state response cannot be reached prior to failure. i-PP molecular weight has very little affect on the overall steady-state response as seen in Figure 5.8c. As such, its influence on steady-state behavior is not incorporated into the proposed model.

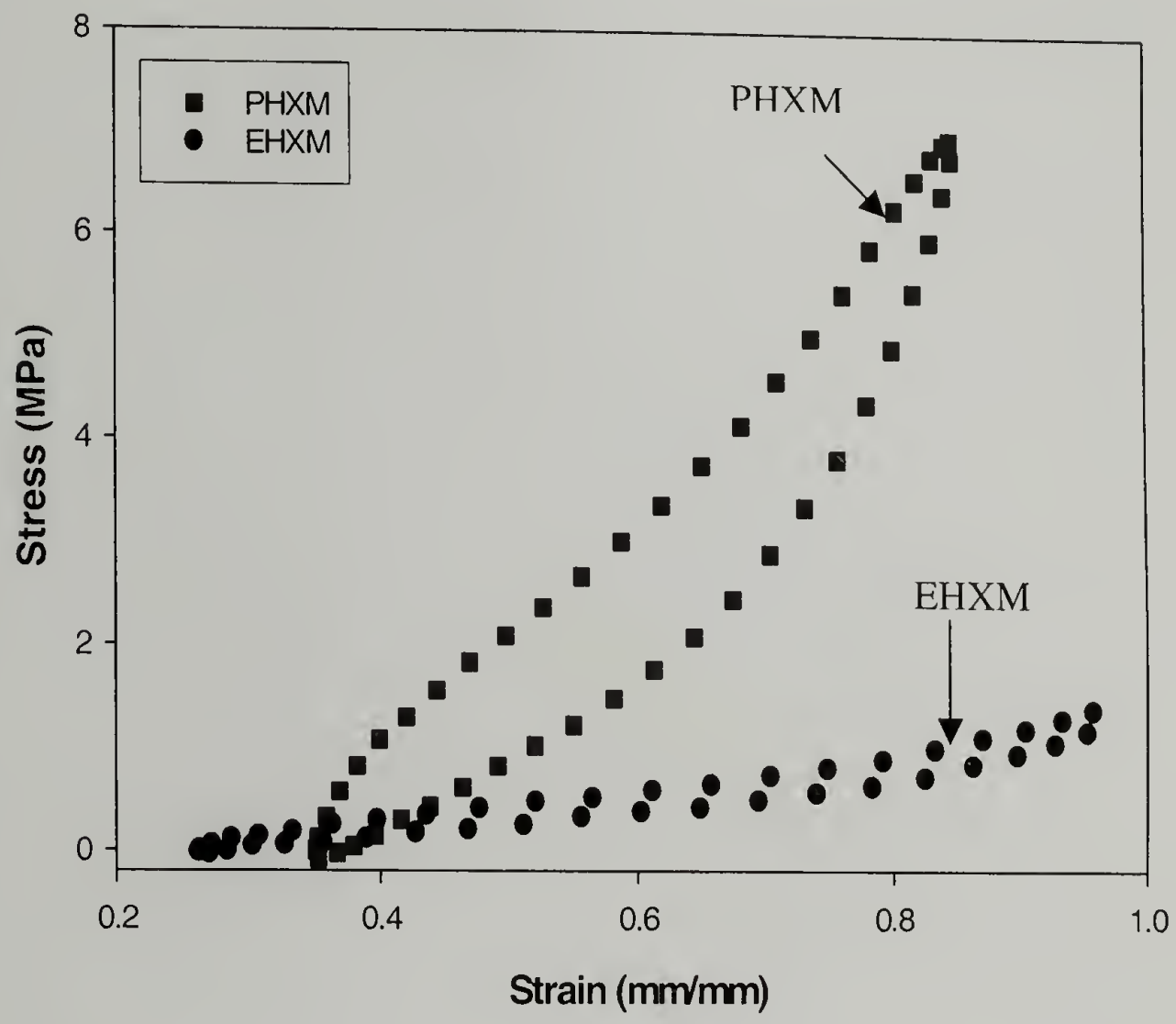

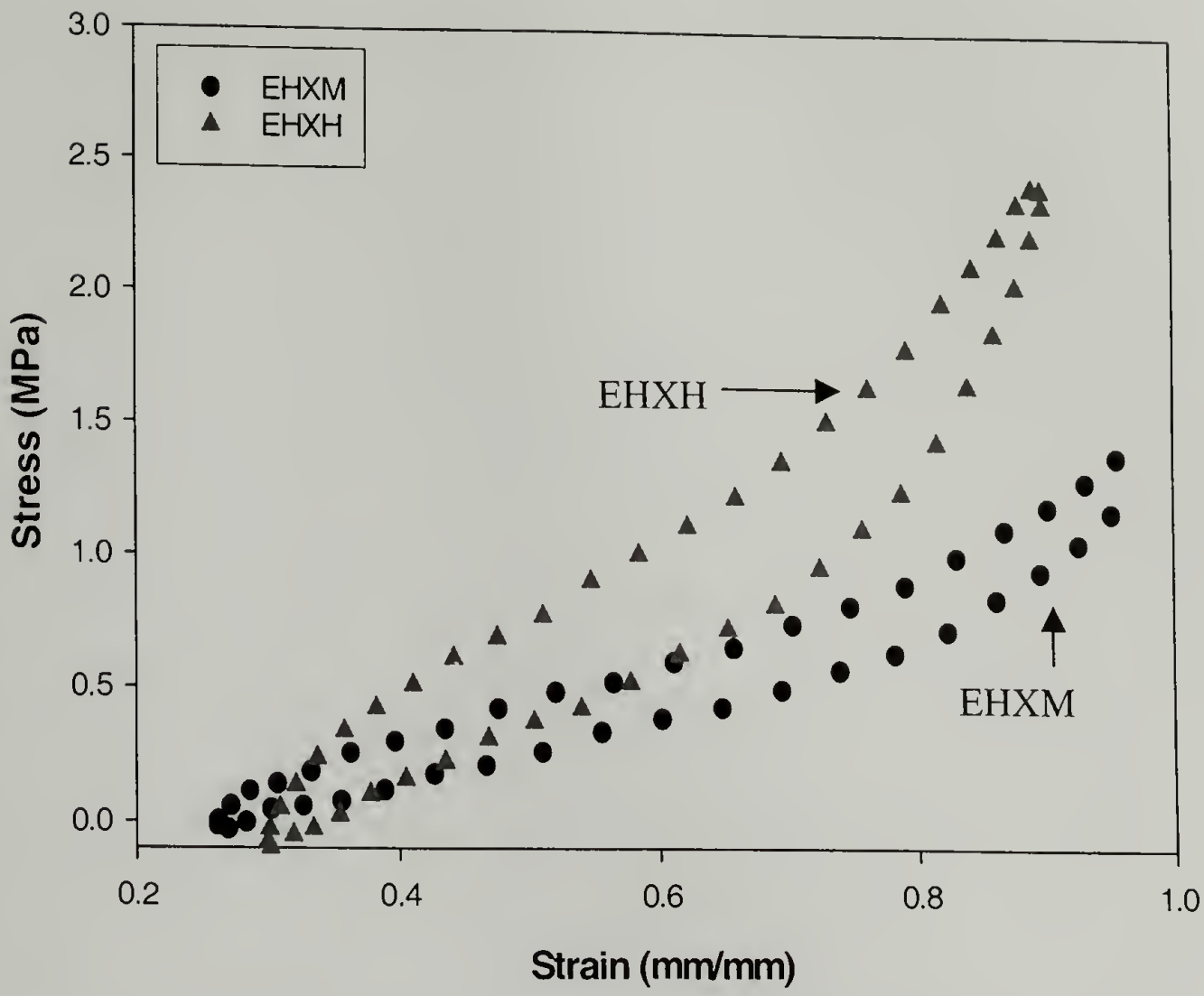

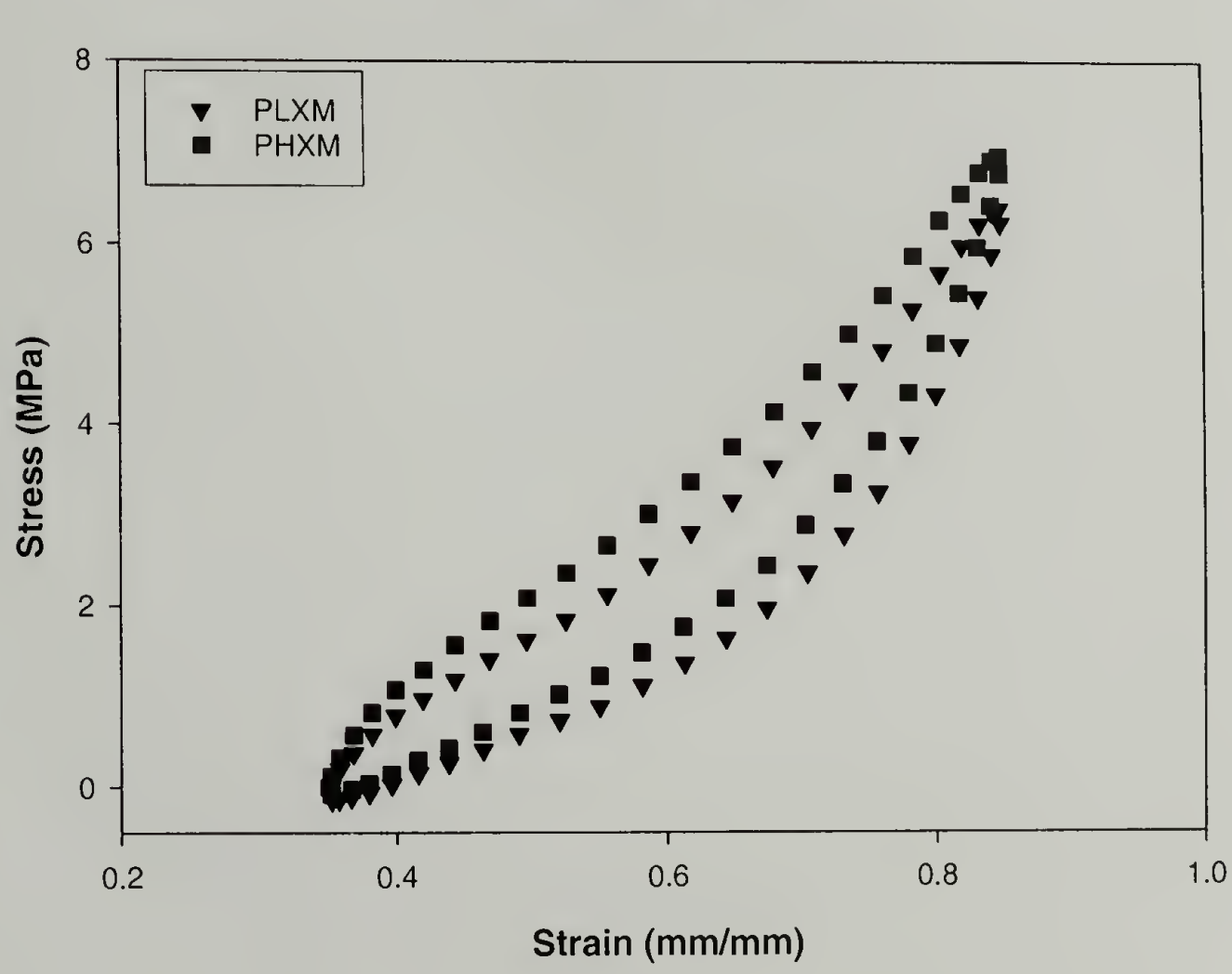

Figure 5.8 Steady state hysteresis loops of EPDM/i-PP TPVs

Table 2 lists the material properties of interest for the constituent materials. The stiffness and yield stress of neat i-PP is independent of molecular weight within experimental error. The shear moduli of crosslinked virgin EPDM samples all have similar values. Presumably the shear modulus should be a function of cure state; however, this is not observed for the limited amount of sample provided. As a result the constituent properties used in the model simulations are as follows: E = 200 MPa, σ_y = 35 MPa, and G = 0.2 MPa and G = 0.25 for medium and high crosslinking densities, respectively. It has been shown that the paraffin oil has an equal affinity for the EPDM and amorphous i-PP regions and as such it is ignored when estimating i-PP concentration. Since volume fraction cannot be measured due to the presence of the processing oil, concentration values are estimated as C = 0.33 and C = 0.67 for EPDM rich and i-PP rich blends, respectively. The factor α determines the amount of constraint on the system and affects when plastic hinges form; in all cases a α value of 100 is used.

Constituent	E_P (MPa)	σ_y (MPa)	G' (MPa)*
0.7 MFR i-PP	192	36	----
20 MFR i-PP	170	36	----
EPDM low cure	----	----	0.21
EPDM medium cure	----	----	0.15
EPDM high cure	----	----	0.20

* values obtained at 1 Hz.

Table 5.2 Material properties of pure i-PP and EPDM rubber systems

Four experimental steady-state hysteresis loops for PHXM are shown in figure 5.9 as the open symbols.

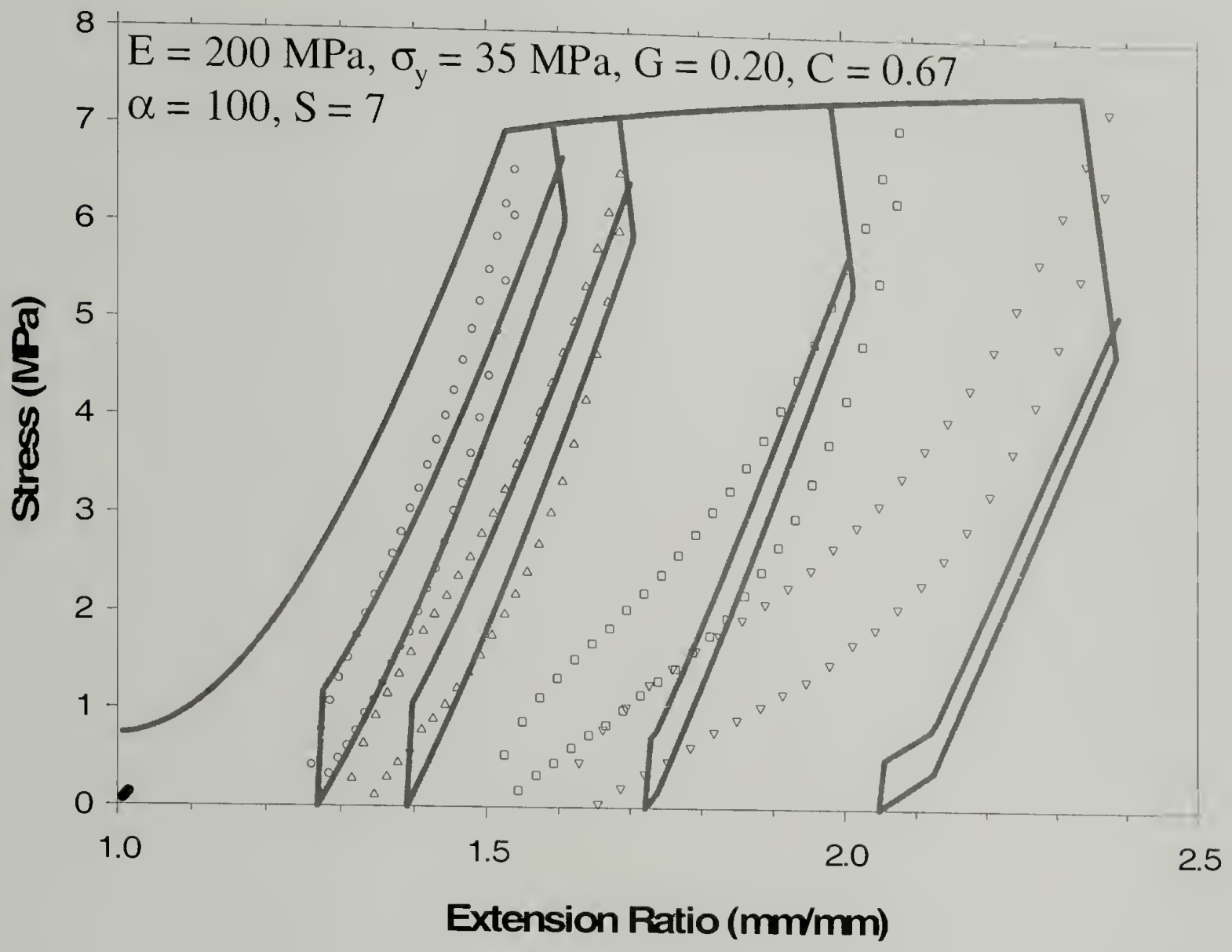

Figure 5.9 Comparison of experimental steady state behavior with that predicted by the microcellular model for PHXM

The solid curves are the predicted stress-strain response calculated from the microcellular model using S = 7. A strut density of 7 corresponds to a non-cubic representative volume element. Three slopes are observed upon unloading and two upon reloading. The initial negative unloading slope is due to reversal of direction at the plastic hinge sites. The following positive unloading slope occurs after the hinges have rotated back and now the i-PP struts are unloading elastically. The next inflection

point occurs when the i-PP struts are placed in compression and there is competition between the compressive force on the struts and lateral expansion of the rubber phase. Some general observations can be made regarding the modes of deformation by comparing the experimental stress-strain curves with those calculated from the microcellular model.

The stiffness, critical stress, and permanent deformation are predicted reasonably well at low strains ($\lambda < 1.7$). In this regime, the irreversible work is also estimated reasonably well. However at high strains, the predicted stress-strain response is very different from that observed experimentally. Very little hysteresis and a higher degree of permanent deformation are predicted. Overall, the strain hardening response in terms of the stress upon unloading is predicted reasonably well however this trend is lost upon reloading. It appears that for an i-PP rich composition the predicted response at large strain is more highly dominated by i-PP strut deformation than is observed experimentally. As such, it can be deduced that not all of the i-PP is in the form of deformable struts. In fact there may be a large amount of dead volume or regions of i-PP merely undergoing a rigid body motion instead of inelastic deformation.

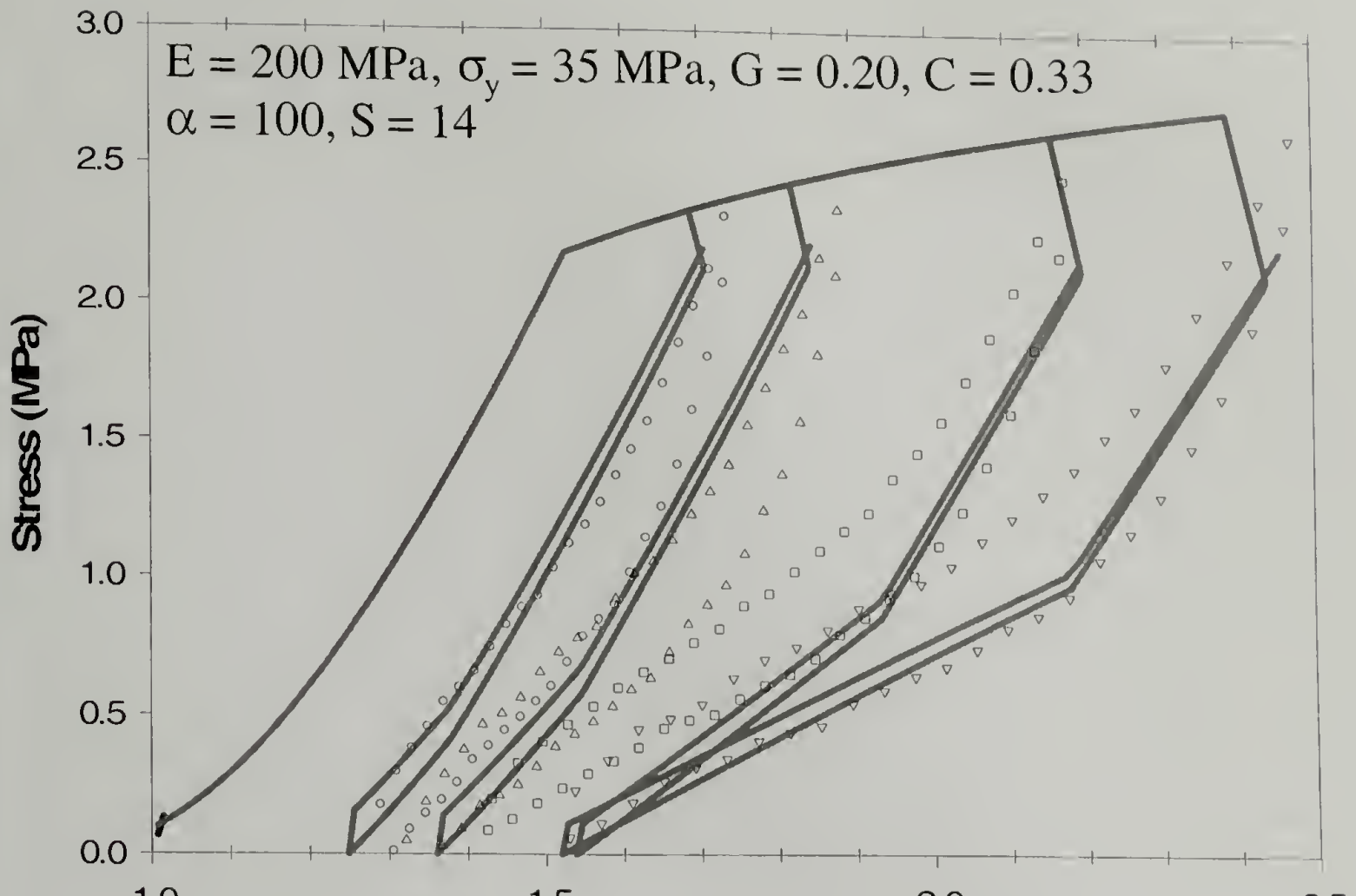

Figure 5.10 Comparison of experimental steady state behavior with that predicted by the microcellular model for EHXM

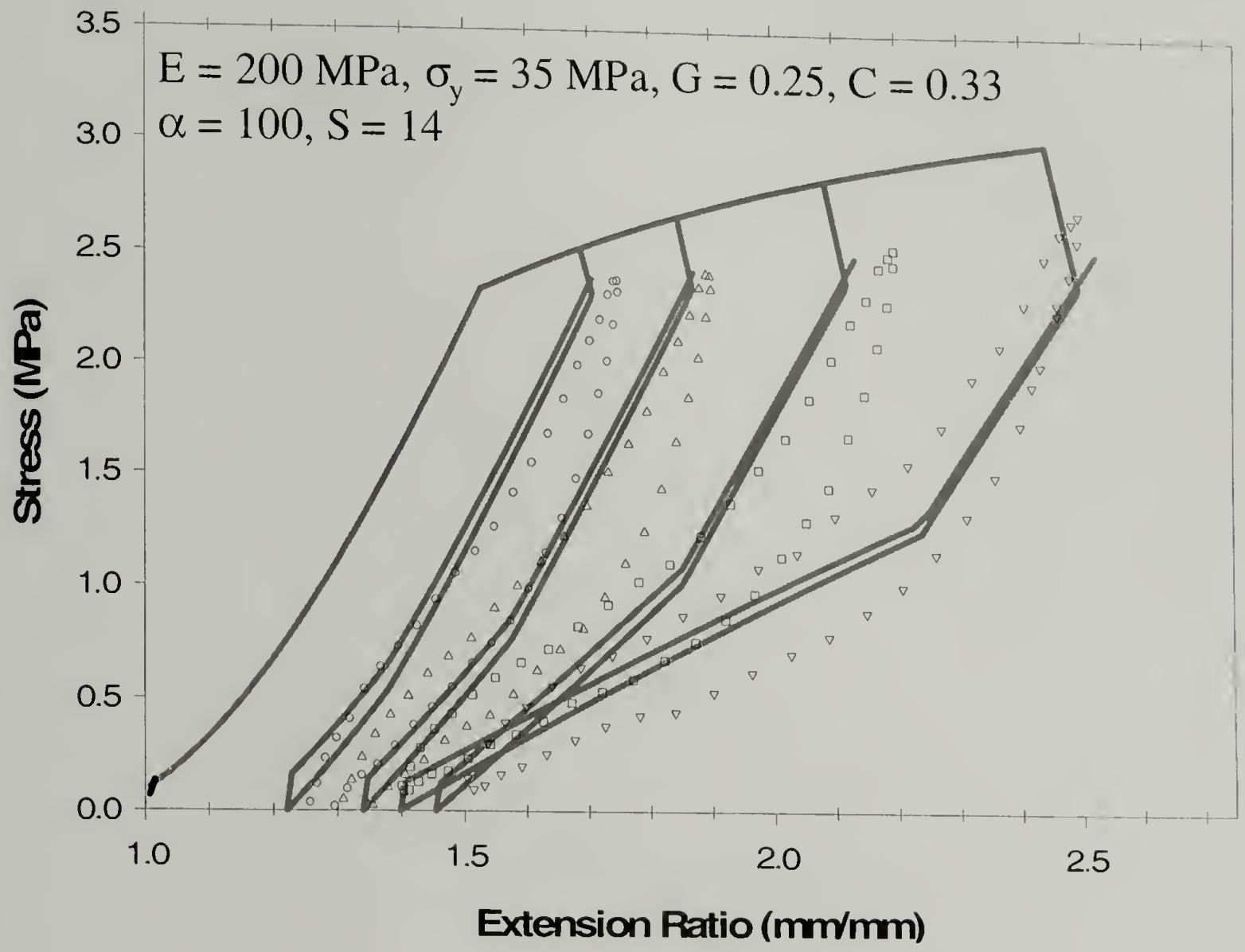

Figure 5.11 Comparison of experimental steady state behavior with that predicted by the microcellular model for EHXH

Similar steady-state hysteresis loops for EHXM are shown in Figure 5.10. The open symbols again represent data at four strain amplitudes. The solid curves are predictions calculated from the microcellular model with S = 14. A strut density of 14 represents a volume element close to a cubic structure, as S would equal 12 for a true cubic structure as drawn in figure 5.7a. For the EPDM rich material, the predicted stress-strain response is much closer to that observed experimentally. The critical

stress, permanent deformation, and stiffness are all approximately reasonably well at small and large strains. The experimental hysteresis loops exhibit two slopes. The slope/ stiffness is predicted reasonably well. The model indicates that the higher stiffness is due to deformation of the i-PP struts while the lower stiffness is due to deformation of the rubber domains. The strain hardening response in terms of the critical stress upon unloading is due to the deformation of the rubber domains as EHXM exhibits a much higher degree of strain hardening than does PHXM. However, at all strains the magnitude of irreversible work or hysteresis is not capture by the proposed model. Figure 5.11 shows the same type of analysis for EHXH. Again, the critical stress, permanent deformation, and stiffness are predicted reasonably well while irreversible work is not captured. However, by adjusting the shear modulus commensurately with an increase in crosslinking density, very little difference is observed in terms of the experimental and predicted responses.

The proposed microcellular model can provide insight regarding the mode of deformation when the deformation is dominated by the rubber phase. However, when the majority of the deformation occurs in the i-PP struts, as in PHXM, the predicted stress-strain response becomes very inaccurate at large deformation. In all cases the magnitude of irreversible work is not captured. The objective of developing an analytical model was to be able to predict the steady-state behavior over a range of compositions. However, this is not achieved as the proposed microcellular model does not capture the response for i-PP rich systems upon large deformations. As such this approach does not reveal how composition and morphology influence the deformation characteristics any more than do previous finite element studies. It appears that at high

levels of i-PP concentration, the model predicts too much deformation in the i-PP struts and not enough deformation in the EPDM. As such, it is apparent that not all of the i-PP deforms. It is possible that there is a considerable degree of dead volume or i-PP that is simply undergoing rigid body motion similar with the findings of Boyce and coworkers.

5.6 Conclusions

Morphological studies prove that the structure resembles a 'filled' microcellular foam. Based on these observations, a microcellular model has been developed that qualitatively describes some aspects of the steady-state deformation of EPDM/ i-PP blends. The imposed deformation includes: elastic deformation of the rubber phase, elastic and plastic deformation of the i-PP struts, and localized elastic and plastic rotation of the i-PP junction points. The model predicts the critical stress, permanent deformation, and stiffness for EPDM rich compositions at all strains tested and i-PP rich compositions only at small strains. The proposed model does not capture the amount of irreversible work at any level of deformation or for any i-PP concentration. The strut density appears to be related to i-PP concentration; as i-PP concentration is doubled the strut density must be reduced by a factor of two in order to obtain agreement with experimental data. The proposed model results in an analytical solution that includes compositional information. However it does not indicate how composition and morphology influence deformational characteristics to any greater degree than previous finite element studies.

5.7 Appendix – Microcellular Model Derivation

Three types of deformation are accounted for in the proposed model: elastic deformation of the EPDM, elastic and plastic deformation of the i-PP struts, and localized elastic and plastic rotation at the strut junction points through the formation of plastic hinges. Derivation of the microcellular model is based on the representative volume element (RVE) shown in Figure 5.7a where t is the strut thickness, ℓ is the strut length, and 2θ is the angle at the junction of two i-PP struts. For microcellular geometry, the volume fraction of strut material (C) is directly proportional to the strut density (S) as well as the square of the thickness to length ratio given by equation A1[20,21].

$$\frac{V_{pp}}{V_{Tot}} = S\left(\frac{t}{\ell}\right)^2 = C \qquad (A1)$$

A two-dimensional uniaxial deformation is imposed on the RVE as shown in Figure 5.7b. The total force acting on the RVE is given by equation A2 where σ_∞ is the far-field stress and $\sqrt{2}\ell^2$ is the cross-sectional area of the RVE center plane.

$$F = \sigma_\infty \sqrt{2}\ell^2 \qquad (A2)$$

A free body diagram of one strut is shown in Figure A1 where F is the total force acting on the RVE, T is the shear force acting on the elastomer, M is the rotational moment about hinge sites, and F_{x1}, F_{x2}, and F_y are unknown reaction forces. F_y and F_{x1} are determined as in equations A3 and A4, respectively.

$$\Sigma F_y = 0 \qquad F_y = \frac{F}{4} - \frac{T}{2} \qquad (A3)$$

$$\Sigma M_B = 0 \qquad F_{x1} = \frac{T}{2} - F_y \cot\theta + \frac{2M}{\ell \sin\theta} \qquad (A4)$$

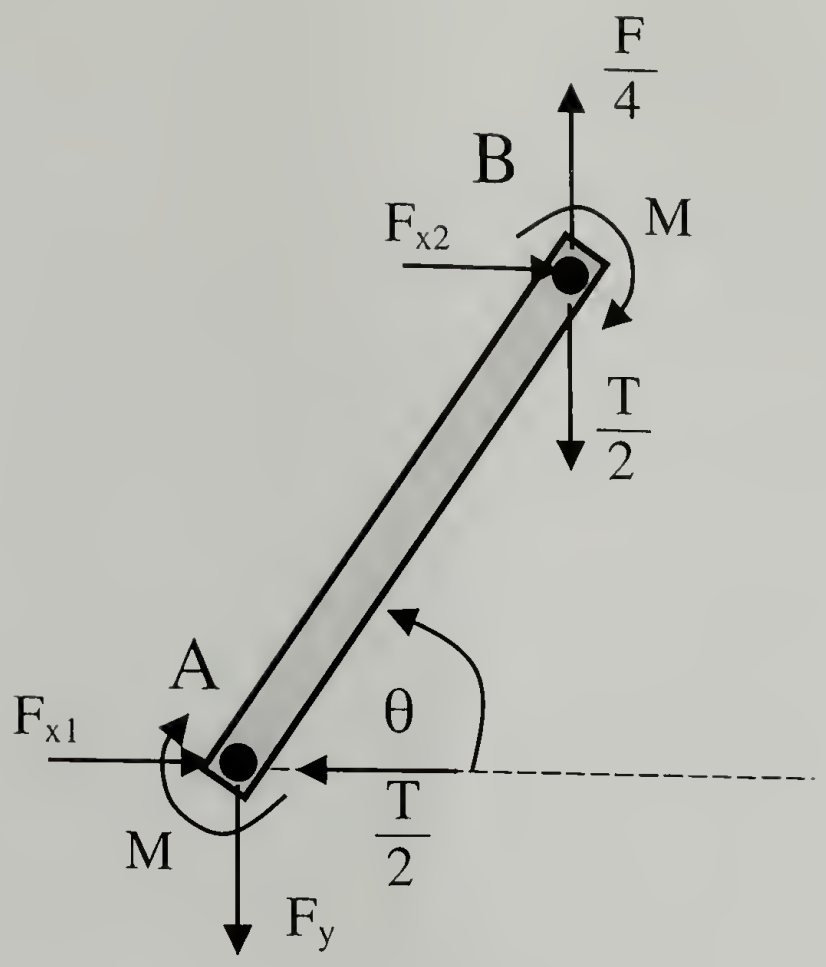

Figure A1 Free body diagram of a strut

The axial force acting on the strut at point A is given by equation A5.

$$F_a = \left(\frac{T}{2} - F_{x1}\right)\cos\theta + F_y \sin\theta \qquad (A5)$$

By combining equation A3, A4, and A5, the axial force acting on a strut becomes:

$$F_a = \left(\frac{F}{4} - \frac{T}{2}\right)\left(\frac{\cos^2\theta}{\sin\theta} + \sin\theta\right) - \frac{2M}{\ell}\cot\theta \qquad (A6)$$

The shear force on the elastomer is given by equation A7 where G is the shear modulus of the EPDM, $\tan(\theta - \pi/4)$ is the shear strain, and $(1-C)^{2/3}$ is the area fraction of elastomer.

$$T = (1-C)^{2/3}\,\ell^2 G \tan(\theta - \pi/4) \qquad (A7)$$

An expression for the axial strain in a strut is given by equation A8.

$$\varepsilon = \frac{F_a}{AE} = \frac{F_a}{t^2 E} \qquad (A8)$$

By combining equations A2, A6, and A7 and substituting into equation A8 an expression for the axial strain in a strut is given by equation A9.

$$\varepsilon = \frac{S}{EC}\left\{\left[\frac{\sqrt{2}}{4}\sigma_\infty - \frac{(1-C)^{2/3}}{2} G \tan(\theta - \pi/4)\right]\left[\frac{1}{\sin\theta}\right] \mp \frac{2M}{\ell^3}\cot\theta\right\} \qquad (A9)$$

The first term in equation A9 is due to deformation of i-PP struts. The second term is due to shear deformation of the EPDM. The third term of equation A9 is due to i-PP plastic hinge rotation. The minus sign is used for loading and the plus sign is used for unloading. The rotational moment (M) will have two values: one corresponding to initial deformation that is within and elastic regime (M_e) and one corresponding to high levels of deformation within the plastic regime (M_p). M_e is given by equation A10 where σ is the maximum stress in the strut due to elastic bending.

$$M_e = \frac{1}{6}\sigma t^3 \qquad (A10)$$

A constraint is imposed so that the curvature of the strut remains constant. The strut curvature is given by equation A11.

$$\frac{1}{\rho} = \frac{M}{EI} = \frac{(\theta - \pi/4)}{\ell} \qquad (A11)$$

Upon substitution of equation A10 into A11, the maximum stress in the strut due to elastic bending is determined as equation A12.

$$\sigma = \frac{E}{2}\left(\frac{t}{\ell}\right)(\theta - \pi/4) \qquad (A12)$$

In the plastic regime deformation takes place through the formation of plastic hinges at the strut junction points. The plastic moment (M_p) of a fully plastic hinge is given by equation A13.

$$M_p = \frac{1}{4}\sigma_y t^3 \qquad (A13)$$

The normalized rotational moment (m) is defined as M/t^3. m_e is found by substituting equation A1 into A12 and combining with equation A10. The elastic and plastic values of m are given by equation A14 where the first term corresponds to m_e and the second corresponds to m_p.

$$m = \begin{Bmatrix} \alpha\sqrt{\frac{C}{S}}E(\theta - \pi/4) \\ 1/4\,\sigma_y \end{Bmatrix} \qquad (A14)$$

In equation A14, α is a factor that defines the degree of constraint on the struts and its value determines when plastic hinges form.

Assuming the elastomer to be incompressible, a relationship between θ and ε can be determined as in equation A15. Since there is no deformation in the third dimension, this is derived by keeping the area constant.

$$\theta = 1/2\sin^{-1}\left(\frac{1}{1+\varepsilon}\right)^2 \qquad (A15)$$

When equations A9, A14 and A15 are combined and rearranged an expression for the far-field stress can be written as in equation A16. Where the plus portion refers to the loading curve while the minus portion refers to the unloading curve.

$$\sigma_\infty = \sqrt{2}\left\{\frac{2EC\sin\theta}{S}\left(\frac{1}{\sqrt{\sin 2\theta}} - 1\right) + (1-C)^{2/3} G\tan(\theta - \pi/4) \pm 4m\left(\frac{C}{S}\right)^{3/2}\cos\theta\right\} \qquad (A16)$$

The corresponding uniaxial extension ratio (λ) is given by equation A17.

$$\lambda = \sqrt{2}(1+\varepsilon)\sin\theta \qquad (A17)$$

At large deformations the i-PP struts undergo plastic yielding. As a result, the deformation response of the RVE will be dependent on the strain history. As such it is necessary to calculate the imposed strain in relation to the maximum previous strain. The new unstrained length of a drawn strut (ℓ'_o) is given by equation A18 where ε_f is the maximum previous strain and ℓ_o is its original length.

$$\ell'_o = \ell_o\left(1+\varepsilon_f - \frac{\sigma_y}{E}\right) \qquad (A18)$$

A relationship between the new length of the drawn strut and its original length is given by equation A19.

$$\ell'_o + \Delta\ell' = \ell_o(1+\varepsilon) \qquad (A19)$$

The elastic strain (ε') in a newly drawn strut is then given by equation A20.

$$\frac{\Delta\ell'}{\ell'_o} = \varepsilon' \qquad (A20)$$

By combining equations A18, A19, and A20, an expression for the elastic strain in a newly drawn strut in terms of the maximum previous strain and strut material properties is given by equation A21.

$$\varepsilon' = \frac{\frac{\sigma_y}{E}+\varepsilon-\varepsilon_f}{1+\varepsilon_f-\frac{\sigma_y}{E}} \qquad (A21)$$

The resulting stress-strain behavior of the RVE can be calculated using A9, A16, A17, and A21. This analytical result describes the steady-state mechanical behavior in

terms of i-PP concentration (C), basic constituent properties (E, σ_y, and G), and geometric parameters (θ and α). Two critical conditions result from this type of analysis. The critical angle for plastic hinge formation occurs when $m_e = m_p$ and is given by equation A24.

$$\theta_{cp} = \left(\frac{\sigma_y}{4}\right)\frac{1}{\alpha\sqrt{\frac{C}{S}E}} + \frac{\pi}{4} \qquad (A24)$$

A critical angle also exists for the onset of strut yielding. This is derived by including the yield strain in equation A16 and is given by equation A25.

$$\theta_{cs} = \pi - \sin^{-1}\left(\frac{1}{1+\left(\frac{\sigma_y}{E}\right)}\right)^2 \qquad (A25)$$

Once the critical angle is reached, the i-PP struts begin to plastically yield and draw as they orient in the direction of the applied load. This strut orientation captures geometrical strain hardening to some degree.

5.8 References

(1) Karger-Kocsis, J. In *Polymer Blends and Alloys*; Shonaike, G. O.; Simon, G. P., Eds.; Marcel Dekker Inc.: New York, 1999; p 125.

(2) Coran, A. Y. In *Thermoplastic Elastomers - A Comprehensive Review*; Legge, N. R.; Holden, G.; Schroeder, H. E., Eds.; Hanser Publishers: Munich, 1987; Vol. 7, p 133.

(3) Coran, A. Y. *Rubber Chemistry and Technology* **1995**, *68*, 351.

(4) Coran, A. Y. *Industria della Gomma* **1992**, *36*, 46-48.

(5) Karger-Kocsis, J.; Kallo, A.; Szafner, A.; Bodor, G. *Polymer* **1979**, *20*, 37-43.

(6) Choudhary, V.; Varma, H. S.; Varma, I. K. *Polymer* **1991**, *32*, 2534-2540.

(7) Ellul, M. D.; Patel, J.; Tinker, A. J. *Rubber Chemistry and Technology* **1995**, *68*, 573-584.

(8) Ellul, M. D. *Plastics, Rubber and Composites Processing and Applications* **1997**, *26*, 137.

(9) Ellul, M. D. *Rubber Chemistry and Technology* **1998**, *71*, 244-276.

(10) Ellul, M. D. *Rubber Chemistry and Technology* **1998**, *71*, 1087.

(11) Wright, K. J.; Lesser, A. J. *Rubber Chemistry and Technology* **2001**, *74*, 677-687.

(12) Kikuchi, Y.; Fukui, T.; Okada, T.; Inoue, T. *Polymer Engineering and Science* **1991**, *31*, 1029-1032.

(13) Okamoto, M.; Shiomi, K.; Inoue, T. *Polymer* **1994**, *35*, 4618-4622.

(14) Boyce, M. C.; Kear, K.; Socrate, S.; Shaw, K. *Journal of the Mechanics and Physics of Solids* **2001**, *49*, 1073-1098.

(15) Boyce, M. C.; Socrate, S.; Kear, K.; Yeh, O.; Shaw, K. *Journal of the Mechanics and Physics of Solids* **2001**, *49*, 1323-1342.

(16) Boyce, M. C.; Yeh, O.; Socrate, S.; Kear, K.; Shaw, K. *Journal of the Mechanics and Physics of Solids* **2001**, *49*, 1343-1360.

(17) Arruda, E. M.; Boyce, M. C. *Journal of the Mechanics and Physics of Solids* **1993**, *41*, 389.

(18) Li, J. X.; Cheung, W. L. *Journal of Applied Polymer Science* **1999**, *72*, 1529-1538.

(19) Sano, H.; Usami, T.; Nakagawa, H. *Polymer* **1986**, *27*, 1497.

(20) Aurora, K. A.; Lesser, A. J.; McCarthy, T. J. *Polymer Engineering and Science* **1998**, *38*, 2055-2062.

(21) Gibson, L. G.; Ashby, M. F. *Cellular Solids: Structure and Properties*; Pergamon Press: Oxford, 1988.

CHAPTER 6

CONCLUSIONS AND SUGGESTIONS FOR FUTURE WORK

Strain-induced crystallization occurring in certain SEBS systems has been established by studying the internal energy changes using deformation calorimetry. Also, in-situ SAXD/WAXD deformation studies not only confirm strain-induced crystallization, but also provide a detailed picture of mechanisms of deformation in these materials. Additionally, continuous processing methods that produce long-range order in these materials have been demonstrated. The effect of these processing conditions on the modulus, apparent yield stress of these materials has been evaluated.

Strain-induced crystallization is a reversible way of enhancing the strength of SEBS materials. There is no crystallinity present in these SEBS materials at room temperature, thus making them good elastomers at service temperatures. But when they are stretched and the system starts to undergo damage, strain crystallization sets in and provides the extra strength required. This feature of strain-crystallization can be built into new block copolymer design so as to provide the additional enhancement in mechanical and thermal properties. For the specific case of SEBS systems, tuning the ratio of ethylene to butylene segments in the mid-block is the key to obtaining these desired properties. Inspired by the observations on SEBS block copolymers, new styrene ethylene-propylene styrene (SEPS) thermoplastic elastomeric systems are being tested for interesting energy changes using deformation calorimetry.

Also elastomeric ethylene-propylene, ethylene-butene and ethylene-hexene random copolymers with large comonomer contents could be studied for their ability to strain crystallize. Designing new systems such that they possess very little crystallinity at service temperatures, but enough regularity so that they strain-crystallize is just one of the directions that could be taken to enhance the mechanical behavior in applications. Deformation calorimetry could provide important information about the energetics of their deformation. Thus interesting ethylene-olefin systems can be intelligently designed keeping specific properties in mind.

In-situ SAXD/WAXD studies on block copolymers provide information about structural changes in morphology on deformation. Controlled SAXD/WAXD studies devoted to comparing the changes in structural features by changing the mid and end-blocks systematically can provide important information regarding the micro-buckling instability that occurs in these materials.

Processing SEBS block copolymers using simple techniques like extrusion and calendering produces ultra long-range order. These highly oriented systems produce property enhancement in one direction similar to unidirectional fiber reinforced composites. Producing laminates out of these with layers laid out in specific directions can produce systems with improved properties. Also, further in-situ morphological studies need to be performed on oriented systems to study their mechanical properties. Such studies could provide additional information about the onset of cylindrical rod breakage in these systems. Deformational calorimetry studies on such highly oriented systems could provide additional information about their energetics on deformation.

Confocal microscopy studies on EPDM/i-PP studies, along with SEM data provide evidence for treating these systems as filled-foams. Detailed morphological studies of deformation using an in-situ stretching device for confocal microscopy could validate the different modeling studies conducted. Further work needs to be done on characterizing the energetics of deformation of these materials. Additionally, the interface between these EPDM/i-PP blends needs to be studied more closely. Incorporating interface effects could further refine the analytical model presented for these EPDM/i-PP systems.

BIBILOGRAPHY

(1) Adams, G. W.; Farris, R. J. *J. Polym. Sci., Part B: Polym. Phys.* **1988**, *26*, 433-445.

(2) Adams, G. W., *Ph.D. Thesis*, Polymer Science and Engineering; University of Massachusetts: Amherst, 1987; p 255.

(3) Adams, J. L.; Quiram, D. J.; Graessley, W. W.; Register, R. A.; Marchand, G. R. *Macromolecules* **1998**, *31*, 201-204.

(4) Agarwal, N. *Ph.D. Thesis*, Polymer Science and Engineering; University of Massachusetts: Amherst, 1998; p 249.

(5) Aggarwal, S. L. *Polymer* **1976**, *17*, 938-956.

(6) Aggarwal, S. L.; Livigni, R. A. *Polym. Eng. Sci.* **1977**, *17*, 497-504.

(7) Albalak, R. J.; Thomas, E. L. *J. Polym. Sci., Part B: Polym. Phys.* **1993**, *31*, 37-46.

(8) Andrews, E. H. *Proc. Roy. Soc. (London)* **1964**, *A277*, 562-570.

(9) Andrews, E. H. *Proc. Royal Soc. (London) Ser. A* **1962**, *270*, 232-241.

(10) Androsch, R.; Stribeck, N.; Lupke, T.; Funari, S. S. *J. Polym. Sci. :Part B: Polym. Phys.* **2002**, *40*, 1919-1930.

(11) Arridge, R. G. C.; Folkes, M. J. *J. Phys. D: Appl. Phys.* **1972**, *5*, 344-360.

(12) Arruda, E. M.; Boyce, M. C. *Journal of the Mechanics and Physics of Solids* **1993**, *41*, 389.

(13) Aurora, K. A.; Lesser, A. J.; McCarthy, T. J. *Polymer Engineering and Science* **1998**, *38*, 2055-2062.

(14) Bates, F. S.; Fredrickson, G. H. *Ann. Rev. Phys. Chem.* **1990**, *41*, 525-557.

(15) Bates, F. S.; Fredrickson, G. H. *Physics Today* **1999**, *52*, 32.

(16) Beecher, J. F.; Marker, L.; Bradford, R. D.; Aggarwal, S. L. *J. Polym. Sci., Part C* **1969**, *26*, 117-134.

(17) Bekkedahl, N. *J. Research Natl. Bur. Standards (Research Paper No. 717)* **1934**, *13*, 411-431.

(18) Bekkedahl, N.; Wood, L. A. *J. Chem. Phys.* **1941**, *9*, 193.

(19) Bening, R. C.; Handlin J.R., D. L.; Sterna, L. L.; Willis, C., L.; US Patent Application Publication: USA, 2003.

(20) Boyce, M. C.; Kear, K.; Socrate, S.; Shaw, K. *Journal of the Mechanics and Physics of Solids* **2001**, *49*, 1073-1098.

(21) Boyce, M. C.; Yeh, O.; Socrate, S.; Kear, K.; Shaw, K. *Journal of the Mechanics and Physics of Solids* **2001**, *49*, 1343-1360.

(22) Boyce, M. C.; Socrate, S.; Kear, K.; Yeh, O.; Shaw, K. *Journal of the Mechanics and Physics of Solids* **2001**, *49*, 1323-1342.

(23) Bradford, E. B.;Vanzo, E. *J. Polym. Sci. : Part A-1* **1968**, *6*, 1661-1670.

(24) Campos-Lopez, E.; McIntyre, D.; Fetters, L. J. *Macromolecules* **1973**, *6*, 415-423.

(25) Choudhary, V.; Varma, H. S.; Varma, I. K. *Polymer* **1991**, *32*, 2534-2540.

(26) Coran, A. Y. In *Thermoplastic Elastomers - A Comprehensive Review*; Legge, N. R.; Holden, G.; Schroeder, H. E., Eds.; Hanser Publishers: Munich, 1987; Vol. 7, p 133.

(27) Coran, A. Y. *Industria della Gomma* **1992**, *36*, 46-48.

(28) Coran, A. Y. *Rubber Chemistry and Technology* **1995**, *68*, 351.

(29) Dale, W. C.; Baer, E. *Journal of Materials Science* **1974**, *9*, 369-382.

(30) Daniel, C.; Hamley, I. W.; Mortensen, K. *Polymer* **2000**, *41*, 9239-9247.

(31) Darby, M. I.; Kanellopoulos, V. N. *J. Phys. D: Appl. Phys.* **1987**, *20*, 298.

(32) Diamant, J.; Williams, M., C. *Polym. Eng. Sci.* **1989**, *28*, 207-220.

(33) Diamant, J.; Williams, M., C. *Polym. Eng. Sci.* **1989**, *29*, 227-234.

(34) Diamant, J.; Williams, M., C. *Polym. Eng. Sci.* **1989**, *29*, 235-243.

(35) Dlugosz, J.; Keller, A.; Pedemonte, E. *Kolloid Z. Polym.* **1970**, *242*, 1125.

(36) Ellul, M. D. *Rubber Chemistry and Technology* **1998**, *71*, 1087.

(37) Ellul, M. D.; Patel, J.; Tinker, A. J. *Rubber Chemistry and Technology* **1995**, *68*, 573-584.

(38) Ellul, M. D. *Plastics, Rubber and Composites Processing and Applications* **1997**, *26*, 137.

(39) Ellul, M. D. *Rubber Chemistry and Technology* **1998**, *71*, 244-276.

(40) Erman, B.; Mark, J. E. *Structures and Properties of RubberLike Networks*; Oxford University Press, 1997.

(41) Eynde, V. S.; Mathot, V.; Koch, M. H. J.; Reynaers, H. *Polymer* **2000**, *41*, 3437-3453.

(42) Fairclough, J. P. A.; Salou, C. L. O.; Ryan, A. J.; Hamley, I. W.; Daniel, C.; Helsby, W. I.; Hall, C.; Lewis, R. A.; Gleeson, A. J.; Diakun, G. P.; Mant, G. R. *Polymer* **2000**, *41*, 2577-2582.

(43) Falabella, R. *Ph.D. Thesis*, Polymer Science and Engineering; University of Massachusetts: Amherst, 1980; p 213.

(44) Farris, R. J.; Goldfarb, J. L. *Materials Research Society Symposium Proceedings* **1993**, *309*, 21-34.

(45) Farris, R. J.; Goldfarb, J. L. *Journal of Adhesion Science and Technology* **1993**, *7*, 853-868.

(46) Farris, R. J. *Ph.D. Thesis*, Civil Engineering; University of Utah, 1970.

(47) Farris, R. J.; Vrtis, J. K.; Jou, C.-S.; Chen, M. J.; Sheth, K. C. In *Relaxation Phenomenon in Polymers*; Ramamurthy, A. C., Ed.; ESD, The Engineering Society: Deaborn, Michigan, 1994; pp 37-53.

(48) Flory, P., J. *J. Chem. Phys.* **1947**, *1947*, 397-408.

(49) Folkes, M. J.; Keller, A. *Polymer* **1971**, *12*, 222-236.

(50) Folkes, M. J.; Keller, A.; Scalisi, F. P. *Kolloid Z.* **1973**, *251*, 1-4.

(51) Folkes, M. J., Ed. *Processing, structure, and properties of block copolymers / edited by M.J. Folkes*; Elsevier Applied Science Publishers, 1985.

(52) Fox, T. G., Jr.; Flory, P. J.; Marshall, R. E. *Rubb. Chem. Tech.* **1950**, *23*, 576-580.

(53) Fox, T. G., Jr.; Flory, P. J.; Marshall, R. E. *Rubb. Chem. Tech.* **1950**, *23*, 576-580.

(54) Gent, A. N. *Trans. Faraday. Soc.* **1954**, *50*, 521-533.

(55) Gent, A. N. *Rubb. Chem. Tech.* **1955**, *28*, 36-50.

(56) Gent, A. N.; Zhang, L.-Q. *J. Polym. Sci. : Part B: Polym. Phys.* **2001**, *39*, 811-817.

(57) Gibson, L. G.; Ashby, M. F. *Cellular Solids: Structure and Properties*; Pergamon Press: Oxford, 1988.

(58) Godovskii, Y. K.; Tarasov, S. G. *Vysokomolekulyarnye Soedineniya Seriya A* **1980**, *22*, 1613-1621.

(59) Godovskii, Y. K.; Tarasov, S. G. *Vysokomolekulyarnye Soedineniya Seriya A* **1977**, *19*, 2097-2103.

(60) Godovsky, Y. K.; Bessonova, N. P. *Thermochimica Acta* **1994**, *247*, 19-33.

(61) Godovsky, Y. K.; Bessonova, N. P. *Colloid. Polym. Sci.* **1983**, *261*, 645-651.

(62) Godovsky, Y. K. *Makromol. Chem. Suppl.* **1984**, *6*, 117-140.

(63) Goldfarb, J. L. *Ph.D. Thesis*, Polymer Science and Engineering; University of Massachusetts: Amherst, 1992; p 332.

(64) Hadziioannou, G.; Mathis, A.; Skoulis, A. *Colloid. Polym. Sci.* **1979**, *257*.

(65) Hamley, I. W. *Crystallization in Block Copolymers*; Springer-Verlag, 1999; Vol. 148.

(66) Hashimoto, T.; Saijo, K.; Kosc, M.; Kawai, H.; Wasiak, A.; Ziabicki, A. *Macromolecules* **1985**, *18*, 472-482.

(67) Hashiyama, M.; Gaylord, R.; Stein, R. S. *Makromolekulare Chemie* **1975**, *Suppl. 1*, 579-597.

(68) Hill, M. J.; Keller, A. *J. Macromol. Sci. , Phys.* **1971**, *5*, 591-615.

(69) Hill, M. J.; Keller, A. *J. Macromol. Sci., Phys.* **1969**, *3*, 153-169.

(70) Holden, G.; Legge, N. R.; Quirk, R.; Schroeder, H. E. *Thermoplastic Elastomers*, 2nd ed.; Hanser Publishers, 1996.

(71) Honeker, C. C.; Thomas, E. L. *Chem. Mater.* **1996**, 1702-1714.

(72) Honeker, C. C.; Thomas, E. L.; Albalak, R. J.; Hajduk, D. A.; Gruner, S. M.; Capel, M. C. *Macromolecules* **2000**, *33*, 9395-9406.

(73) Honeker, C. C.; Thomas, E. L. *Macromolecules* **2000**, *33*, 9407-9417.

(74) Hosoda, S.; Nomura, H.; Gotoh, Y.; Kihara, H. *Polymer* **1990**, *31*, 1999-2005.

(75) Huy, T. A.; Adhikari, R.; Michler, G. H. *Polymer* **2003**, *44*, 1247-1257.

(76) Indukuri, K. K.; Lesser, A. J. *Polymer* **2005**, *46*, 7218-7229.

(77) Indukuri, K. K.; Lesser, A. J. *Abstracts of Papers of the American Chemical Society* **2004**, *228*, U508-U508.

(78) Indukuri, K. K.; Atkins, E. T.; Lesser, A. J. *Journal of Applied Polymer Science* **2005**, *Submitted.*

(79) Indukuri, K. K.; Atkins, E. T.; Lesser, A. J. *Macromolecules* **2005**, *Submitted.*

(80) Inoue, T.; Masahiko, M.; Hashimoto, T.; Kawai, H. *Macromolecules* **1971**, *4*, 500-507.

(81) James, R. W. *The Optical Principles of the Diffraction of X-rays*; G. Bell and Sons: London, 1967; Vol. II.

(82) Karger-Kocsis, J.; Kallo, A.; Szafner, A.; Bodor, G. *Polymer* **1979**, *20*, 37-43.

(83) Karger-Kocsis, J. In *Polymer Blends and Alloys*; Shonaike, G. O.; Simon, G. P., Eds.; Marcel Dekker Inc.: New York, 1999; p 125.

(84) Keller, A.; Machin, M. J. *J. Macromol. Sci. Phys.* **1967**, *B1*, 41-91.

(85) Kikuchi, Y.; Fukui, T.; Okada, T.; Inoue, T. *Polymer Engineering and Science* **1991**, *31*, 1029-1032.

(86) Kofinas, P.; Cohen, R. E. *Macromolecules* **1994**, *27*, 3002-3008.

(87) Lee, S. H.; Bae, Y. C. *Macromecular chemistry and physics* **2000**, *201*, 1286-1291.

(88) Legge, N. R. *Rubb. Chem. Tech.* **1987**, *60*.

(89) Li, J. X.; Cheung, W. L. *Journal of Applied Polymer Science* **1999**, *72*, 1529-1538.

(90) Liu, L.; Hsiao, B. S.; Fu, B. X.; Ran, S.; Toki, S.; Chu, B.; Tsou, A. H.; Agarwal, P. K. *Macromolecules* **2003**, *36*, 1920-1929.

(91) Lodge, T., P. *Macromol. Chem. Phys.* **2003**, *204*, 265-273.

(92) Loo, Y. L.; Register, R. A.; Adamson, D. H. *Journal of Polymer Science Part B-Polymer Physics* **2000**, *38*, 2564-2570.

(93) Loo, Y. L.; Register, R. A.; Ryan, A. J. *Macromolecules* **2002**, *35*, 2365-2374.

(94) Loo, Y. L.; Register, R. A.; Adamson, D. H. *Macromolecules* **2000**, *33*, 8361-8366.

(95) Loo, Y. L.; Register, R. A.; Ryan, A. J.; Dee, G. T. *Macromolecules* **2001**, *34*, 8968-8977.

(96) Loo, Y.-L.; Register, R. A. *Developments in Block Copolymer Science and Technology*; Wiley, 2004.

(97) Luch, D.; Yeh, G. S. Y. *J. Appl. Phys.* **1972**, *43*, 4326-4338.

(98) Luch, D.; Yeh, G. S. Y. *J. Macromol. Sci. , Phys.* **1973**, *7*, 121-155.

(99) Luch, D.; Yeh, G. S. Y. *J. Polym. Sci., Polym. Phys. Ed.* **1973**, *11*, 467-486.

(100) Ludwik, L. *Macromolecules* **1980**, *13*, 1602-1617.

(101) Lyon, R. E.; Farris, R. J. *Thermochimica Acta* **1990**, *161*, 287-296.

(102) Lyon, R. E.; Raboin, P. J. *J. Therm. Anal.* **1995**, *44*, 777-793.

(103) Lyon, R. E.; Wang, D. X.; Farris, R. J.; MacKnight, W. J. *J. Appl. Polym. Sci.* **1984**, *29*, 2857-2872.

(104) Lyon, R. E. *Ph.D. Thesis*, Polymer Science and Engineering; University of Massachusetts: Amherst, 1985; p 214.

(105) Lyon, R. E.; Farris, R. J. *Rev. Sci. Instrum.* **1986**, *57*, 1640-1646.

(106) Lyon, R. E.; Farris, R. J. *Polym. Eng. Sci.* **1984**, *24*, 908-914.

(107) Mark, J. E. *Polym. Eng. Sci.* **1979**, *19*, 409-413.

(108) Mathot, V. B. F.; Scherrenberg, R. L.; Pijpers, T. F. J. *Polymer* **1998**, *39*, 4541-4559.

(109) Milberg, M. E. *J. Polym. Sci., Polym. Chem. Ed.* **1966**, *4*, 801-810.

(110) Morrison, F. A.; Winter, H. H. *Macromolecules* **1989**, *22*, 3533-3540.

(111) Mueller, C.; Gorius, A.; Nazarenko, S.; Hiltner, A.; Baer, E. *Journal of Materials Science* **1995**, *31*, 2747-2755.

(112) Muller, F. H.; Engelter, A. *Rheol. Acta* **1958**, *1*.

(113) Odell, J. A.; Keller, A. *Polym Eng & Sci* **1977**, *17*, 544.

(114) Okamoto, M.; Shiomi, K.; Inoue, T. *Polymer* **1994**, *35*, 4618-4622.

(115) Pakula, T.; Saijo, K.; Kawai, H.; Hashimoto, T. *Macromolecules* **1985**, *18*, 1294-1302.

(116) Seguela, R.; Prudhomme, J. *Macromolecules* **1988**, *21*, 635-643.

(117) Rangarajan, P.; Register, R. A.; Fetters, L. J. *Abstracts of Papers of the American Chemical Society* **1992**, *204*, 233-POLY.

(118) Rangarajan, P.; Register, R. A.; Fetters, L. J. *Macromolecules* **1993**, *26*, 4640-4645.

(119) Read, D. J.; Duckett, R. A.; Sweeney, J.; McLeish, T. C. B. *J. Phys. D: Appl. Phys.* **1999**, *32*, 2087-2099.

(120) Roberts, D. E.; Mandelkern, L. *J. Am. Chem. Soc.* **1958**, *80*, 1289-1297.

(121) Roberts, D. E.; Mandelkern, L. *J. Am. Chem. Soc.* **1955**, *77*, 781-786.

(122) Rottele, A.; Thurn-Albrecht, T.; Sommer, J.-U.; Reiter, G. *Macromoles* **2003**, *36*, 1257-1260.

(123) Sadowsky, M. A.; Pu, S. L.; Hussian, M. A. *J. Appl. Mech.* **1967**, *34*, 1967.

(124) Pakula, T.; Saijo, K.; Kawai, H.; Hashimoto, T. *Macromolecules* **1985**, *18*, 1294-1302.

(125) Hashimoto, T.; Saijo, K.; Kosc, M.; Kawai, H.; Wasiak, A.; Ziabicki, A. *Macromolecules* **1985**, *18*, 472-482.

(126) Sano, H.; Usami, T.; Nakagawa, H. *Polymer* **1986**, *27*, 1497.

(127) Scott, D. B.; Waddon, A. J.; Lin, Y.; Karasz, F. E.; Winter, H. H. *Macromolecules* **1992**, *25*, 4175-4181.

(128) Seguela, R.; Prudhomme, J. *Macromolecules* **1988**, *21*, 635-643.

(129) Okamoto, M.; Shiomi, K.; Inoue, T. *Polymer* **1994**, *35*, 4618-4622.

(130) Shirayama, K.; Kita, S.-I.; Watabe, H. *Die Makromolekulare Chemie* **1972**, *151*, 97-120.

(131) Sierra, C. A.; Galan, C.; Fatou, J. G.; Parellada, M. D.; Barrio, J. A. *Polymer* **1997**, *38*, 4325-4335.

(132) Rottele, A.; Thurn-Albrecht, T.; Sommer, J.-U.; Reiter, G. *Macromoles* **2003**, *36*, 1257-1260.

(133) Stein, R. S. *Polym. Eng. Sci.* **1976**, *16*, 152-157.

(134) Tarasov, S. G.; Tsvankin, D. Y.; Godovskii, Y. K. *Vysokomolekulyarnye Soedineniya Seriya A* **1978**, *20*, 1534-&.

(135) Tarasov, S. G.; Godovskii, Y. K. *Vysokomolekulyarnye Soedineniya Seriya A* **1980**, *22*, 1879-1885.

(136) Toki, S.; Fujimaki, T.; Okuyama, M. *Polymer* **2000**, *41*, 5423-5429.

(137) Trabelsi, S.; Albouy, P.-A.; Rault, J. *Macromolecules* **2003**, *36*, 7624-7639.

(138) Treolar, L. R. G. *The Physics of Rubber Elasticity*; Oxford University Press, 1975.

(139) Ungar, G.; Keller, A. *Polymer* **1980**, *21*, 1273-1277.

(140) Wright, K. J.; Lesser, A. J. *Rubber Chemistry and Technology* **2001**, *74*, 677-687.

(141) Wright, K. J.; Indukuri, K. K.; Lesser, A. J. *Rubber Chemistry and Technology* **2003**, *43*, 531-542.

(142) Yan, G.; White, J. R. *Polymer Engineering and Science* **1999**, *39*, 1856-1865.

(143) Yeh, G. S. Y. *Polym. Eng. Sci.* **1976**, *16*, 138-144.

(144) Zhao, Y. *Macromolecules* **1992**, *25*, 4705-4711.

(145) Zhu, Y.; Weidisch, R.; Gido, S., P.; Velis, G.; Hadjichristidis, N. *Macromolecules* **2002**, *35*, 5903-5909.